Optimally tuned secondary system with viscous damping for vibration suppression in torsional systems

Juan Melchor BACA VASQUEZ

A Thesis

in

The Department

of

Mechanical and Industrial Engineering

Presented in Partial Fulfillment of the Requirements

for the Degree of Master of Applied Science at

Concordia University

Montreal, Québec

Canada

June 2007

Your file Votre référence
ISBN: 978-0-494-34733-1
Our file Notre référence
ISBN: 978-0-494-34733-1

ABSTRACT

Optimally tuned secondary system with viscous damping for vibration suppression in torsional systems

Juan Melchor BACA VASQUEZ

Dynamic vibration absorbers and dampers are used to reduce the vibration responses of mechanical systems. A dynamic vibration absorber reduces vibrations of a primary system over a desired frequency range by absorbing the energy through responding with opposite phase to that of the force acting on the primary system. A damper, on the other hand, is a device used for reducing the magnitude of a shock or vibration by energy dissipation methods. The latter is extensively used in automotive engines to reduce torsional oscillations and in aircraft landing gears to damp out shimmy oscillations. This thesis aims to study and understand an optimally tuned viscous torsional vibration damper which is a combination of a dynamic vibration absorber and damper.

The primary system whose vibration is to be suppressed, along with the optimally tuned viscous torsional vibration damper, will form a two-degree-of-freedom system which will be studied for its dynamic behaviour. The analytical model includes parameters such as primary inertia, damping and stiffness and secondary inertia, damping and stiffness. Numerical determination of optimum damping and stiffness for a secondary system is carried out and simulated

results are presented and discussed. Validation of some aspects of the analytical studies is carried out with experimental investigation for the optimally tuned viscous torsional vibration damper and viscous damper. The test results of the two damping devices and the analytical investigations are compared.

In addition, the study is extended, applying the optimally tuned viscous torsional vibration damper to a seven-degree-of-freedom torsional system namely to a four-stroke six-in-line cylinder internal combustion engine. This numerical study compares the engine response with and without damping. For both cases same excitation torque per cylinder was applied. The optimally tuned viscous damper reduces the vibrations.

Dedicated to my mother

ACKNOWLEDGEMENTS

The author wishes to express his sincere appreciation and thanks to his supervisor Dr. Rama Bhat for his guidance, suggestions and continued encouragement throughout the course of this investigation.

Thanks also go to colleagues, faculty and staff at Concordia University and the Department of Mechanical Engineering.

Finally, the author would like to express his special thanks to his mother and his sister for their love, support and encouragement along the way.

TABLE OF CONTENTS

CHAPTER 2: ANALYTICAL INVESTIGATION

CHAPTER 3: EXPERIMENTAL INVESTIGATION

LIST OF FIGURES

LIST OF TABLES

LIST OF ABBREVATIONS

ISO	International Standard Organization
DOFS	Degree-of-Freedom System

NOMENCLATURE

Notation	Description	Units
	CHAPTER 1	
N_c	Running speed	RPM
	CHAPTER 2	
H_∞	H space	-
J_1	Moment of inertia, primary system	$kg.m^2$
J_2	Moment of inertia, secondary system	$kg.m^2$
K_1	Stiffness, primary system	$N.m/rad$
K_2	Stiffness, secondary system	$N.m/rad$
T_O	Excitation torque, amplitude	$N.m$
$T(t)$	Excitation torque	$N.m$
c_1	Damping, primary system	$N.m.s/rad$
c_2	Damping, secondary system	$N.m.s/rad$
c_c	Critical damping	$N.m.s/rad$
i	$\sqrt{-1}$	-
k	Stiffness ratio	-

k_{opt}	Optimum stiffness ratio	-
t	Time	s
x	Frequency ratio	-
Θ_1	Dynamic amplification factor, primary system	-
$\Theta_1 . K_1 / To$	Amplitude ratio, primary system	-
$\left\{ \Theta_1 . K_1 / To \right\}_{\min}$	Minimum maximum amplitude ratio, primary system	-
Θ_2	Dynamic amplification factor, secondary system	-
ε_1	Damping ratio, primary system	-
ε_2	Damping ratio, secondary system	-
ε_{2opt}	Optimum damping ratio, secondary system	-
θ_1	Angular displacement, primary system	rad
θ_2	Angular displacement, secondary system	rad
$\dot{\theta}_1$	Angular velocity, primary system	rad/s
$\dot{\theta}_2$	Angular velocity, secondary system	rad/s
$\ddot{\theta}_1$	Angular acceleration, primary system	rad/s^2
$\ddot{\theta}_2$	Angular acceleration, secondary system	rad/s^2
μ	Inertia mass ratio	-
ω	Excitation frequency	rad/s

ω_1	Natural frequency, primary system	rad/s
ω_2	Natural frequency, secondary system	rad/s

CHAPTER 3

A	Angle between horizontal axis and centerline of helical spring	deg
D	Rod diameter	m
G	Modulus of rigidity of steel shaft	GPa
I_p	Rod polar moment of inertia	m^4
J_{2A}	Moment of inertia, secondary system due to type A seismic mass	$kg.m^2$
J_{2B}	Moment of inertia, secondary system due to type B seismic mass	$kg.m^2$
K_{HS}	Helical spring stiffness	N/mm
K_1	Stiffness, primary system	$kg.m^2$
K_2	Stiffness, secondary system due to type A seismic mass	$kg.m^2$
L	Rod length	m
L_{SA}	Seismic mass width, type A	m
L_{SB}	Seismic mass width, type B	m
R	Radius for location of helical springs	m
Ro	Seismic-mass outer radius	m
c_{2A}	Damping, secondary system due to type A seismic mass	$N.m.s/rad$

c_{2B}	Damping, secondary system due to type B seismic mass	$N.m.s/rad$
dc	Lateral and peripheral clearance between seismic mass and casing	mm
ε_{1A}	Damping ratio, primary system due to type A seismic mass	-
ε_{1B}	Damping ratio, primary system due to type B seismic mass	-
ν_{SA}	Viscous fluid viscosity due to type A seismic mass	$centistokes$
ν_{SB}	Viscous fluid viscosity due to type B seismic mass	$centistokes$
ω_{1N}	Natural frequency, primary system without damper	rad/s
ω_1	Natural frequency, primary system with damper	rad/s
ω_2	Natural frequency, secondary system due to type A seismic mass	rad/s

CHAPTER 4

A	Piston area	m^2
A_j	Fourier constant for j th harmonic	$N.m$
A_0	Fourier constant	$N.m$
A_{0i}	Fourier constant for i th term of equivalent system	$N.m$
A_n	Fourier constant for n th term	$N.m$
B_j	Fourier constant for j th harmonic	$N.m$
B_n	Fourier constant for n th term	$N.m$
$F_G(\phi)$	Total pressure gas force	N

$F_{cG}(\phi)$	Connecting rod force, component from total pressure gas force	N
$F_{tG}(\phi)$	Tangential force	N
J_{E1}	Moment of inertia of damping device	$kg.m^2$
J_{E2}	Moment of inertia for cylinder 1	$kg.m^2$
J_{E2}	Moment of inertia for cylinder 1	$kg.m^2$
J_{E3}	Moment of inertia for cylinder 2	$kg.m^2$
J_{E4}	Moment of inertia for cylinder 3	$kg.m^2$
J_{E5}	Moment of inertia for cylinder 4	$kg.m^2$
J_{E6}	Moment of inertia for cylinder 5	$kg.m^2$
J_{E7}	Moment of inertia for cylinder 6	$kg.m^2$
J_{E8}	Moment of inertia for flywheel	$kg.m^2$
$\tilde{J}_c$	Decoupled moment of inertia for c th mode (without damping)	$kg.m^2$
K_{E2}	Stiffness between cylinder 1 and 2	$N.m/rad$
K_{E3}	Stiffness between cylinder 2 and 3	$N.m/rad$
K_{E4}	Stiffness between cylinder 3 and 4	$N.m/rad$
K_{E5}	Stiffness between cylinder 4 and 5	$N.m/rad$
K_{E6}	Stiffness between cylinder 5 and 6	$N.m/rad$
K_{E7}	Stiffness between cylinder 6 and flywheel	$N.m/rad$

$\tilde{K}_c$	Decoupled stiffness for c th mode (without damping)	$N.m/rad$
L	Connecting rod length	mm
M_C	Total connecting rod mass	kg
M_O	Total oscillating mass	kg
M_P	Total piston mass	kg
M_R	Total rotating mass	kg
M_{jc}	Dynamic magnifier for j th harmonic for a given c th mode	-
P_G	Combustion gas pressure	bar
P_{IO}	Inertia oscillation force	N
P_{IR}	Inertia rotating force	N
Ro	Journal radius	mm
T	Period for a four stroke engine	°
T_T	Total excitation torque on cylinder	$N.m$
T_{FT}	Total Fourier excitation torque per cylinder	$N.m$
$T_{FT}(t)_i$	Total Fourier excitation torque for i th term of equivalent system	$N.m$
T_{Ei}	Total excitation torque for i th term of equivalent system	$N.m$
T_G	Gas excitation torque on cylinder	$N.m$
T_I	Inertia excitation torque on cylinder	$N.m$

T_{IO}	Inertia oscillation torque	$N.m$
T_{IR}	Inertia rotating torque	$N.m$
d	Piston diameter	m
j	Number of harmonic	-
$y_p(\phi)$	Vertical displacement of piston at given crank angle ϕ	m
$\dot{y}_p(\phi)$	Vertical piston velocity at given crank angle ϕ	m/s
$\ddot{y}_p(\phi)$	Vertical piston acceleration at given crank angle ϕ	m/s^2
Ω	Excitation engine speed or engine running speed	rad/s
Ω_{nc}	c th natural frequency	rad/s
γ_c	Engine dynamic twist amplitude for c th mode	rad
δ_i	Phase angle for i th term (for cylinder only)	deg
φ	Connecting rod angle	deg
ξ_{jc}	Phase angle for j th harmonic for a given c th mode	deg
ϕ	Crank angle	deg
$\dot{\phi}$	Angular velocity of crankshaft	rad/s
ψ	Angular twist	rad
$\dot{\psi}$	Angular velocity	rad/s

$\ddot{\psi}$	Angular acceleration	rad/s^2
$[C_E]$	Damping matrix of multi DOFS	-
$[J_E]$	Inertia matrix of multi DOFS	-
$[K_E]$	Stiffness matrix of multi DOFS	-
$\{T_E\}$	Total excitation torque vector	-
$\{\Gamma_c\}$	c th mode shape vector	-
$\{\gamma\}$	Modal or principal coordinate vector	-
$\{\psi\}$	Angular twist vector	-
$\{\dot{\psi}\}$	Angular velocity vector	-
$\{\ddot{\psi}\}$	Angular acceleration vector	-

CHAPTER 1

INTRODUCTION

1.1 Introduction

A vibration absorber or damper is a device mounted on vibrating mechanical systems in order to suppress excessive vibrations and prevent discomfort, damage or failure due to vibration. In the present study, we will be studying a vibration absorber for torsional vibrations.

The torsional vibration absorber consists of an annular seismic mass, with a counter bore to hold the springs, enclosed in a casing. The peripheral and lateral gaps between the seismic mass and casing are filled with a viscous fluid. The optimum values for the spring stiffness and for the viscous fluid damping are determined from the dynamic analysis of the system behavior.

This new vibration absorber can be considered as the combination of two known types of dampers: the viscous damper type, also known as Houdaille damper and the spring damper type, also known as Frahm type. Further description of the two known types is covered in section 1.2.

The four definitions given below by ISO 2041:1990 (British Standard 3015) [5] are used for better understanding of the difference between a damper, an absorber and a detuner, which will be referred to throughout the thesis.

A- Damper; absorber: In vibration applications, a device used for reducing the magnitude of a shock or vibration by energy dissipation methods.

B- Dynamic vibration absorber: A device for reducing vibrations of a primary system over a desired frequency range by the transfer of energy to an auxiliary system in resonance so tuned that the force exerted by the auxiliary system is opposite in phase to the force acting on the primary system.

C- Detuner: An auxiliary vibratory system with an amplitude-dependent frequency characteristic which modifies the vibration characteristics of the main system to which it is attached. Note: An example is an auxiliary mass controlled by a non-linear spring.

D- Damping: The dissipation of energy with time or distance. Note: In the context of vibration and shock, damping is the progressive reduction of the amplitude with time.

1.2. Devices for controlling torsional vibrations [3]

In addition to the two types of dampers mentioned in section 1.1: viscous and spring dampers, there are, friction, rubber and pendulum dampers. In accordance with the definitions, there are also the dynamic vibration absorbers (without damping or with damping) and pendulum detuners. The pendulum damper is also considered as a rotating pendulum vibration absorber (without damping or with damping).

1.2.1 Viscous damper

The viscous damper, also known as untuned viscous-shear damper, or Houdaille damper, or torsional viscous-friction damper consists of an annular seismic mass enclosed in a casing. The peripheral and lateral gaps between these two members are filled with a viscous fluid, most commonly, silicone fluid [1]. As the silicone fluid is non-Newtonian fluid, the effective viscosity in the actuation is different from that in the operating condition with its complicated characteristics [2].

The viscous damper is considered untuned, since the seismic mass is acted upon only by the viscous torque transmitted by the fluid, and the complex elastic coupling member between the seismic mass and the casing is minimal or disregarded. Unlike 'tuned' dampers, the untuned viscous damper does not

introduce any additional resonance, but lowers the value of the natural frequency of the entire system while reducing the vibration amplitudes.

1.2.2 Spring damper

The spring damper is also known as tuned damper, because it is tuned to the resonant frequency of the system to reduce the torsional vibrations, while at other frequencies it may not be quite effective. The springs, due to the constant tension and compression, have a short life just like the damper.

1.2.3 Friction damper

The friction damper is also known as Lanchester damper. The friction damper absorbs energy when the torsional vibration force is greater than the static friction force set between the surfaces of the damping mass and the vibrating system.

1.2.4 Dynamic vibration absorber with damping

The tuning disk with damping or dynamic vibration absorber with damping is the type of damper which has its seismic mass elastically and directly connected to the crankshaft and for which the damping can be regarded as proportional to vibration velocity; i.e., rubber dampers, and dampers of the viscous type (with silicone fluid).

As a general rule, all such types of dampers require tuning. In contrast to tuning disks without damping, those with damping do not necessarily fulfill all requirements when tuned to the natural frequency of the original system.

1.2.5 Dynamic vibration absorber without damping

The tuning disk without damping is also known as tuning flywheel, harmonic balancer or dynamic vibration absorber without damping. Where a resonance peak occurs at speed N_c in the running range of an engine, it is possible to reduce the torsional vibration amplitude at this speed by mounting, at the front end of the crankshaft, a disk with suitable moment of inertia.

Although the tuning disk eliminates the peak at engine speed N_c, it also adds a further possible mode of vibration to the engine system so that with the tuning disk, two peaks are obtained on either side of the original resonance curve.

1.2.6 The pendulum damper or rotating pendulum vibration absorber

The pendulum damper or rotating pendulum vibration absorber or auxiliary vibratory system (damped or undamped) is a device elastically connected to the main system to modify the vibration characteristics of the main system to which it is attached.

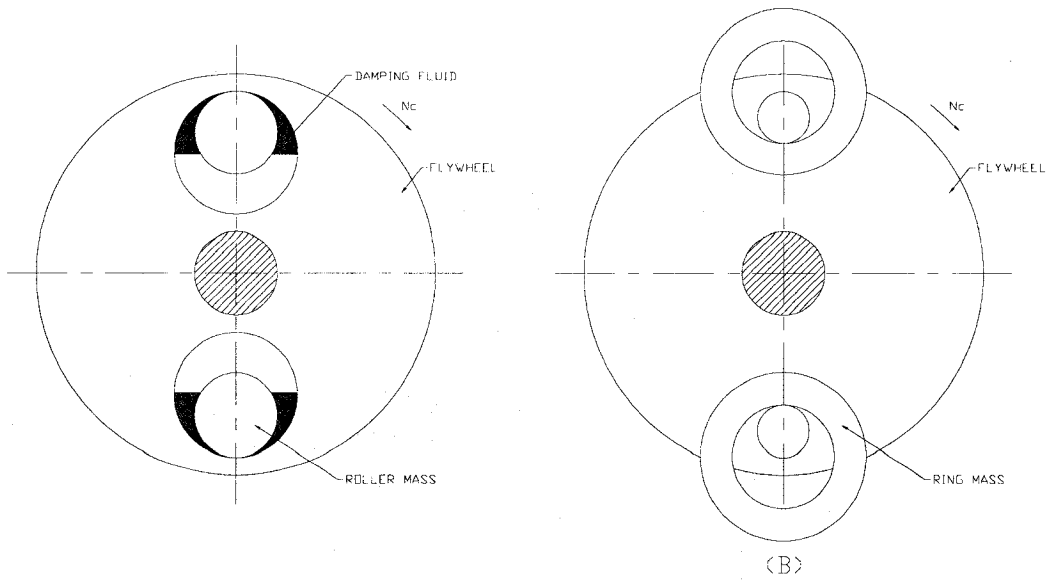

Figure 1.1: Rotating pendulum vibration absorbers. (A) Roll form (damped) and (B) Ring form (undamped)

The flywheel on figure 1.1 rotating at its natural speed N_c, causes the system to vibrate. Then, the roller or ring masses absorb the torsional oscillations by an opposing torque.

1.2.7 Detuner

A detuner is one of the solutions for reducing the galloping [31] in overhead conductors (bundles). Galloping on transmission lines (overhead conductors) is a low frequency, large amplitude, wind-induced vibration of both single and bundle-overhead transmission lines, with a single or a few standing waves per span [32]

(see figure 1.2 [33]). The ice formation in colder climates facilitates such galloping motion [8].

This anti-galloping device is based on the fact that the torsional motion of the bundle interacts dynamically with the vertical motion. The moderate cross-blowing wind over the conductor with asymmetric cross section due to ice formations produces the torsional motion. When this torsional motion tunes with the frequency of the vertical movement, it produces instability. In order to separate these frequencies from the vertical and torsional motion, a detuner (see figure 1.3) is used in order to suppress the galloping phenomenon.

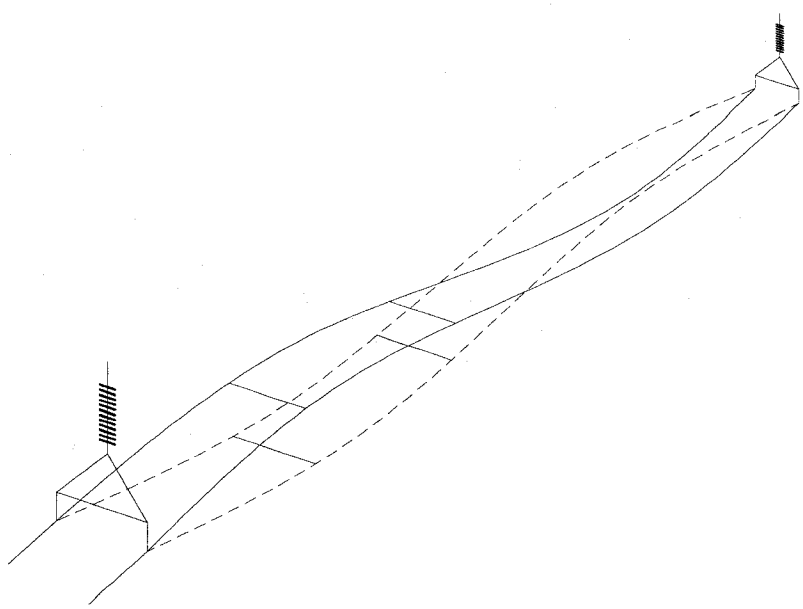

Figure 1.2: Vertical / horizontal galloping on overhead transmission lines [33]

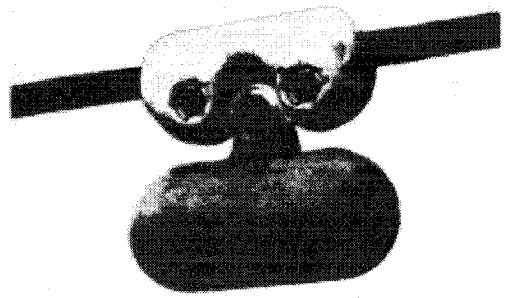

Figure 1.3: Detuner for vertical / horizontal galloping

1.3 Shimmy damper

The shimmy damper is another type of torsional vibration damper used in landing gears of aircraft. The surface irregularities on the runway for landing and takeoff, tire non-uniformity, and worn landing gear components induce oscillatory motion in small aircraft nose wheels during takeoff, landing, and taxiing. This oscillation, called nose-wheel shimmy, is similar to a caster wheel wobbling on a shopping cart. Instability results if the oscillation grows, and hence small aircraft nose gear typically uses shimmy dampers to lessen oscillatory effects by reducing the amplitude or preventing shimmy oscillations [10].

1.4 Survey of work done.

History

The use of torsional vibration dampers started around 1909. The main reason for their use was to reduce the torsional dynamic twist in engine crankshafts in order

to prevent serious damage. It was found that this torsional dynamic twist was severe when the engine was running near or at the resonant speed of the crankshaft. Several types of dampers were being developed at around that time: spring, friction, pendulum, rubber, pumper and viscous dampers [14].

Around 1930, George J. Dashefsky, developed a viscous damper similar in construction to the later Houdaille damper. For the viscous medium he used furniture glue, which made it quite successful [18].

The mathematical model for the viscous damper was developed by Bernard E. O'Connor in 1947. This model showed the silicone fluid as efficient damping medium. Therefore, the invention of this viscous damper is attributed to Bernard E. O'Connor[13].

Viscous damper

The viscous damper has been extensively investigated from different points of view such as its manufacturing, dynamic characteristics, design, and test experiments.

One of the manufacturing considerations for the viscous damper with regard to the silicone fluid is the shear rate, which is a direct function of the speed, and inversely related to the clearance between the casing and seismic mass of damper. The shear rate will be relatively low and hence steel on steel using

silicone oil will operate satisfactorily. However, when the shear rate is high and the quality of the silicone oil is poor, the rubber surfaces of the damper may gall and eventually the seismic mass will weld onto the casing. Therefore, nickel or cadmium is recommended for plating the surfaces when silicone oil is used [11].

The complicated dynamic characteristics of the silicone oil generally depend on the temperature, frequency and strain rate effects. Theoretical and experimental studies for these characteristics were carried out using the transfer matrix method for three dampers with diverse viscosity of silicone oils [2].

One design consideration is the peripheral and lateral gaps between the seismic mass and the casing. The gaps play an important role in the energy dissipation by shear resistance of the silicone oil due to the relative velocity between the seismic mass and the casing. Experiments were carried out with changes of the viscosity and gap dimension [1].

Experiments on a viscous friction damper for vibrations in axial, torsional and two lateral directions were carried out. The effects of these vibrations that simultaneously occur in the crankshaft of a multi-cylinder engine fitted with a viscous damper were investigated analytically and experimentally [12].

The desirable properties for the viscous fluid are that the fluid be stable and noncorrosive at fairly high temperatures and have a relatively flat viscocity-

temperature curve over a wide range and furthermore, the viscosity should not change appreciably with high rates of shear [18]. An undesirable property of silicone oil is its lack of oiliness under thin-film conditions with certain combinations of materials. Reference [34] gives a list of good, indifferent, and poor combinations of metals using silicone oil.

Vibration absorbers

Early studies on the dynamic vibration absorbers considered springs for both primary and secondary systems. The secondary one (auxiliary mass) tuned to primary one at a suitable location and properly designed, reduces vibrations of the machine. However, it creates two critical speeds in the machine system making it suitable for constant-speed machinery only [6, 9, 19, 20, 24, 25, 30, 36].

For studies on a complete dynamic vibration absorber: spring for each, primary and secondary systems were included, with damping for primary and secondary systems as well. When there is damping in the primary system, there are no points of intersection of all curves; however, there will still be a curve with two minimum equal values of magnification factor that can only be determined numerically [21, 22, 23, 24, 25]. An analytical solution using series was performed up to certain limits with error and so far, an exact solution is probably impossible [15, 16].

1.5 Objectives and scope of the thesis

This thesis aims to study a viscous vibration damper with elastic coupling between the seismic mass and casing. The primary system whose vibration is to be suppressed, along with the spring dashpot damper, will form a 2-DOFS which will be studied for its dynamics. Numerical results will be presented and discussed.

Results will be compared with those for conventional viscous dampers and the analytical results will be validated using experiments.

In addition, the research is extended to the application on a 7-DOFS, four-stroke six-in-line cylinder internal combustion engine for the comparison of two different responses.

1.6 Organization of the thesis

In Chapter 1, an introduction to the spring dashpot vibration absorber, definitions and a short description for some of each different type of damping device are given. The literature review mentions references on the viscous damper, the viscous fluid, and the dynamic vibration absorber. The application of the spring dashpot damper in landing gears gives an insight into the research, motivation and scope of the thesis undertaken.

In Chapter 2, a detailed mathematical model for the equation of motion is derived from the 2-DOFS. Numerical derivation of optimum damping and stiffness for secondary system is performed and simulated results are presented and discussed.

In Chapter 3, the design and manufacture of main components for an actual 2-DOFS are carried out for the experimental investigation to validate theoretical results with two types of seismic mass allocated in the same casing. The two types of seismic mass are used to compare the experimental results between optimally tuned viscous damper and viscous damper.

In Chapter 4, we extend the study, applying some of those optimum values found in Chapter 2, to a 7-DOFS: four-stroke six-in-line cylinder internal combustion engine. The analytical study compares the response for two different cases. The first case is the amplitude response of the engine without a damping device and the second case is the response with the optimally tuned viscous damper. For both cases, the same excitation torque per cylinder was applied.

In Chapter 5, conclusions of results are presented for the work undertaken, and recommendations for future work are given.

CHAPTER 2

ANALYTICAL INVESTIGATION

2.1 Introduction

In this chapter, a detailed mathematical model for the equation of motion is derived for the 2-DOFS. Numerical derivation of optimum damping and stiffness for secondary system is performed, and simulated results are presented and discussed.

The new optimally tuned viscous damper with the elastic coupling K_2 and damping c_2, will also consist of an annular seismic mass enclosed in a casing. The peripheral and lateral gaps between these two members are also filled with silicone fluid. In addition, a counter bore on the outer periphery of the seismic mass will locate the helical springs which are also immersed in the viscous fluid.

The optimally tuned viscous damper could be considered either as untuned, since the seismic mass is freely floating in oil inside the casing and acted upon by the viscous torque transmitted by the fluid, or as tuned since the seismic mass is acting elastically, coupled by the torque transmitted.

2.2 Equations of motion

The two-degree-of-freedom system is excited by a torque $T(t) = T_O.e^{i\omega t}$ on the primary system as shown on figure 2.0.

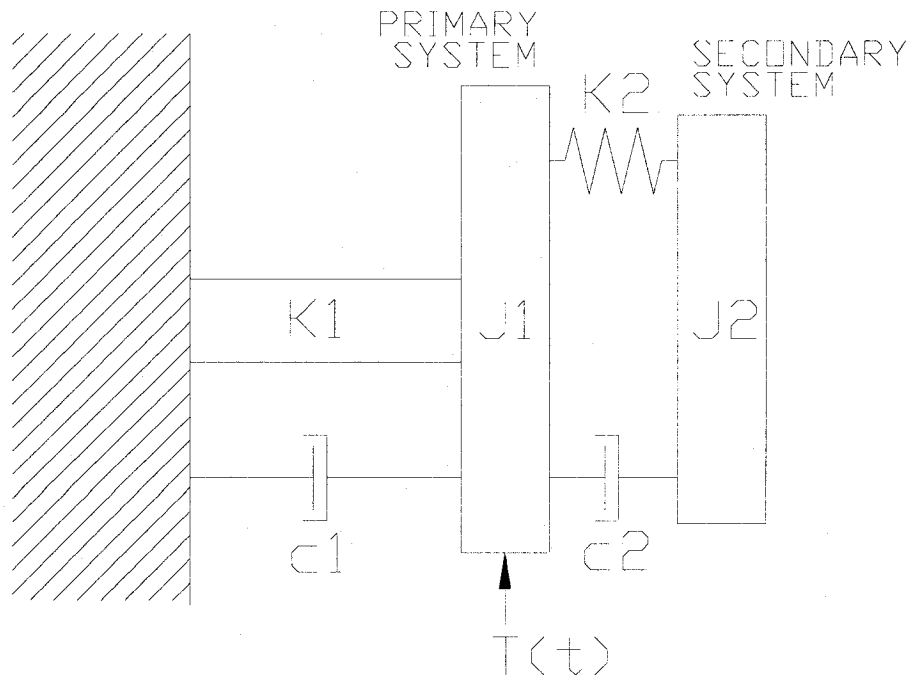

Figure 2.1: Two-degree-of-freedom system with stiffness and damping on primary and secondary systems.

$$J_1.\ddot{\theta}_1 + c_1.\dot{\theta}_1 + K_1.\theta_1 + c_2.(\dot{\theta}_1 - \dot{\theta}_2) + K_2.(\theta_1 - \theta_2) = T_O.e^{i\omega t} \quad (2.1)$$

$$J_2.\ddot{\theta}_2 + c_2.(\dot{\theta}_2 - \dot{\theta}_1) + K_2.(\theta_2 - \theta_1) = 0 \quad (2.2)$$

Let the solutions for the angular amplitudes of the above equations be:

$$\begin{aligned} \theta_1(t) &= \Theta_1.e^{i\omega t} & \theta_2(t) &= \Theta_2.e^{i\omega t} \\ \dot{\theta}_1(t) &= \omega.i.\Theta_1.e^{i\omega t} & \dot{\theta}_2(t) &= \omega.i.\Theta_2.e^{i\omega t} \\ \ddot{\theta}_1(t) &= -\omega^2.\Theta_1.e^{i\omega t} & \ddot{\theta}_2(t) &= -\omega^2.\Theta_2.e^{i\omega t} \end{aligned} \quad (2.3)$$

Replacing equation 2.3 on equations 2.1 and 2.2 and rearranging the variables we obtain:

$$\{J_1.(-\omega^2.\Theta_1)+c_1.(\omega.i.\Theta_1)+K_1.(\Theta_1)+c_2.[\omega.i.(\Theta_1-\Theta_2)]+K_2.(\Theta_1-\Theta_2)\}.e^{i\omega t}=T_O.e^{i\omega t}$$

$$\left(-J_1.\omega^2+c_1.\omega.i+K_1+c_2.\omega.i+K_2\right).\Theta_1+(-c_2.\omega.i-K_2).\Theta_2=T_O \qquad (2.4)$$

$$\{J_2.(-\omega^2.\Theta_2)+c_2.[\omega.i.(\Theta_2-\Theta_1)]+K_2.(\Theta_2-\Theta_1)\}.e^{i\omega t}=0$$

$$(-c_2.\omega.i-K_2).\Theta_1+\left(-J_2.\omega^2+c_2.\omega.i+K_2\right).\Theta_2=0 \qquad (2.5)$$

Expressing equations (2.4) and (2.5) in matrix form:

$$\begin{bmatrix}\left(-J_1.\omega^2+(c_1+c_2).\omega.i+K_1+K_2\right) & (-c_2.\omega.i-K_2)\\ (-c_2.\omega.i-K_2) & \left(-J_2.\omega^2+c_2.\omega.i+K_2\right)\end{bmatrix}\begin{Bmatrix}\Theta_1\\ \Theta_2\end{Bmatrix}=\begin{Bmatrix}T_O\\ 0\end{Bmatrix} \qquad (2.6)$$

Introducing the five following nondimensional variables:

$$\begin{aligned}\varepsilon_1 &= c_1 \big/ 2.J_1.\omega_1\\ \varepsilon_2 &= c_2 \big/ 2.J_2.\omega_2\\ k &= K_2/K_1\\ \mu &= J_2/J_1\\ x &= \omega/\omega_1\end{aligned} \qquad (2.7)$$

where: $\omega_1=\sqrt{\dfrac{K_1}{J_1}}$ and $\omega_2=\sqrt{\dfrac{K_2}{J_2}}$

Substituting the nondimensional variables 2.7 in equation 2.6, expanding and rearranging the variables we obtain:

$$\begin{bmatrix}\left(-x^2+2.\varepsilon_1.x.i+2.\varepsilon_2.\sqrt{\mu.k}.x.i+1+k\right) & (-2.\varepsilon_2.\sqrt{\mu.k}.x.i-k)\\ (-2.\varepsilon_2.\sqrt{\mu.k}.x.i-k) & \left(-\mu.x^2+2.\varepsilon_2.\sqrt{\mu.k}.x.i+k\right)\end{bmatrix}\begin{Bmatrix}\dfrac{\Theta_1.K_1}{T_O}\\ \dfrac{\Theta_2.K_1}{T_O}\end{Bmatrix}=\begin{Bmatrix}1\\ 0\end{Bmatrix} \qquad (2.8)$$

Solving matrix equation (2.8) using Cramer's rule:

$$\frac{\Theta_1.K_1}{T_O} = \frac{\begin{vmatrix} 1 & (-2.\varepsilon_2.\sqrt{\mu.k}.x.i - k) \\ 0 & \left(-\mu.x^2 + 2.\varepsilon_2.\sqrt{\mu.k}.x.i + k\right) \end{vmatrix}}{\begin{vmatrix} \left(-x^2 + 2.\varepsilon_1.x.i + 2.\varepsilon_2.\sqrt{\mu.k}.x.i + 1 + k\right) & (-2.\varepsilon_2.\sqrt{\mu.k}.x.i - k) \\ (-2.\varepsilon_2.\sqrt{\mu.k}.x.i - k) & \left(-\mu.x^2 + 2.\varepsilon_2.\sqrt{\mu.k}.x.i + k\right) \end{vmatrix}} \tag{2.9}$$

$$\frac{\Theta_2.K_1}{T_O} = \frac{\begin{vmatrix} \left(-x^2 + 2.\varepsilon_1.x.i + 2.\varepsilon_2.\sqrt{\mu.k}.x.i + 1 + k\right) & 1 \\ (-2.\varepsilon_2.\sqrt{\mu.k}.x.i - k) & 0 \end{vmatrix}}{\begin{vmatrix} \left(-x^2 + 2.\varepsilon_1.x.i + 2.\varepsilon_2.\sqrt{\mu.k}.x.i + 1 + k\right) & (-2.\varepsilon_2.\sqrt{\mu.k}.x.i - k) \\ (-2.\varepsilon_2.\sqrt{\mu.k}.x.i - k) & \left(-\mu.x^2 + 2.\varepsilon_2.\sqrt{\mu.k}.x.i + k\right) \end{vmatrix}} \tag{2.10}$$

Note that instead of the stiffness ratio $k = K_2 / K_1$, we could have used the frequency ratio $f = \omega_2 / \omega_1$. However, for the optimally tuned viscous damper, the behavior of the elastic coupling is directly seen on the stiffness K_2 for the secondary system through the stiffness ratio k.

2.3 Numerical analysis

The numerical analysis consists of the numerical evaluation of equation 2.9. The amplitude ratio $\Theta_1.K_1 / T_O$ is a function of five variables (ε_1 , ε_2 , k , μ , x) in search of the optimum values for all the variables.

An exact analytical solution is practically impossible when primary damping ratio ε_1 is different from zero and the optimization method used in this numerical evaluation is the H_∞ optimization which minimizes the dynamic magnifier Θ_1 of the primary system [15].

The equation 2.9 is solved and the numerical results are presented in two sections: section 2.3.1 which corresponds to the primary damping ratio ε_1 = 0, and section 2.3.2, which corresponds to $\varepsilon_1 \neq 0$.

2.3.1 Numerical analysis when ε_1 = 0

This section presents plots when the primary system has no damping ε_1 = 0, which is the common case also studied and discussed in several papers.

Figures 2.2, 2.3 and 2.4 correspond to the plots in 2D space for equation 2.9, $\Theta_1.K_1/T_O$ versus x for six different values for each ε_2 , k and μ.

A 3D representation of results of equation 2.9 is presented in figures 2.5, 2.8 and 2.11, $\Theta_1.K_1/T_O$ versus x and ε_2 , k and μ , respectively.

Figures 2.6 and 2.7 are side views for figure 2.5; 2.9 and 2.10 for 2.8; 2.12 and 2.13 for 2.11.

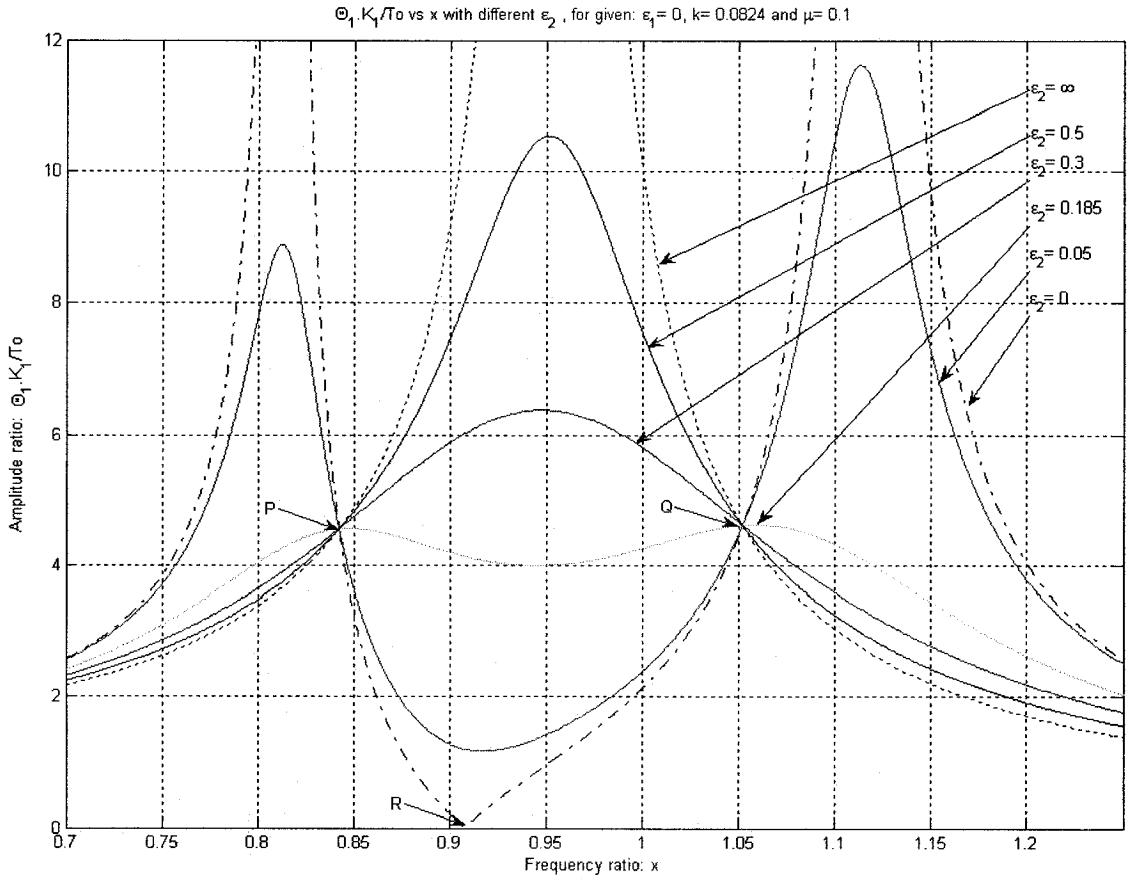

Figure 2.2 Plot of amplitude versus frequency, given: primary damping $\varepsilon_1 = 0$, for different secondary damping ε_2, stiffness k = 0.0826 and mass $\mu = 0.1$

Figure 2.2 shows the plot of amplitude ratio $\Theta_1.K_1/T_o$ vs frequency ratio x for different secondary damping ratio ε_2 = 0, 0.05, 0.185, 0.3, 0.5, ∞; given the other variables as constants: primary damping ratio ε_1 = 0, stiffness ratio k = 0.0826 and mass ratio $\mu = 0.1$.

All the curves pass by two fixed points P and Q. A curve with two equal peaks passes through these two fixed points, where ε_2 = 0.185 , $\Theta_1.K_1/T_o$ = 4.595 and, x = 0.848 and 1.06.

In the case where ε_2 = 0, the system is undamped and the two natural frequencies are obtained as the roots of the frequencies equation, which is the denominator of equation 2.9 equated to zero, where the amplitude ratio is infinity at x = 0.8144 and 1.1160 . Figure 2.2 also shows that the amplitude ratio is zero at point R when x = 0.9077, which is obtained equating the numerator of equation 2.9 to zero.

When ε_2 = ∞, there is only one natural frequency which corresponds to that in figure 2.2 where the amplitude ratio is infinity, which occurs at x = 0.9535.

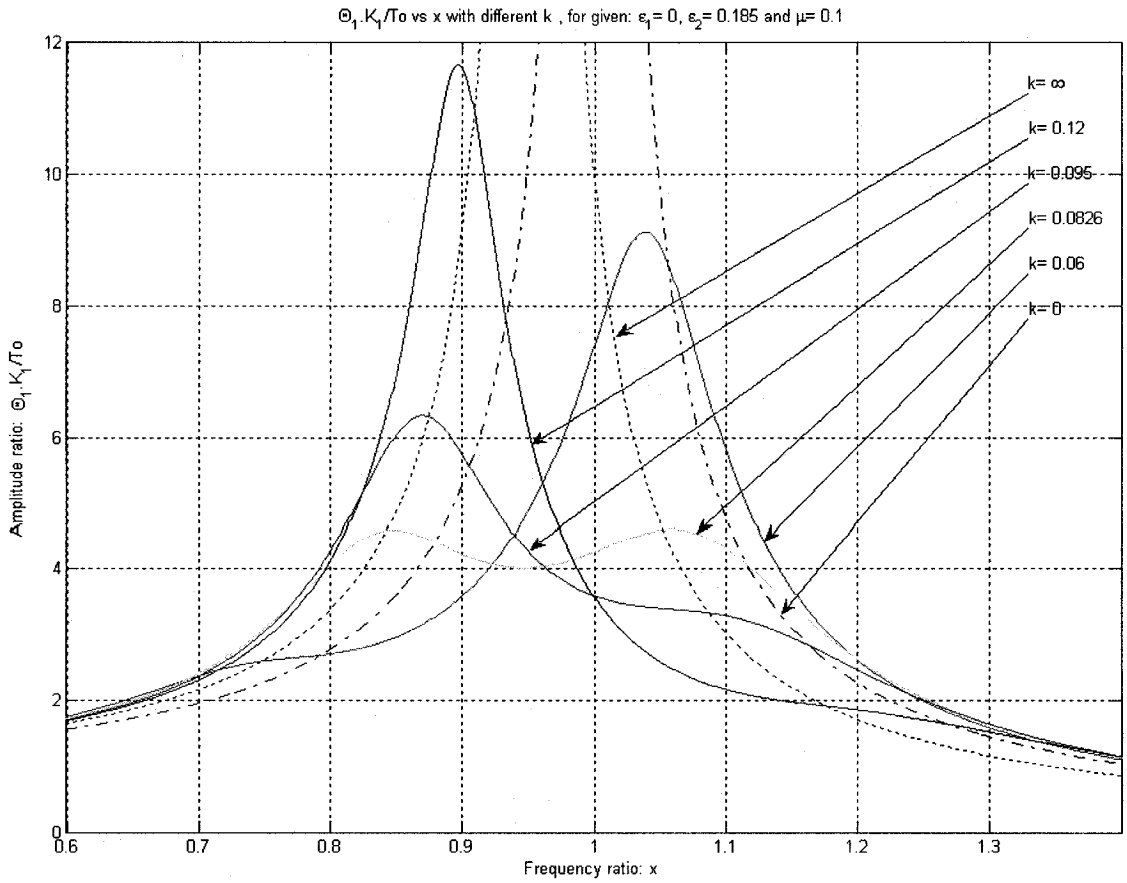

Figure 2.3 Plot of amplitude versus frequency, given: primary damping $\varepsilon_1 = 0$, for secondary damping $\varepsilon_2 = 0.185$, different stiffness k and mass $\mu = 0.1$

Figure 2.3 shows the plot of amplitude ratio $\Theta_1.K_1/T_O$ vs frequency ratio x for different stiffness ratio k = 0, 0.06, 0.0826, 0.095, 0.12, ∞; given the other variables as constants: primary damping ratio $\varepsilon_1 = 0$, secondary damping ratio $\varepsilon_2 = 0.185$, and mass ratio $\mu = 0.1$.

All the curves do not pass through any common fixed point nor are the curves contained within the limits for k = 0 and k = ∞; however, the curve with two equal

peaks has the same values for k = 0.0826, $\Theta_1.K_1/T_o$ = 4.595 and, x = 0.848 and 1.06.

In the case where k = 0, there is only one maximum peak with $\Theta_1.K_1/T_o$ = 5000 (not shown in figure 2.3) at x = 1. When $k = \infty$, there is also only one maximum peak with $\Theta_1.K_1/T_o$ = 12730 (not shown in figure 2.3) at x = 0.9535, which is the same value obtained in figure 2.2.

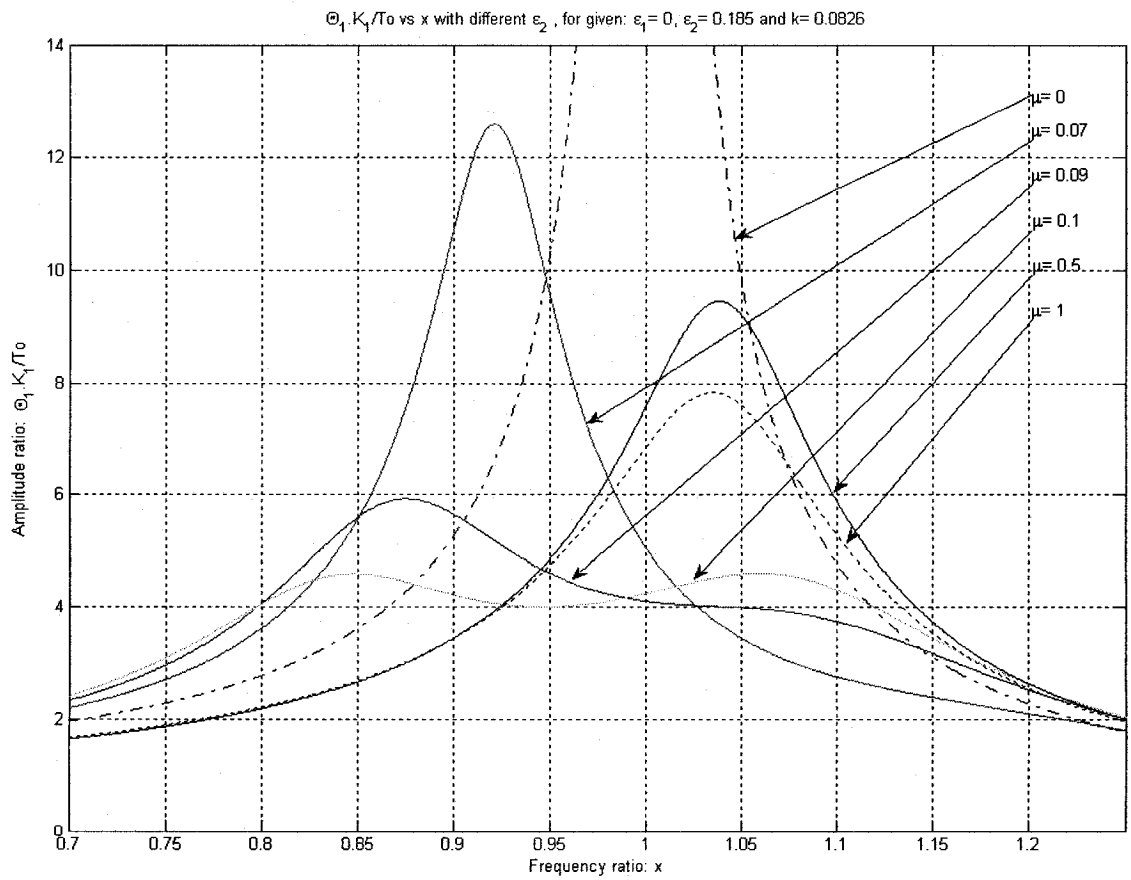

Figure 2.4 Plot of amplitude versus frequency, given: primary damping $\varepsilon_1 = 0$, for secondary damping ε_2 = 0.185, stiffness k = 0.0826 and different mass μ.

Figure 2.4 shows the plot of amplitude ratio $\Theta_1.K_1/T_o$ vs frequency ratio x for different mass ratio μ = 0, 0.07, 0.09, 0.1, 0.1, 1; given the other variables as constants: primary damping ratio $\varepsilon_1 = 0$, secondary damping ratio ε_2 = 0.185, and stiffness ratio k = 0.0826.

All curves do not pass through any common fixed point nor are the curves contained within the limits for μ = 0 and μ = 1; however, the curve with two equal peaks has the same values for k = 0.0826, $\Theta_1.K_1/T_o$ = 4.595 and, x = 0.848 and 1.06, as shown in figure 2.2.

It is also seen in figure 2.4 that when μ = 0, there is only one maximum peak with $\Theta_1.K_1/T_o$ = 10000 at x = 1; and when μ = 1, there is also only one peak with $\Theta_1.K_1/T_o$ = 7.831 at x = 1.035.

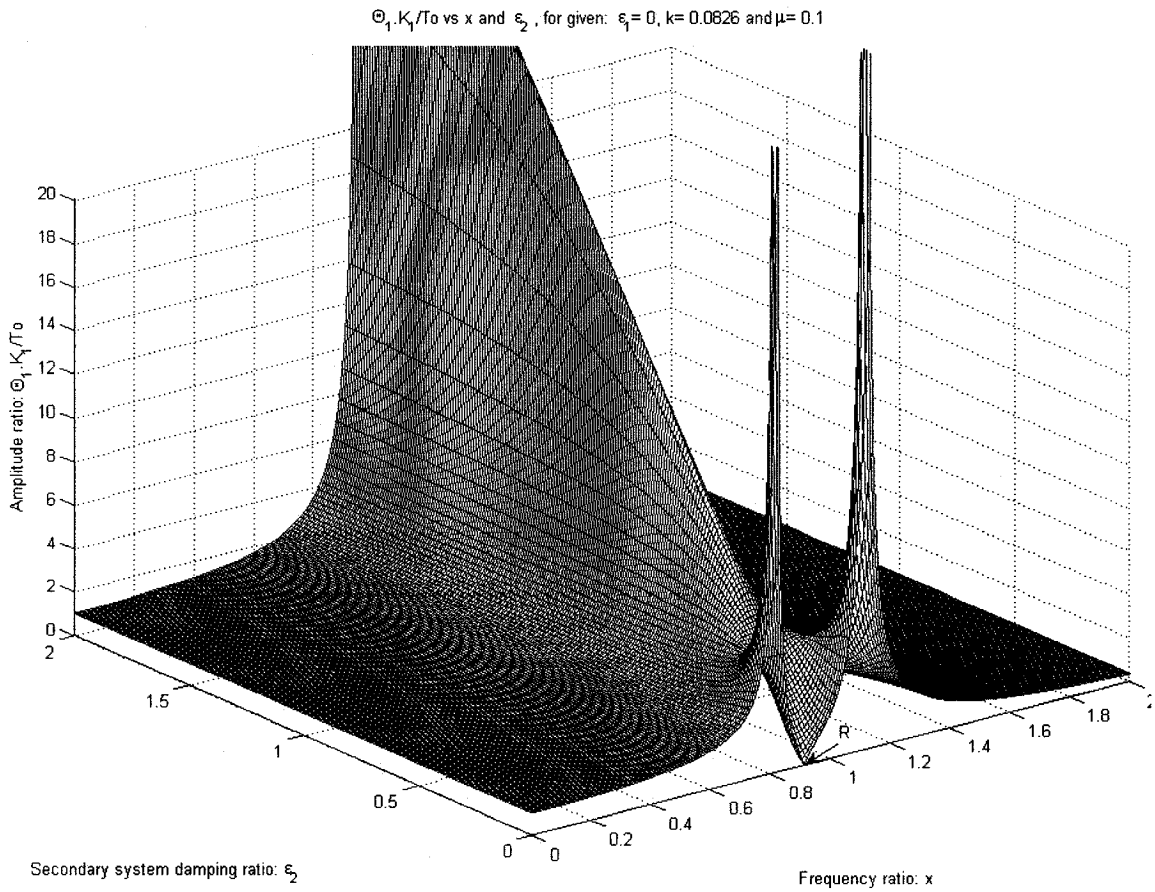

Figure 2.5 Plot of amplitude versus frequency and secondary system damping, given: primary damping $\varepsilon_1 = 0$, stiffness k = 0.0826 and mass μ = 0.1.

Figure 2.5 shows a 3D plot of amplitude ratio $\Theta_1.K_1/T_O$ vs frequency ratio x and secondary damping ratio ε_2; given the other variables as constants: primary damping ratio $\varepsilon_1 = 0$, stiffness ratio k = 0.0826 and mass ratio μ = 0.1.

In the case where ε_2 = 0, the system is undamped and the two natural frequencies are obtained as the roots of the frequencies equation, which is the denominator of equation 2.9 equated to zero. These are also seen in figure 2.2

and 2.5 where the amplitude ratio is infinity, which happens at x = 0.8144 and 1.1160.

When $\varepsilon_2 = \infty$, there is only one natural frequency which corresponds to that in figure 2.2 and 2.5 where the amplitude ratio is infinity, which occurs at x = 0.9535.

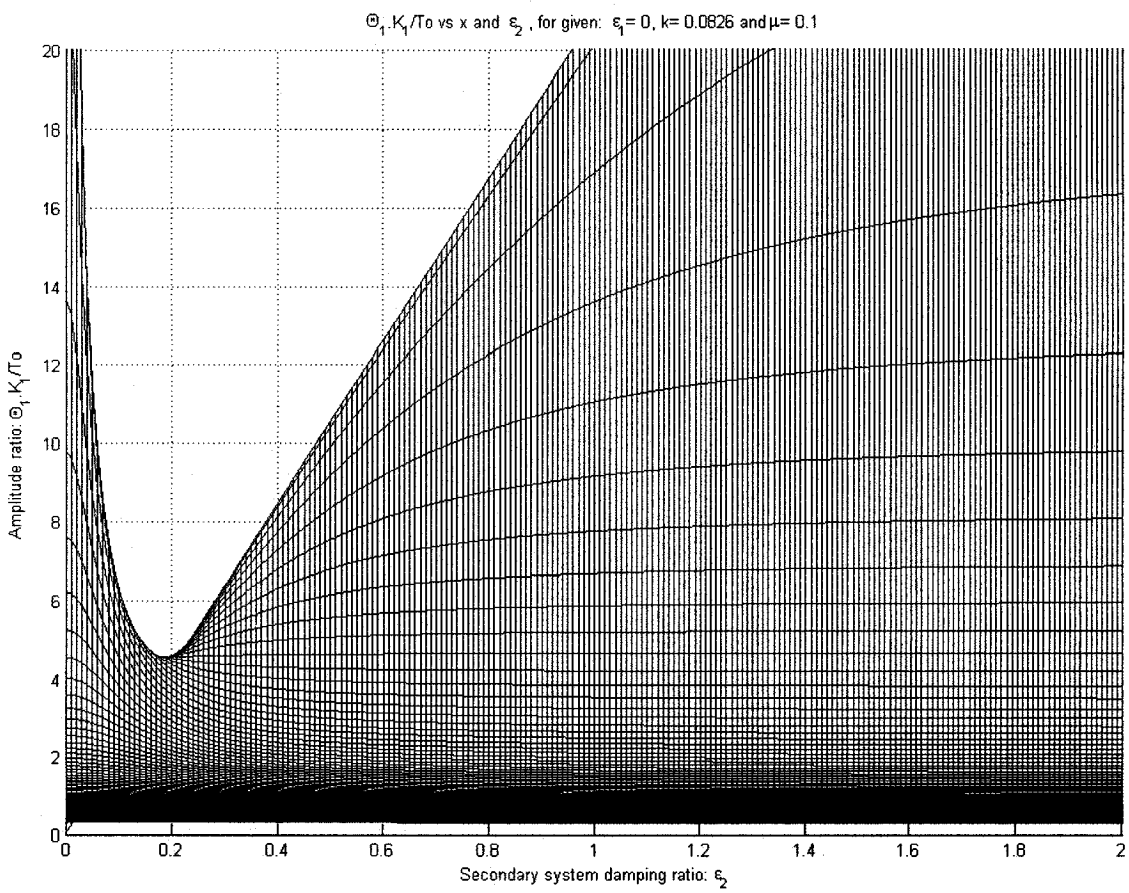

Figure 2.6 Side view of 3D figure 2.5 projected over amplitude and secondary damping axis

Figure 2.6 is a side view of 3D figure 2.5 projected over the axis for amplitude ratio $\Theta_1.K_1/T_O$ and secondary system damping ratio ε_2 .

We can see an approximate location of the minimum amplitude ratio $\Theta_1.K_1/T_o$ = 4.595 at the secondary system damping ratio $\varepsilon_2 \cong 0.2$ from the side view.

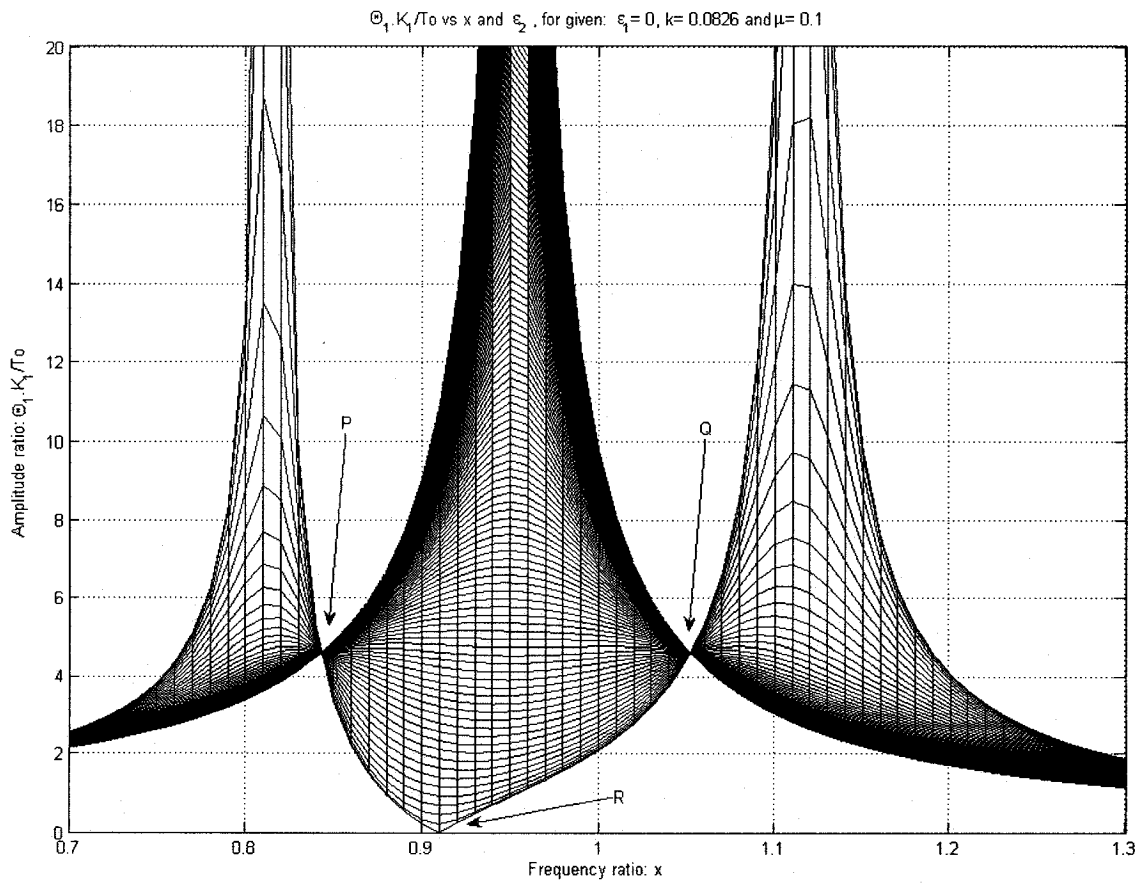

Figure 2.7 Front view of 3D figure 2.5 projected over amplitude and frequency axis

Figure 2.7 is the front view of 3D figure 2.5 projected over the axis for amplitude ratio $\Theta_1.K_1/T_o$ and frequency ratio x .

We can see the location of points P, Q and R; and that all the curves for different values of secondary system damping ratio ε_2 are contained inside the curves when ε_2 = 0 and ε_2 = ∞.

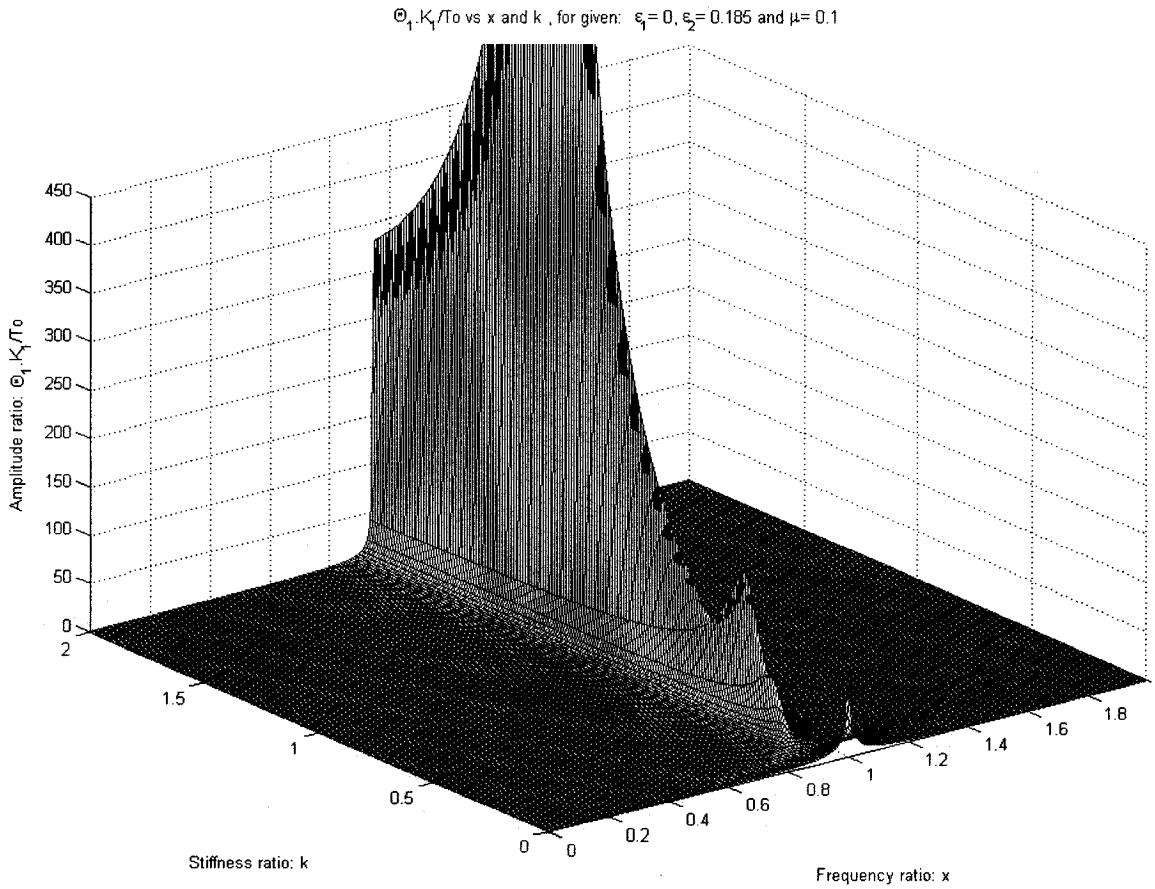

Figure 2.8 Plot of amplitude versus frequency and stiffness, given: primary damping $\varepsilon_1 = 0$, secondary damping ε_2 = 0.185 and mass μ = 0.1.

Figure 2.8 shows a 3D plot of amplitude ratio $\Theta_1.K_1/T_O$ vs frequency ratio x and stiffness ratio k; given the other variables as constants: primary damping ratio $\varepsilon_1 = 0$, secondary damping ratio ε_2 = 0.185 and mass ratio μ = 0.1.

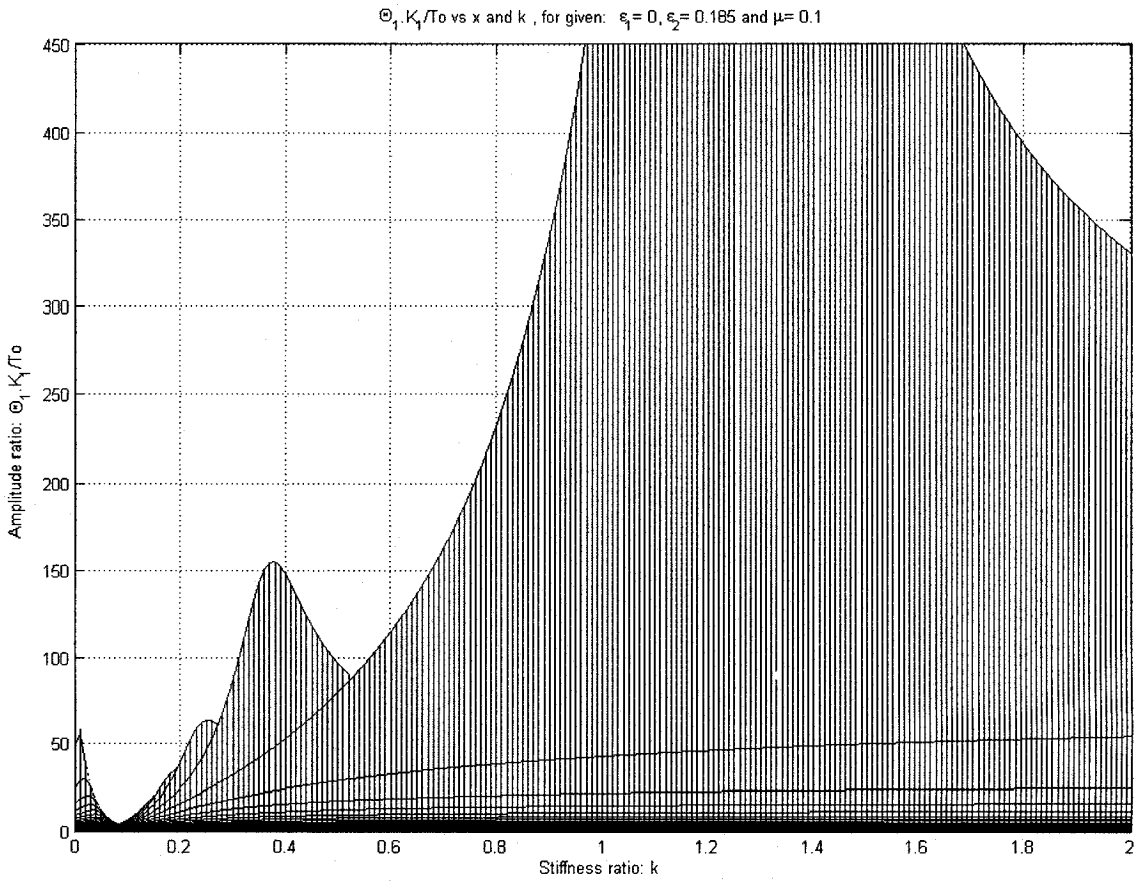

Figure 2.9 Side view of 3D figure 2.8 projected over amplitude and stiffness axis

Figure 2.9 is the side view of 3D figure 2.8 projected over the axis for amplitude ratio $\Theta_1.K_1/T_O$ and stiffness ratio k .

We can see an approximate location of the minimum amplitude ratio $\Theta_1.K_1/T_O$ = 4.595 and the stiffness ratio k, less than 0.1 from the side view. Also seen in this view are several peaks showing the resonance with change of stiffness.

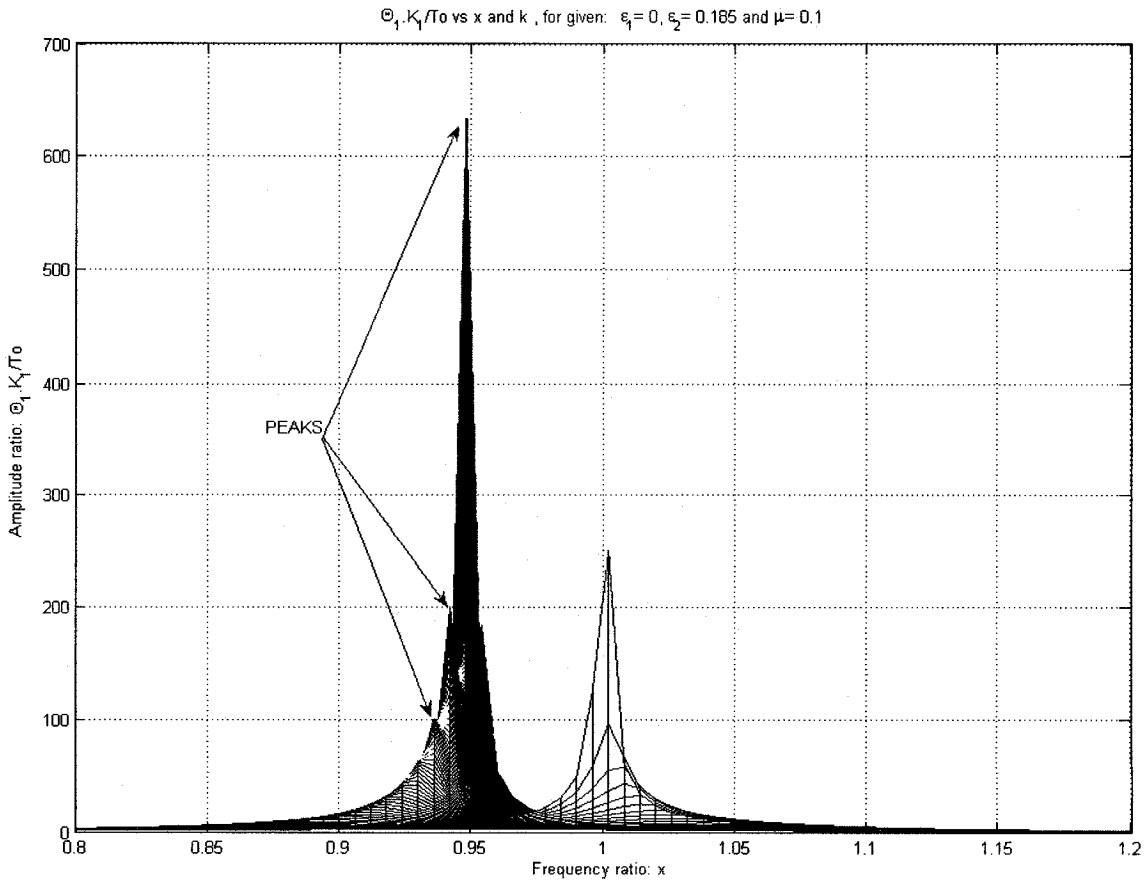

Figure 2.10 Front view of 3D figure 2.8 projected over amplitude and frequency axis

Figure 2.10 is the front view of 3D figure 2.8 projected over the axis for amplitude ratio $\Theta_1.K_1/T_o$ and stiffness ratio k .

The several peaks generated by the plot of the equation are more prominent in this view and they are located over a small range of frequency ratios, from x = 0.93 to x = 1.02. As mentioned before, they show the change in resonance with stiffness variation.

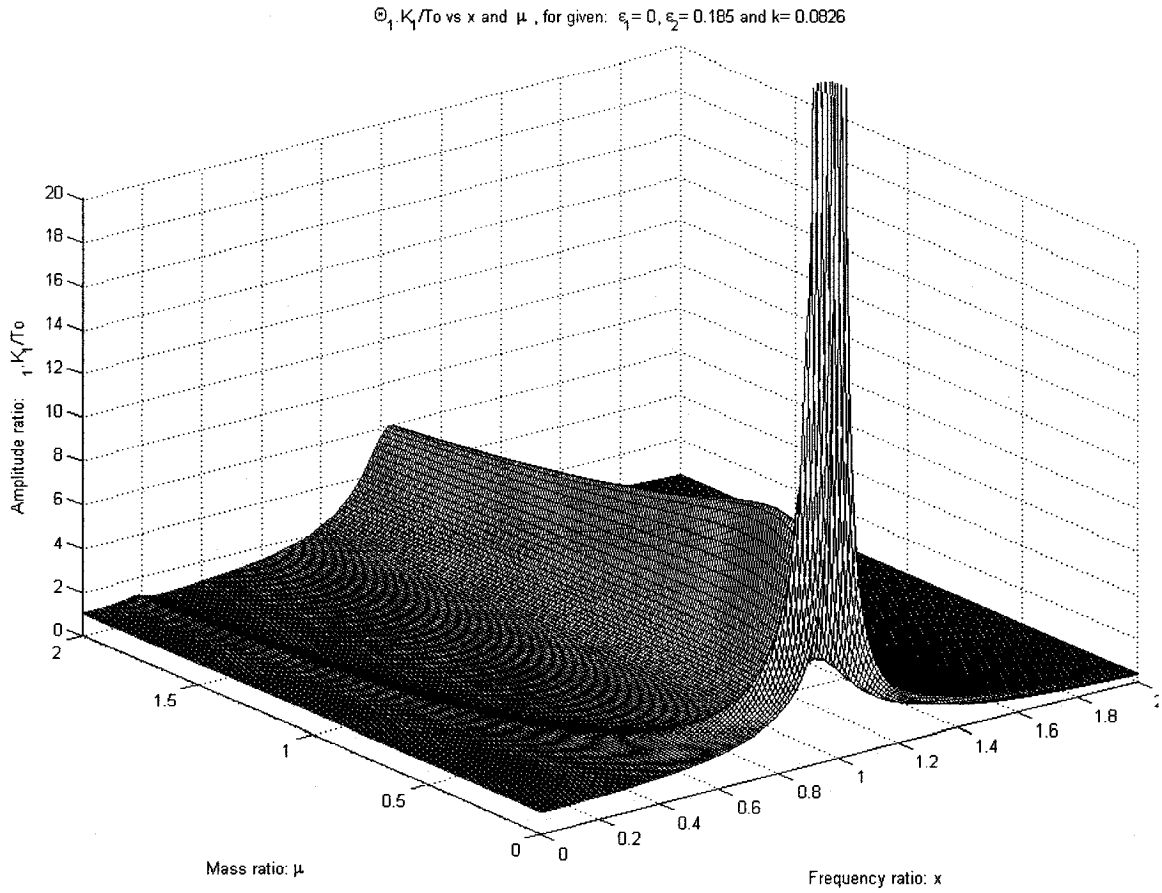

Figure 2.11 Plot of amplitude versus frequency and mass, given: primary damping $\varepsilon_1 = 0$, secondary damping $\varepsilon_2 = 0.185$ and stiffness $k = 0.0826$.

Figure 2.11 shows a 3D plot of amplitude ratio $\Theta_1.K_1/T_O$ vs frequency ratio x and mass ratio μ; given the other variables as constants: primary damping ratio $\varepsilon_1 = 0$, secondary damping ratio $\varepsilon_2 = 0.185$ and stiffness ratio $k = 0.0826$.

A small valley starting from the highest peak moves along the axis for mass ratio μ and also moves apart from the bigger valley until it reaches a point where both valleys tend to go parallel to each other.

Figure 2.12 is the front 3D view of figure 2.11 projected over the axis amplitude ratio $\Theta_1.K_1/T_o$ and frequency ratio x .

Most of the higher amplitudes are around the frequency ratio x = 1 in the range of x = 0.8 to x = 1.2.

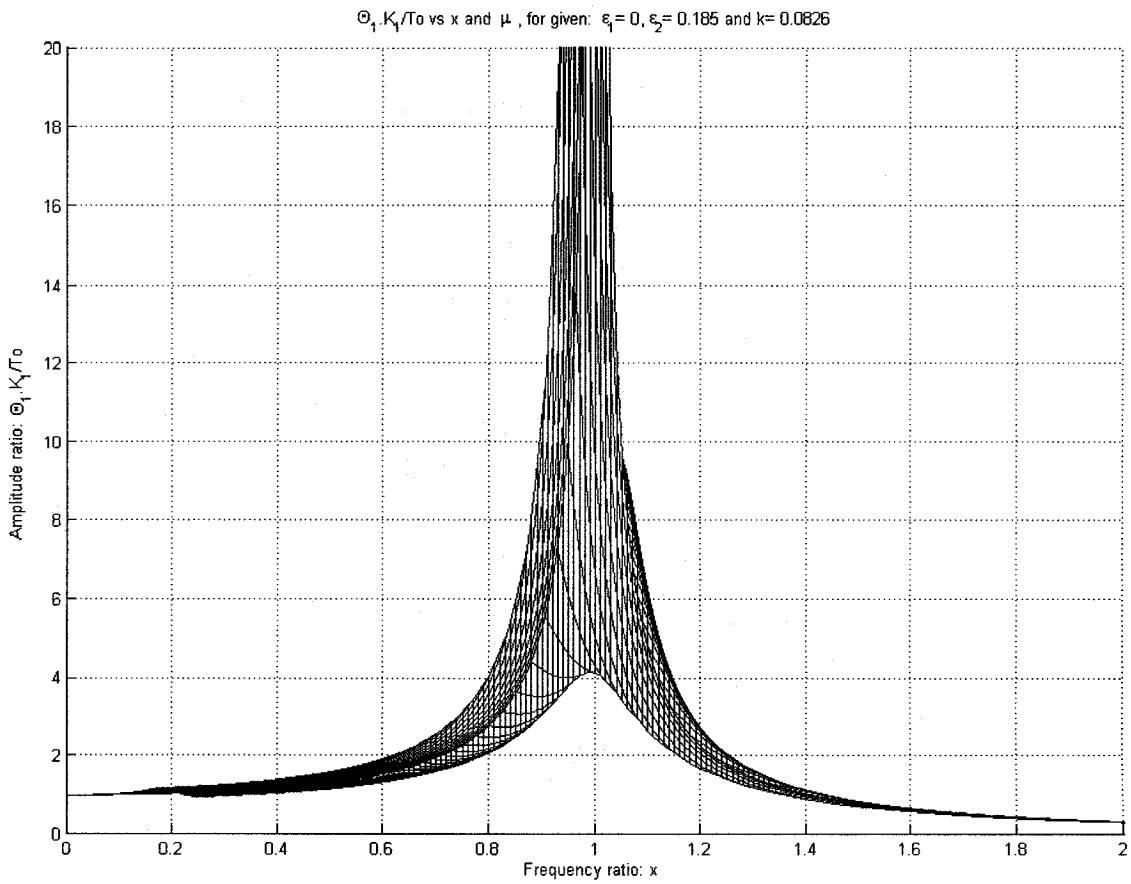

Figure 2.12 Front view of 3D figure 2.11 projected over amplitude and frequency axis

Figure 2.13 is the 3D side view of figure 2.11 projected over the axis amplitude ratio $\Theta_1.K_1/T_o$ and mass ratio μ .

The minimum amplitude ratio $\Theta_1.K_1/T_o$ = 4.595 and the mass ratio μ, close to 0.1 from the side view is prominent.

Also, amplitudes with mass ratio μ less than 0.1 are high in slope and amplitudes with μ more than 0.1 increase until μ = 0.3 when the amplitudes gradually decrease. The minimum for μ is at a very sharp point, at μ = 0.1

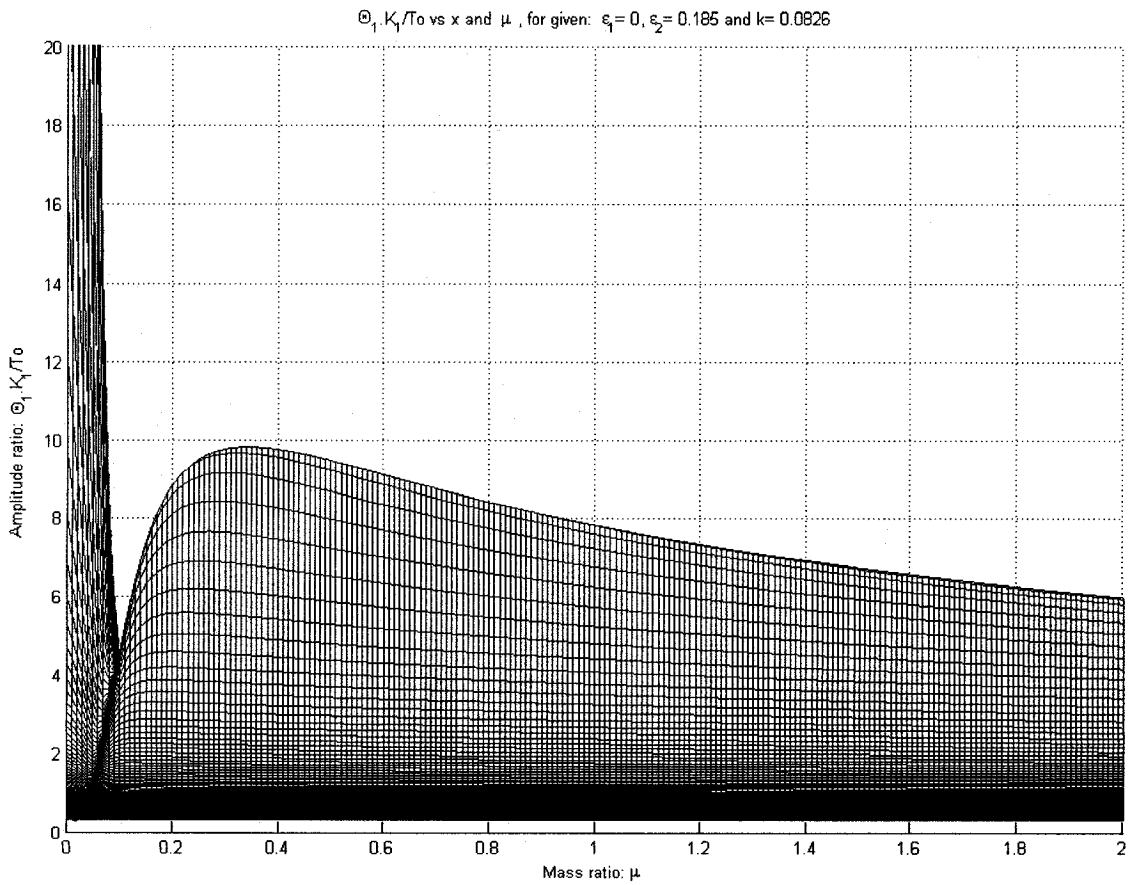

Figure 2.13 Side view of 3D figure 2.11 projected over amplitude and mass axis

2.3.2 Numerical analysis when $\varepsilon_1 \neq 0$

This section presents plots when the primary system has damping ε_1 = 0.04. Figure 2.14 plots in 2D space equation 2.9, $\Theta_1.K_1/To$ versus x for the same six different values as for ε_1 = 0, for each ε_2 , k and μ.

A similar combination as in section 2.3.1 in 3D space for figures 2.15, 2.16 and 2.17 is presented for equation 2.9, $\Theta_1.K_1/To$ versus x and ε_2 , k and μ, respectively.

Figures 2.18 is the only side view presented for figure 2.18.

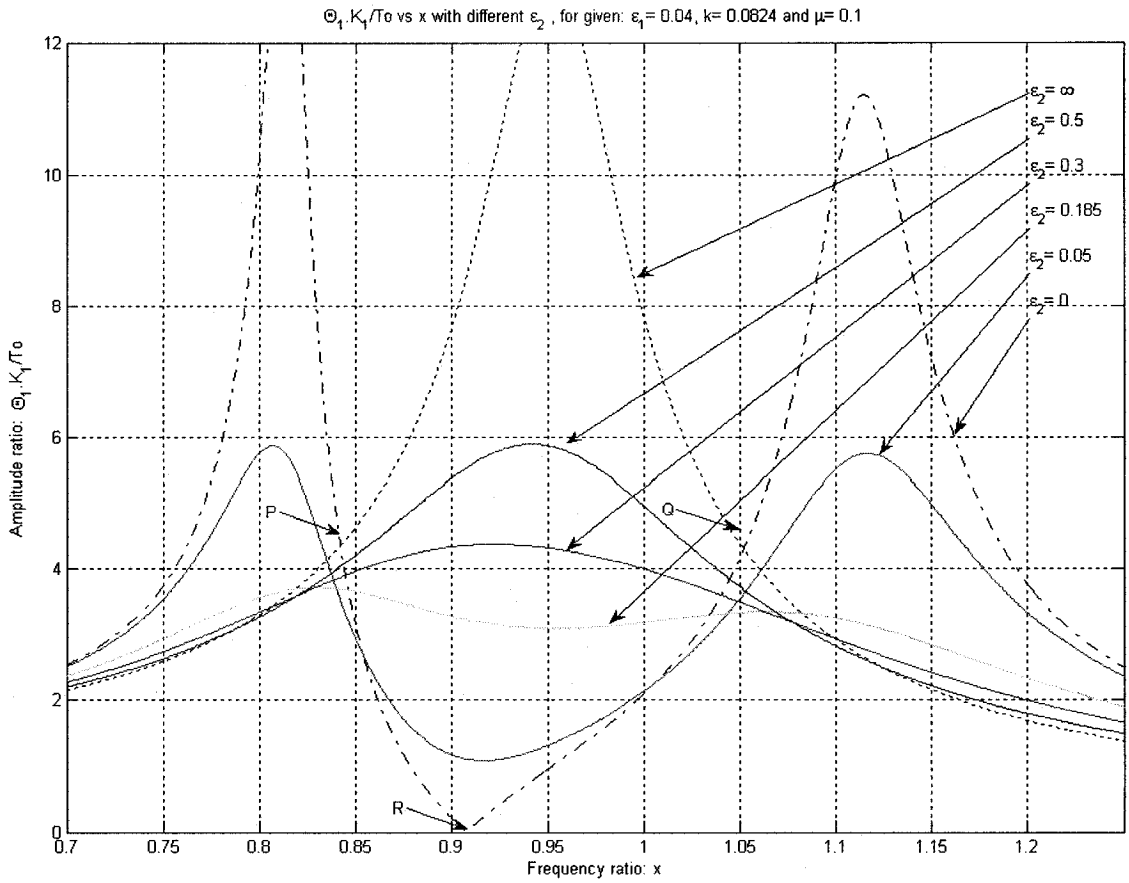

Figure 2.14 Plot of amplitude versus frequency, given: primary damping $\varepsilon_1 = 0.04$, for different secondary damping ε_2, stiffness k = 0.0826 and mass $\mu = 0.1$

Figure 2.14 shows the plot of amplitude ratio $\Theta_1.K_1/T_o$ vs frequency ratio x for different secondary damping ratios ε_2 = 0, 0.05, 0.185, 0.3, 0.5, infinite; given the other variables as constants: primary damping ratio ε_1 = 0.04, stiffness ratio k = 0.0826 and mass ratio $\mu = 0.1$.

The two former fixed points P and Q are not seen anymore and all the curves do not pass through any common point.

In figure 2.14, when ε_2 = 0.04, there are two maximum peaks with $\Theta_1.K_1/T_o$ = 15.35 and 11.21; and, x = 0.8144 and 1.1160, respectively. The frequency ratios remain the same as in figure 2.2 for ε_1 = 0 and the amplitudes for the maximum peaks are the ones that change.

Also in figure 2.14, when ε_2 = ∞, there is only one maximum peak with $\Theta_1.K_1/T_o$ = 13.12 and x = 0.9535. Here also, the frequency ratio remains the same as in figure 2.2 for ε_1 = 0, and the amplitude for the maximum peak is the only one that changes. Point R remains in the same location even though ε_2 = 0.04 and intersects the frequency x axis at x = 0.9088 and all the curves are not contained within the limits of ε_2 = 0 and ε_2 = ∞ anymore.

In addition, although the amplitudes for ε_1 = 0.04 in figure 2.14 have decreased about half from when ε_1 = 0 in figure 2.2, in figure 2.14, it can be seen that the amplitudes for ε_2 = 0 have dropped significantly by more than half.

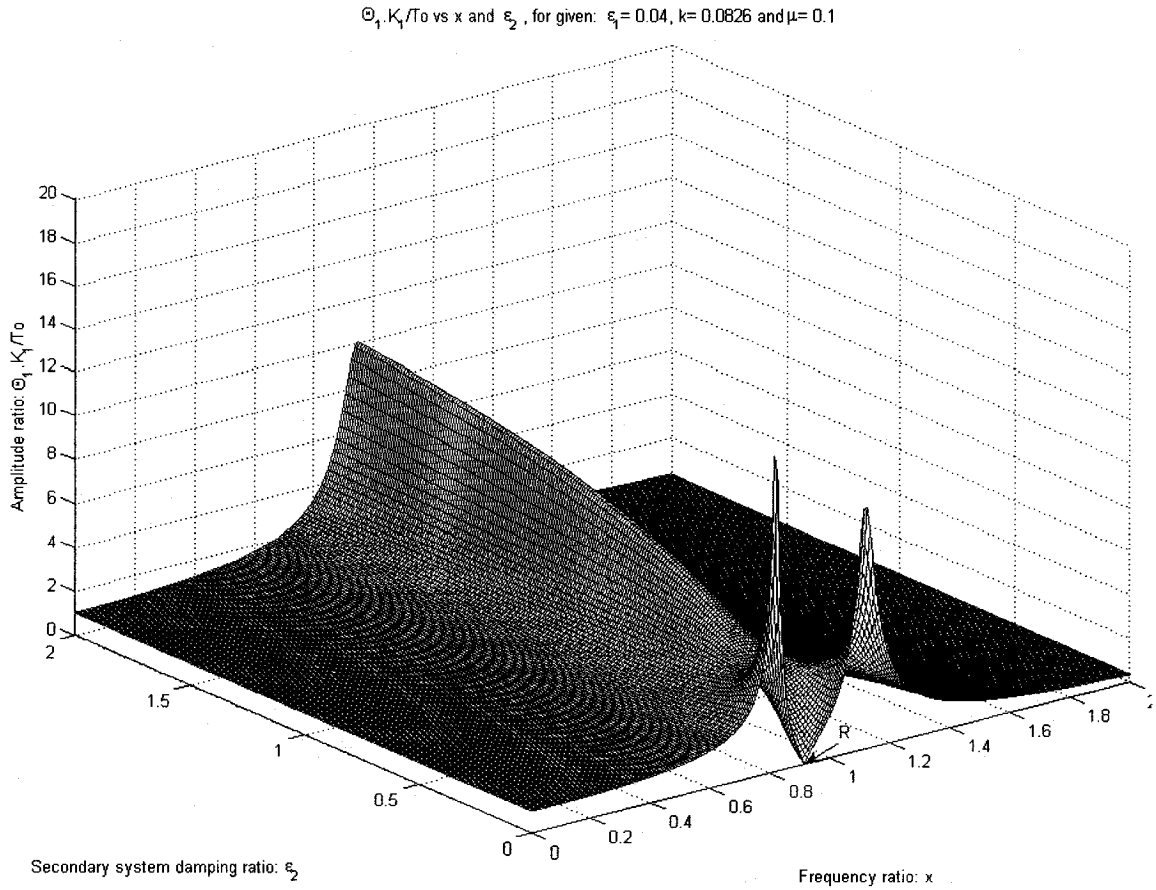

Figure 2.15 Plot of amplitude versus frequency, given: primary damping $\varepsilon_1 = 0.04$, for different secondary damping ε_2, stiffness k = 0.0826 and mass $\mu = 0.1$

Figure 2.15 shows a 3D plot of amplitude ratio $\Theta_1.K_1/T_o$ vs frequency ratio x and secondary damping ratio ε_2; given the other variables as constants: primary damping ratio $\varepsilon_1 = 0.04$, stiffness ratio k = 0.0826 and mass ratio μ = 0.1.

When ε_2 = 0, the two maximum peaks and point R are present. The curve with ε_2 = 0 intersects the frequency x axis at x = 0.9088.

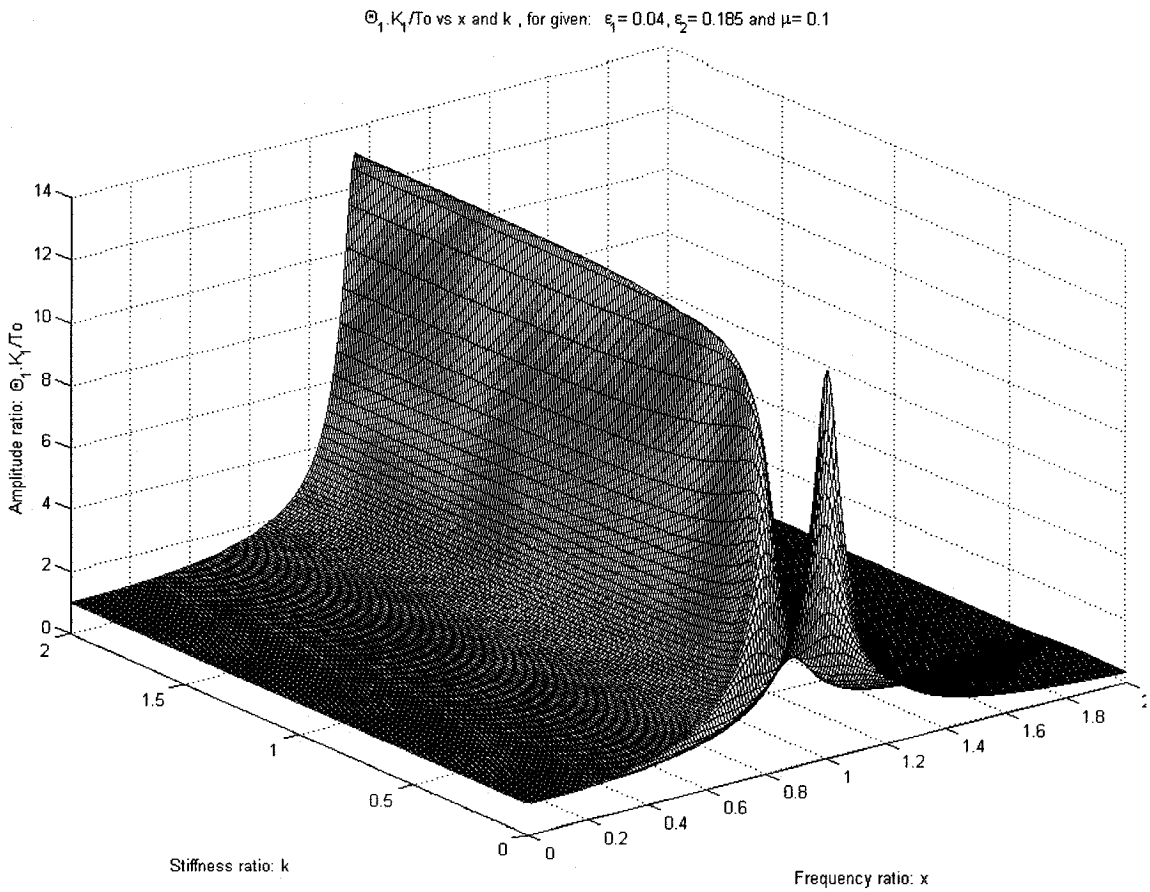

Figure 2.16 Plot of amplitude versus frequency and stiffness, given: primary damping $\varepsilon_1 = 0.04$, secondary damping $\varepsilon_2 = 0.185$ and mass $\mu = 0.1$.

Figure 2.16 shows a 3D plot of amplitude ratio $\Theta_1.K_1/T_o$ vs frequency ratio x and stiffness ratio k; given the other variables as constants: primary damping ratio $\varepsilon_1 = 0.04$, secondary damping ratio $\varepsilon_2 = 0.185$ and mass ratio $\mu = 0.1$.

The multiple peaks generated, as shown in figures 2.8, 2.9 and 2.11, no longer appear on figure 2.16.

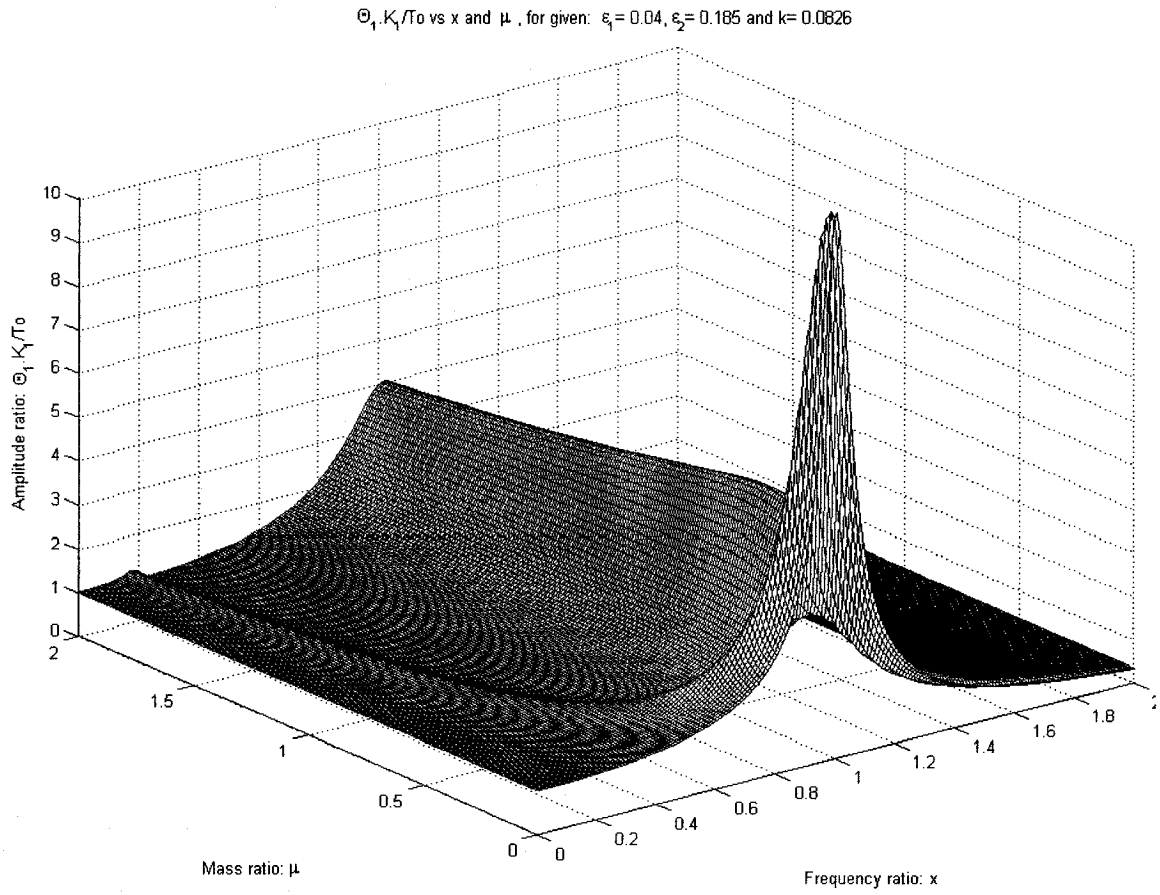

Figure 2.17 Plot of amplitude versus frequency and mass, given: primary damping $\varepsilon_1 = 0.04$, secondary damping $\varepsilon_2 = 0.185$ and stiffness $k = 0.0826$.

Figure 2.17 shows a 3D plot of amplitude ratio $\Theta_1.K_1/T_o$ vs frequency ratio x and mass ratio μ ; given the other variables as constants: primary damping ratio $\varepsilon_1 = 0.04$, secondary damping ratio $\varepsilon_2 = 0.185$ and stiffness ratio $k = 0.0826$.

As seen in figure 2.14: the small valley starting from the highest peak moves along the axis for mass ratio μ and also moves apart from the bigger valley until it reaches a point where both valleys tend to go parallel to each other.

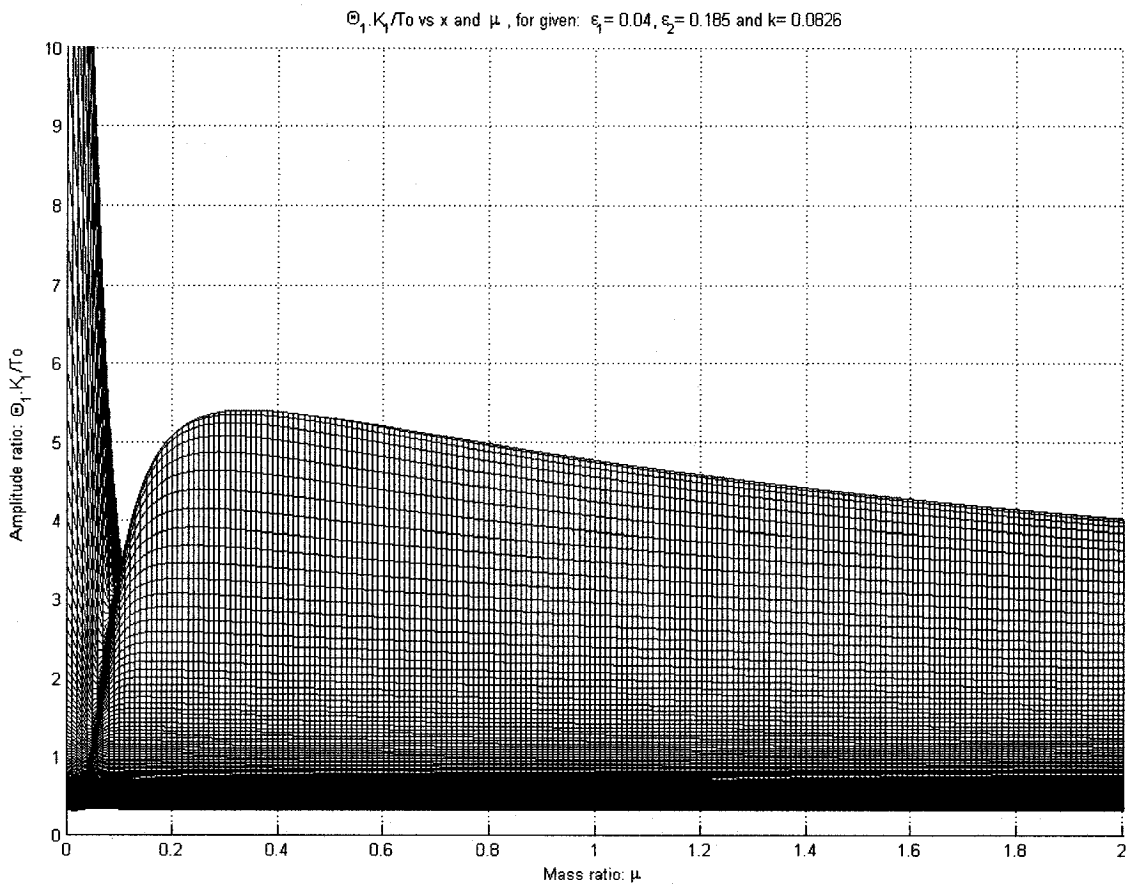

Figure 2.18 Side view of 3D figure 2.17 projected over amplitude and mass axis

Figure 2.18 is the side view of 3D figure 2.17 projected over the axis for amplitude ratio $\Theta_1.K_1/T_o$ and mass ratio μ .

In the graph, we can see an approximate location of the minimum amplitude ratio $\Theta_1.K_1/T_o$ and the mass ratio μ, close to 0.1 from this side view. Similar results were obtained in figure 2.16.

Also as in figure 2.16, amplitudes with μ less than 0.1 are high and amplitudes with μ more than 0.1 increase until μ = 0.3 when the amplitudes gradually decrease. Again, the minimum for μ is at a very sharp point.

2.4 Calculation of optimum values

The optimum parameters correspond to the minimum value of $\Theta_1.K_1/T_O$. The optimization problem is stated as follows:

Objective function to be minimized: $\Theta_1.K_1/T_O$.

Design variables: ε_2 and k.

To obtain the optimum values numerically, the following steps were also used for the Matlab program shown in appendix I:

Firstly, in equation 2.9, out of the five variables ε_1 , μ , k , ε_2 and x, constant values are assigned to ε_1 and μ.

Secondly, vary each parameter k and ε_2 from 0 to 1 at intervals of 0.001. For each pair of k and ε_2, equation 2.9 becomes a one-variable equation with x. With the given pair, vary x from 0 to 1 at intervals of 0.001 and find its maximum

amplitude $\Theta_1.K_1/T_o$ as shown in figure 2.19. Note that x is no longer in figure 2.19.

Thirdly, find the minimum of the maximum amplitude $\left[\Theta_1.K_1/T_o\right]_{\min}$. For this corresponding $\left[\Theta_1.K_1/T_o\right]_{\min}$ there will be one pair of k and ε_2 which are k_{opt} and ε_{2opt}, respectively.

Finally, repeat the above process for each ε_1 = [0.01, 0.1, 0.2, 0.3, 0.4, 0.5, 0.6, 0.7] and μ from 0 to 1 at intervals of 0.01 to find the curve for each ε_1.

Figures 2.19, 2.20, 2.21, 2.22 and 2.23 show a graphic representation of the above steps.

Figure 2.19 shows a 3D plot of MAXIMUM amplitude ratio $\Theta_1.K_1/T_o$ vs secondary damping ratio ε_2 and stiffness ratio k; given the other variables as constants: primary damping ratio $\varepsilon_1 = 0$ and mass ratio μ = 0.1.

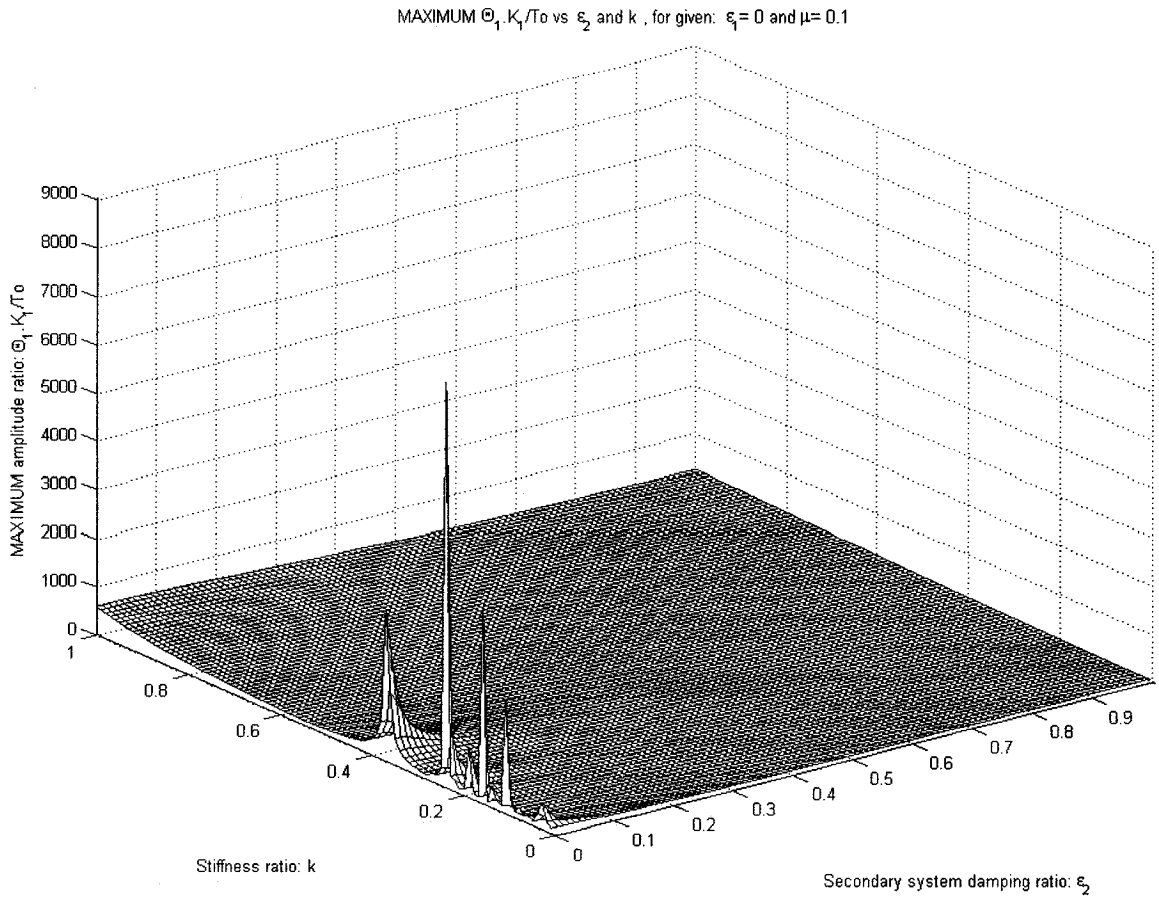

Figure 2.19 Plot of MAXIMUM amplitude versus secondary damping and stiffness, given: primary damping $\varepsilon_1 = 0$ and $\mu = 0.1$.

This 3D plot visibly does not show any minimum value for optimum secondary damping and stiffness ratios.

Figure 2.20 shows a zoomed view in 3D of figure 2.17 for MAXIMUM amplitude ratio $\Theta_1.K_1/T_O$ axis.

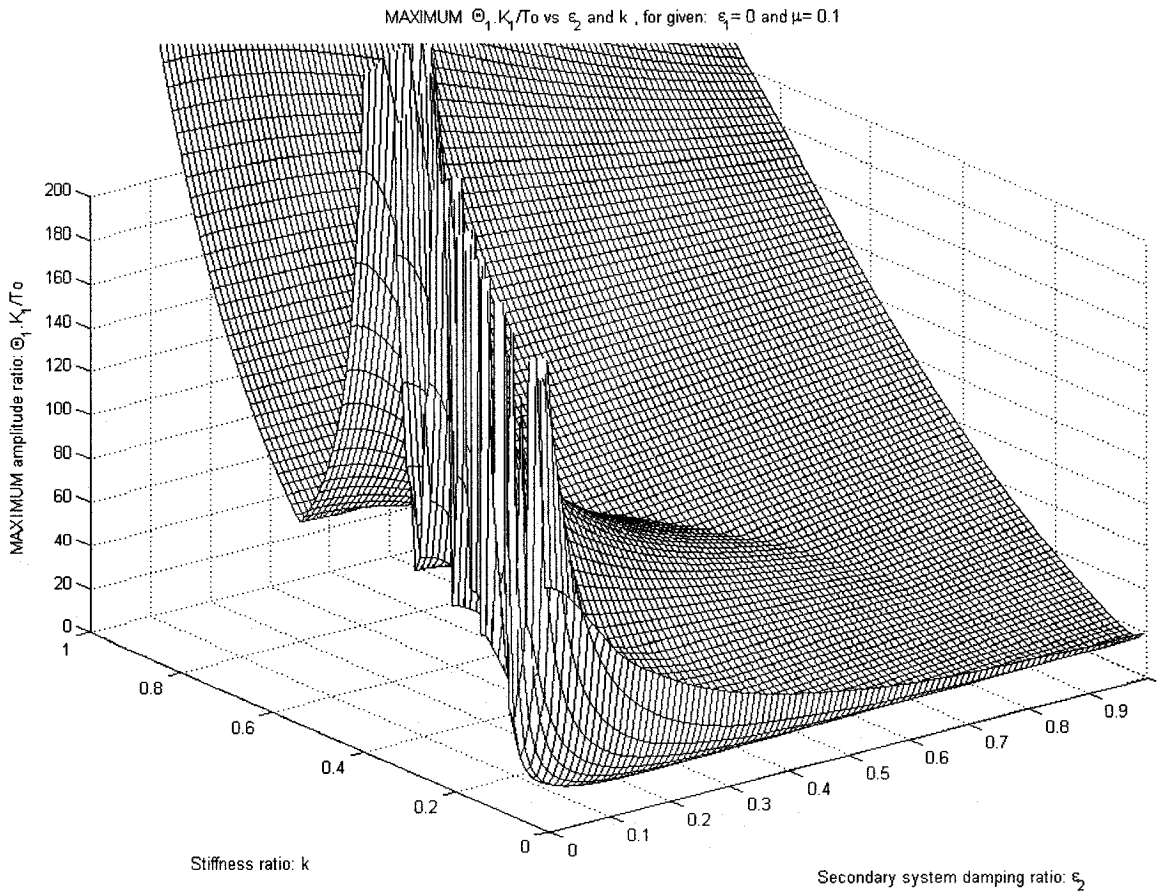

Figure 2.20 Zoomed view of figure 2.19

This 3D plot shows the bottom surface where the minimum amplitude $\left[\Theta_1.K_1/T_O\right]_{\min}$ for optimum secondary damping ε_{2opt} and stiffness k_{opt} ratios.

Figure 2.21 is the back view of 3D figure 2.17 projected over the axis for MAXIMUM amplitude ratio $\Theta_1.K_1/T_o$ and stiffness ratio k.

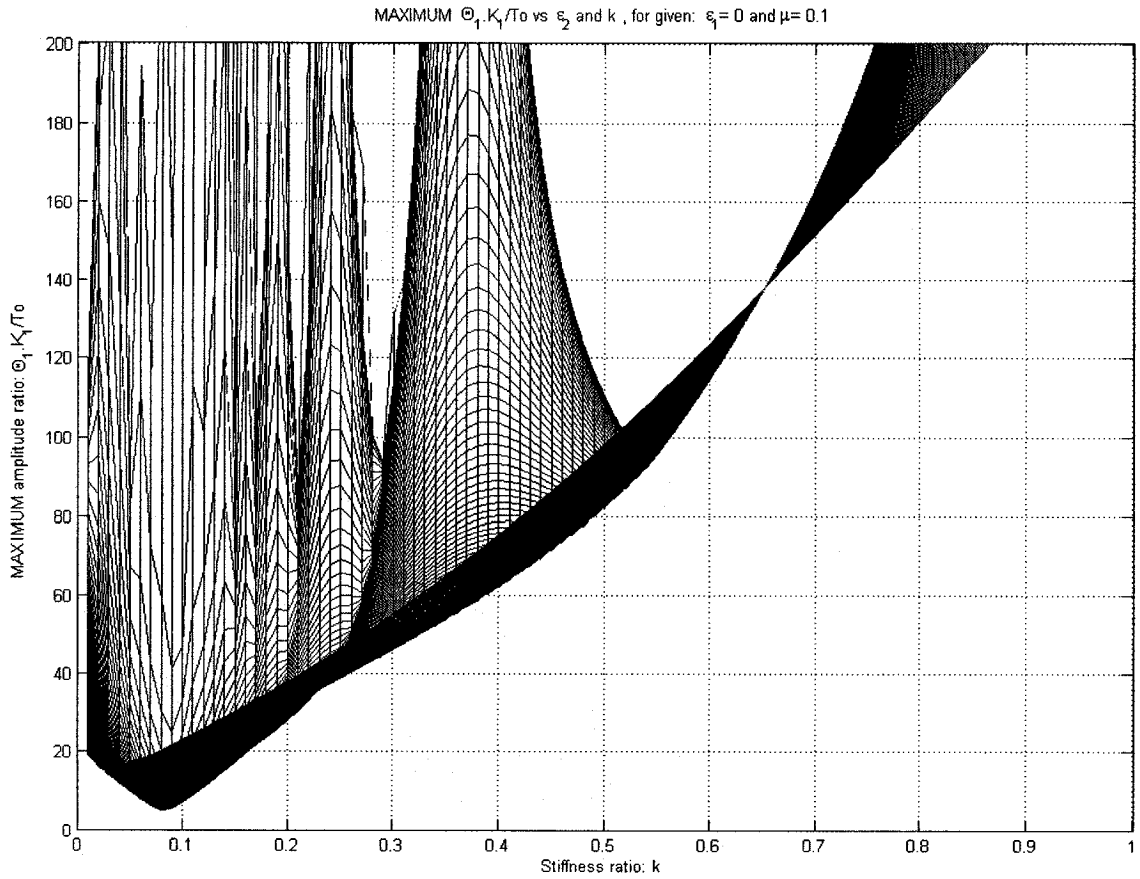

Figure 2.21 Back view of 3D figure 2.20 projected over MAXIMUM amplitude and stiffness axis

The optimum stiffness ratio k_{opt} can be determined graphically from figure 2.19 to be $k_{opt} \cong 0.08$ with its minimum amplitude ratio being $\left[\Theta_1.K_1/T_O\right]_{\min} \cong 4.5$.

Figure 2.22 is the side view of 3D figure 2.17 projected over the axis for MAXIMUM amplitude ratio $\Theta_1.K_1/T_O$ and secondary damping ratio ε_2.

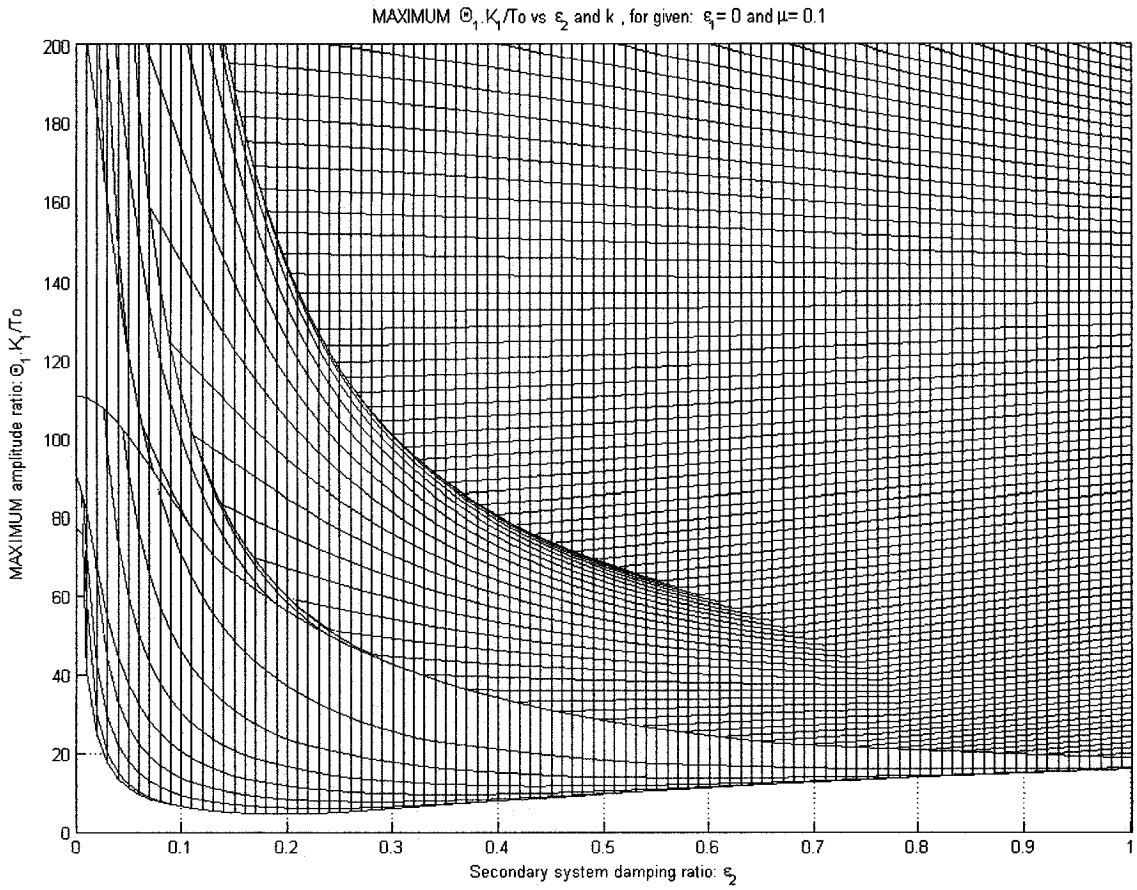

Figure 2.22 Side view of 3D figure 2.20 projected over MAXIMUM amplitude and secondary damping axis

The optimum secondary damping ratio ε_{2opt} is difficult to determine from the view at this scale, but its minimum amplitude ratio is $\left[\Theta_1.K_1/T_O\right]_{\min} \cong 4.5$.

Figure 2.20 is the 3D side view of figure 2.17 in log scale projected over the axis for MAXIMUM amplitude ratio $\Theta_1.K_1/T_O$ and secondary damping ratio ε_2.

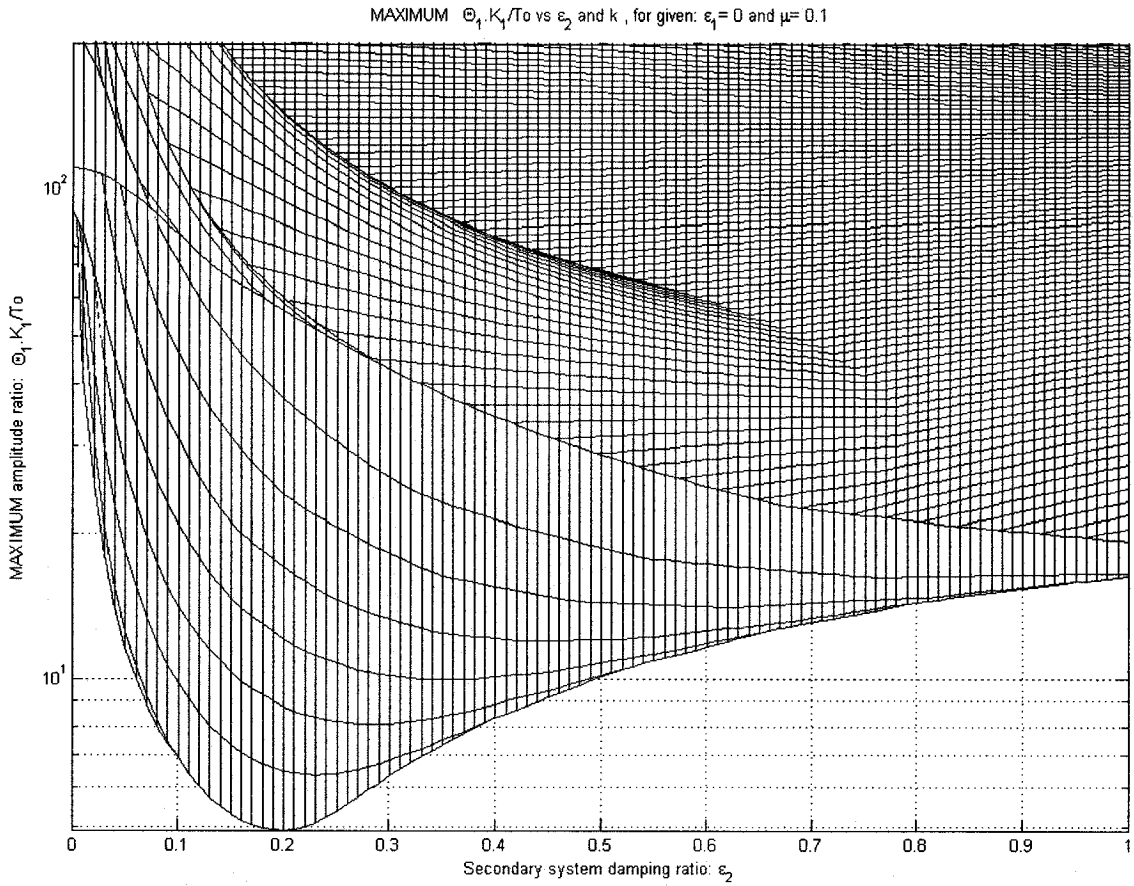

Figure 2.23 Log scale of figure 2.22

In this figure 2.23 in log scale, the minimum amplitude ratio $\left[\Theta_1.K_1/T_o\right]_{\min}$ is difficult to determine graphically, but the optimum secondary damping ratio is ε_2 = 0.2.

2.5 Analysis of optimum values

As mentioned in section 2.3, the optimization method used in this numerical evaluation is the H_∞ optimization which minimizes the dynamic magnifier Θ_1 for primary system [36] to minimize $\left[\Theta_1.K_1/T_O\right]$ in order to obtain the optimum values for k_{opt} and ε_{2opt}.

For each pair of optimum values k_{opt} , ε_{2opt}, there corresponds a $\left[\Theta_1.K_1/T_O\right]_{\min}$ that was obtained in section 2.4 given ε_1 and μ as constant values.

In this section we will study and analyze the behavior of these optimum values for different ε_1 = [0, 0.1, 0.2, 0.3, 0.4, 0.5, 0.6, 0.7] and μ = [0.01, 0.02 ...0.99, 1].

Figures 2.24, 2.26, 2.28 show the behavior of $\left[\Theta_1.K_1/T_O\right]_{\min}$ versus μ , ε_{2opt} and k_{opt} , respectively. And figures 2.25, 2.27 show the linear trend of $\left[\Theta_1.K_1/T_O\right]_{\min}$ versus μ and $\left[\Theta_1.K_1/T_O\right]_{\min}$ versus ε_{2opt}, respectively.

Figures 2.29, 2.30 show the behavior of μ versus ε_{2opt} and k_{opt} , respectively. And figure 2.31 shows ε_{2opt} versus k_{opt} .

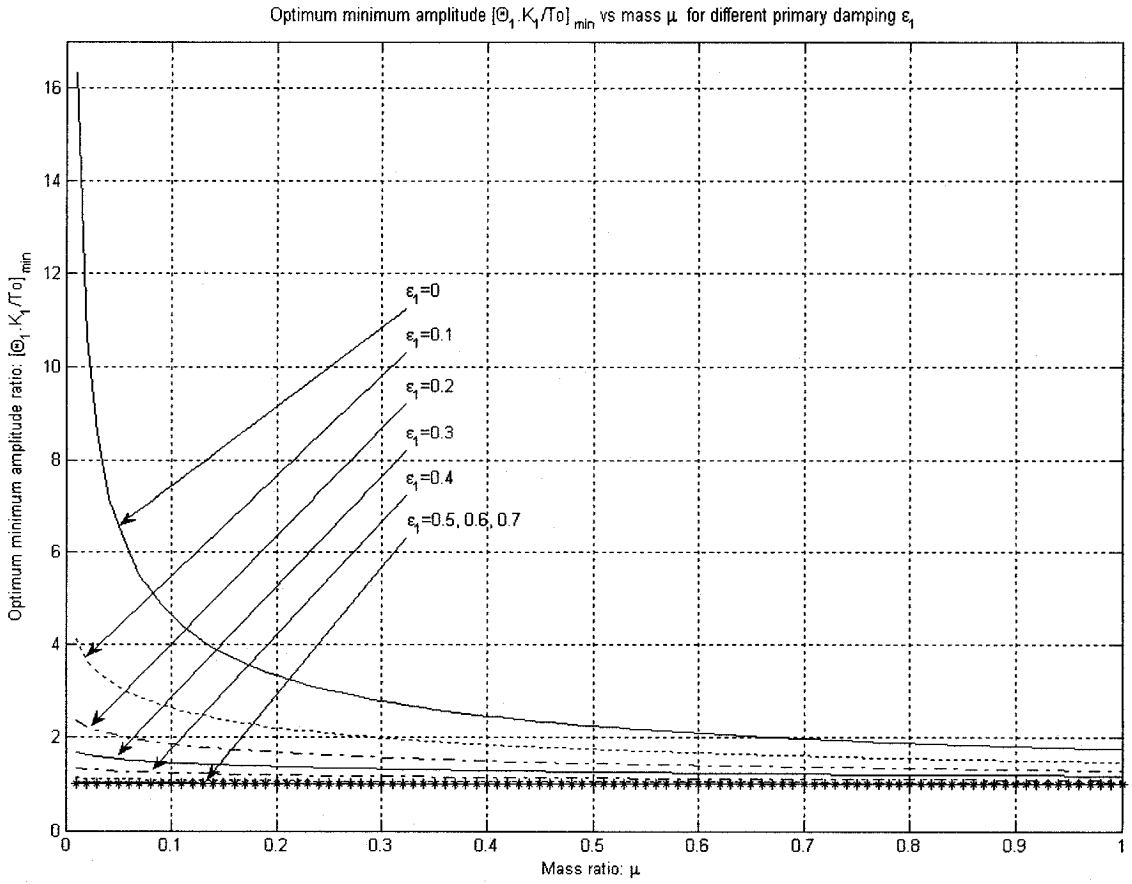

Figure 2.24 Plot of optimum minimum amplitude ratio vs mass ratio for different primary damping

Figure 2.24 shows the plot of optimum minimum amplitude ratio $\left[\Theta_1.K_1/T_O\right]_{\min}$ vs mass ratio μ for different primary damping ratios ε_1 :

$$1 \le \left[\Theta_1.K_1/T_O\right]_{\min} \le 2, \text{ for } 0.6 \le \mu \le 1 \text{ and } 0 \le \varepsilon_1 \le 1 \qquad (2.11)$$

$$1.1 \le \left[\Theta_1.K_1/T_O\right]_{\min} \le 17, \text{ for } 0.01 \le \mu < 0.6 \text{ and } 0 \le \varepsilon_1 \le 0.4 \qquad (2.12)$$

From the above relations it is evident that the mass ratio μ has significant influence on the amplitude for different values of primary damping ratio ε_1.

Also, for μ < 0.6 we can limit our study to the range of curves ε_1 of [0, 0.4] where it shows a variable amplitude $\left[\Theta_1.K_1/T_O\right]_{\min}$ since for the range of curves, ε_1 of [0.4, 1] the amplitude can be approximated $\left[\Theta_1.K_1/T_O\right]_{\min} \cong 1$.

According to figure 2.24, the best case is in the zone indicated by the relation 2.11; however, a system with μ > 0.6 would not be economical in real situations. Thus, relation 2.12 is required.

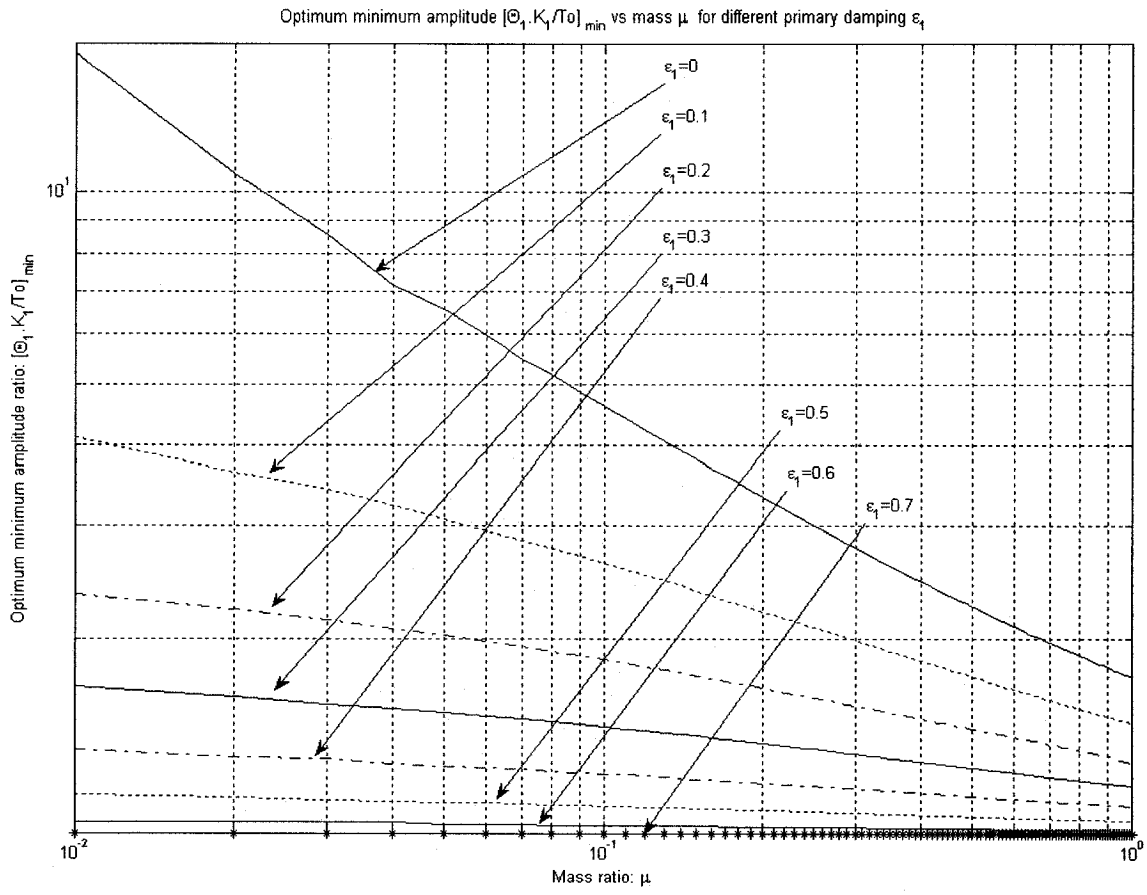

Figure 2.25 Log scale plot for optimum minimum amplitude ratio vs mass ratio for different primary damping

Figure 2.25 shows the log scale plot for optimum minimum amplitude ratio $\left[\Theta_1.K_1/T_O\right]_{\min}$ vs mass ratio μ for different primary damping ratio ε_1. On this log scale we can see the linear trend relation between the optimum minimum amplitude ratio $\left[\Theta_1.K_1/T_O\right]_{\min}$ and mass ratio μ for each ε_1 curve.

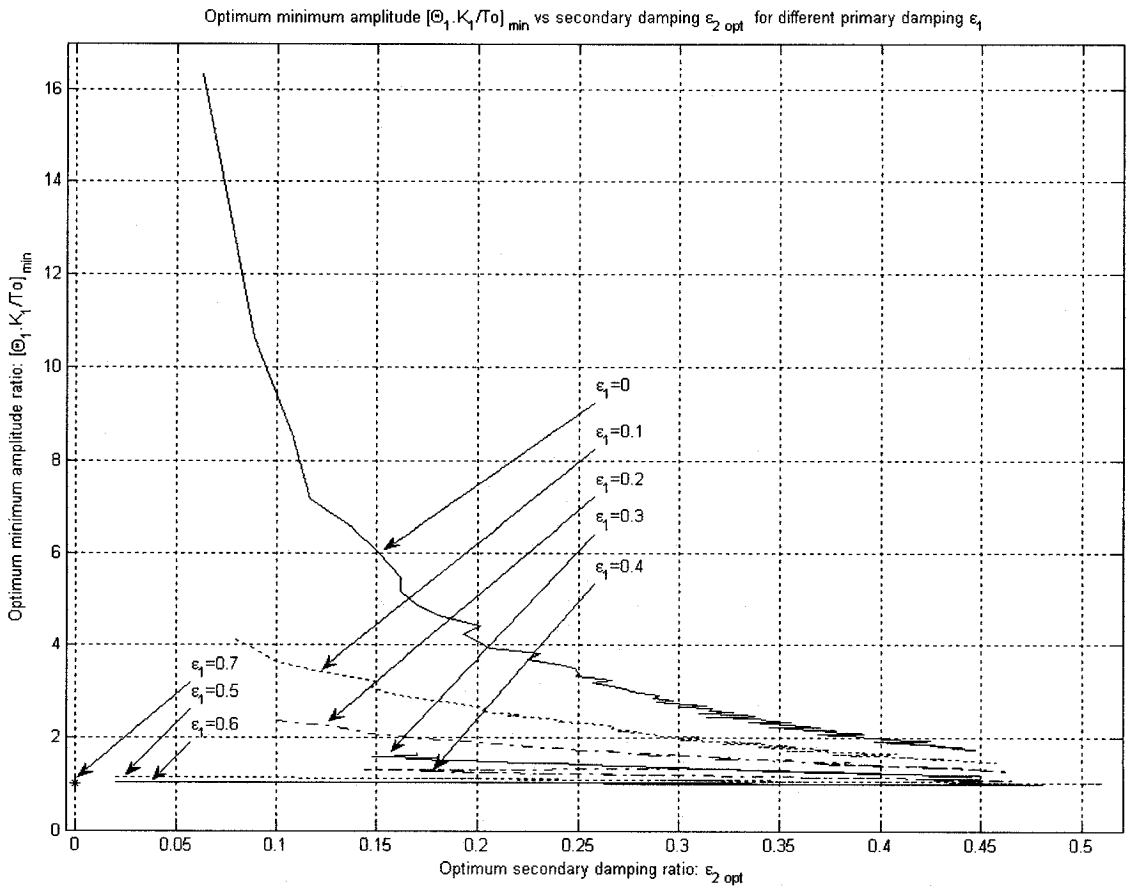

Figure 2.26 Plot of optimum minimum amplitude vs optimum secondary damping for different primary damping ratios

Figure 2.26 shows the plot of optimum minimum amplitude ratio $\left[\Theta_1.K_1/T_O\right]_{\min}$ vs optimum secondary damping ratio ε_{2opt} for different primary damping ratios ε_1.

As expected, the increase of ε_1 given ε_{2opt} reduces the amplitude $\left[\Theta_1.K_1/T_O\right]_{\min}$; and also, the increase of ε_{2opt} given ε_1 reduces $\left[\Theta_1.K_1/T_O\right]_{\min}$.

Note that the ε_{2opt} ranges from 0.02 to 0.50 for the different values of ε_1. However, the optimum range that contains all ε_1 curves for a given ε_{2opt} is [0.15, 0.45]. It is clear that out of this optimum range for ε_{2opt}, the amplitude change would be unclear.

Also, for the given optimum range of ε_{2opt} [0.15, 0.45] a range for amplitude $\left[\Theta_1 . K_1 / T_O\right]_{\min}$ = [1, 6] is obtained, which is given by the external damping ε_1 curves.

During the design stages in a real case situation, the external damping ε_1 in a system is difficult to calculate but, during testing of the manufactured system, it can be measured. In contrast, the internal damping ε_{2opt} (in the optimum range [0.15, 0.45]) during the design stages is possible to calculate. Measurements during testing will be directly related to the external damping ε_1.

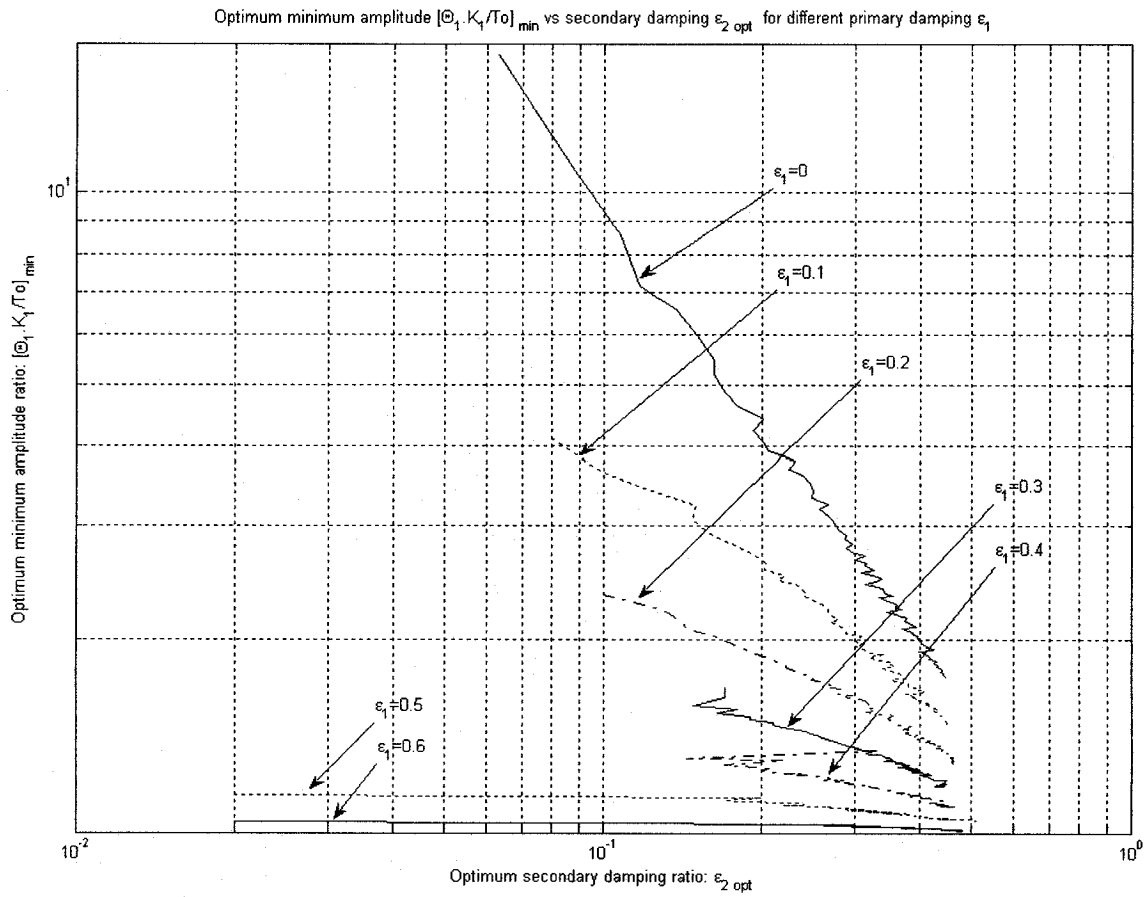

Figure 2.27 Log scale plot for optimum minimum amplitude vs optimum secondary damping for different primary damping ratios

Figure 2.27 shows the log scale plot for optimum minimum amplitude ratio $\left[\Theta_1.K_1/T_O\right]_{\min}$ vs optimum secondary damping ratio ε_{2opt} for different primary damping ratios ε_1. On this log scale we can see the linear trend relation between the optimum minimum amplitude ratio $\left[\Theta_1.K_1/T_O\right]_{\min}$ and optimum secondary damping ratio ε_{2opt} for each ε_1 curve.

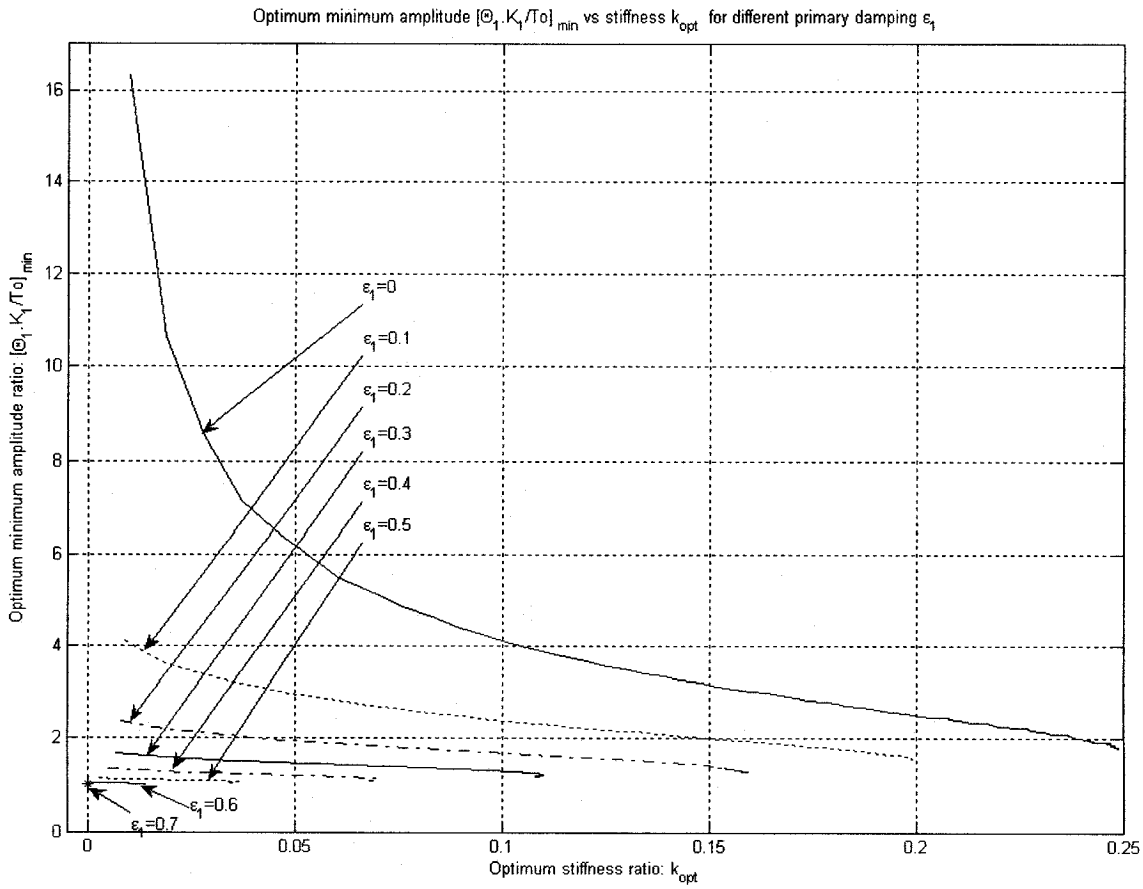

Figure 2.28 Plot of optimum minimum amplitude vs optimum stiffness for different primary damping ratios

Figure 2.28 shows the plot of optimum minimum amplitude ratio $\left[\Theta_1.K_1/T_O\right]_{\min}$ vs optimum stiffness ratio k_{opt} for different primary damping ratios ε_1.

Note the tendency of all ε_1 curves to converge in a point. In this case the point starts when ε_1 = 0.7 and there is a linear relation between $\left[\Theta_1.K_1/T_O\right]_{\min}$ and k_{opt} for ε_1 > 0.2.

From figure 2.28 alone, it is difficult to establish a relation without the help of the other figures.

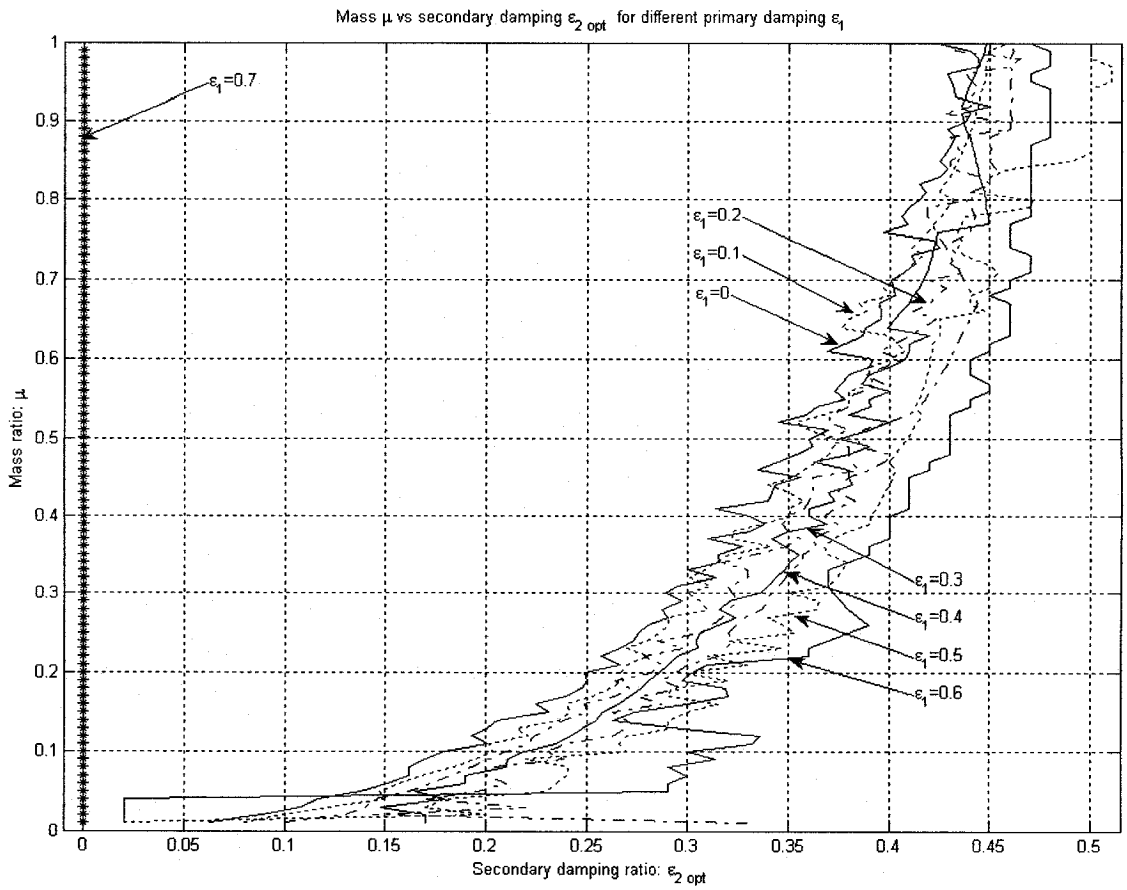

Figure 2.29 Plot of mass vs optimum secondary damping for different primary damping ratios

Figure 2.29 shows the plot of mass ratio μ vs optimum secondary damping ratio ε_{2opt} for different primary damping ratios ε_1.

It is clear that the behavior of each ε_1 curve is different from the others and that these curves are not contained between curves ε_1 = 0 to ε_1 = 0.6; however, they tend to agglomerate within a range.

For a given value of μ, an approximate graphical range ε_{2opt} can be obtained. I.e. for μ = 0.5, the approximate graphical range for ε_{2opt} is [0.36, 0.43]. This range can be narrowed down using the limitation from figure 2.24, where we limited our study to ε_1 = 0, 0.1, 0.2, 0.3, 0.4 curves.

Also, for ε_1 = 0.7 the value for ε_{2opt} = 0, the physical meaning is that the external damping ε_1 is already high enough that it does not require internal damping ε_{2opt}.

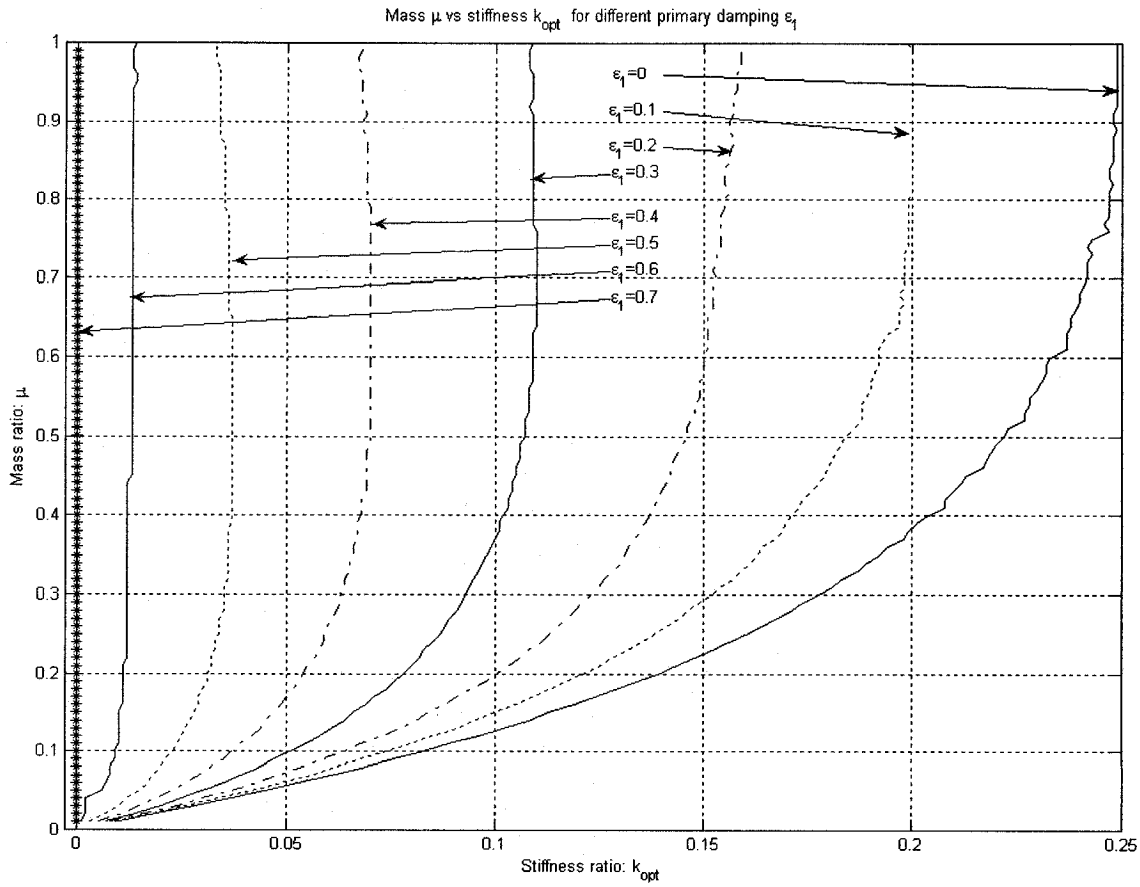

Figure 2.30 Plot of mass vs optimum stiffness for different primary damping ratios

Figure 2.30 shows the plot of mass ratio μ vs optimum stiffness ratio k_{opt} for different primary damping ratios ε_1.

It is clear from figure 2.30 that the range for k_{opt} is [0, 0.25]. This range for k_{opt} is for curves ε_1 in the range of [0, 0.7].

The value of k_{opt} = 0 is for all the curves ε_1 > 0.7. Physically, this means that the system has a high external damping ε_1, and that an k_{opt} is not required.

Also, for a given value of μ, a specific value of k_{opt} is found. This means that k_{opt} is very sensitive with respect to μ.

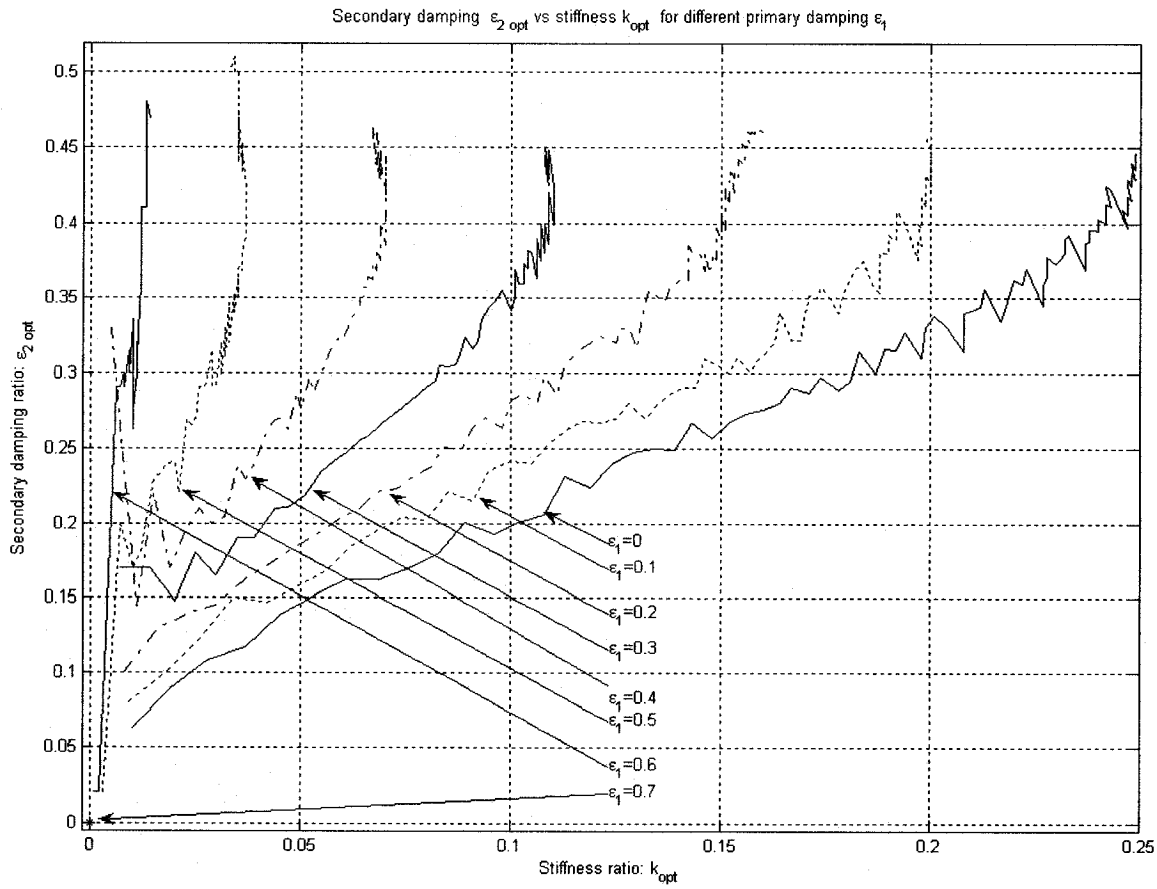

Figure 2.31 Plot of optimum secondary damping vs optimum stiffness for different primary damping ratios

Figure 2.31 shows the plot of optimum secondary damping ratio ε_{2opt} vs optimum stiffness ratio k_{opt} for different primary damping ratios ε_1.

In this scale, we do not see a linear relation; however, an approximation to a linear relation could possibly exist for some curves: ε_1 = 0, ε_1 = 0.1 and ε_1 = 0.2.

Also, in this figure we can see the optimum range of ε_{2opt} = [0.15, 0.45] mentioned for figure 2.26, which gives a relation to k_{opt} through curves ε_1.

Note the tendency of the ε_1 curves to become more vertical than inclined with the increase of the external damping ε_1, which, as similarly mentioned for figure 2.30 the k_{opt} is very sensitive with ε_{2opt} also.

We also see that for ε_1 > 0.6 the optimum values ε_{2opt} = 0 and k_{opt} = 0. This implies that the external damping ε_1 is high enough that neither internal damping nor stiffness is required.

In this chapter, we presented the mathematical model for the equation of motion derived from a 2-DOFS. The numerical derivation of optimum damping and stiffness for secondary systems was performed and simulated results were presented and discussed. In Chapter 3, we will do the experimental and theoretical investigation for a 2-DOFS for 2 different types, A and B, of seismic masses J_2, subject to a sinusoidal external variable torque $T(t) = S_V \sin(\omega\, t) = S_V \sin(2\pi f\, t)$.

CHAPTER 3

EXPERIMENTAL INVESTIGATION

3.1 Introduction

In Chapter 2 we did the analytical study for torsional vibration of a 2-DOFS subject to an external variable torque $T(t) = T_O.e^{i\omega t}$. Optimum values for internal or secondary damping ε_{2opt} and stiffness k_{opt} ratios were found for different inertia-mass μ and external or primary damping ε_1 ratios. The optimization method used was the H_∞ optimization [15] which minimizes the maximum amplitude $\left[\Theta_1.K_1/T_O\right]$.

In this chapter, we will do the experimental and theoretical investigation for a 2-DOFS for 2 different types, A and B, of seismic masses J_2, subject to a sinusoidal external variable torque, $T(t) = S_V \sin(\omega t) = S_V \sin(2\pi f t)$. For type A, the optimum theoretical values for internal or secondary damping ε_{2Aopt} and stiffness k_{opt} ratios are found for 3 different inertia-mass μ_A and external or primary damping ε_1 ratios. For type B, the optimum theoretical values for internal or secondary damping ε_{2Bopt} ratio is found for 3 different inertia mass μ_B and for the same external or primary damping ε_1 ratios. The frequency response for

each seismic mass will be compared between theoretical and experimental values.

3.2 Calculation of optimum values for seismic mass Type A

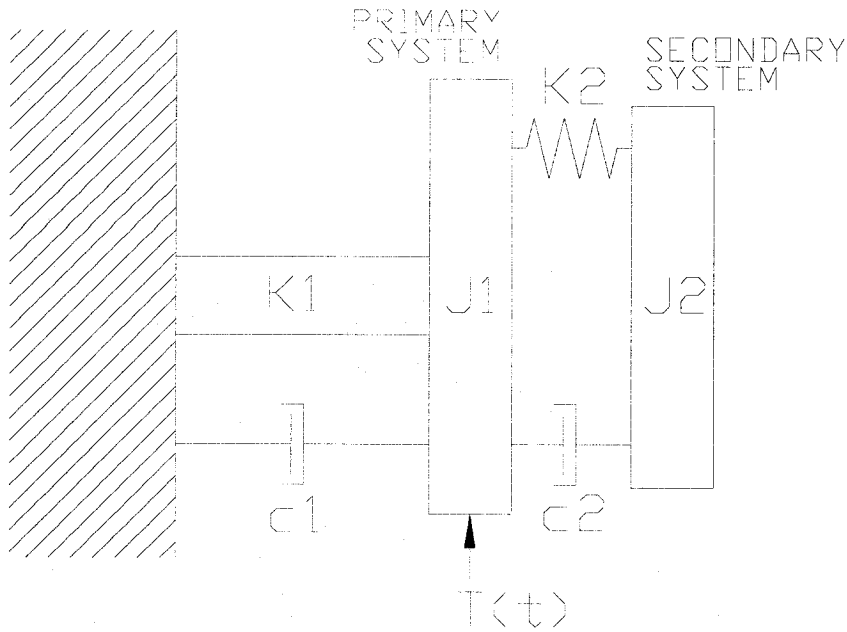

Figure 3.1 Free body diagram for type A seismic-mass system

$$J_1.\ddot{\theta}_1 + c_1.\dot{\theta}_1 + K_1.\theta_1 + c_2.(\dot{\theta}_1 - \dot{\theta}_2) + K_2.(\theta_1 - \theta_2) = T(t) = T_O \sin(\omega.t) = \mathrm{Im}[T_O\, e^{i\omega t}] \quad (3.1)$$

$$J_2.\ddot{\theta}_2 + c_2.(\dot{\theta}_2 - \dot{\theta}_1) + K_2.(\theta_2 - \theta_1) = 0 \quad (3.2)$$

Let the solutions for the angular amplitudes of the above equations be:

$$\begin{aligned} \theta_1(t) &= \mathrm{Im}[\Theta_1\, e^{i\omega t}] & \theta_2(t) &= \mathrm{Im}[\Theta_2\, e^{i\omega t}] \\ \dot{\theta}_1(t) &= \mathrm{Im}[\omega i \Theta_1\, e^{i\omega t}] & \dot{\theta}_2(t) &= \mathrm{Im}[\omega i \Theta_2\, e^{i\omega t}] \\ \ddot{\theta}_1(t) &= \mathrm{Im}[-\omega^2 \Theta_1\, e^{i\omega t}] & \ddot{\theta}_2(t) &= \mathrm{Im}[-\omega^2 \Theta_2\, e^{i\omega t}] \end{aligned} \quad (3.3)$$

Substituting equations 3.3 in equations 3.1 and 3.2 and rearranging the variables, we obtain the matrix form:

$$\begin{bmatrix} \left(-J_1.\omega^2+(c_1+c_2).\omega.i+K_1+K_2\right) & (-c_2.\omega.i-K_2) \\ (-c_2.\omega.i-K_2) & \left(-J_2.\omega^2+c_2.\omega.i+K_2\right) \end{bmatrix} \begin{Bmatrix} \Theta_1 \\ \Theta_2 \end{Bmatrix} = \begin{Bmatrix} T_O \\ 0 \end{Bmatrix} \tag{3.4}$$

Recalling the five following nondimensional variables from equation 2.7

$$\begin{aligned} \varepsilon_1 &= c_1 \Big/ 2J_1\omega_1 \\ \varepsilon_2 &= c_2 \Big/ 2J_2\omega_2 \\ k &= K_2/K_1 \\ \mu &= J_2/J_1 \\ x &= \omega/\omega_1 \end{aligned} \tag{3.5}$$

where: $\omega_1 = \sqrt{\dfrac{K_1}{J_1}}$ and $\omega_2 = \sqrt{\dfrac{K_2}{J_2}}$

and substituting 3.5 in equation 3.4, we get

$$\begin{bmatrix} \left(-x^2+2.\varepsilon_1.x.i+2.\varepsilon_2.\sqrt{\mu.k}.x.i+1+k\right) & (-2.\varepsilon_2.\sqrt{\mu.k}.x.i-k) \\ (-2.\varepsilon_2.\sqrt{\mu.k}.x.i-k) & \left(-\mu.x^2+2.\varepsilon_2.\sqrt{\mu.k}.x.i+k\right) \end{bmatrix} \begin{Bmatrix} \dfrac{\Theta_1.K_1}{T_O} \\ \dfrac{\Theta_2.K_1}{T_O} \end{Bmatrix} = \begin{Bmatrix} 1 \\ 0 \end{Bmatrix} \tag{3.6}$$

Solving the matrix equation (3.5) using determinants we have

$$\frac{\Theta_1.K_1}{T_O} = \frac{\begin{vmatrix} 1 & (-2.\varepsilon_2.\sqrt{\mu.k}.x.i-k) \\ 0 & \left(-\mu.x^2+2.\varepsilon_2.\sqrt{\mu.k}.x.i+k\right) \end{vmatrix}}{\begin{vmatrix} \left(-x^2+2.\varepsilon_1.x.i+2.\varepsilon_2.\sqrt{\mu.k}.x.i+1+k\right) & (-2.\varepsilon_2.\sqrt{\mu.k}.x.i-k) \\ (-2.\varepsilon_2.\sqrt{\mu.k}.x.i-k) & \left(-\mu.x^2+2.\varepsilon_2.\sqrt{\mu.k}.x.i+k\right) \end{vmatrix}} \tag{3.7}$$

With given values of inertia mass μ and primary damping ε_1 ratios and using the optimization H_∞ method in this numerical evaluation as in section 2.3 [15],

which minimizes the dynamic magnifier Θ_1 of the primary system, we find the optimum stiffness k_{opt} and secondary damping ε_{2Aopt} ratios shown in table 3.1. The values for μ_A and ε_1 are discussed in sections 3.6 and 3.12 respectively.

ε_1	μ_A	k_{opt}	ε_{2Aopt}
--	--	--	--
0.010	S: 0.246	0.157	0.263
0.010	M: 0.179	0.128	0.229
0.010	L: 0.129	0.100	0.217

Table 3.1 Optimum stiffness k_{opt} and secondary damping ε_{2Aopt} ratios

3.3 Calculation of optimum values for seismic mass Type B

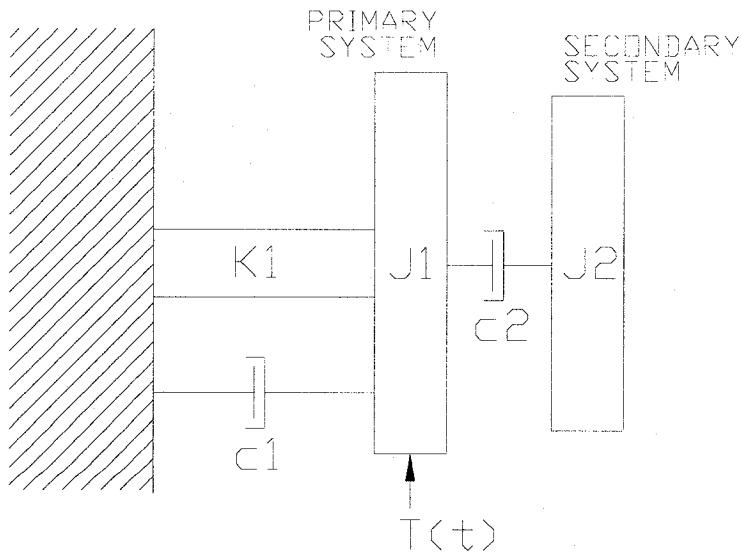

Figure 3.2 Free body diagram for type B seismic-mass system

$$J_1.\ddot{\theta}_1 + c_1.\dot{\theta}_1 + K_1.\theta_1 + c_2.\left(\dot{\theta}_1 - \dot{\theta}_2\right) = T(t) = T_O \sin(\omega\, t) = \mathrm{Im}[T_O\, e^{i\omega t}] \tag{3.8}$$

$$J_2.\ddot{\theta}_2 + c_2.\left(\dot{\theta}_2 - \dot{\theta}_1\right) = 0 \tag{3.9}$$

Let the solutions for the angular amplitudes of the above equations be:

$$\begin{aligned} \theta_1(t) &= \mathrm{Im}[\Theta_1\, e^{i\omega t}] & \theta_2(t) &= \mathrm{Im}[\Theta_2\, e^{i\omega t}] \\ \dot{\theta}_1(t) &= \mathrm{Im}[\omega i \Theta_1\, e^{i\omega t}] & \dot{\theta}_2(t) &= \mathrm{Im}[\omega i \Theta_2\, e^{i\omega t}] \\ \ddot{\theta}_1(t) &= \mathrm{Im}[-\omega^2 \Theta_1\, e^{i\omega t}] & \ddot{\theta}_2(t) &= \mathrm{Im}[-\omega^2 \Theta_2\, e^{i\omega t}] \end{aligned} \tag{3.10}$$

Substituting equations 3.10 in equations 3.8 and 3.9 and rearranging the variables we obtain the matrix form:

$$\begin{bmatrix} \left(-J_1.\omega^2 + (c_1 + c_2).\omega.i + K_1\right) & (-c_2.\omega.i) \\ (-c_2.\omega.i) & \left(-J_2.\omega^2 + c_2.\omega.i\right) \end{bmatrix} \begin{Bmatrix} \Theta_1 \\ \Theta_2 \end{Bmatrix} = \begin{Bmatrix} T_O \\ 0 \end{Bmatrix} \tag{3.11}$$

Introducing the four following nondimensional variables:

$$\begin{aligned} \varepsilon_1 &= c_1 \Big/ 2.J_1.\omega_1 \\ \varepsilon_2 &= c_2 \Big/ 2.J_1.\omega_1 \\ \mu &= J_2 / J_1 \\ x &= \omega / \omega_1 \end{aligned} \tag{3.12}$$

and substituting 3.12 in equation 3.11, we get

$$\begin{bmatrix} \left(-x^2 + 2.\varepsilon_1.x.i + 2.\varepsilon_2.\mu.x.i + 1\right) & (-2.\varepsilon_2.\mu.x.i) \\ (-2.\varepsilon_2.\mu.x.i) & \left(-\mu.x^2 + 2.\varepsilon_2.\mu.x.i\right) \end{bmatrix} \begin{Bmatrix} \dfrac{\Theta_1.K_1}{T_O} \\ \dfrac{\Theta_2.K_1}{T_O} \end{Bmatrix} = \begin{Bmatrix} 1 \\ 0 \end{Bmatrix} \tag{3.13}$$

Solving the matrix equation (3.13) using determinants, we get

$$\frac{\Theta_1.K_1}{T_O} = \frac{\begin{vmatrix} 1 & (-2.\varepsilon_2.\mu.x.i) \\ 0 & \left(-\mu.x^2 + 2.\varepsilon_2.\mu.x.i\right) \end{vmatrix}}{\begin{vmatrix} \left(-x^2 + 2.\varepsilon_1.x.i + 2.\varepsilon_2.\mu.x.i + 1\right) & (-2.\varepsilon_2.\mu.x.i) \\ (-2.\varepsilon_2.\mu.x.i) & \left(-\mu.x^2 + 2.\varepsilon_2.\mu.x.i\right) \end{vmatrix}} \tag{3.14}$$

With given values of inertia mass μ_B and primary damping ε_1 ratios and using the optimization H_∞ method in this numerical evaluation [15], which minimizes the dynamic magnifier Θ_1 of the primary system, we find the optimum secondary damping ε_{2Bopt} ratios shown in table 3.2. The values for μ_B and ε_1 are discussed in sections 3.6 and 3.12, respectively.

ε_1	μ_B	ε_{2Bopt}
--	--	--
0.010	S: 0.451	0.371
0.010	M: 0.327	0.399
0.010	L: 0.236	0.422

Table 3.2 Optimum secondary damping ε_{2Bopt} ratio

3.4 Experimental 2-DOFS layout

The experimental layout of the 2-DOFS is shown in figure 3.3 with its components: the shaker, signal analyzer, accelerometer input, accelerometer output, pivot arm, rod, flywheels and flange.

The horizontal oscillating movement of the shaker is transformed into angular oscillating movement through the mechanism over the pivot arm. The generator inputs the voltage S_V = 10 mV resulting in a sinusoidal torque of $T(t)=10\sin(2\pi f\, t)$ and sweeps a range of frequencies from 4 Hz to 22 Hz for all the experimental tests shown in figures 3.10, 3.11 and 3.12.

The rod with stiffness K_1 rests on 2 ball bearings. The pivot arm transmits the oscillating motion through the rod to the flange and thus to the flywheels. For this experimental investigation we used 3 different flywheel sizes: S, M and L; their moments of inertia are presented in table 3.5.

The 2 linear accelerometers measuring the input and the output accelerations are positioned at the same radial distance from the center line of the rod, as shown. The accelerometer input located on the pivot arm records the tangential acceleration from the pivot arm a_{ti} , and the accelerometer output located on the flange records the tangential acceleration a_{to} from the flywheel or the damper (see figure 3.3).

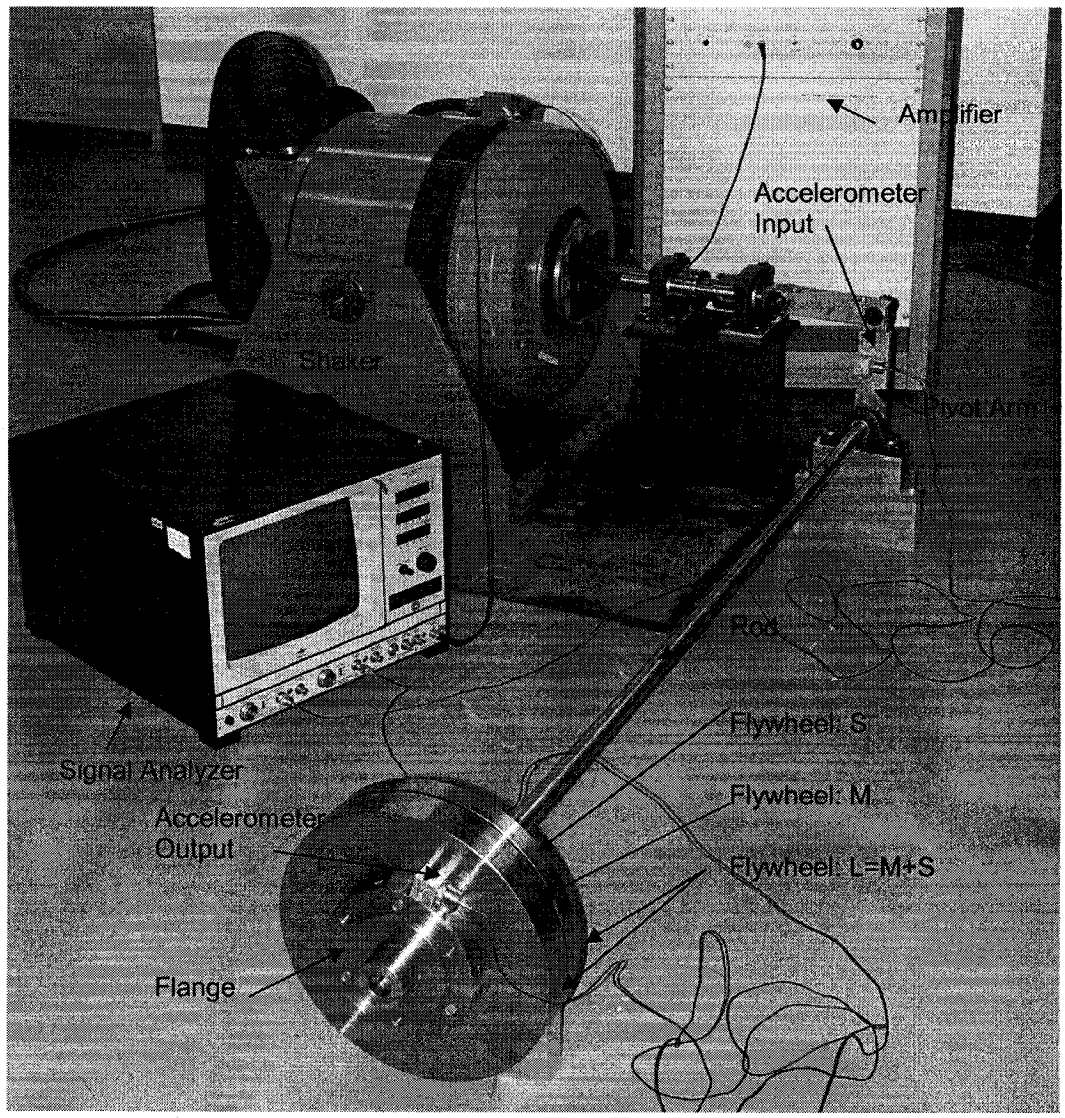

Figure 3.3 Experimental 2-DOFS layout

The technical specifications for the equipment and measuring devices used in the experiment are:

Shaker model: : S 062

Peak sine force : 600 lbs (2.67 kN)

Displacement max : 2 inches (51 mm)

Armature weight : 10 lbs (4.5 kg)

Armature diameter : 7 inches (178 mm)

Amplifier model : TA 250

Signal analyzer : Type 2035

Accelerometers : Type 4370

3.5 Moment of inertia secondary system J_{2A} and J_{2B}

Since an existing model of damper was modified to suit the two seismic masses, the cavity size was already given by the casing of the existing damper, and the outer dimensions for the seismic masses correspond to it.

The first type, type A seismic mass J_{2A}, has a solid steel donut shape but with a counter bore on the peripheral diameter of the seismic mass. The counter bore accommodates the four helical springs, two at the top and two at the bottom as shown in figure 3.4; the bottom springs are not seen in figure 3.4. The moment of inertia for type A seismic mass $J_{2A} = 0.077\ kg.m^2$.

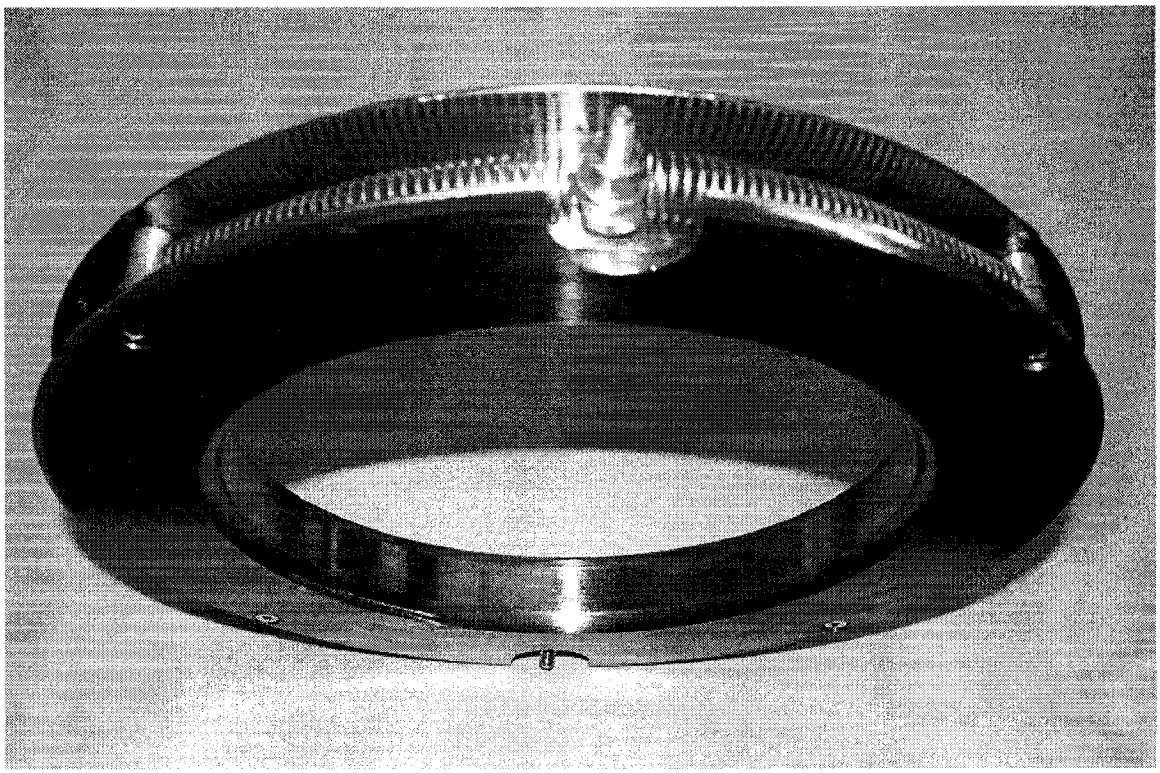

Figure 3.4 Type A seismic mass with counter bore to allocate four helical springs

The second type, type B seismic mass J_{2B}, has the same shape as found in the standard viscous damper; i.e., a solid steel donut, without a counter bore, as shown in figure 3.5. The moment of inertia for type B seismic mass J_{2B} = 0.141 $kg.m^2$.

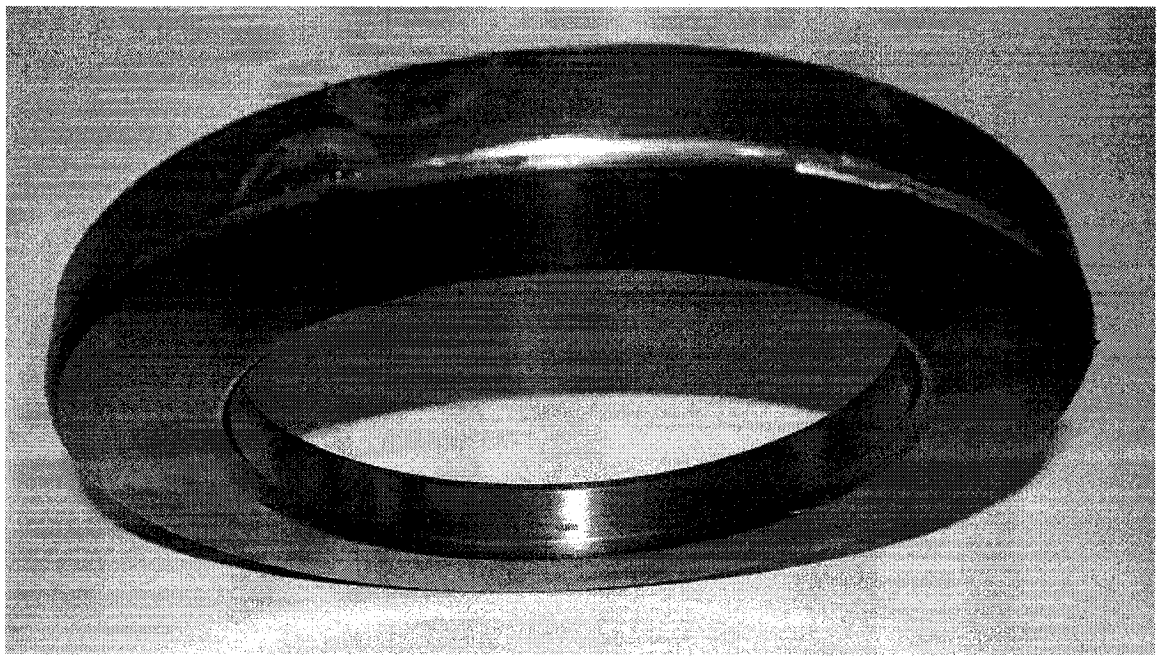

Figure 3.5 Type B seismic mass (without counter bore)

3.6 The primary system J_1

The flywheel mounted on the back of the flange, the casing mounted on the front part of the flange, the 6 spacers, the 6 C-clamps and the lid, constitute the primary system J_1. All those 5 components together without the respective seismic mass constitute the moment of inertia for the primary system (see figure 3.6).

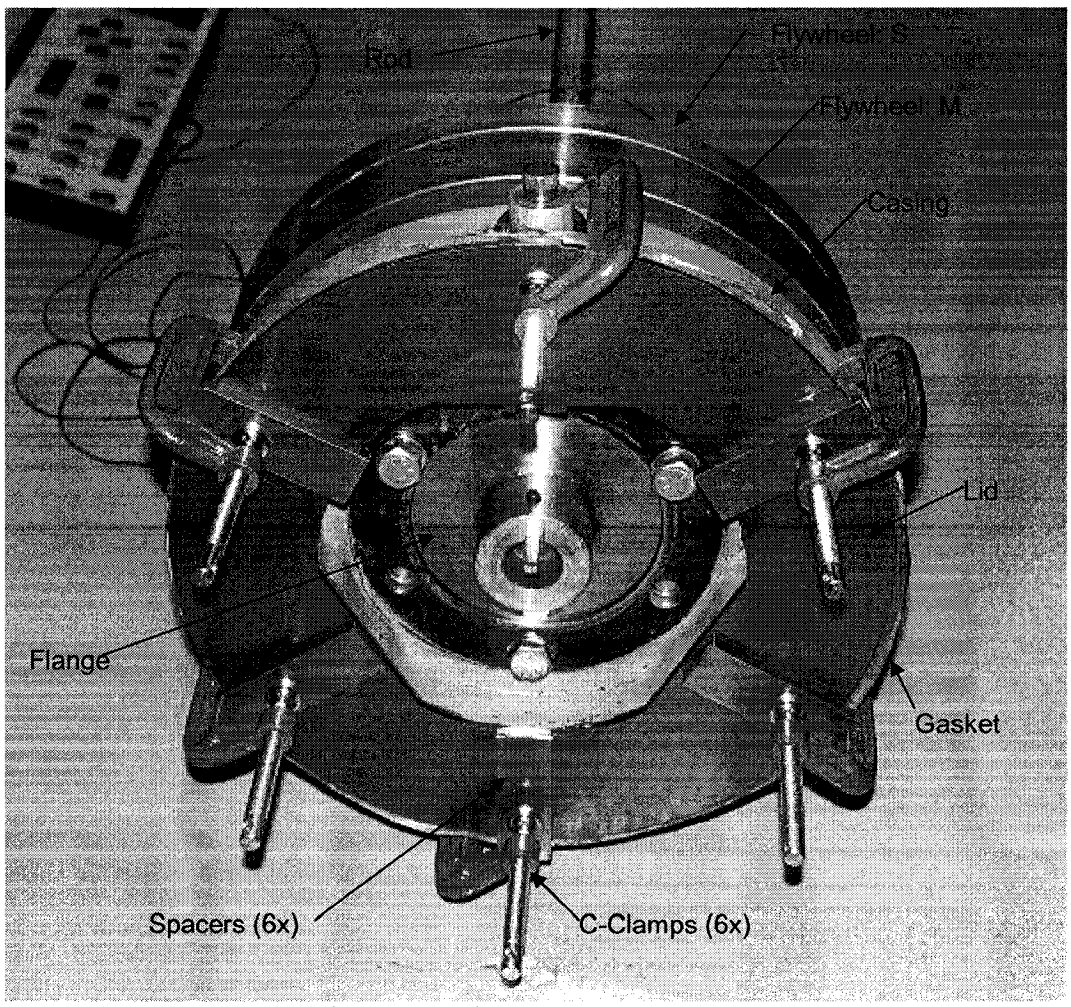

Figure 3.6 Damper with seismic mass A or B assembled

Table 3.3 shows the moments of inertia of the primary system J_1 , and of the secondary system, J_{2A} and J_{2B}, and their ratios μ_A and μ_B, respectively, for the 3 different sizes of flywheels.

J_1	J_{2A}	J_{2B}	μ_A	μ_B
$kg.m^2$	$kg.m^2$	$kg.m^2$	--	--
S: 0.313	0.077	0.141	0.246	0.451
M: 0.431	0.077	0.141	0.179	0.327
L: 0.599	0.077	0.141	0.129	0.236

Table 3.3 Inertia ratio for seismic mass A and B

3.7 Stiffness of primary system K_1

The rod on figure 3.3 was prepared to the required stiffness of the 2-DOFS given by:

$$K_1 = \frac{G.I_p}{L} = 1925.7 \ N.m/rad$$

where:

$L =$ 1.6764 m, rod length

$D = 0.0254 \ m$, rod diameter

$G =$ 79 GPa, modulus of rigidity of steel shaft in gigapascal.

$I_p = \frac{\pi}{32}.D^4 \quad m^4$, rod polar moment of inertia

3.8 Stiffness of secondary system K_2

For type A, the stiffness of the secondary system is calculated using equation 3.5, $K_2 = k_{opt}.K_1$. where: k_{opt} from section 3.2 and K_1 = 1925.7 $N.m/rad$ from section 3.7. Note that this is the stiffness of the secondary system and not the stiffness of each helical spring.

The stiffness for each helical spring K_{HS} is calculated using the formula [4]:

$$K_{HS} = \frac{K_2}{4.R^2.\cos(A)} \tag{3.15}$$

where:

R = 0.138 m, which is the distance from hook-end center to damping-device center, as shown in figure 3.7.

The angle that the helical spring makes with horizontal axis is A = 20 ° (see figure 3.7).

J_1	k_{opt}	K_1	K_2	K_{HS}
$kg.m^2$	--	$N.m/rad$	$N.m/rad$	N/mm
S: 0.313	0.157	1925.7	302.3	4.22
M: 0.431	0.128	1925.7	246.5	3.44
L: 0.599	0.100	1925.7	192.6	2.69

Table 3.4 Helical spring stiffness K_{HS} for type A seismic mass and for 3 different primary moments of inertia

The above formula for the linear stiffness calculation is used under the assumption that all the torsional torque is transmitted through the helical springs, disregarding the torque transmitted through the viscous fluid.

For the experimental investigation for the 3 different sizes of flywheels: S, M and L, a commercial helical spring with the following calculated [72] characteristics was chosen:

d_{HS} = 1.37 mm, wire diameter of helical spring

D_{HS} = 14.43 mm, diameter of helical spring

K_{HS} = 0.342 N/mm, helical spring stiffness

N_{HS} = 34, number of turns of helical spring

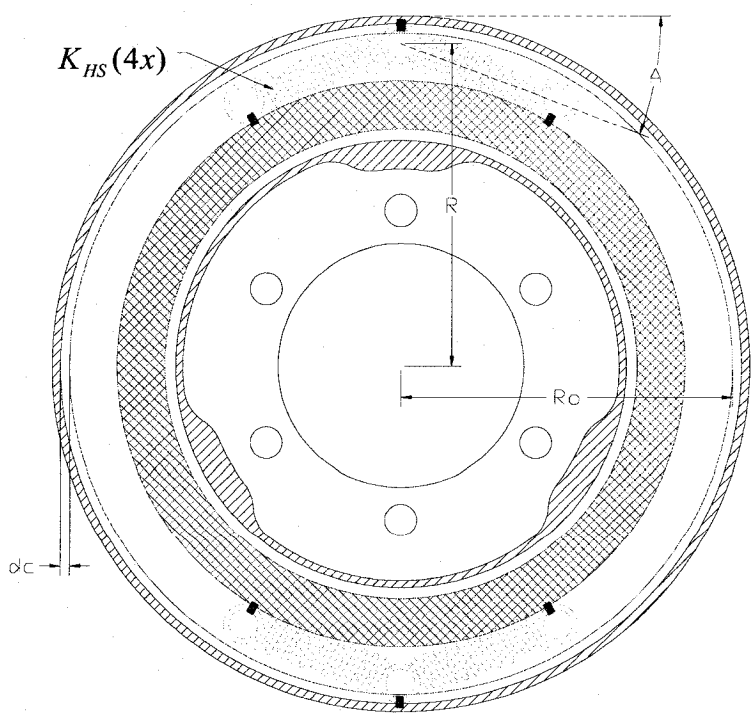

Figure 3.7 Type A seismic mass with counter bore and four helical springs

It is clear that for type B seismic mass, with viscous fluid as the only torque-transmitting media, the stiffness on the secondary system is K_2 = 0, as shown in section 3.3.

3.9 Natural frequency of primary system ω_{1N} without damper

The natural frequency of the primary system ω_{1N} without a damper for this experimental investigation is calculated as $\omega_{1N} = \sqrt{K_1 / J_{1N}}$, where K_1 = 1925.7 $N.m/rad$ from section 3.7, and J_{1N} is the moment of inertia of each flywheel size plus the moment of inertia of the flange only, as shown in figure 3.3. The calculated natural frequencies are given in table 3.5.

J_{1N} $Kg.m^2$	K_1 $N.m/rad$	ω_{1N} rad/s	f_{1N} Hz
S_N : 0.179	1925.7	103.7	16.5
M_N : 0.297	1925.7	80.5	12.8
L_N : 0.465	1925.7	64.4	10.2

Table 3.5 Natural frequencies primary system for each flywheel size: S_N, M_N and L_N

3.10 Natural frequency of primary system ω_1 with damper

The natural frequency of the primary system ω_1 for both dampers is calculated as $\omega_1 = \sqrt{K_1 / J_1}$, where K_1 = 1925.7 $N.m/rad$ and J_1 is the moment of inertia of the primary system of each flywheel size from section 3.4. The natural frequencies are given in table 3.6.

J_1 $Kg.m^2$	K_1 $N.m/rad$	ω_1 rad/s	f_1 Hz
S: 0.313	1925.7	78.4	12.5
M: 0.431	1925.7	66.8	10.6
L: 0.599	1925.7	56.7	9.0

Table 3.6 Natural frequencies primary system for each flywheel size: S, M and L with damper

3.11 Natural frequency of secondary system ω_2

For type A seismic mass, the natural frequency of the secondary system is $\omega_2 = \sqrt{K_2 / J_{2A}}$. where K_2 is from section 3.8 and J_{2A} = 0.077 $kg.m^2$ from section 3.5. The natural frequencies are given in table 3.7.

J_{2A}	K_1	k_{opt}	K_2	ω_2	f_2
$Kg.m^2$	$N.m/rad$	---	$N.m/rad$	rad/s	Hz
0.077	1925.7	0.157	302.3	62.7	10.0
0.077	1925.7	0.128	246.5	56.6	9.0
0.077	1925.7	0.100	192.6	50.0	8.0

Table 3.7 Natural frequencies secondary system for each flywheel size: S, M and L

Although it is possible to calculate the natural frequency of the secondary system for type A theoretically, it is clear that in practice it is almost impossible to control or measure the actual value, ω_2 .

It is also clear, that for type B seismic mass, its natural frequency is $\omega_2 = \omega_1$ as shown in equation 3.12.

3.12 Damping of primary system c_1

As mentioned in figure 2.26, during the design stage in a real case situation, the primary damping or external damping ratio ε_1, is difficult to evaluate; however, it is present and different from zero. In addition, according to the analytical evaluation in sections 3.2 and 3.3, the primary damping ratio ε_1 has a direct

relation with primary damping c_1 through equations 3.5 and 3.12, respectively ($c_1 = 2\varepsilon_1 J_1 \omega_1$).

For our experimental investigation we assume ε_1 = 0.01.

3.13 Damping of secondary system c_{2A} and c_{2B}

For type A seismic mass, with viscous fluid and helical springs, the selection of the proper viscous fluid depends on its viscosity ν_{SA} which is calculated from the optimum damping c_{2A}, using the theoretical formula [4] below. From equation 3.5: $c_{2A} = 2.\varepsilon_{2A}.J_{2A}.\omega_{2A}$, where: $\varepsilon_{2A} = \varepsilon_{2Aopt}$ from section 3.2, J_{2A} = 0.077 $kg.m^2$ from section 3.5, and $\omega_{2A} = \omega_2$ from section 3.11. The viscosity is given by [4]:

$$\nu_{SA} = \frac{c_{2A}.dc.\left(1 - \frac{1}{1 + \frac{2.L_{SA}}{Ro}}\right)}{1.019x10^{-8}.2.\pi.L_{SA}.Ro^3} \qquad (3.16)$$

where:

Ro = 14.834 cm, seismic mass outer radius

L_{SA} = 0.70 cm , seismic mass width at peripheral outer radius, Ro

dc = 0.052 cm , clearance

J_{2A} $kg.m^2$	ω_2 rad/s	ε_{2Aopt} ---	(c_{2A}) $kg.m^2.rad/s$	c_{2A} $kg.cm.s/rad$	ν_{SA} $centistokes$
S: 0.077	62.7	0.263	2.538	25.871	793.0
M: 0.077	56.6	0.229	1.995	20.340	623.5
L: 0.077	50.0	0.217	1.671	17.036	522.2

Table 3.8 Secondary damping c_{2A} and viscosity ν_{SA} for type A seismic mass

The above formula is used under the assumption that all the torque is transmitted through the viscous fluid only, disregarding the torque transmitted through the helical springs. This assumption is not the real case in the system and it is used for reference to determine the viscosity of the viscous fluid.

For type B seismic mass with viscous fluid only, the formula [4] is a good approximation for the viscosity ν_{SB} calculation, since it is assumed that the torque is transmitted only through the viscous fluid. From equation 3.12, we have $c_{2B} = 2.\varepsilon_{2B}.J_1.\omega_1$, where: $\varepsilon_{2B} = \varepsilon_{2Bopt}$ from section 3.3, J_1 from section 3.6, and ω_1 from section 3.10.

$$\nu_{SB} = \frac{c_{2B}.dc.\left(1 - \frac{1}{1 + \frac{2.L_{SB}}{Ro}}\right)}{1.019x10^{-8}.2.\pi.L_{SB}.Ro^3} \qquad (3.17)$$

where:

Ro = 14.834 cm, seismic-mass outer radius

L_{SB} = 3.00 cm , seismic-mass width at peripheral outer radius Ro

dc = 0.052 cm , clearance

Table 3.9 provides the damping c_{2B} and the viscosity ν_{SB} values.

J_1 $kg.m^2$	ω_1 rad/s	ε_{2Bopt} ---	(c_{2B}) $kg.m^2.rad/s$	c_{2B} $kg.cm.s/rad$	ν_{SB} $centistokes$
S: 0.313	78.4	0.371	18.217	185.696	4435.4
M: 0.431	66.8	0.399	22.990	234.351	5597.6
L: 0.599	56.7	0.422	28.665	292.201	6979.3

Table 3.9 Secondary damping c_{2B} and viscosity ν_{SB} for type B seismic mass

Note that the width L_{SA} = 0.70 cm for type A seismic mass is not the same as for type B, L_{SB} = 3.00 cm. The difference in width between the two seismic masses is due to the counter bore on the peripheral diameter of type A seismic mass to accommodate the 4 helical springs.

For our experimental investigation we use commercial fluid lubricant, for both types of seismic masses A and B, with viscosity system grade identification ISO VG 680 [69]: SAE 10 W 40 with viscosity values: 86 *centistokes* at 40 °C and 13.8

centistokes at 100 °C, measured with standard [71]. The viscosity value at 20 °C is found with the formula [70]:

$$\log(\log(\nu + 0.7)) = F - G.\log(T) \tag{3.18}$$

where:

F, G = constants

T = temperature in °K

ν = viscosity in *centistokes*

The constants F, G are found replacing the viscosity and temperature values given: 86 *centistokes* at 40 °C and 13.8 *centistokes* at 100 °C in equation 3.18. Then, with the found constants F, G, we find the viscosity of the lubricant oil SAE 10 W 40: ν_S = 224.6 *centistokes* at 293.15 °K = 20 °C, obtained from same equation 3.18.

3.14 Clearance dc between seismic mass and casing

The clearance dc that contains the viscous fluid was not modified from the original damper model which was used for this experimental investigation. It was left at the original actual range between 0.019 *in* and 0.022 *in*, which is within the theoretical value obtained with the formula [4]:

$$dc = 0.010 + 0.010.\sqrt{\frac{2.Ro}{10}} = 0.021 \ in \ = 0.52 \ mm \tag{3.19}$$

where:

Ro = 5.891 in, actual seismic-mass outer radius.

3.15 Comparison of theoretical and experimental results

For type A and B seismic masses, following the approach in section 3.13 with liquid lubricant, SAE 10 W 40 has the viscosity ν_S = 224.6 $centistokes$. Consequently, the secondary damping ratios are obtained as ε_{2A} = 0.094 and ε_{2B} = 0.014, respectively.

For type A, the helical spring stiffness K_{HS} = 0.342 N/mm corresponds to the stiffness ratio k = 0.013, using the approach in section 3.8.

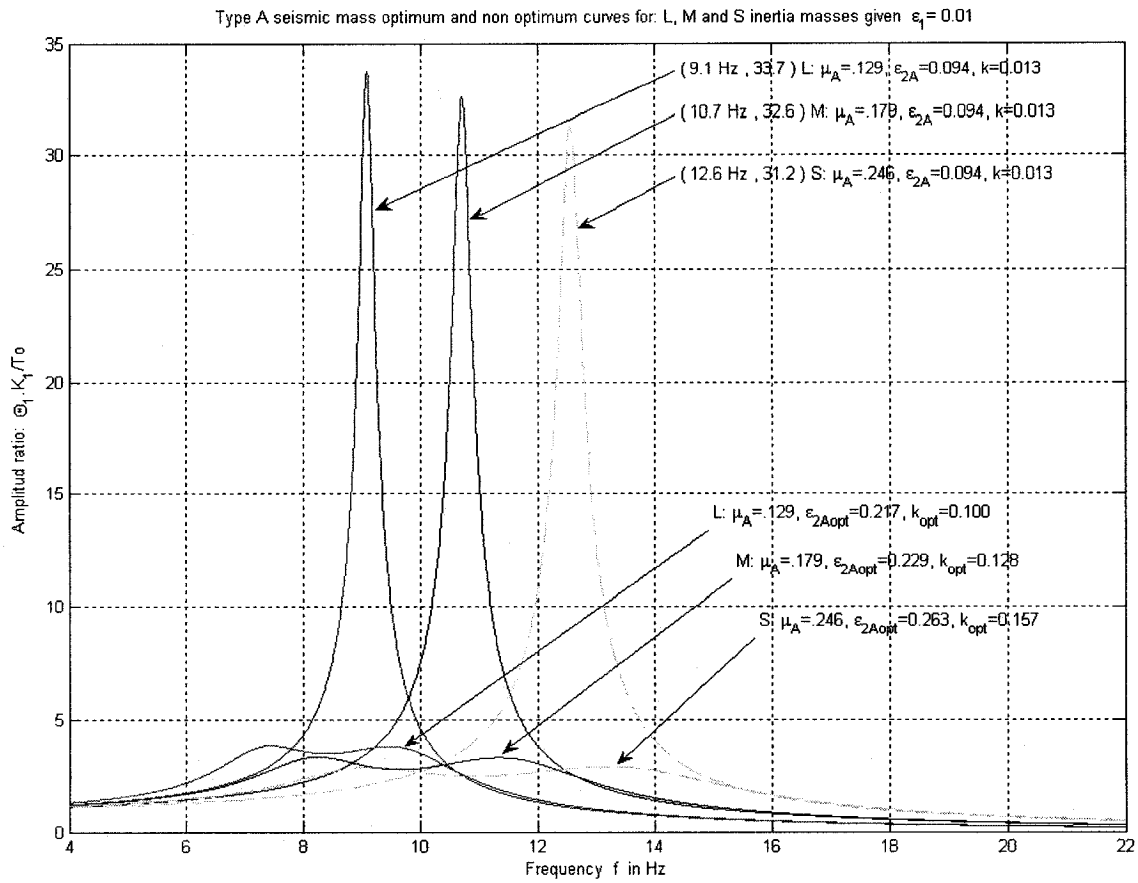

Figure 3.8 Type A seismic-mass optimum and non-optimum curves for L, M and S inertia masses given primary damping ratio ε_1 = 0.01

Figures 3.8 shows the theoretical frequency response for type A seismic mass of equation 3.7 for the optimum values from table 3.1 for S, M and L inertia masses. In the same figure, 3.8, we also have the frequency response for the experimental parameters ε_{2A} = 0.094 and k = 0.013 presented at the beginning of section 3.15.

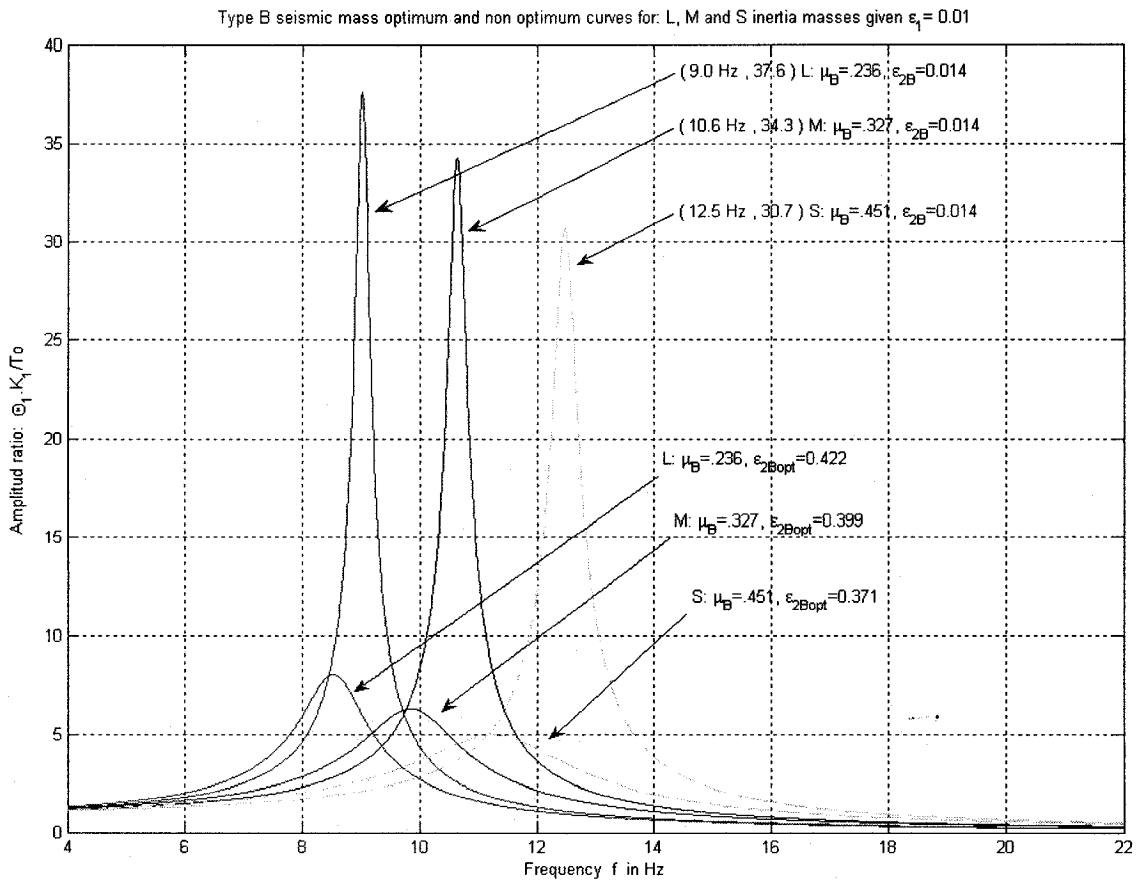

Figure 3.9 Type B seismic-mass optimum and non-optimum curves for L, M and S inertia masses given primary damping ratio ε_1 = 0.01

Figure 3.9 shows the theoretical frequency response for type B seismic mass of equation 3.14 for the optimum values from table 3.2 for S, M and L inertia masses. In the same figure, 3.9, we also have the frequency response for the experimental parameter ε_{2B} = 0.014 presented at the beginning of section 3.15.

In figures 3.8 and 3.9, the theoretical frequency response for the flywheels of type A and B follow the same trend. These results show that the response can be

reduced up to 20% of the original value by using the optimum parameters. The experimental results of figures 3.11 and 3.12 also follow the same trend.

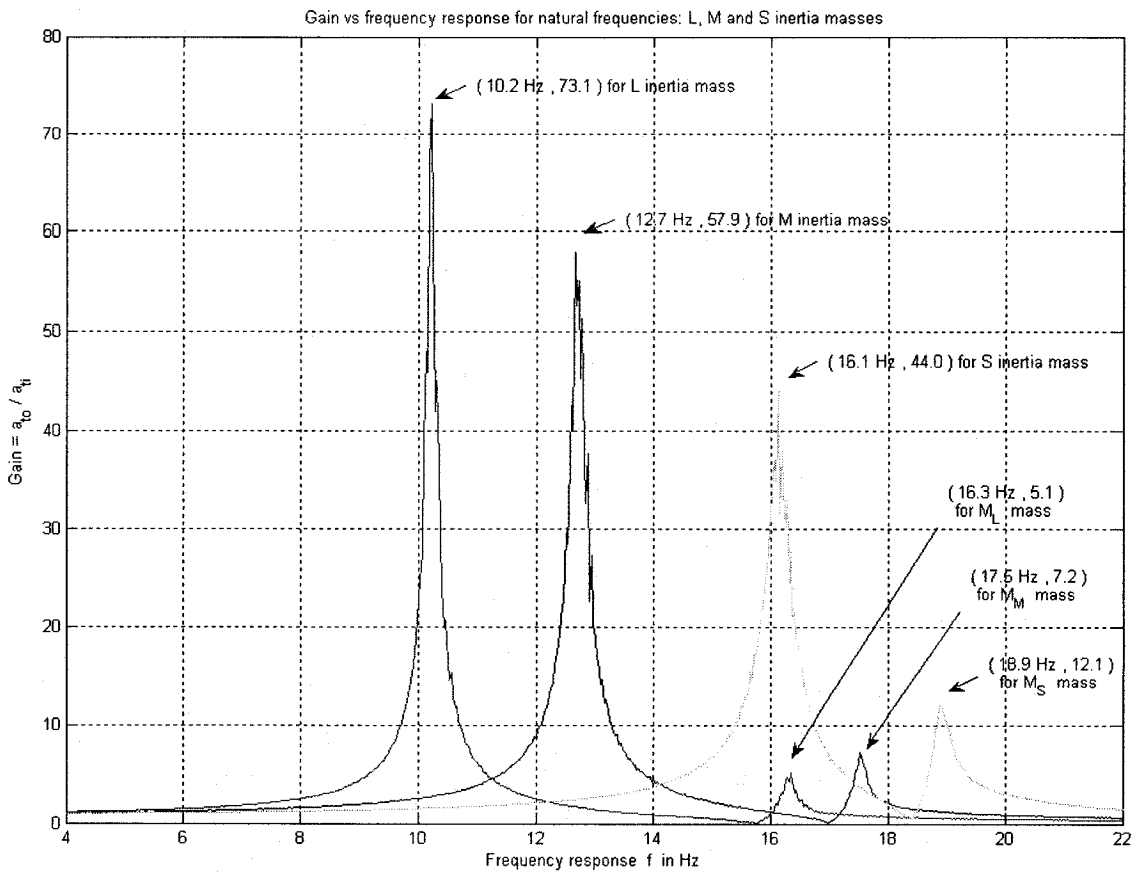

Figure 3.10 Experimental natural frequencies f_{1N} response for L, M and S inertia masses

Figure 3.10 shows the experimental frequency response for the system shown in figure 3.3. The theoretical natural frequencies of this system are calculated in section 3.9 and the comparison is shown in table 3.10.

It is clear that the theoretical amplitude ratio $\Theta_1.K_1/T_O$ = ∞ for the 3 natural frequencies of each S, M and L inertia masses; however, the experimental $Gain \neq \infty$ in figure 3.10. In addition, this $Gain \neq \infty$ has a descending trend from L to S inertia masses. The physical explanation is that the shaker, the 2 self-aligning ball-bearing supports for the rod and the mechanisim between the shaker and pivot arm, together are acting as primary or external damping c_1 for the whole system (see figures 3.3 and 3.13).

Inertia mass --	Theoretical f_{1N} *Hz*	Experimental f_{1N} *Hz*
S	16.5	16.1
M	12.8	12.7
L	10.2	10.2

Table 3.10 Comparison between theoretical and experimental natural frequencies f_{1N} for L, M and S inertia masses

Figure 3.11 shows the experimental frequency response for type A seismic mass inside the casing, properly mounted on the flange for the test (see figure 3.6).

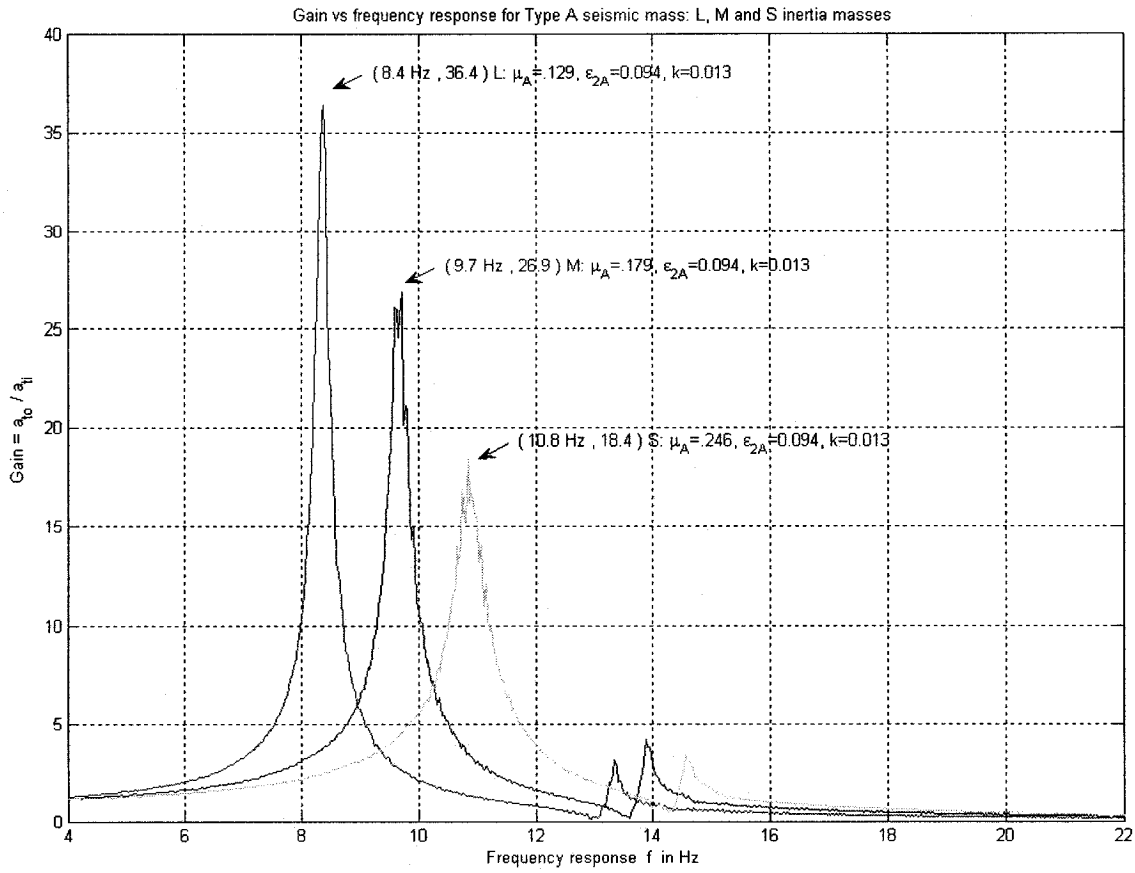

Figure 3.11 Frequency response for type A seismic mass for L, M and S inertia masses

Inertia mass	Theoretical		Experimental	
	f	$\Theta_1.K_1/T_o$	f	*Gain*
--	*Hz*	--	*Hz*	--
S	12.6	31.2	10.8	18.4
M	10.7	32.6	9.7	26.9
L	9.1	33.7	8.4	36.4

Table 3.11 Type A seismic-mass comparison between theoretical (Fig 3.8) and experimental (Fig 3.11) natural frequencies f for L, M and S inertia masses

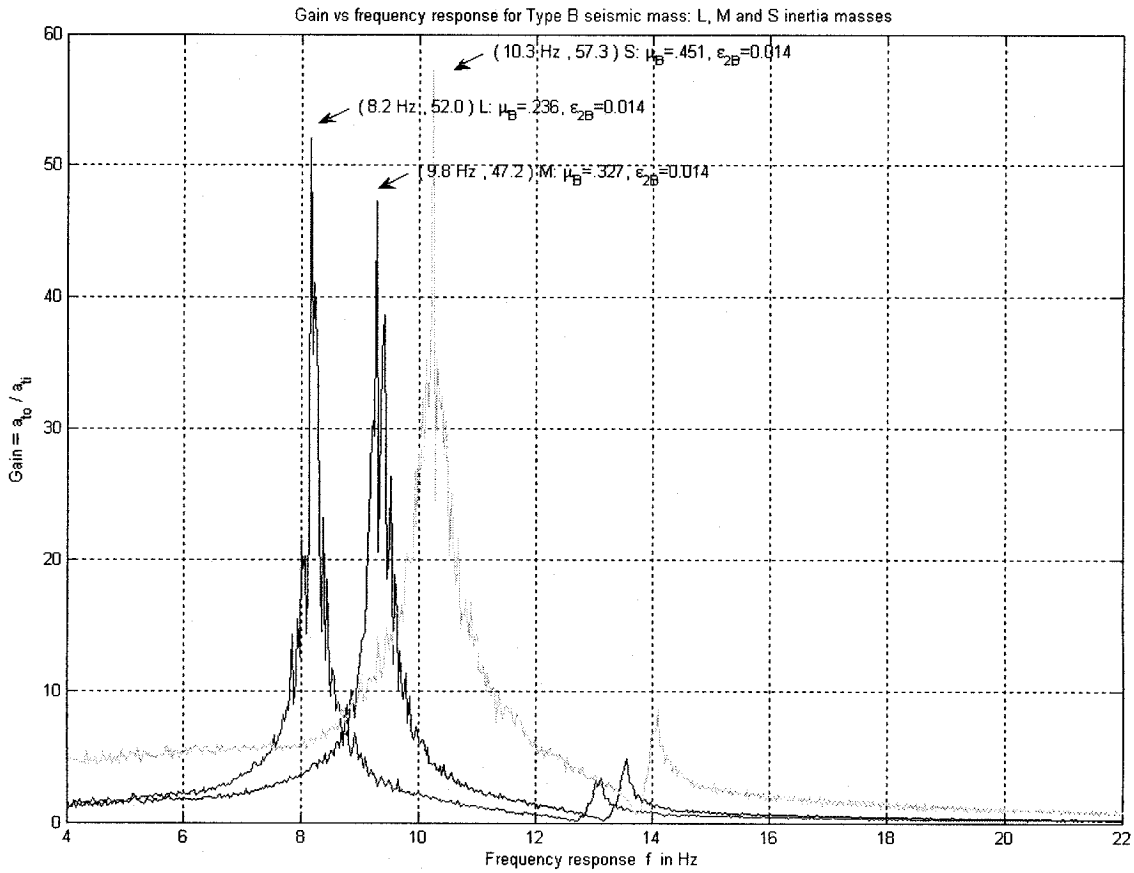

Figure 3.12 Frequency response for type B seismic mass for L, M and S inertia masses

Figure 3.12 shows the experimental frequency response for type B seismic mass inside the casing and properly mounted on the flange for test (see figure 3.6).

Inertia mass	Theoretical		Experimental	
	f	$\Theta_1.K_1/T_O$	f	*Gain*
--	*Hz*	--	*Hz*	--
S	12.5	30.7	8.2	52.0
M	10.6	34.3	8.0	47.2
L	9.0	37.6	10.3	57.3

Table 3.12 Type B seismic-mass comparison between theoretical (Fig 3.9) and experimental (Fig 3.12) natural frequencies f for L, M and S inertia masses

Table 3.12 shows the comparison between the theoretical and experimental natural frequencies, and the comparison of theoretical amplitude ratio and experimental gain.

Table 3.13 shows the comparison between the theoretical and experimental natural frequencies, and the comparison of theoretical amplitude ratio and experimental gain for similar mass ratios, μ_A = 0.246 (S inertia mass) and μ_B = 0.236 (L inertia mass), or for practical considerations, $\mu_A \cong \mu_B$ = 0.241. Note that the experimental gain drops from 52 to 18.4, about 35%.

Inertia mass	Inertia ratio	Theoretical		Experimental	
		f	$\Theta_1.K_1/T_O$	f	$Gain$
--	--	Hz	--	Hz	--
S	μ_A = 0.246	12.6	31.2	10.8	18.4
L	μ_B = 0.236	9.0	37.6	8.2	52.0

Table 3.13 Comparison between similar inertia ratios μ_A = 0.246 and μ_B = 0.236 for theoretical and experimental frequencies, amplitude ratio and gain.

3.16 Experimental bending vibration

On figures 3.10, 3.11 and 3.12, the bending vibration was present on each experimental curve at the smaller peak. Physically, during the test to obtain each curve, the rod could be seen vibrating vertically and horizontally, with the respective flywheel presenting a gyroscopic effect at the frequency range from 13 Hz to 19 Hz.

The experimental results show that the amplitude response for the bending vibration is also reduced from type B to type A as shown in figures 3.11 and 3.12.

To calculate the theoretical fundamental natural bending vibration frequencies, we use the Rayleigh method and an assumed sinusoidal deflection curve.

$$KE_j = 0.5.M_{rod}.\omega_j^2.\int_0^{L_{TR}}(b(x))^2.dx + 0.5.M_j.\omega_j^2.[b(L_{TR})]^2$$

$$PE_j = 0.5.E_{rod}.I_{rod}.\int_0^{L_{TR}}(b''(x))^2.dx$$

$$b(x) = B.\sin(x.\pi / L)$$

where:

$b(x)$: assumed sinusoidal deflection curve in m

j : index for mass size L, M or S

x : variable rod length in m, from 0 to L_{TR}

B : amplitude constant (it will cancel out during calculations)

E_{rod} = $200x10^9\ N/m^2$, modulus of elasticity of steel

I_{rod} = $2.0432x10^{-8}\ m^4$, moment of inertia (not polar moment of inertia)

KE_j : j kinetic energy in $N.m$

L = 1.6 m, rod length between self aligning ball bearing supports (see figure 3.13).

L_{TR} = 1.7 m, total rod length

M_j : j flywheel mass in kg (not inertia mass)

M_{rod} = 6.7 kg, rod mass

PE_j : j potential energy in $N.m$

$f_j = \frac{\omega_j}{2\pi}$: j fundamental theoretical frequency in Hz

J_{1N} $Kg.m^2$	f_j Theoretical Hz	M_j kg	f_j Experimental Hz
S_N : 0.179	14.5	M_S : 13.8	18.9
M_N : 0.297	14.0	M_M : 23.5	17.6
L_N : 0.465	13.5	M_L : 37.3	16.3

Table 3.14 Comparison between theoretical and experimental (figure 3.10) bending natural frequencies

Table 3.14 shows the comparison between theoretical and experimental (figure 3.10) bending natural frequencies. Although the values are not similar to the corresponding inertia mass or mass j, we can see a trend of the difference between each mass of 0.5 Hz for the theoretical, and 1.3 Hz for the experimental frequencies.

3.17 Rod support and shaker armature vibration

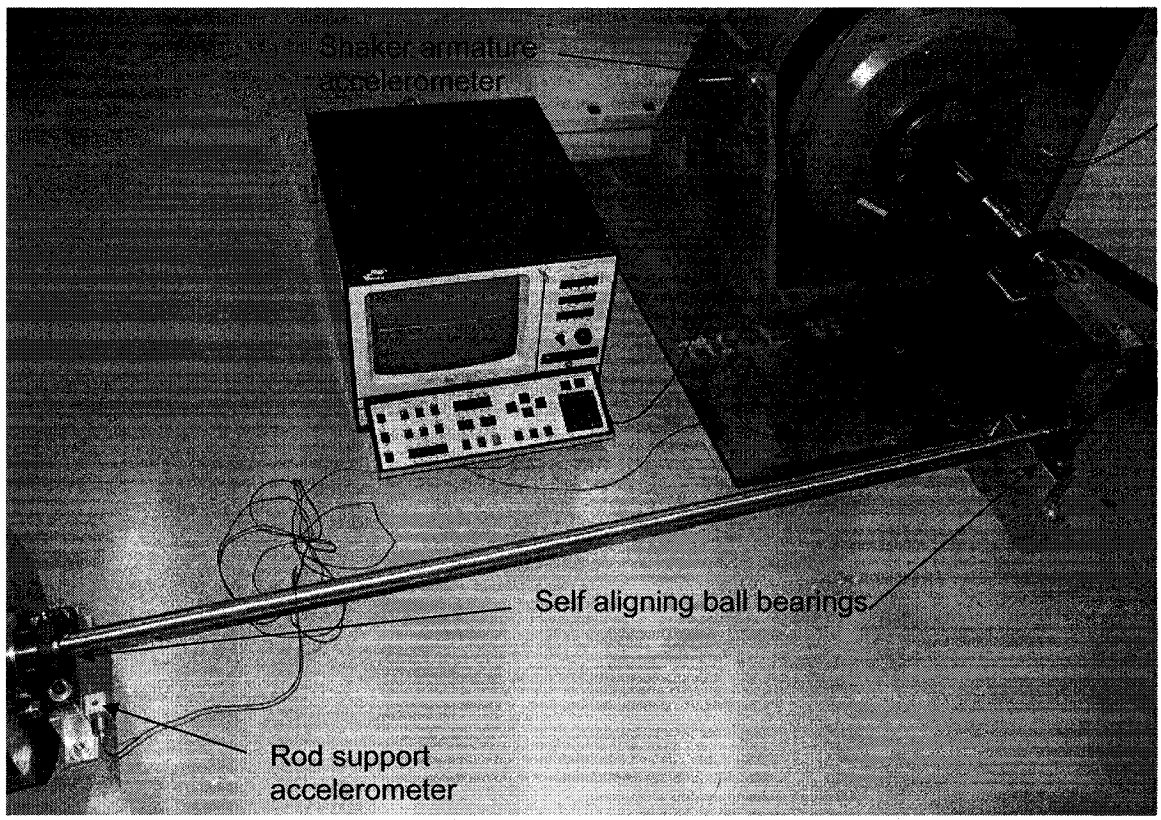

Figure 3.13 Location of accelerometers on rod support and shaker armature, and self-aligning ball-bearings

Figure 3.13 shows the location of accelerometers on rod support and shaker armature, and self-aligning ball-bearings. The test for the rod support and shaker armature vibration was performed for the natural frequencies of the primary system as described in section 3.9.

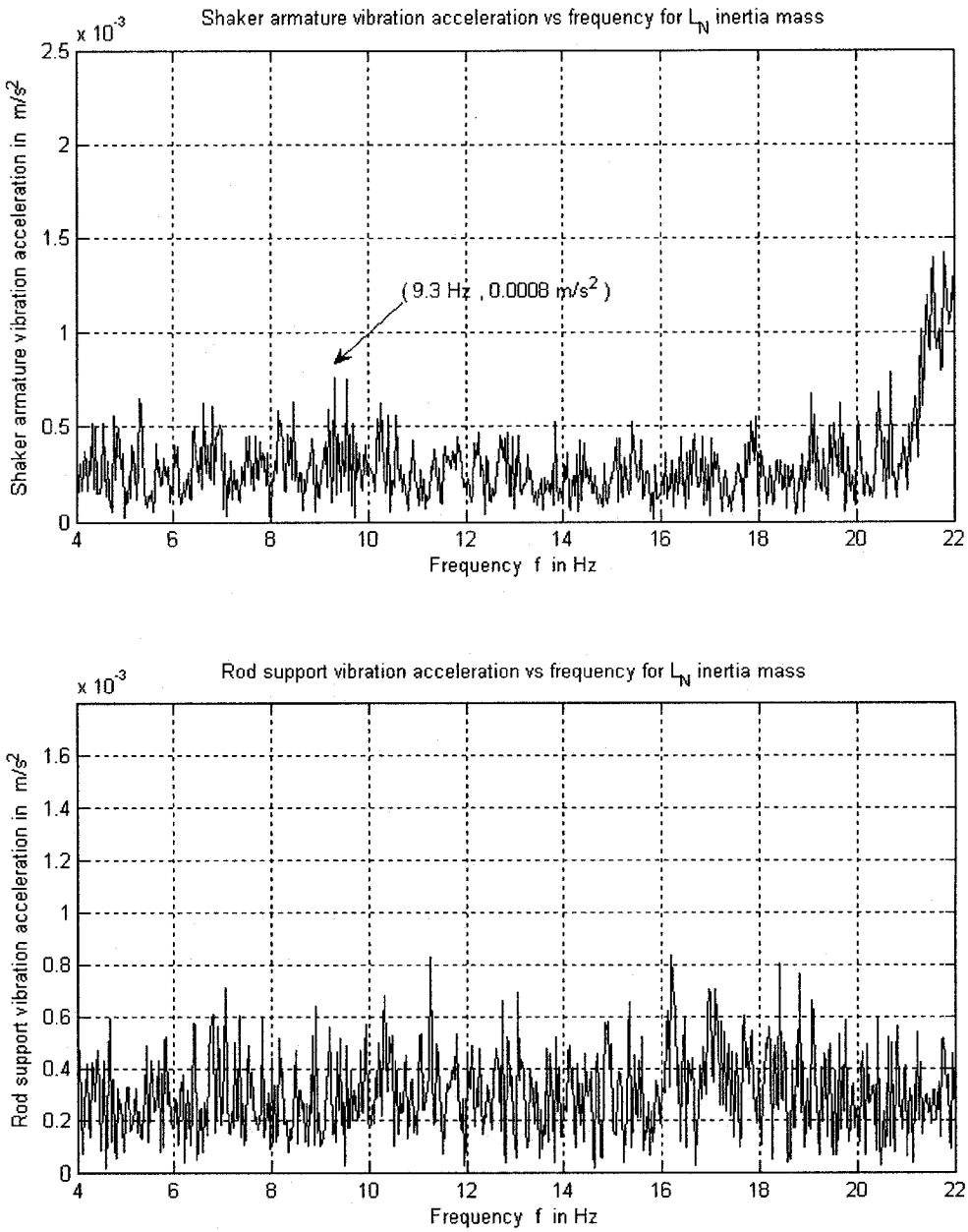

Figure 3.14 Rod support and shaker armature vibration for L_N inertia mass

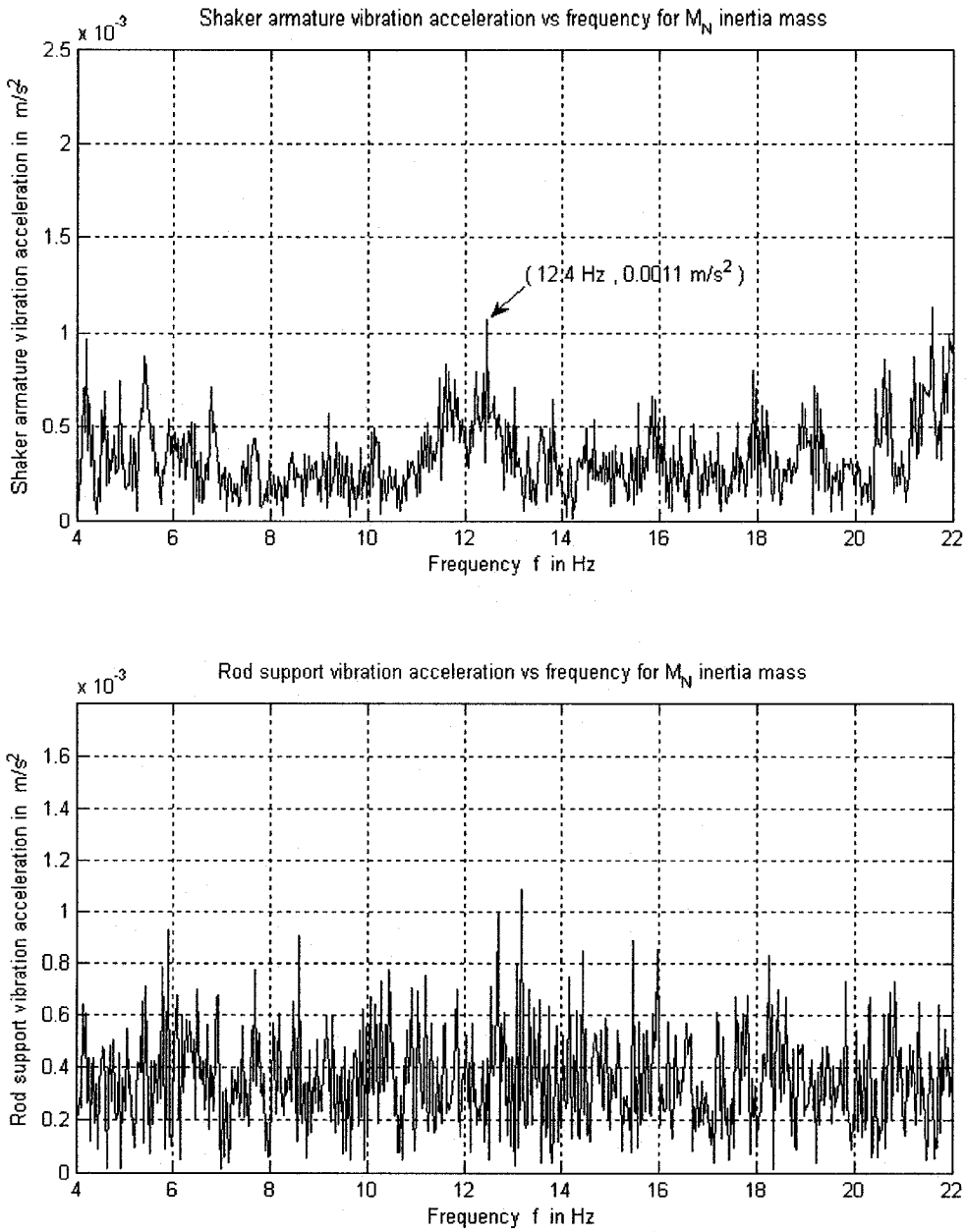

Figure 3.15 Rod support and shaker armature vibration for M_N inertia mass

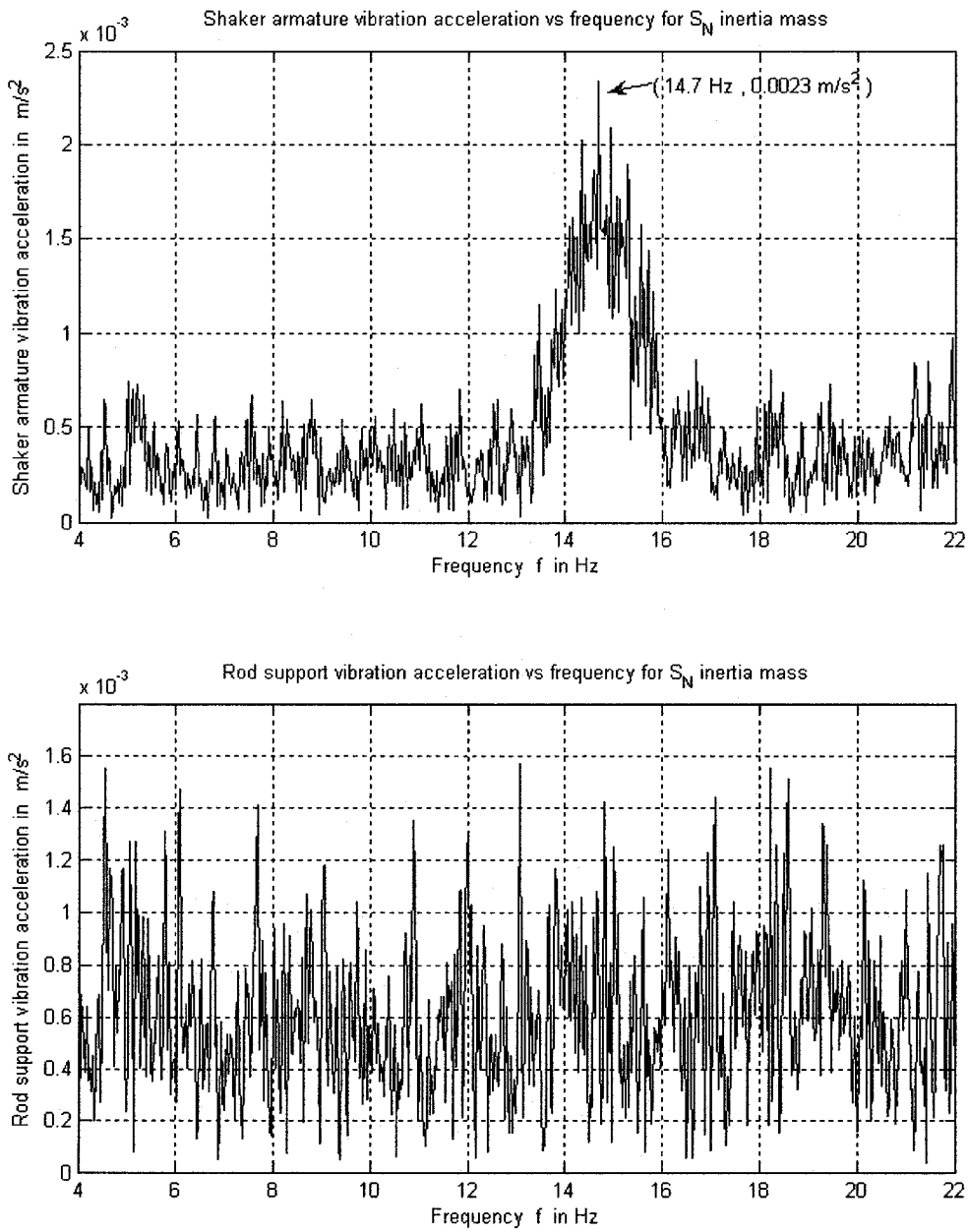

Figure 3.16 Rod support and shaker armature vibration for S_N inertia mass

J_{1N} $Kg.m^2$	f_j (Shaker armature) Hz	M_j kg	f_j (Torsion) Hz
S_N : 0.179	14.7	M_S : 13.8	16.1
M_N : 0.297	12.4	M_M : 23.5	12.7
L_N : 0.465	9.3	M_L : 37.3	10.2

Table 3.15 Comparison between experimental torsional (figure 3.10) and armature frequencies

The top plot of figures 3.14, 3.15 and 3.16 shows the armature frequency response with higher amplitude at 9.3 Hz, 12.4 Hz and 14.7 Hz respectively.

The bottom plot of figures 3.14, 3.15 and 3.16 shows the rod support frequency response with a sinusoidal trend for S_N , M_N and L_N respectively. In addition the trend for the amplitude is $S_N > M_N > L_N$.

In table 3.15, we observe that the range for the peak frequencies for the shaker armature and torsion are similar for the 3 sizes of J_{1N}, which means physically that the shaker, as part of the system, was also vibrating, tuned with the vibration of the flywheels.

In this chapter, results of the experimental investigation were presented and discussed. It was seen that the optimum damping parameters could reduce the response of the primary system up to 20% of the original value. Note that this experimental investigation showed the effect of these two damping devices in the torsional and bending vibration of the primary system.

The next chapter will discuss the application of the damper in an IC engine shaft to reduce its torsional vibrations.

CHAPTER 4

ANALYTICAL STUDY ON AN IC ENGINE

4.1 Introduction

In Chapter 3, we did the experimental study for a 2-DOFS with the optimum values from Chapter 2. In this chapter, we are going to extend the study by using the damper in a four-stroke 6-in-line cylinder internal combustion engine, in order to reduce the crankshaft torsional vibrations. A sketch of the crankshaft system is shown in figure 4.1.

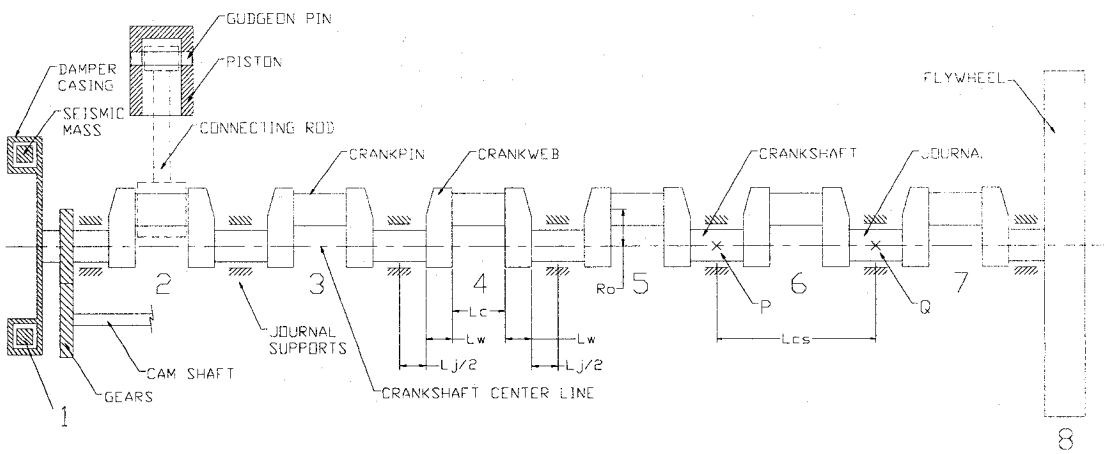

Figure 4.1: Engine crank throw showing parts for torsional vibrations study

The analytical study corresponds to two different cases. The first case will be the amplitude response of the engine without a damper and the second, with the optimally tuned viscous damper similar to type A seismic mass described in Chapter 3. In both cases, the same excitation torque per cylinder is applied with its respective phase angle.

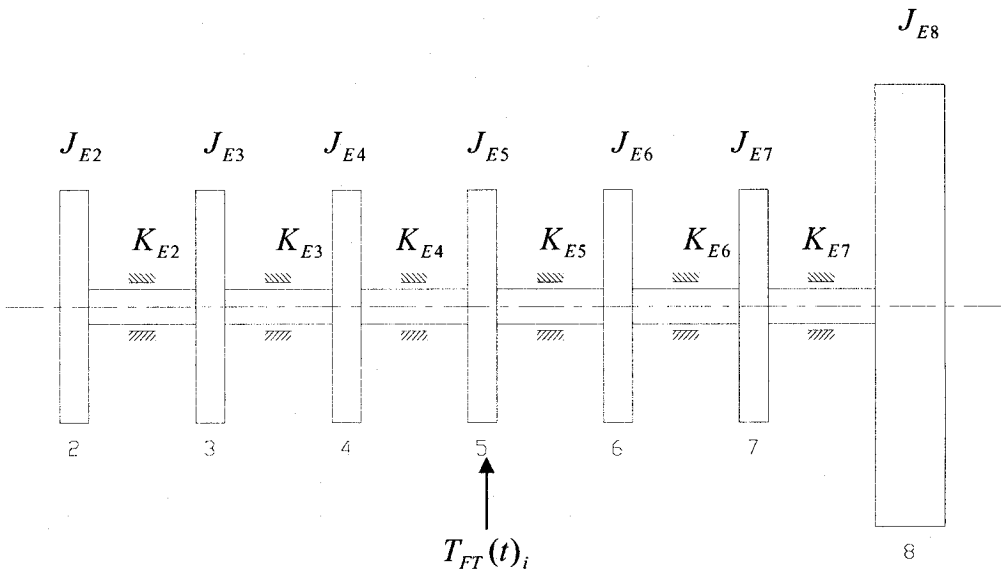

Figure 4.2: 7-DOFS equivalent system showing excitation torque, moments of inertia, internal damping and stiffness

The equivalent 7-DOFS without damper is shown in figure 4.2. The addition of the damper changes the 7-DOFS to a 8-DOFS shown in figure 4.3. As a reference, we apply the optimum values found in Chapter 2 to size the damping device; however, derivation for the actual optimum values for this 8-DOFS is required as in Chapter 2 for a 2-DOFS.

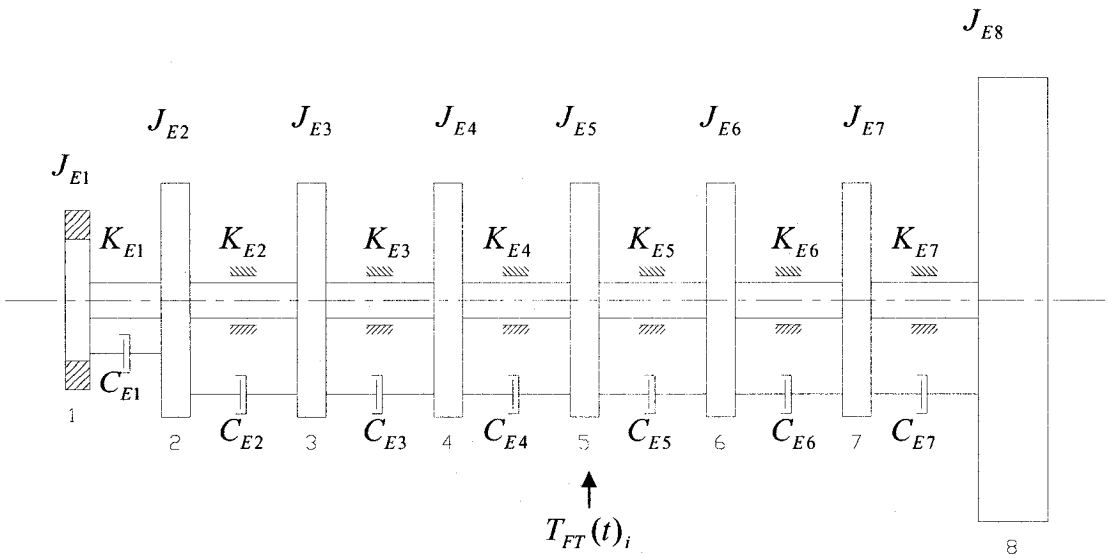

Figure 4.3: 8-DOFS equivalent system showing damper, excitation torque, moments of inertia, internal damping and stiffness

For the numerical calculations we have considered the following engine data for the crankshaft drive:

$d = 76\ mm$, piston diameter

$R_O = 35\ mm$, journal or crank radius

$L = 123\ mm$, connecting rod length

$M_P = 0.363\ kg$, total piston mass

$M_C = 0.096\ kg$, total connecting rod mass

The combustion gas pressure P_G distribution vs crankshaft angle ϕ coordinates are in Appendix II and plotted in figure 4.4.

The moments of inertia for each cylinder are $J_{E2} = J_{E3} = J_{E4} = J_{E5} = J_{E6} = J_{E7}$ = 18.64 $kg.m^2$ and for the flywheel J_{E8} = 2655 $kg.m^2$; the stiffnesses for each crank throw are $K_{E2} = K_{E3} = K_{E4} = K_{E5} = K_{E6}$ = $22.82 x10^6$ $N.m/rad$ and K_{E7} = $19.21 x10^6$ $N.m/rad$.

4.2 Excitation torque

The crankshaft system in an internal combustion engine shown in figure 4.1 is constantly under thermal and mechanical loads. In the present study, the thermal loads are not considered. The mechanical loads generated by the combustion gas and masses provide the excitation torque on the crankshaft system. The combustion gas force produces the gas torque, T_G, and inertial forces from the piston, connecting rod, gudgeon pin and counter weight, produce the inertial torque, T_I. Thus, the total excitation torque $T_T = T_G + T_I$.

In the present study, we are not including the additional vibration generated by the camshaft on the gears and from other vibratory devices of the engine. Also, the gyroscopic effect on the crankshaft due to the bending moments are not considered in this torsional vibration study [66, 67, 68].

4.2.1 Gas torque T_G

The gas pressure P_G on the piston is variable in the working cycle of the engine with respect to the crankshaft angle ϕ of rotation. Figure 4.4 shows 2 curves that overlap each other. The solid line corresponds to the actual data from Appendix II and the dotted line curve corresponds to the Fourier series approximation using Matlab in Appendix III and from the data of Appendix II for cylinder 1 with phase angle δ_1.

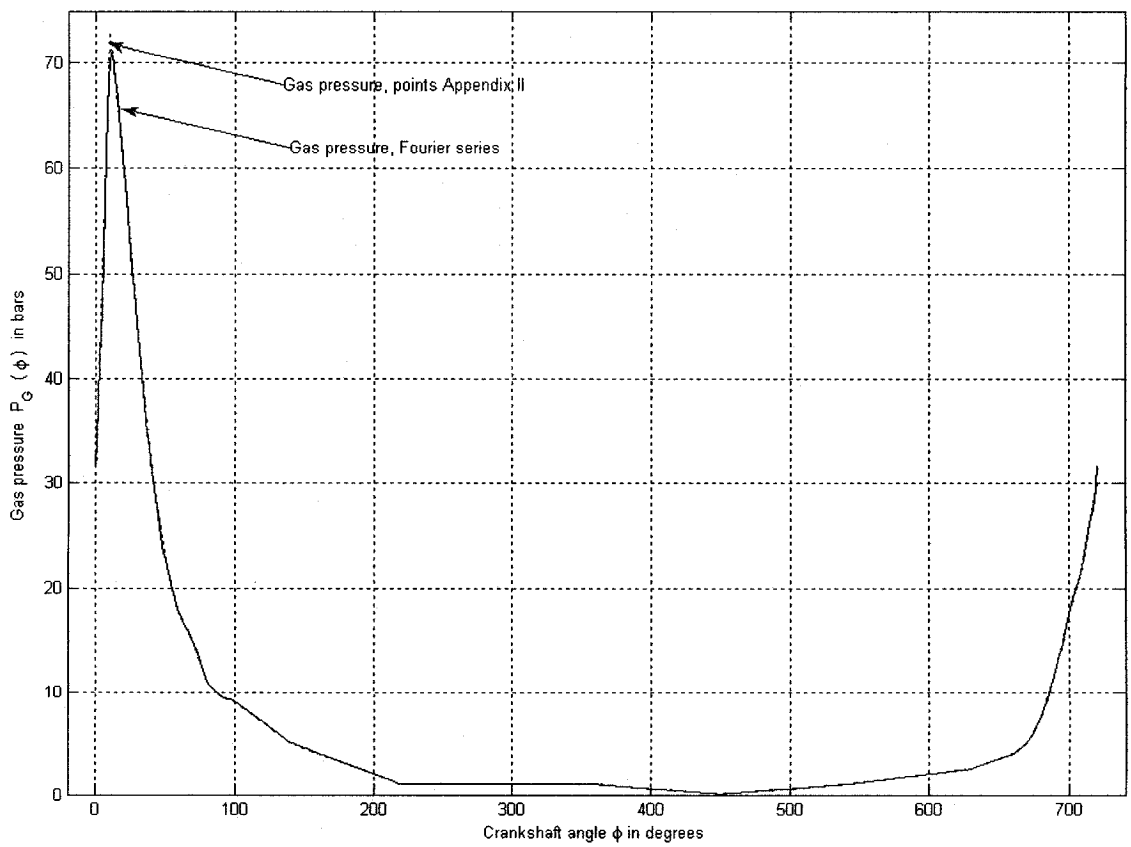

Figure 4.4: Gas pressure on piston versus crankshaft angle for one cylinder

Consider the crankshaft derive mechanism shown in figure 4.5. The geometrical relations and force diagram from figure 4.3 are

$F_G(\phi) = P_G(\phi).A$: gas force

$F_{cG} = F_G(\phi)/\cos(\varphi)$: gas force component over connecting rod

$F_{tG} = F_{cG}.\sin(\phi+\varphi)$: tangential gas force perpendicular to crank

$R_O.\sin(\phi) = L.\sin(\varphi)$

The gas torque, $T_G = F_{tG}.R_O$ is obtained as

$$T_G(\phi) = P_G(\phi).A.R_O.\left\{\frac{\frac{R_O}{L}.\sin(\phi).\cos(\phi)}{\sqrt{\left[1-\left(\frac{R_O.\sin(\phi)}{L}\right)^2\right]}}+\sin(\phi)\right\} \quad (4.1)$$

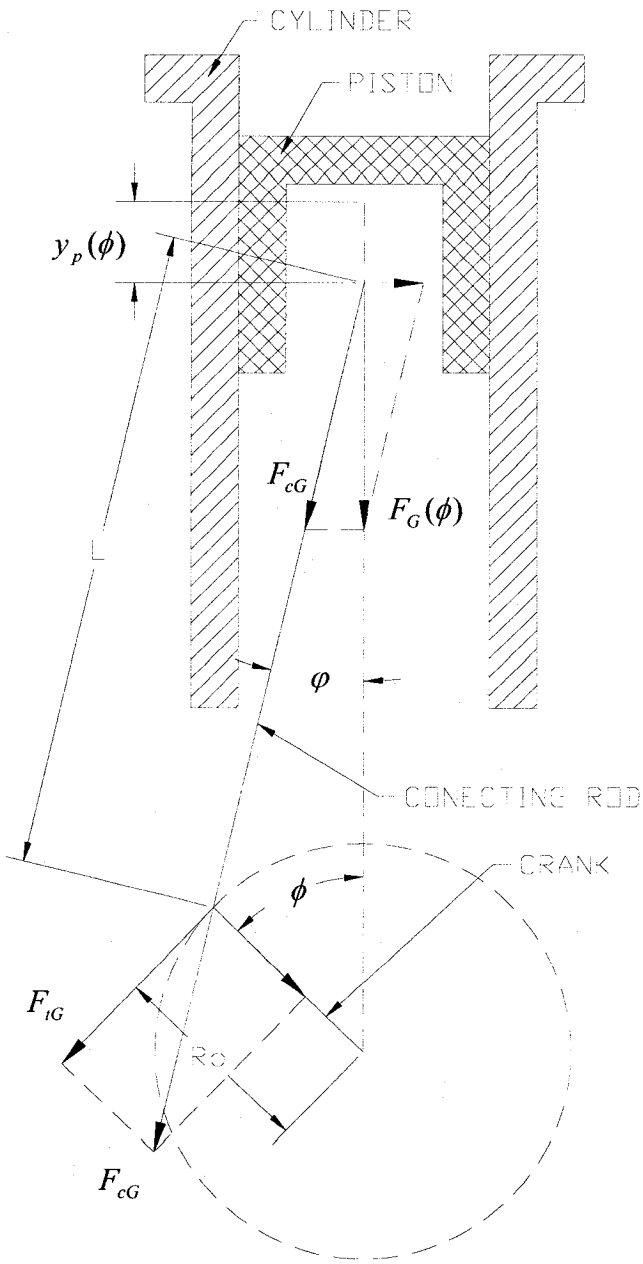

Figure 4.5: Geometrical relation and force diagram of the crankshaft drive

4.2.2 Inertia torque T_I

The inertial torque is produced by the inertial reciprocating and rotating forces due to the accelerating masses. The reciprocating forces are from the piston, the portion of the connecting rod (normally taken as that of the two-thirds of the connecting rod lumped at the piston end), and the gudgeon pin; and the rotating forces are from the portion of the connecting rod (normally taken as one third of the connecting rod lumped at the crank tip) and the counter weight. These parts accelerate and decelerate at every single rotation of the crankshaft.

The location of these masses that produce the reciprocating and rotating forces are considered as if they were rotating around the crankshaft centerline with radius R_O [40]. However, at the actual location of each of these masses, there is a variable inertia during rotation [41] not considered in the following kinematics analysis.

A standard procedure is to consider the reciprocating mass $M_O = M_P + \frac{2.M_C}{3}$ and the rotating mass $M_R = \frac{M_C}{3}$. Thus, the total inertia torque $T_I = T_{IO} + T_{IR}$.

Referring to figure 4.5, the reciprocating torque, T_{IO} is obtained by considering the reciprocating torque as a reciprocating pressure at the piston and the force transmitted through the connecting rod [40] as:

$$T_{IO}(\phi) = -P_{IO}(\phi).A.R_O.\left\{\frac{\frac{R_O}{L}.\sin(\phi).\cos(\phi)}{\sqrt{\left[1-\left(\frac{Ro.\sin(\phi)}{L}\right)^2\right]}} + \sin(\phi)\right\} \quad (4.2)$$

The rotating torque T_{IR} is due to the one-third of the connecting rod and the counter weight masses as they rotate around the crankshaft centerline and is obtained as

$$T_{IR}(\phi) = -F_{IR}(\phi).R_O \quad (4.3)$$

The physical interpretation of the negative sign on equations 4.2 and 4.3 is that the inertial forces act in the opposite direction to that of the movement of the piston.

where:

$$P_{IO}(\phi) = \frac{(M_P + \frac{2.M_C}{3}).\ddot{y}_p(\phi)}{A} \quad \text{: reciprocating pressure in } N.mm$$

$$F_{IR}(\phi) = \frac{M_C}{3}.\frac{(\dot{y}_p(\phi))^2}{R_O} \quad \text{: rotating force in } N$$

$$y_p(\phi) = R_O + L - [R_O.\cos(\phi) + L.\cos(\varphi)]$$

$$y_p(\phi) = R_O + L - \left[R_O.\cos(\phi) + L.\left[1-\left(\frac{R_O.\sin(\phi)}{L}\right)^2\right]^{1/2}\right]$$

$$\dot{y}_p(\phi) = \dot{\phi}.\left\{R_O.\sin(\phi) + L.\left[\left(1-\left(\frac{R_O.\sin(\phi)}{L}\right)^2\right)^{-1/2}.\left(\left(\frac{R_O}{L}\right)^2.\sin(\phi).\cos(\phi)\right)\right]\right\}$$

$$\ddot{y}_p(\phi) = \dot{\phi}^2 . \left\{ Ro.\cos(\phi) + L. \left[\begin{array}{l} -\left(1-\left(\frac{R_O.\sin(\phi)}{L}\right)^2\right)^{-3/2} . \left(\left(\frac{R_O}{L}\right)^4 .\sin^2(\phi).\cos^2(\phi)\right) \\ -\left(1-\left(\frac{R_O.\sin(\phi)}{L}\right)^2\right)^{-1/2} . \left(\frac{R_O}{L}\right)^2 .\cos^2(\phi) \\ +\left(1-\left(\frac{R_O.\sin(\phi)}{L}\right)^2\right)^{-1/2} . \left(\frac{R_O}{L}\right)^2 .\sin^2(\phi) \end{array} \right] \right\} \quad (4.4)$$

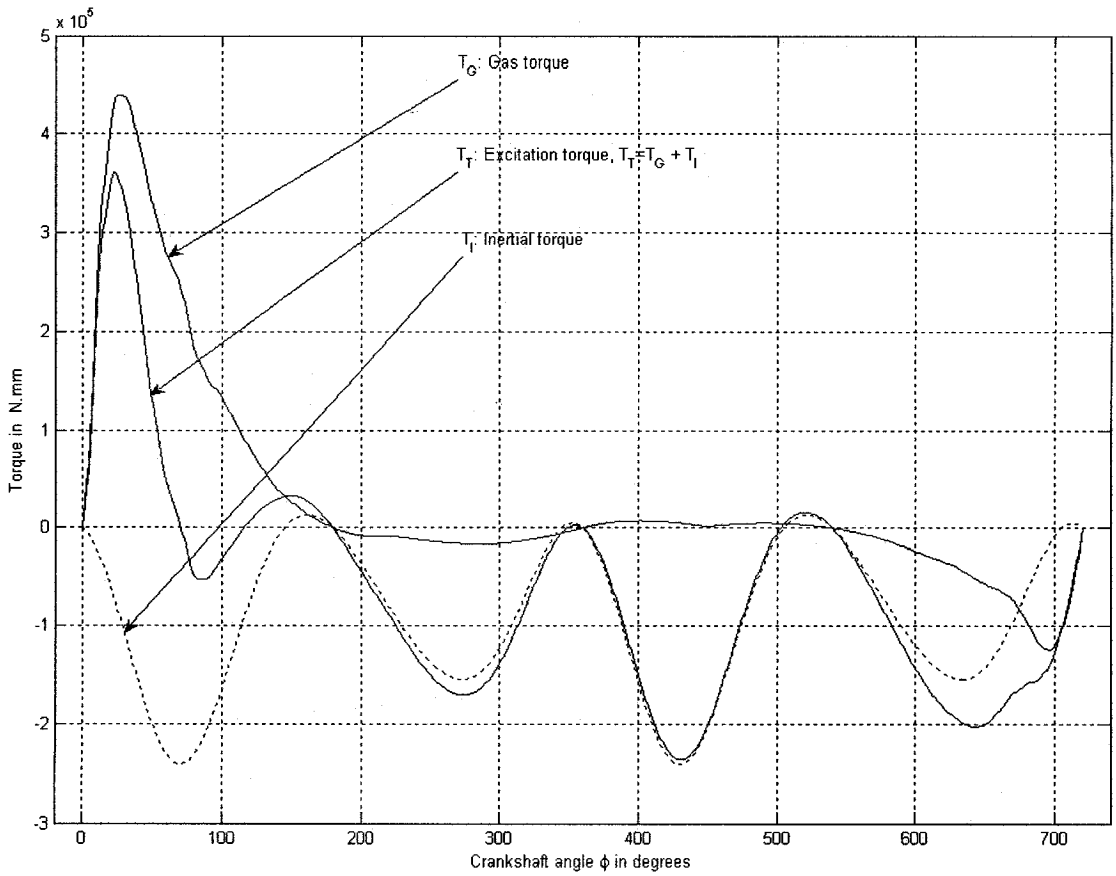

Figure 4.6: Plot of gas, inertial and total excitation torque for engine speed of 400 rad/sec

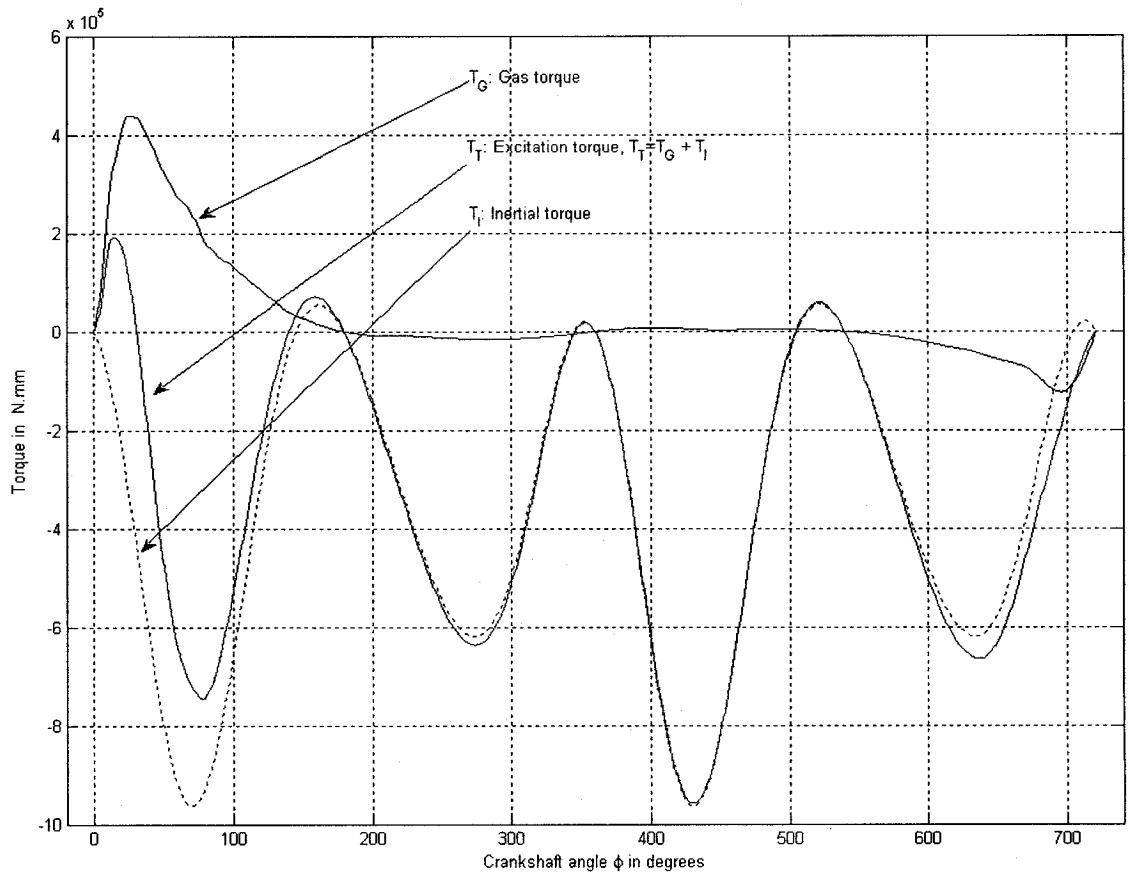

Figure 4.7: Plot of gas, inertial and total excitation torque at 800 rad/sec engine speed

Figures 4.6 and 4.7 show gas torque T_G, inertial torque T_I and total excitation torque T_T for 2 engine rotation speeds: $\dot{\phi}$ = 400 rad/sec and $\dot{\phi}$ = 800 rad/sec for cylinder 1 with its respective phase angle $\delta_1 = 0$.

4.2.3 Total excitation torque $T_T = T_G + T_I$

For the total excitation torque $T_T = T_G + T_I$ per cylinder, we used the constant engine speed of $\dot{\phi} = \Omega$ = 400 rad/sec, which will be kept constant along the numerical calculations.

4.2.4 Total Fourier excitation torque T_{FT}

The total Fourier excitation torque is the approximation of the total excitation torque $T_T = T_G + T_I$. The approximation to Fourier series of the total excitation torque is possible since $T_T = T_G + T_I$ is a periodic function.

$$T_{FT}(\phi) = A_0 + \sum_{n=1}^{\infty}\left[A_n.\cos(n.\phi) + B_n.\sin(n.\phi)\right] \tag{4.5}$$

where:

$$A_0 = \frac{1}{T}.\int_0^T T_T(\phi).d\phi$$

$$A_n = \frac{1}{T}\int_0^T T_T.\cos(n.\phi)d\phi$$

$$B_n = \frac{1}{T}\int_0^T T_T.\sin(n.\phi)d\phi$$

$T_{FT}(\phi)$: general Fourier series equation

ϕ : crankshaft angle

n : number of terms of Fourier series

The six-cylinder engine has six different phase angles δ_i for each piston that depend not only on the order of firing but also on the geometry of the crankshaft. In this particular case, the order of firing is shown in figure 4.8. Every 60° in figure 4.8 equals double the phase angle (i.e. 120°), since it is a four-stroke internal combustion (IC) engine with period T =720°.

Thus, we have

δ_1 =0° δ_2 = 480° = 8.π/3 δ_3 = 240° = 4.π/3

δ_4 = 600° = 10.π/3 δ_5 = 120° = 2.π/3 δ_6 = 360° = 2.π

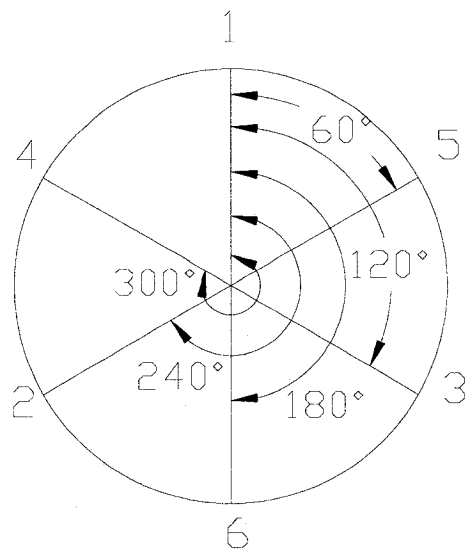

Figure 4.8: Firing order and angles for phase angles

In equation 4.5, we add the phase angle due to the firing order, and the total Fourier excitation torque $T_{FT}(t)_i$ for any of each of the six cylinders of the engine can be expressed as:

$$T_{FT}(t)_i = A_{0i} + \sum_{j=1}^{30}\left[A_j.\cos(\frac{j}{s}.\Omega.t - \frac{j}{s}.\delta_i) + B_j.\sin(\frac{j}{s}.\Omega.t - \frac{j}{s}.\delta_i)\right] \quad (4.6)$$

where:

$A_j = A_n$
$B_j = B_n$ j-th Fourier series coefficient

$n = j$ j : Number of the harmonic

$s = 2$ (for four-stroke engine and 1 for two-stroke engine)

$\phi = \Omega.t = \dot{\phi}.t$ $\Omega = \dot{\phi}$: Excitation engine speed or engine running speed

i : Index for the number of terms in the equivalent system (see figure 4.10). Note that it is not the index for the number of cylinders of the engine.

The total number of harmonics used are j = 30 [46].

Rearranging and simplifying equation 4.6 we have:

$$T_{FT}(t)_i = A_{0i} + \sum_{j=1}^{30} \left\{ \begin{array}{l} \left[A_j.\cos(\frac{j}{s}.\delta_i) - B_j.\sin(\frac{j}{s}.\delta_i) \right].\cos(\frac{j}{s}.\Omega.t) \\ + \left[A_j.\sin(\frac{j}{s}.\delta_i) + B_j.\cos(\frac{j}{s}.\delta_i) \right].\sin(\frac{j}{s}.\Omega.t) \end{array} \right\}$$

$$T_{FT}(t)_i = A_{0i} + \sum_{j=1}^{30} \left\{ a_{ji}.\cos(\frac{j}{s}.\Omega.t) + b_{ji}.\sin(\frac{j}{s}.\Omega.t) \right\} \quad (4.7)$$

where:

$$a_{ji} = A_j.\cos(\frac{j}{s}.\delta_i) - B_j.\sin(\frac{j}{s}.\delta_i)$$

$$b_{ji} = A_j.\sin(\frac{j}{s}.\delta_i) + B_j.\cos(\frac{j}{s}.\delta_i)$$

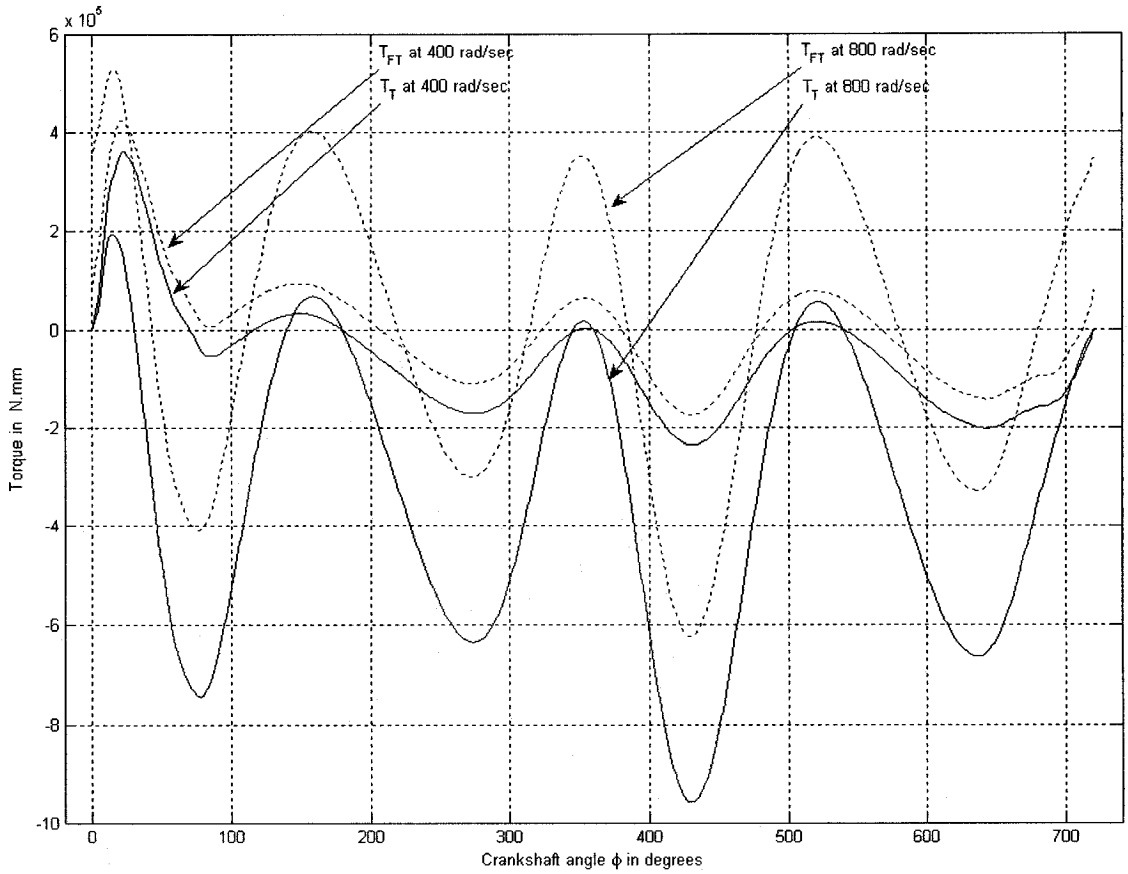

Figure 4.9: Total excitation torque with its respective Fourier approximation for engine speed of 400 rad/sec and 800 rad/sec

4.3 Equivalent system

The basic equivalent system consists of a number of concentrated masses or disks, situated at various points along an equivalent straight shaft of circular cross-sections as shown in figure 4.10.

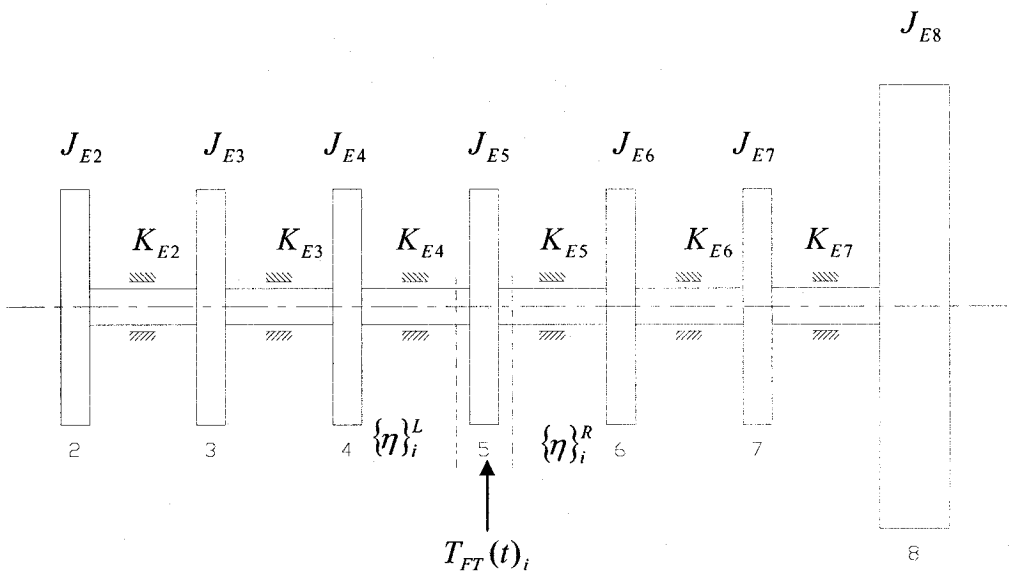

Figure 4.10: 7-DOFS equivalent system showing state vectors, excitation torques, moments of inertia and stiffness

4.3.1 Moment of inertia [4]

The standard procedure is to concentrate all the moments of inertia of each crankthrow, rotating and reciprocating parts to a reference axis which is the journal centre-line. The moment of inertia per cylinder is obtained by evaluating the individual terms of the following expression (see figure 4.1):

$$J_{cylinder} = J_{journal} + J_{crankpin} + J_{crankweb(2x)} + J_{conecting-rod} + J_{piston} + J_{gudgeonpin} + J_{balance-weight}$$

The general formula above is for information only on how to determine the moment of inertia on a crankshaft. For our analytical study, the values for the moments of inertia are given in section 4.1.

4.3.2 Stiffness of crankshaft [4]

For a shaft with a more complicated shape, it is possible to determine its stiffness: $\kappa = \Im / \partial$, where $\Im$ is the applied torque and ∂ is the torsional deflection. Experimentally, the stiffness can be determined by clamping the shaft at one end and applying a torque at the other end and measuring the overall angle of twist ∂. The theoretical way is to use the equivalent length method. To be equivalent, the complicated portion of crankshaft length Lcs (see figure 4.1) must be equivalent to a straight shaft Le, provided an equivalent diameter D_e is given:

$\kappa = \dfrac{G.I_{pe}}{Le}$, where $I_{pe} = \dfrac{\pi.D_e^4}{32}$

To determine the equivalent length Le between points P and Q, which is the actual length of the crankshaft portion Lcs (see figure 4.1), the total twist ∂_{PQ} between points P and Q is:

$$\partial_{PQ} = \partial_{journal} + \partial_{crankpin} + 2.\partial_{crankweb}$$

Considering that the torque $\Im$ is constant along the actual length Lcs between points P and Q:

$$\partial_{PQ} = \frac{\Im}{K_e} = \frac{\Im}{K_{journal}} + \frac{\Im}{K_{crankpin}} + 2.\frac{\Im}{K_{crankweb}}$$

$$\frac{Le}{G.I_{pe}} = \frac{Lj}{G.I_{p-journal}} + \frac{Lc}{G.I_{p-crankpin}} + 2.\frac{Lw}{G.I_{p-crankweb}}$$

Rearranging and replacing the inertia for each element:

$$Le = D_e^4.\left(\frac{Lj}{Dj^4} + \frac{Lc}{Dc^4} + \frac{0.93.Ro}{Lw.B^3}\right) \text{ or } K = \frac{G.\pi}{32.\left(\frac{Lj}{Dj^4} + \frac{Lc}{Dc^4} + \frac{0.93.Ro}{Lw.B^3}\right)} \quad (4.9)$$

The above derivation and theoretical formula is for information only on how to determine the stiffness of a crankshaft using the equivalent length method, and for our analytical study the stiffness values are given in section 4.1.

4.4 Vibration calculation

The governing equation of motion for torsional vibration of a multi DOFS with external excitation torque is:

$$[J_E].\{\ddot{\psi}\} + [C_E].\{\dot{\psi}\} + [K_E].\{\psi\} = \{T_E\} \quad (4.10)$$

where:

$[J_E]$ = inertia matrix of multi DOFS

$[C_E]$ = damping matrix of multi DOFS

$[K_E]$ = stiffness matrix of multi DOFS

$\{T_E\}$ = total excitation torque vector

$\{\psi\}$ = angular twist vector

4.4.1 Vibration calculation for 7-DOFS without damping

With the equivalent system shown in figure 4.10, the equations of motion for a 7-DOFS without damping, $[C_E]$ = 0, are:

$$
\begin{aligned}
&J_{E2}.\ddot{\psi}_2 + K_{E2}.(\psi_2 - \psi_3) = T_{E2}\\
&J_{E3}.\ddot{\psi}_3 + K_{E2}.(\psi_3 - \psi_2) + K_{E3}.(\psi_3 - \psi_4) = T_{E3}\\
&J_{E4}.\ddot{\psi}_4 + K_{E3}.(\psi_4 - \psi_3) + K_{E4}.(\psi_4 - \psi_5) = T_{E4}\\
&J_{E5}.\ddot{\psi}_5 + K_{E4}.(\psi_5 - \psi_4) + K_{E5}.(\psi_5 - \psi_6) = T_{E5}\\
&J_{E6}.\ddot{\psi}_6 + K_{E5}.(\psi_6 - \psi_5) + K_{E6}.(\psi_6 - \psi_7) = T_{E6}\\
&J_{E7}.\ddot{\psi}_7 + K_{E6}.(\psi_7 - \psi_6) + K_{E7}.(\psi_7 - \psi_8) = T_{E7}\\
&J_{E8}.\ddot{\psi}_8 + K_{E7}.(\psi_8 - \psi_7) = T_{E8}
\end{aligned}
$$

where:

$$
[J_E] = \begin{bmatrix}
J_{E2} & 0 & 0 & 0 & 0 & 0 & 0\\
0 & J_{E3} & 0 & 0 & 0 & 0 & 0\\
0 & 0 & J_{E4} & 0 & 0 & 0 & 0\\
0 & 0 & 0 & J_{E5} & 0 & 0 & 0\\
0 & 0 & 0 & 0 & J_{E6} & 0 & 0\\
0 & 0 & 0 & 0 & 0 & J_{E7} & 0\\
0 & 0 & 0 & 0 & 0 & 0 & J_{E8}
\end{bmatrix}
$$

$$
[K_E] = \begin{bmatrix}
K_{E2} & -K_{E2} & 0 & 0 & 0 & 0 & 0\\
-K_{E2} & K_{E2}+K_{E3} & -K_{E3} & 0 & 0 & 0 & 0\\
0 & -K_{E3} & K_{E3}+K_{E4} & -K_{E4} & 0 & 0 & 0\\
0 & 0 & -K_{E4} & K_{E4}+K_{E5} & -K_{E5} & 0 & 0\\
0 & 0 & 0 & -K_{E5} & K_{E5}+K_{E6} & -K_{E6} & 0\\
0 & 0 & 0 & 0 & -K_{E6} & K_{E6}+K_{E7} & -K_{E7}\\
0 & 0 & 0 & 0 & 0 & -K_{E7} & K_{E7}
\end{bmatrix}
$$

$$\{T_E\}=\begin{Bmatrix}T_{E2}\\T_{E3}\\T_{E4}\\T_{E5}\\T_{E6}\\T_{E7}\\T_{E8}\end{Bmatrix}=\begin{Bmatrix}T_{FT}(t)_2\\T_{FT}(t)_3\\T_{FT}(t)_4\\T_{FT}(t)_5\\T_{FT}(t)_6\\T_{FT}(t)_7\\0\end{Bmatrix}=\begin{Bmatrix}A_{02}+\sum_{j=1}^{30}\left\{a_{j2}.\cos(\frac{j}{s}.\Omega.t)+b_{j2}.\sin(\frac{j}{s}.\Omega.t)\right\}\\A_{03}+\sum_{j=1}^{30}\left\{a_{j3}.\cos(\frac{j}{s}.\Omega.t)+b_{j3}.\sin(\frac{j}{s}.\Omega.t)\right\}\\A_{04}+\sum_{j=1}^{30}\left\{a_{j4}.\cos(\frac{j}{s}.\Omega.t)+b_{j4}.\sin(\frac{j}{s}.\Omega.t)\right\}\\A_{05}+\sum_{j=1}^{30}\left\{a_{j5}.\cos(\frac{j}{s}.\Omega.t)+b_{j5}.\sin(\frac{j}{s}.\Omega.t)\right\}\\A_{06}+\sum_{j=1}^{30}\left\{a_{j6}.\cos(\frac{j}{s}.\Omega.t)+b_{j6}.\sin(\frac{j}{s}.\Omega.t)\right\}\\A_{07}+\sum_{j=1}^{30}\left\{a_{j7}.\cos(\frac{j}{s}.\Omega.t)+b_{j7}.\sin(\frac{j}{s}.\Omega.t)\right\}\\0\end{Bmatrix}$$

4.4.1.1 Mode shapes and natural frequencies, $\{T_E\}=0$

For the mode shape vectors $\{\Gamma_c\}$ and natural frequency Ω_{nc} calculation of the 7-DOFS, we use the transfer matrix method [47]:

$$\{\eta\}_8^R=\left(\prod_{h=3}^{8}[P]_h.[Q]_h\right).[P]_2.\{\eta\}_2^L$$

$$\{\eta\}_8^R=[M]_8.[N]_8.[M]_7.[N]_7.[M]_6.[N]_6.[M]_5.[N]_5.[M]_4.[N]_4.[M]_3.[N]_3[M]_2.\{\eta\}_2^L \quad (4.11a)$$

$$\begin{Bmatrix}\psi_8\\T_8\end{Bmatrix}^R=\begin{bmatrix}\sigma_1 & \sigma_2\\\sigma_3 & \sigma_4\end{bmatrix}\begin{Bmatrix}\psi_2\\T_2\end{Bmatrix}^L \quad (4.11b)$$

where:

$\{\eta\}_i^R=\begin{Bmatrix}\psi_i\\T_i\end{Bmatrix}^R=\begin{Bmatrix}\psi\\T\end{Bmatrix}_i^R$: Right side state vector with angular displacement ψ_i and torque T_i (see figure 4.10)

$$\{\eta\}_i^L = \begin{Bmatrix} \psi_i \\ T_i \end{Bmatrix}^L = \begin{Bmatrix} \psi \\ T \end{Bmatrix}_i^L$$: Left side state vector with angular displacement ψ_i and torque T_i (see figure 4.10)

$$[M]_i = \begin{bmatrix} 1 & 1/K_{Ei} \\ 0 & 1 \end{bmatrix} = \begin{bmatrix} 1 & 1/K_E \\ 0 & 1 \end{bmatrix}_i$$: Field transfer matrix or field matrix

$$[N]_i = \begin{bmatrix} 1 & 0 \\ -\Omega_n^2 . J_{Ei} & 1 \end{bmatrix} = \begin{bmatrix} 1 & 0 \\ -\Omega_n^2 . J_E & 1 \end{bmatrix}_i$$: Point transfer matrix

Expanding the terms of equation 4.11a:

$$[M]_i \qquad\qquad [N]_i$$

$$\begin{Bmatrix} \psi \\ T \end{Bmatrix}_3^L = \begin{bmatrix} 1 & 1/K_E \\ 0 & 1 \end{bmatrix}_3 . \begin{Bmatrix} \psi \\ T \end{Bmatrix}_2^R \qquad \begin{Bmatrix} \psi \\ T \end{Bmatrix}_2^R = \begin{bmatrix} 1 & 0 \\ -\Omega_n^2 . J_E & 1 \end{bmatrix}_2 . \begin{Bmatrix} \psi \\ T \end{Bmatrix}_2^L$$

$$\begin{Bmatrix} \psi \\ T \end{Bmatrix}_4^L = \begin{bmatrix} 1 & 1/K_E \\ 0 & 1 \end{bmatrix}_4 . \begin{Bmatrix} \psi \\ T \end{Bmatrix}_3^R \qquad \begin{Bmatrix} \psi \\ T \end{Bmatrix}_3^R = \begin{bmatrix} 1 & 0 \\ -\Omega_n^2 . J_E & 1 \end{bmatrix}_3 . \begin{Bmatrix} \psi \\ T \end{Bmatrix}_3^L$$

$$\begin{Bmatrix} \psi \\ T \end{Bmatrix}_5^L = \begin{bmatrix} 1 & 1/K_E \\ 0 & 1 \end{bmatrix}_5 . \begin{Bmatrix} \psi \\ T \end{Bmatrix}_4^R \qquad \begin{Bmatrix} \psi \\ T \end{Bmatrix}_4^R = \begin{bmatrix} 1 & 0 \\ -\Omega_n^2 . J_E & 1 \end{bmatrix}_4 . \begin{Bmatrix} \psi \\ T \end{Bmatrix}_4^L$$

$$\begin{Bmatrix} \psi \\ T \end{Bmatrix}_6^L = \begin{bmatrix} 1 & 1/K_E \\ 0 & 1 \end{bmatrix}_6 . \begin{Bmatrix} \psi \\ T \end{Bmatrix}_5^R \qquad \begin{Bmatrix} \psi \\ T \end{Bmatrix}_5^R = \begin{bmatrix} 1 & 0 \\ -\Omega_n^2 . J_E & 1 \end{bmatrix}_5 . \begin{Bmatrix} \psi \\ T \end{Bmatrix}_5^L$$

$$\begin{Bmatrix} \psi \\ T \end{Bmatrix}_7^L = \begin{bmatrix} 1 & 1/K_E \\ 0 & 1 \end{bmatrix}_7 . \begin{Bmatrix} \psi \\ T \end{Bmatrix}_6^R \qquad \begin{Bmatrix} \psi \\ T \end{Bmatrix}_6^R = \begin{bmatrix} 1 & 0 \\ -\Omega_n^2 . J_E & 1 \end{bmatrix}_6 . \begin{Bmatrix} \psi \\ T \end{Bmatrix}_6^L$$

$$\begin{Bmatrix} \psi \\ T \end{Bmatrix}_8^L = \begin{bmatrix} 1 & 1/K_E \\ 0 & 1 \end{bmatrix}_8 . \begin{Bmatrix} \psi \\ T \end{Bmatrix}_7^R \qquad \begin{Bmatrix} \psi \\ T \end{Bmatrix}_7^R = \begin{bmatrix} 1 & 0 \\ -\Omega_n^2 . J_E & 1 \end{bmatrix}_7 . \begin{Bmatrix} \psi \\ T \end{Bmatrix}_7^L$$

$$\begin{Bmatrix} \psi \\ T \end{Bmatrix}_8^R = \begin{bmatrix} 1 & 0 \\ -\Omega_n^2 . J_E & 1 \end{bmatrix}_8 . \begin{Bmatrix} \psi \\ T \end{Bmatrix}_8^L$$

where the boundary conditions known for equation 4.11b are:

T_2 = 0, because to the left side of the mass J_{E2} there is no torque.

T_8 = 0, because to the right side of the mass J_{E8} there is no torque either.

ψ_2 = 1 radian, assumed angular displacement for mass J_{E2}.

$$\begin{Bmatrix} \psi_8 \\ 0 \end{Bmatrix}^R = \begin{bmatrix} \sigma_1 & \sigma_2 \\ \sigma_3 & \sigma_4 \end{bmatrix} \begin{Bmatrix} 1 \\ 0 \end{Bmatrix}^L \tag{4.12}$$

From equation 4.12, σ_3 has to be equal to zero in order to obtain zero torque to the right side of J_{E8} and at the same time σ_3 is a function of Ω_{nc} and thus we find the natural frequencies $\{\Omega_{nc}\}$ from plot in figure 4.11 . And we find the modes $\{\Gamma_c\}$ from the expanded terms of equation 4.11a

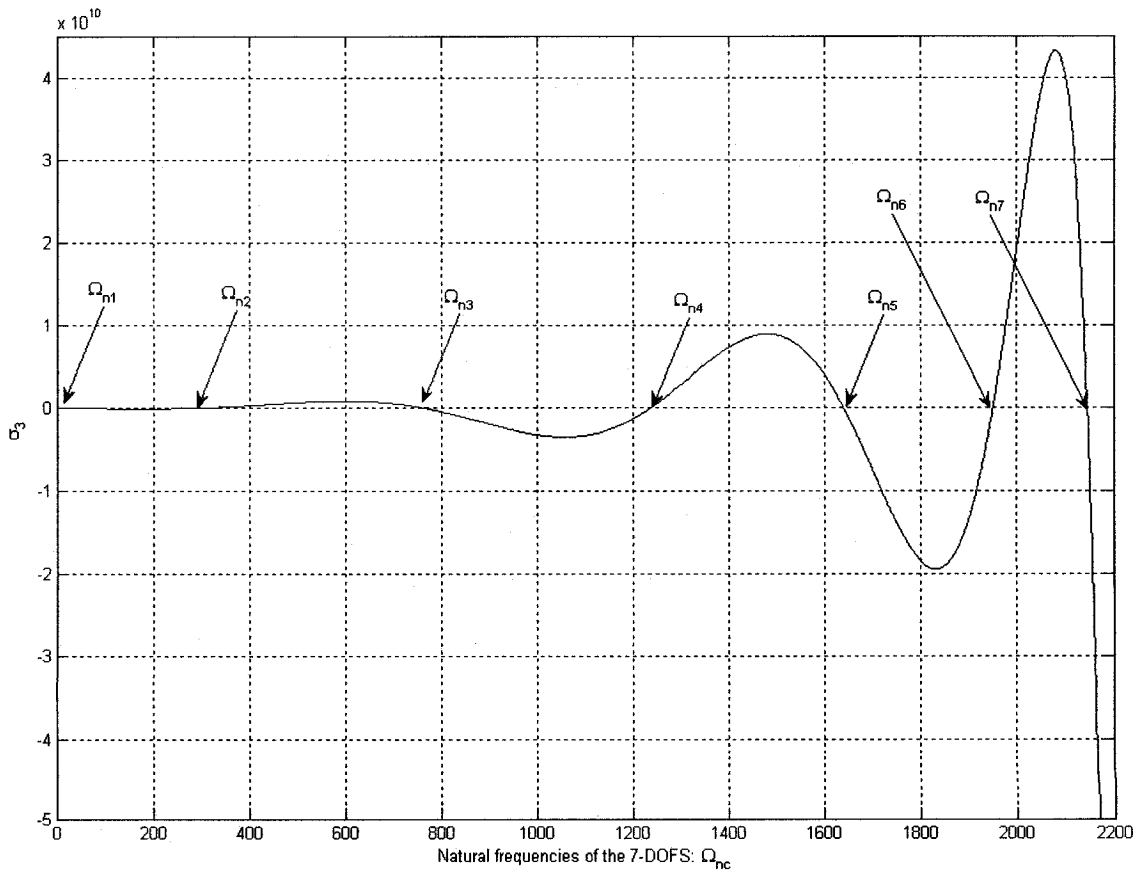

Figure 4.11: Natural frequencies of the 7-DOFS

$$\{\Omega_n\} = \{\Omega_{n1} \quad \Omega_{n2} \quad \Omega_{n3} \quad \Omega_{n4} \quad \Omega_{n5} \quad \Omega_{n6} \quad \Omega_{n7}\}$$

$$[\Gamma] = [\{\Gamma_1\}, \quad \{\Gamma_2\}, \quad \{\Gamma_3\}, \quad \{\Gamma_4\}, \quad \{\Gamma_5\}, \quad \{\Gamma_6\}, \quad \{\Gamma_7\}]$$

where:

$\{\Gamma_c\}$: Modal vector Γ_c for each natural frequency Ω_{nc}

$$\begin{aligned}
\Omega_{n1} &= 0 \\
\Omega_{n2} &= 264.15 \\
\Omega_{n3} &= 767.52 \\
\Omega_{n4} &= 1235.91 \\
\Omega_{n5} &= 1639.16 \\
\Omega_{n6} &= 1949.90 \\
\Omega_{n7} &= 2145.93
\end{aligned}
\qquad
\{\Gamma_c\} = \begin{Bmatrix} \psi_{c2} \\ \psi_{c3} \\ \psi_{c4} \\ \psi_{c5} \\ \psi_{c6} \\ \psi_{c7} \\ \psi_{c8} \end{Bmatrix}$$

$$\{\Gamma_1\} = \begin{Bmatrix} 1 \\ 1 \\ 1 \\ 1 \\ 1 \\ 1 \\ 1 \end{Bmatrix} \quad \{\Gamma_2\} = \begin{Bmatrix} 1.00000 \\ 0.94301 \\ 0.83227 \\ 0.67409 \\ 0.47750 \\ 0.25369 \\ -0.02935 \end{Bmatrix} \quad \{\Gamma_3\} = \begin{Bmatrix} 1.00000 \\ 0.51882 \\ -0.21201 \\ -0.84082 \\ -1.06505 \\ -0.77679 \\ 0.00966 \end{Bmatrix} \quad \{\Gamma_4\} = \begin{Bmatrix} 1.00000 \\ -0.24768 \\ -1.18634 \\ -0.64482 \\ 0.70123 \\ 1.17236 \\ -0.00558 \end{Bmatrix}$$

$$\{\Gamma_5\} = \begin{Bmatrix} 1.00000 \\ -1.19468 \\ -0.76742 \\ 1.34408 \\ 0.50576 \\ -1.44254 \\ 0.00389 \end{Bmatrix} \quad \{\Gamma_6\} = \begin{Bmatrix} 1.00000 \\ -2.10567 \\ 1.32819 \\ 0.63713 \\ -2.03265 \\ 1.61032 \\ -0.00307 \end{Bmatrix} \quad \{\Gamma_7\} = \begin{Bmatrix} 1.00000 \\ -2.76150 \\ 3.86439 \\ -4.04564 \\ 3.26202 \\ -1.70041 \\ 0.00268 \end{Bmatrix}$$

4.4.1.2 Forced vibration $\{T_E\} \neq 0$

From the generalized equation 4.10 and without damping, $[C_E]$ = 0:

$$[J_E].\{\ddot{\psi}\} + [K_E].\{\psi\} = \{T_E\} \tag{4.13}$$

Equation 4.13 will be solved using the normal mode analysis method which provides a new uncoupled equation from inertia $[J_E]$ and stiffness $[K_E]$ matrices of the system, the method is based on the orthogonality properties. The method uses the mode vectors $\{\Gamma_c\}$ as modal coordinates as one of the possible solutions for the response of the system among all other possible solutions for equation 4.13 [45]:

$$\{\psi\} = [\Gamma].\{\gamma\} \tag{4.14}$$

where:

$\{\gamma\}$: Modal or principal coordinate vector

Placing equation 4.14 in 4.13 and multiplying all the terms by the transpose $[\Gamma]^T$ of the mode shape matrix, we have

$$[\Gamma]^T.[J_E].[\Gamma].\{\ddot{\gamma}\} + [\Gamma]^T.[K_E].[\Gamma].\{\gamma\} = [\Gamma]^T.\{T_E\} \tag{4.15}$$

The orthogonality properties can be better visualized as a vector form than in a matrix form as in equation 4.15. For a given cth modal vector $\{\Gamma_c\}$ and its transpose $\{\Gamma_c\}^T$ and natural frequency Ω_{nc} we show the vector form in equation bellow. Note that the excitation vector $\{T_E\}$ is not affected by the sub index c:

$$\{\Gamma_c\}^T.[J_E].\{\Gamma_c\}.\ddot{\gamma}_c + \{\Gamma_c\}^T.[K_E].\{\Gamma_c\}.\gamma_c = \{\Gamma_c\}^T.\{T_E\}$$

$$\tilde{J}_c.\ddot{\gamma}_c + \tilde{K}_c.\gamma_c = \sum_{i=2}^{8} \Gamma_{ic}.T_{Ei}$$

Replacing equation 4.7 on the right end of the above equation, we have

$$\tilde{J}_c.\ddot{\gamma}_c + \tilde{K}_c.\gamma_c = \sum_{i=2}^{8} \Gamma_{ic}.\left[A_{0i} + \sum_{j=1}^{30} \left\{ a_{ji}.\cos(\frac{j}{2}.\Omega.t) + b_{ji}.\sin(\frac{j}{2}.\Omega.t) \right\} \right] \quad (4.16)$$

where:

i : sub index for number of terms for 7-DOFS (see figure 4.10). Note that i is not the sub index for the number of cylinders of the engine.

Then, the general solution for equation 4.16 for a specific mode $\{\Gamma_c\}$ and natural frequency Ω_{nc} is given by

$$\gamma_c = \frac{\sum_{i=2}^{8} A_{0i}.\Gamma_{ic}}{\tilde{K}_c} + \sum_{j=1}^{30} \left\{ \frac{1}{\tilde{J}_c\left[\Omega_{nc}^2 - \left(\frac{j}{2}.\Omega \right)^2 \right]}.\left[\sum_{i=2}^{8} \Gamma_{ic}.a_{ji}.\cos(\frac{j}{2}.\Omega.t) + \sum_{i=2}^{8} \Gamma_{ic}.b_{ji}.\sin(\frac{j}{2}.\Omega.t) \right] \right\}$$

$$\gamma_c = \frac{\sum_{i=2}^{8} A_{0i}.\Gamma_{ic}}{\tilde{K}_c} + \sum_{j=1}^{30} M_{jc}.Q_{jc}\cos(\frac{j}{2}.\Omega.t - \xi_{jc}) \quad (4.17)$$

where:

$$\Omega_{nc} = \sqrt{\frac{\tilde{K}_c}{\tilde{J}_c}}$$

$$Q_{jc} = \frac{\sqrt{\left(\sum_{i=2}^{8} \Gamma_{ic}.a_{ji} \right)^2 + \left(\sum_{i=2}^{8} \Gamma_{ic}.b_{ji} \right)^2}}{\tilde{J}_c.\Omega_{nc}^2}$$

$$\xi_{jc} = tg^{-1}\left(\frac{\sum_{i=2}^{8}\Gamma_{ic}.b_{ji}}{\sum_{i=2}^{8}\Gamma_{ic}.a_{ji}}\right)$$

$$M_{jc} = \frac{1}{1-\left(\frac{j}{2}.\frac{\Omega}{\Omega_{nc}}\right)^2} \qquad (4.18)$$

4.4.1.3. Numerical analysis

The numerical analysis consists of the numerical evaluation of the components of equation 4.17 when $t = 0$. Note that $t = 0$ is not when the engine starts running; the engine is already running, and $t = 0$ is a selected instant to visualize the behavior of the engine for study. See appendix V for Matlab program.

The total engine twist amplitude γ_c is composed of the engine static and dynamic twist. For the purpose of our study, the static twist is neglected. We focus our study on the dynamic twist: dynamic magnifier M_{jc}; harmonic intensity, which is the numerator of Q_{jc}; and the critical speeds of the engine Ω_{nc-w}.

Figure 4.12 shows the plot of equation 4.17, the engine dynamic twist amplitude γ_2 vs engine speed Ω for its natural speed Ω_{n2} = 264.2 rad/s and mode $\{\Gamma_2\}$. The 30 peaks shown in figure 4.12 correspond to the case when the dynamic magnifier M_{jc} tends to infinity. This tendency happens when the engine speed

Ω passes by the critical speed $\Omega_{n2-w} = \frac{2.\Omega_{n2}}{w}$,where w = 1, 2, 3...28, 29, 30. This critical speed Ω_{n2-w} is at the natural speed of the engine Ω_{n2}. Some of the critical speeds for Ω_{n2} = 264.2 rad/s are: Ω_{n2-1} = 528.3 , Ω_{n2-5} = 105.7 , Ω_{n2-10} = 52.8 , Ω_{n2-15} = 35.2 , Ω_{n2-20} = 26.4 , Ω_{n2-25} = 21.1 and Ω_{n2-30} = 17.6 rad/s.

Figure 4.13 shows the plot of equation 4.17, the engine dynamic twist amplitude γ_3 vs engine speed Ω for its natural speed Ω_{n3} = 767.5 rad/s and mode $\{\Gamma_3\}$. The 30 peaks shown in figure 4.13 correspond also when the dynamic magnifier M_{jc} tends to infinity. Some of the critical speeds for Ω_{n3} = 767.5 rad/s are: Ω_{n3-1} = 1535 , Ω_{n3-5} = 307 , Ω_{n3-10} = 153.5 , Ω_{n3-15} = 102.3 , Ω_{n3-20} = 76.8 , Ω_{n3-25} = 61.4 and Ω_{n3-30} = 51.2 rad/s.

Figure 4.14 shows the plot of equation 4.17, the engine dynamic twist amplitude γ_4 vs Ω engine speed for its natural speed Ω_{n4} = 1235.9 rad/s and mode $\{\Gamma_4\}$. The 30 peaks shown in figure 4.14 correspond to the case when the dynamic magnifier M_{jc} tends to infinity. Some of the critical speeds for Ω_{n4} = 1235.9 rad/s are: Ω_{n4-1} = 2471.8 , Ω_{n4-5} = 494.4 , Ω_{n4-10} = 247.2 , Ω_{n4-15} = 164.8 , Ω_{n4-20} = 123.6 , Ω_{n4-25} = 89.9 and Ω_{n4-30} = 82.4 rad/s.

It is clear from figures 4.12, 4.13 and 4.14 that there is no resonance at speeds Ω other than at the critical speeds Ω_{nc-w} for each figure. In addition, the engine

dynamic twist amplitude γ_c at each critical speed Ω_{nc-w} varies considerably.

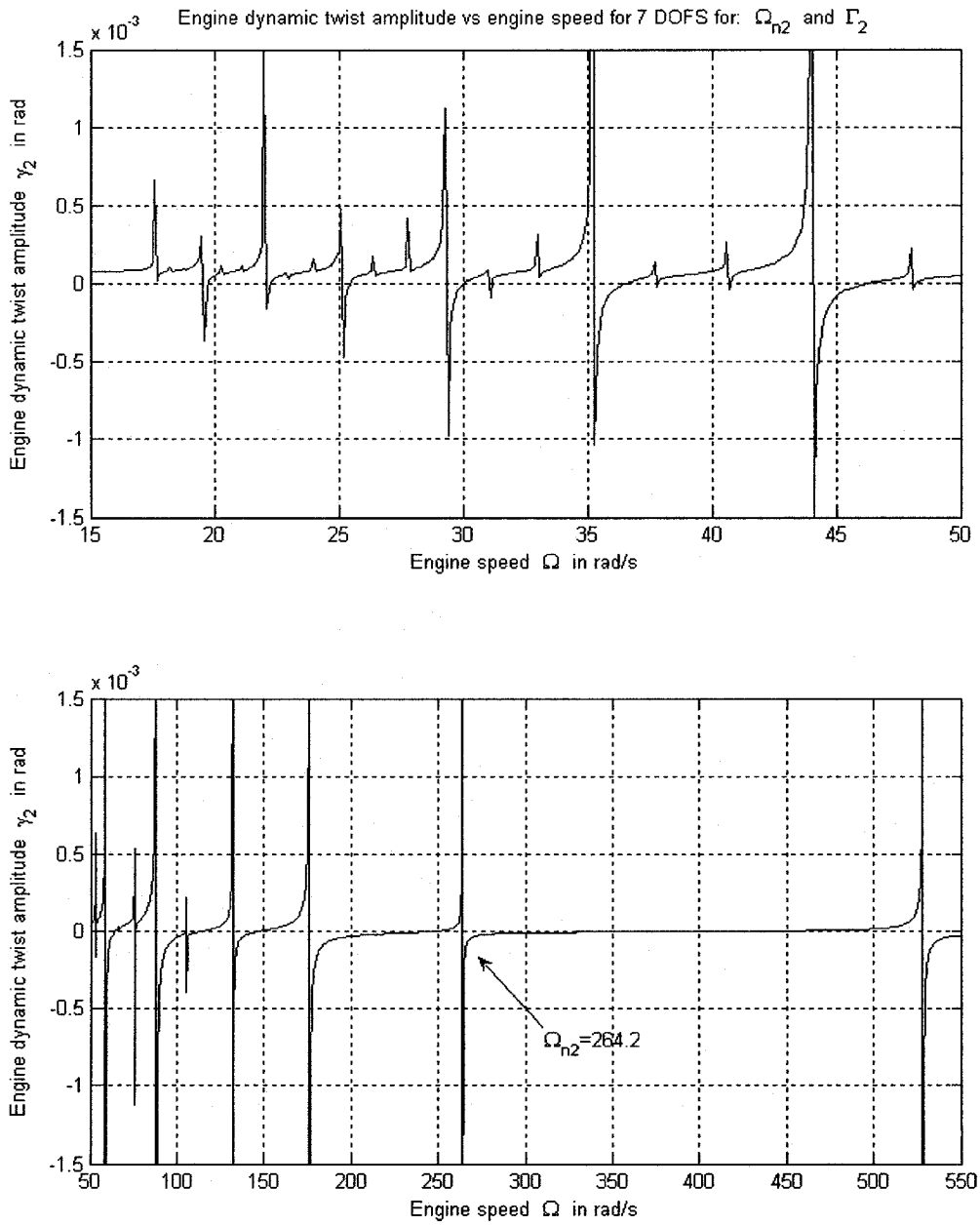

Figure 4.12: Engine dynamic twist amplitude vs engine speed for a 7-DOFS for engine natural frequency Ω_{n2} = 264.2 rad/s and mode $\{\Gamma_2\}$

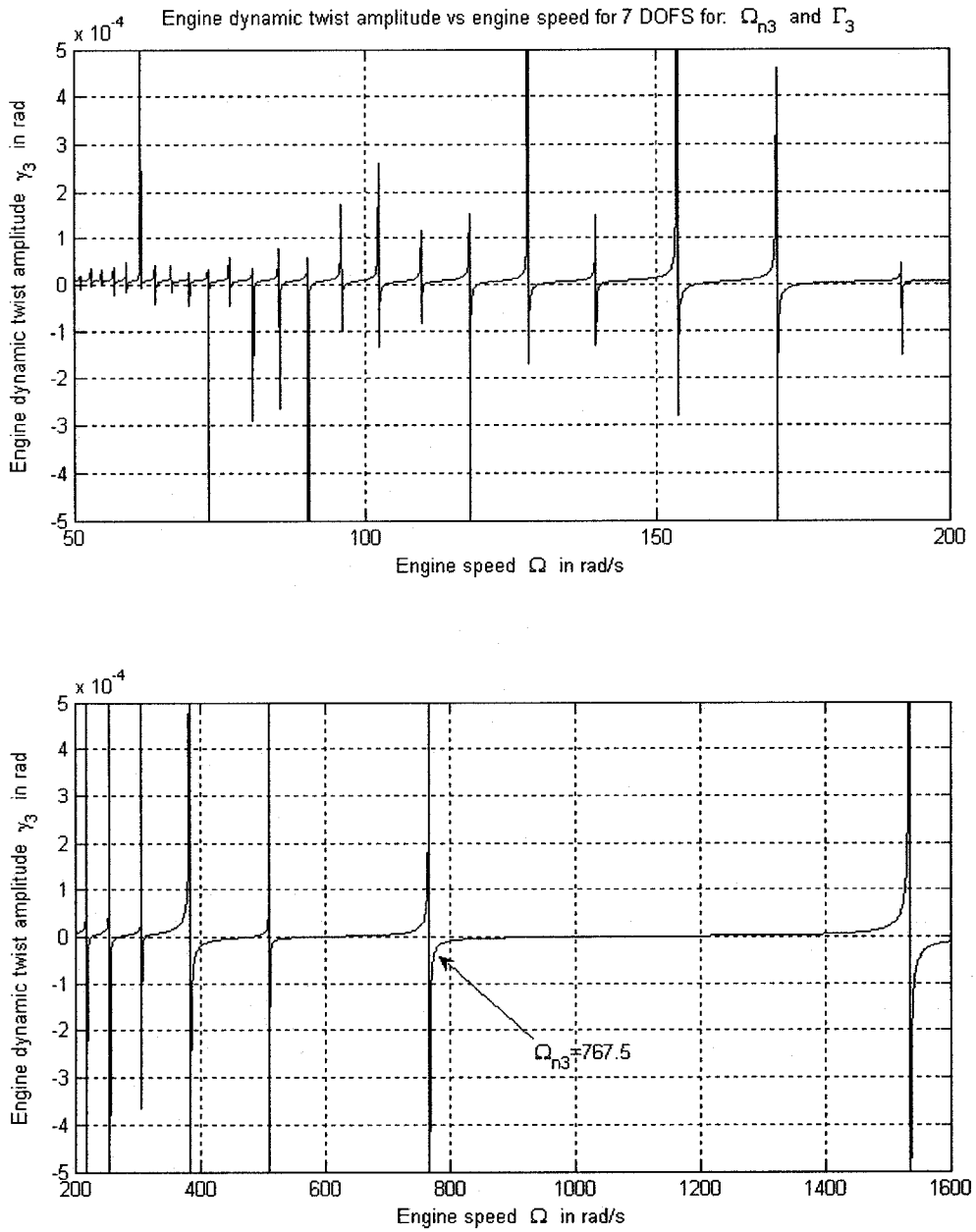

Figure 4.13: Engine dynamic twist amplitude vs engine speed for a 7-DOFS for engine natural frequency $\Omega_{n3} = 767.5\ rad/s$ and mode $\{\Gamma_3\}$

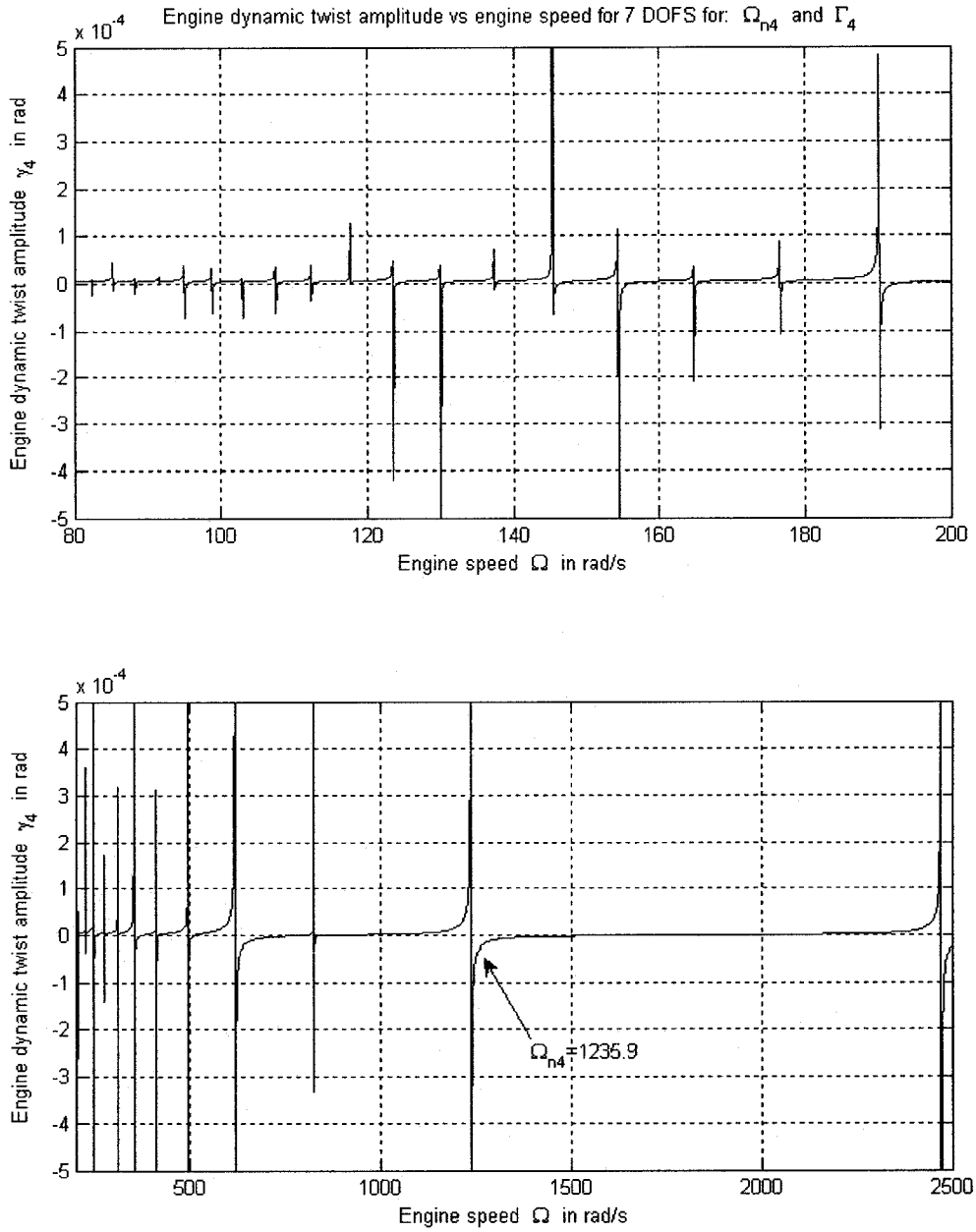

Figure 4.14: Engine dynamic twist amplitude vs engine speed for a 7-DOFS for engine natural frequency Ω_{n4} = 1235.9 rad/s and mode $\{\Gamma_4\}$

In real applications the engine dynamic twist amplitude does not reach infinity or large values because there is always some damping involved. The damping is introduced in the dynamic magnifier. Based on the research and on the experimental results, we are going to use the dynamic magnifier [48] from equation 4.19 for our 7-DOFS:

$$M_{jc} = \frac{3.8}{\sqrt[4]{Q_{jc}}} \tag{4.19}$$

This infinity or large value for the dynamic twist amplitude happens once among the 30 harmonics for each critical speed Ω_{nc-w} . When the critical speed $\Omega_{nc-w} = \frac{2.\Omega_{nc}}{w}$ is replaced in equation 4.18, we have the dynamic magnifier independent from its natural frequency Ω_{nc} :

$$M_{jc} = \frac{1}{1-\left(\frac{j}{w}\right)^2} \tag{4.20}$$

I.e. for the natural frequency Ω_{n2} = 264.2 rad/s, the 1st critical speed Ω_{n2-1} = 528.3 rad/s (w = 1) and the 1st harmonic j = 1, M_{jc} = ∞; therefore, we use equation 4.19. For the other 29 harmonics with $M_{jc} \neq \infty$, we use equation 4.20.

For the same natural frequency Ω_{n2} = 264.2 rad/s, the 2nd critical speed Ω_{n2-2} = 264.2 rad/s (w = 2) and the 2nd harmonic j = 2, M_{jc} = ∞; therefore, we use equation 4.19. For the other 29 harmonics with $M_{jc} \neq \infty$, we use equation 4.20.

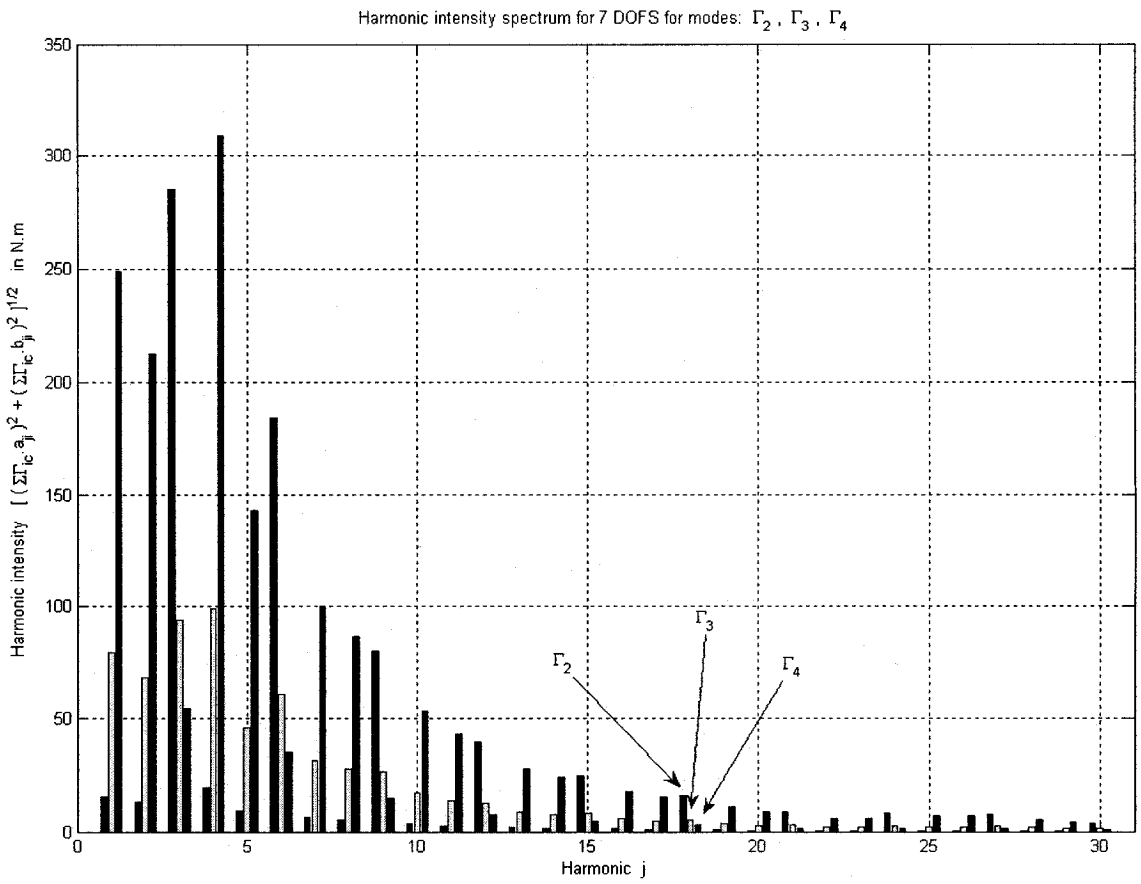

Figure 4.15: Engine harmonic intensity spectrum for a 7-DOFS for modes $\{\Gamma_2\}$, $\{\Gamma_3\}$ and $\{\Gamma_4\}$

Figure 4.15 compares the harmonic intensity for modes $\{\Gamma_2\}$, $\{\Gamma_3\}$ and $\{\Gamma_4\}$. The maximum intensity for 2nd mode is at harmonic j =3, for the 3rd and 4th mode at j =4.

For the 2nd mode, we observe that for every two harmonics there is a sudden increase in the intensity, i.e. for harmonic j = 3 after 1 and 2, for harmonic j =6 after 4 and 5 and so on.

For the 3rd mode, the intensity for harmonics from 1 to 6 is high and after harmonic j =6, it gradually diminishes until harmonic j =30.

For the 4th mode, the behavior of the harmonic intensity is random after the first two highest ones.

The harmonic intensity depends on the modes, firing order, phase angles and harmonic function; however, it is clear that the predominant variable is the mode shape. In general the harmonic intensity power gradually diminishes with the increase of the harmonic number.

Figure 4.16 shows the 30 critical speeds for Ω_{n2-w} on the horizontal axis with its corresponding experimental dynamic twist on the vertical axis. The line with the triangles facing downwards corresponds to the first harmonic (j = 1) for all the 30 critical speeds. In other words, it corresponds to the first term of the sumatorial of equation 4.17: $M_{1c}.Q_{1c}.\cos(-\xi_{1c})$ for every critical speed. Note that the dynamic magnifier used for each critical speed is from equation 4.19.

The line with the triangles facing upwards corresponds to the sumatorial of the 30 harmonics for each critical speed in equation 4.17.

The other 28 lines in figure 4.16 that cannot be clearly seen because some overlap with each other forms an apparent thick line correspond to the partial summation of the harmonics j for each critical speed Ω_{n2-w}; i..e., the second line: $M_{1c}.Q_{1c}\cos(-\xi_{1c}) + M_{2c}.Q_{2c}\cos(-\xi_{2c})$ for each critical speed; the third line: $M_{1c}.Q_{1c}\cos(-\xi_{1c}) + M_{2c}.Q_{2c}\cos(-\xi_{2c}) + M_{3c}.Q_{3c}\cos(-\xi_{3c})$ for each critical speed and so on.

A trend similar to figure 4.16 is seen in figures 4.17 and 4.18.

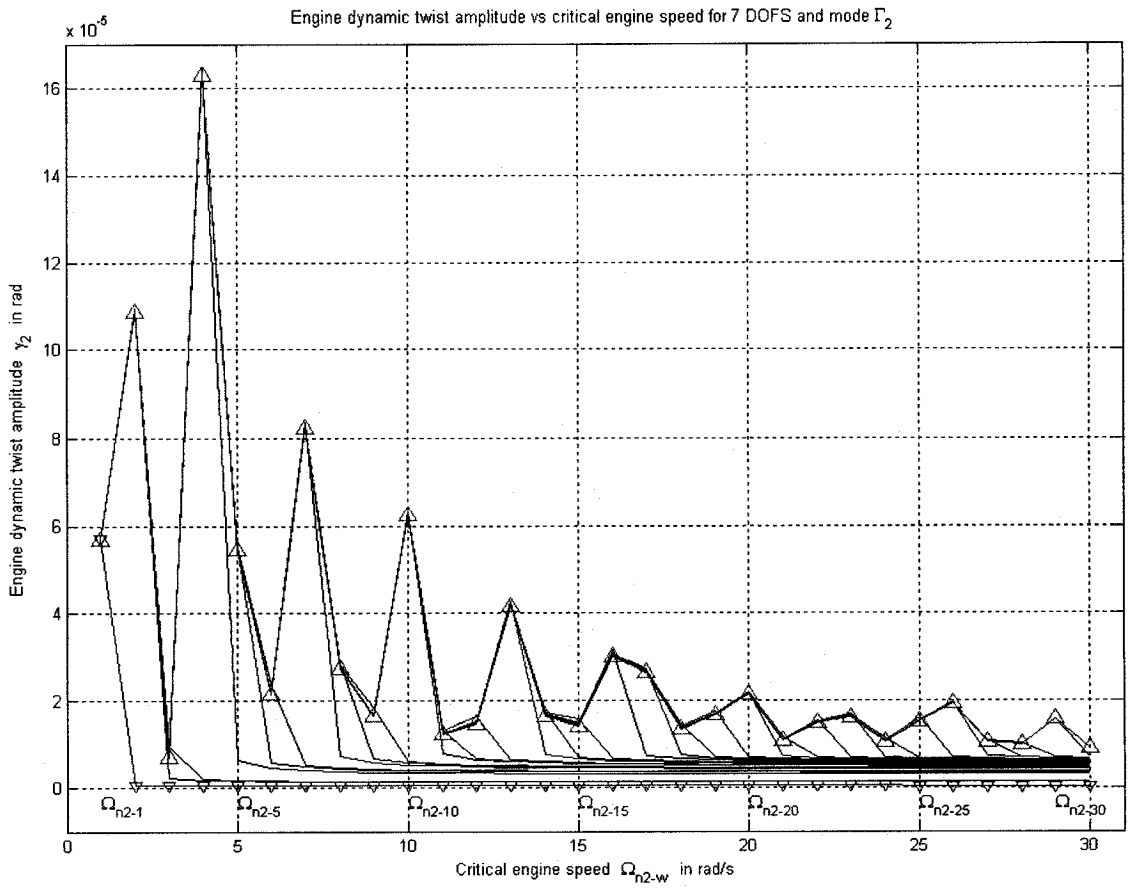

Figure 4.16: Engine dynamic twist amplitude γ_2 vs critical engine speed Ω_{n2-w} for a 7-DOFS and mode $\{\Gamma_2\}$

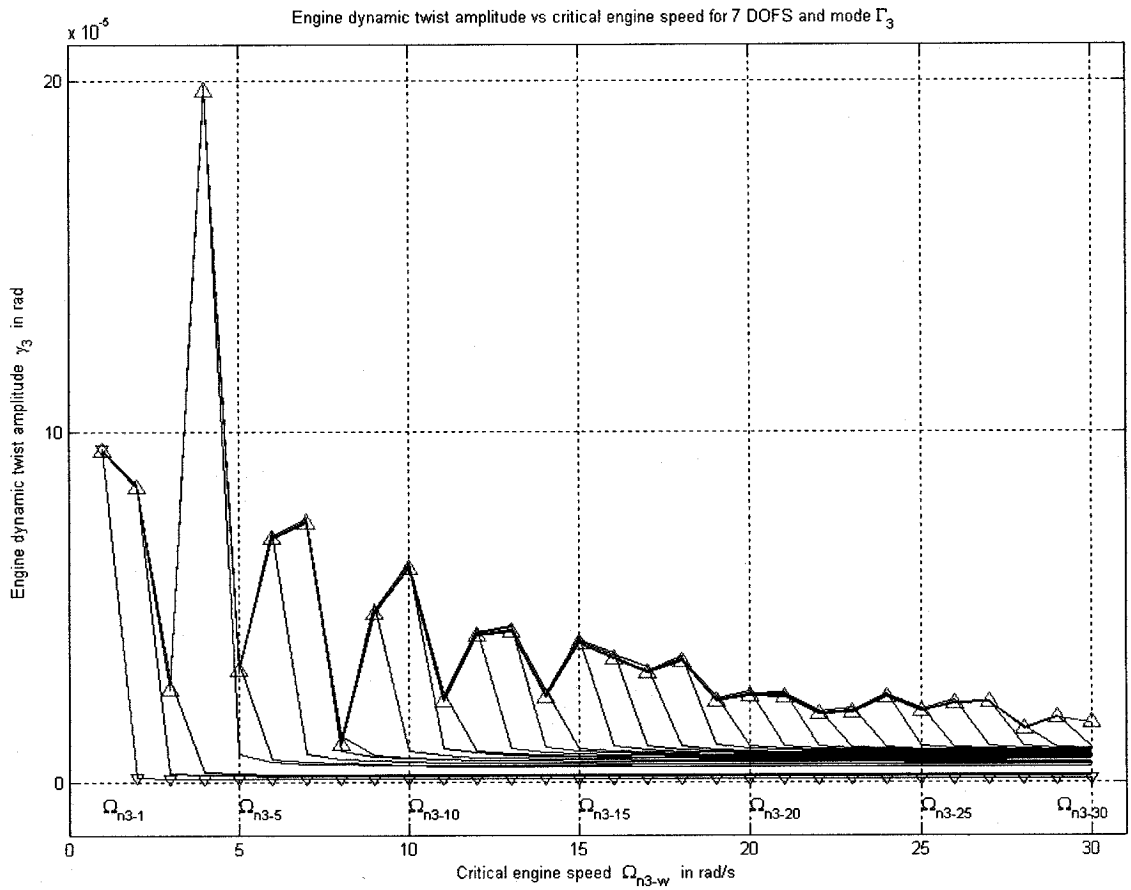

Figure 4.17: Engine dynamic twist amplitude γ_3 vs critical engine speed Ω_{n3-w} for a 7-DOFS and mode $\{\Gamma_3\}$

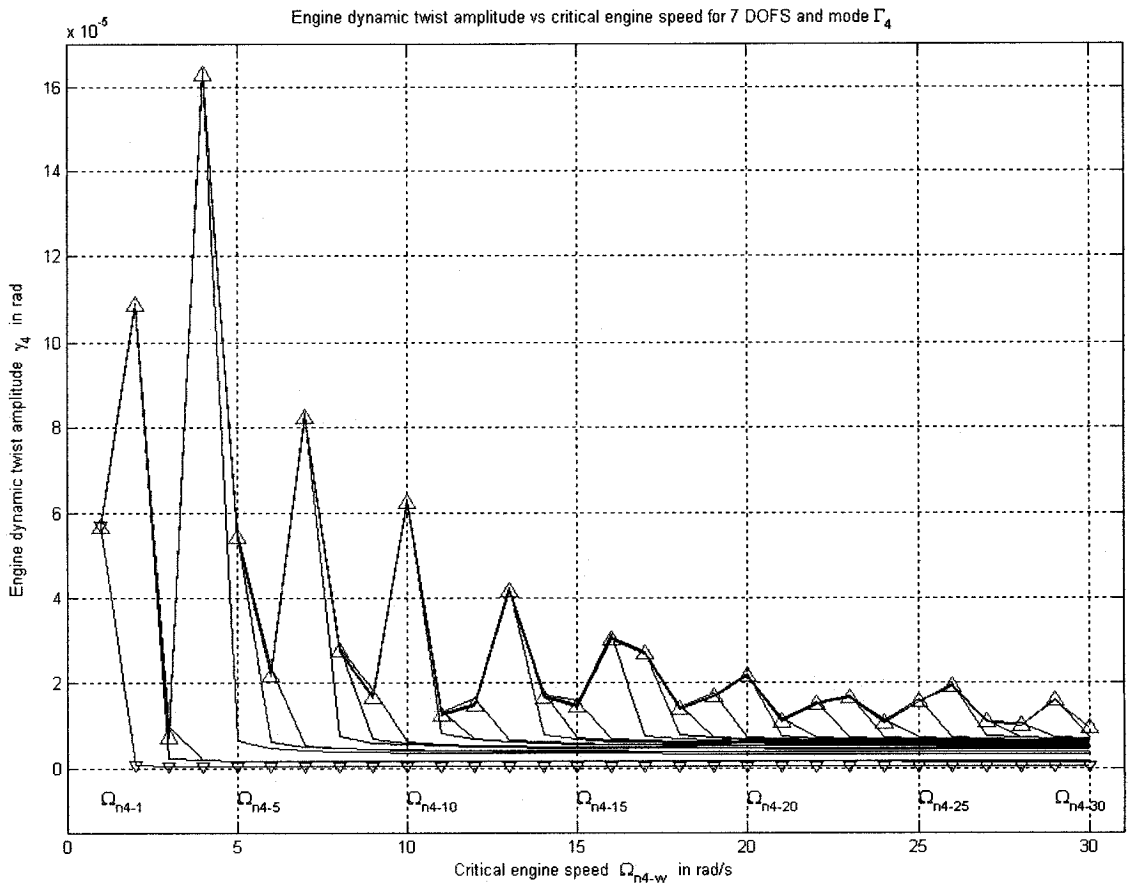

Figure 4.18: Engine dynamic twist amplitude γ_4 vs critical engine speed Ω_{n4-w} for a 7-DOFS and mode $\{\Gamma_4\}$

4.4.2 Vibration calculation for 8-DOFS with damping

The 8-DOFS in this section is the 7-DOFS from section 4.4.1 with the addition of the damping device at the opposite end of the flywheel. For the damping matrix, we use the proportional damping $[\widetilde{C}_E] = \alpha_0 . [\widetilde{J}_E] + \alpha_1 . [\widetilde{K}_E]$.

The damping device is the optimally tuned viscous damper derived in Chapter 2 and the type A seismic mass in Chapter 3.

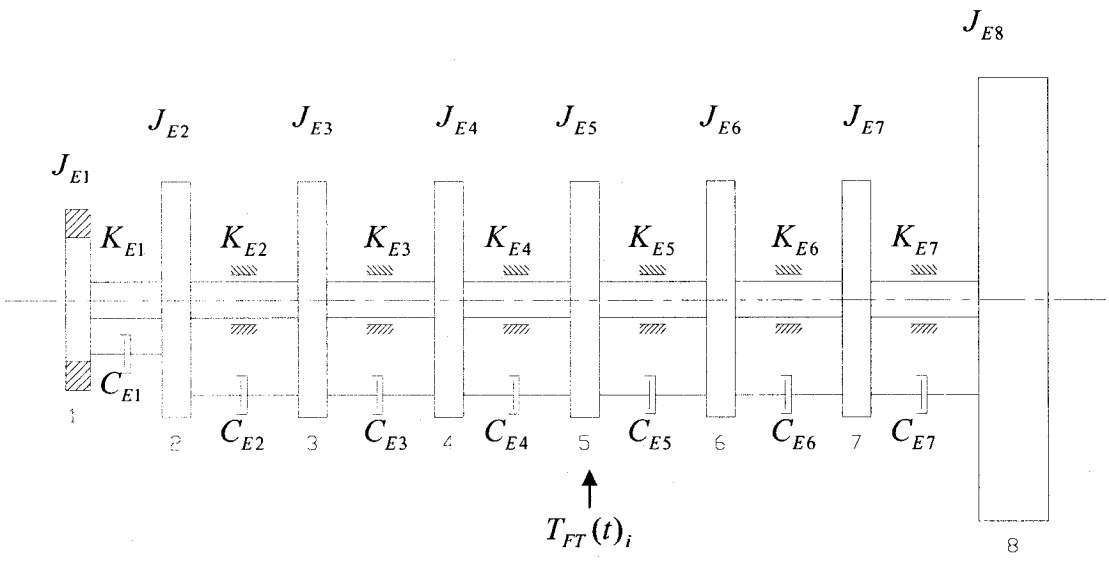

Figure 4.19: 8-DOFS equivalent system showing moments of inertia, damping and stiffness

The equations of motion for the 8-DOFS equivalent system with damping shown in figure 4.19:

$$J_{E1}.\ddot{\psi}_1 + K_{E2}.(\psi_1 - \psi_2) + C_{E2}.(\dot{\psi}_1 - \dot{\psi}_2) = 0$$
$$J_{E2}.\ddot{\psi}_2 + K_{E2}.(\psi_2 - \psi_3) + K_{E1}.(\psi_2 - \psi_1) + C_{E2}.(\dot{\psi}_2 - \dot{\psi}_3) + C_{E1}.(\dot{\psi}_2 - \dot{\psi}_1) = T_{E2}$$
$$J_{E3}.\ddot{\psi}_3 + K_{E3}.(\psi_3 - \psi_4) + K_{E2}.(\psi_3 - \psi_2) + C_{E3}.(\dot{\psi}_3 - \dot{\psi}_4) + C_{E2}.(\dot{\psi}_3 - \dot{\psi}_2) = T_{E3}$$
$$J_{E4}.\ddot{\psi}_4 + K_{E4}.(\psi_4 - \psi_5) + K_{E3}.(\psi_4 - \psi_3) + C_{E4}.(\dot{\psi}_4 - \dot{\psi}_5) + C_{E3}.(\dot{\psi}_4 - \dot{\psi}_3) = T_{E4}$$
$$J_{E5}.\ddot{\psi}_5 + K_{E5}.(\psi_5 - \psi_6) + K_{E4}.(\psi_5 - \psi_4) + C_{E5}.(\dot{\psi}_5 - \dot{\psi}_6) + C_{E4}.(\dot{\psi}_5 - \dot{\psi}_4) = T_{E5}$$
$$J_{E6}.\ddot{\psi}_6 + K_{E6}.(\psi_6 - \psi_7) + K_{E5}.(\psi_6 - \psi_5) + C_{E6}.(\dot{\psi}_6 - \dot{\psi}_7) + C_{E5}.(\dot{\psi}_6 - \dot{\psi}_5) = T_{E6}$$
$$J_{E7}.\ddot{\psi}_7 + K_{E7}.(\psi_7 - \psi_8) + K_{E6}.(\psi_7 - \psi_6) + C_{E7}.(\dot{\psi}_7 - \dot{\psi}_8) + C_{E6}.(\dot{\psi}_7 - \dot{\psi}_6) = T_{E7}$$
$$J_{E8}.\ddot{\psi}_8 + K_{E7}.(\psi_8 - \psi_7) + C_{E7}.(\dot{\psi}_8 - \dot{\psi}_7) = 0$$

where:

$$[\tilde{J}_E] = \begin{bmatrix} J_{E1} & 0 & 0 & 0 & 0 & 0 & 0 & 0 \\ 0 & J_{E2} & 0 & 0 & 0 & 0 & 0 & 0 \\ 0 & 0 & J_{E3} & 0 & 0 & 0 & 0 & 0 \\ 0 & 0 & 0 & J_{E4} & 0 & 0 & 0 & 0 \\ 0 & 0 & 0 & 0 & J_{E5} & 0 & 0 & 0 \\ 0 & 0 & 0 & 0 & 0 & J_{E6} & 0 & 0 \\ 0 & 0 & 0 & 0 & 0 & 0 & J_{E7} & 0 \\ 0 & 0 & 0 & 0 & 0 & 0 & 0 & J_{E8} \end{bmatrix}$$

$$[\tilde{K}_E] = \begin{bmatrix} K_{E1} & -K_{E1} & 0 & 0 & 0 & 0 & 0 & 0 \\ -K_{E1} & K_{E1}+K_{E2} & -K_{E2} & 0 & 0 & 0 & 0 & 0 \\ 0 & -K_{E2} & K_{E2}+K_{E3} & -K_{E3} & 0 & 0 & 0 & 0 \\ 0 & 0 & -K_{E3} & K_{E3}+K_{E4} & -K_{E4} & 0 & 0 & 0 \\ 0 & 0 & 0 & -K_{E4} & K_{E4}+K_{E5} & -K_{E5} & 0 & 0 \\ 0 & 0 & 0 & 0 & -K_{E5} & K_{E5}+K_{E6} & -K_{E6} & 0 \\ 0 & 0 & 0 & 0 & 0 & -K_{E6} & K_{E6}+K_{E7} & -K_{E7} \\ 0 & 0 & 0 & 0 & 0 & 0 & -K_{E7} & K_{E7} \end{bmatrix}$$

$$[\widetilde{C}_E]=\begin{bmatrix} C_{E1} & -C_{E1} & 0 & 0 & 0 & 0 & 0 & 0 \\ -C_{E1} & C_{E1}+C_{E2} & -C_{E2} & 0 & 0 & 0 & 0 & 0 \\ 0 & -C_{E2} & C_{E2}+C_{E3} & -C_{E3} & 0 & 0 & 0 & 0 \\ 0 & 0 & -C_{E3} & C_{E3}+C_{E4} & -C_{E4} & 0 & 0 & 0 \\ 0 & 0 & 0 & -C_{E4} & C_{E4}+C_{E5} & -C_{E5} & 0 & 0 \\ 0 & 0 & 0 & 0 & -C_{E5} & C_{E5}+C_{E6} & -C_{E6} & 0 \\ 0 & 0 & 0 & 0 & 0 & -C_{E6} & C_{E6}+C_{E7} & -C_{E7} \\ 0 & 0 & 0 & 0 & 0 & 0 & -C_{E7} & C_{E7} \end{bmatrix}$$

$$\{T_E\}=\begin{Bmatrix} T_{E1} \\ T_{E2} \\ T_{E3} \\ T_{E4} \\ T_{E5} \\ T_{E6} \\ T_{E7} \\ T_{E8} \end{Bmatrix}=\begin{Bmatrix} 0 \\ T_{FT}(t)_2 \\ T_{FT}(t)_3 \\ T_{FT}(t)_4 \\ T_{FT}(t)_5 \\ T_{FT}(t)_6 \\ T_{FT}(t)_7 \\ 0 \end{Bmatrix}=\begin{Bmatrix} 0 \\ A_{02}+\sum_{j=1}^{30}\left\{a_{j2}.\cos(\frac{j}{s}.\Omega.t)+b_{j2}.\sin(\frac{j}{s}.\Omega.t)\right\} \\ A_{03}+\sum_{j=1}^{30}\left\{a_{j3}.\cos(\frac{j}{s}.\Omega.t)+b_{j3}.\sin(\frac{j}{s}.\Omega.t)\right\} \\ A_{04}+\sum_{j=1}^{30}\left\{a_{j4}.\cos(\frac{j}{s}.\Omega.t)+b_{j4}.\sin(\frac{j}{s}.\Omega.t)\right\} \\ A_{05}+\sum_{j=1}^{30}\left\{a_{j5}.\cos(\frac{j}{s}.\Omega.t)+b_{j5}.\sin(\frac{j}{s}.\Omega.t)\right\} \\ A_{06}+\sum_{j=1}^{30}\left\{a_{j6}.\cos(\frac{j}{s}.\Omega.t)+b_{j6}.\sin(\frac{j}{s}.\Omega.t)\right\} \\ A_{07}+\sum_{j=1}^{30}\left\{a_{j7}.\cos(\frac{j}{s}.\Omega.t)+b_{j7}.\sin(\frac{j}{s}.\Omega.t)\right\} \\ 0 \end{Bmatrix}$$

4.4.2.1 Calculation of J_{E1} and K_{E1}

The damping device, the optimally tuned viscous damper, was derived in Chapter 2 and tested with the type A seismic mass in Chapter 3. As a reference, we use the theoretical values from table 3.1 in order to size the damping device for an 8-DOFS. With the optimum stiffness ratio k_{opt} = 0.157 and mass ratio μ_A = 0.246 corresponding to a primary system damping ratio ε_1 = 0.01, we obtain:

$$K_{E1} = k_{opt} \cdot \frac{1}{\frac{1}{K_{E2}} + \frac{1}{K_{E3}} + \frac{1}{K_{E4}} + \frac{1}{K_{E5}} + \frac{1}{K_{E6}} + \frac{1}{K_{E7}}} = 5.9712x10^5 \ N.m/rad$$

$$J_{E1} = \mu.(J_{E2} + J_{E3} + J_{E4} + J_{E5} + J_{E6} + J_{E7}) = 27.5126 \ kg.m^2$$

Note that we are not including the flywheel moment of inertia J_{E8} to calculate J_{E1} because, in our model in section 2.2, the inertia for primary system are the 6 cylinders only and the inertia of the flywheel can be assumed to be $J_{E8} = \infty$ since $J_{E8} >> J_{E2}$.

It is clear that the addition of the inertia J_{E1} and the stiffness K_{E1} adds another natural frequency to the system, converting it into an 8-DOFS and changes the natural frequencies from those of the 7-DOFS.

4.4.2.2 Mode and natural frequencies, $\{T_E\} = 0$

For the mode shapes and natural frequencies calculation of the 8-DOFS, we use the transfer matrix method [47] used in 4.4.1.1.

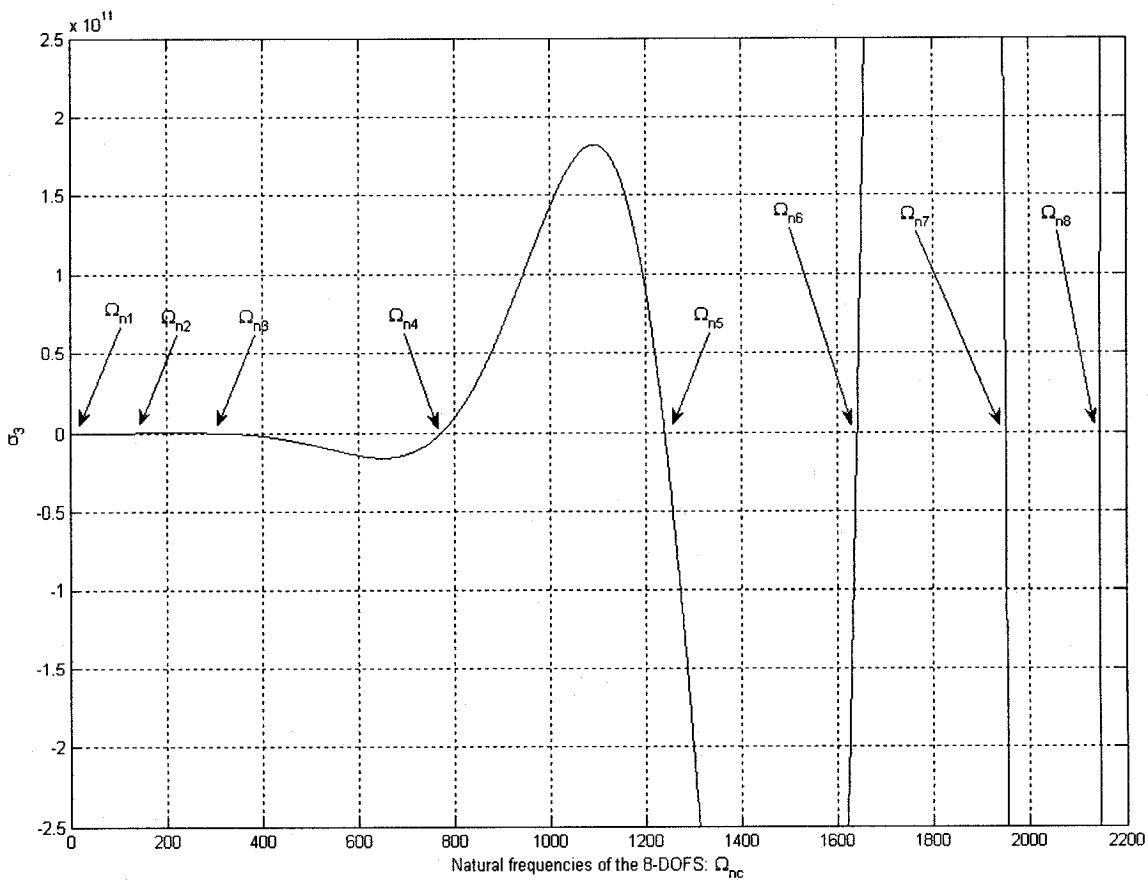

Figure 4.20: Natural frequencies of the 8-DOFS

$$\Omega_{n1} = 0$$
$$\Omega_{n2} = 135.05$$
$$\Omega_{n3} = 286.43$$
$$\Omega_{n4} = 773.29$$
$$\Omega_{n5} = 1238.70$$
$$\Omega_{n6} = 1640.55$$
$$\Omega_{n7} = 1950.49$$
$$\Omega_{n8} = 2146.07$$

$$\{\Gamma_1\} = \begin{Bmatrix} 1 \\ 1 \\ 1 \\ 1 \\ 1 \\ 1 \\ 1 \\ 1 \end{Bmatrix} \quad \{\Gamma_2\} = \begin{Bmatrix} 1.0000 \\ 0.1597 \\ 0.1353 \\ 0.1089 \\ 0.0809 \\ 0.0516 \\ 0.0217 \\ -0.0142 \end{Bmatrix} \quad \{\Gamma_3\} = \begin{Bmatrix} 1.0000 \\ -2.7801 \\ -2.6926 \\ -2.4248 \\ -1.9945 \\ -1.4305 \\ -0.7706 \\ 0.0745 \end{Bmatrix} \quad \{\Gamma_4\} = \begin{Bmatrix} 1.0000 \\ -26.5517 \\ -14.3038 \\ 4.9307 \\ 21.7568 \\ 27.9561 \\ 20.5005 \\ -0.2511 \end{Bmatrix}$$

$$\{\Gamma_5\}=\begin{Bmatrix}1.0000\\-69.6973\\15.8060\\81.4993\\45.0475\\-47.8633\\-80.7860\\0.3827\end{Bmatrix}\quad\{\Gamma_6\}=\begin{Bmatrix}1.0000\\-123.0073\\144.1677\\94.4038\\-162.8978\\-062.0841\\175.2156\\-0.4723\end{Bmatrix}\quad\{\Gamma_7\}=\begin{Bmatrix}1.0000\\-174.2892\\362.7336\\-227.4499\\-110.8254\\350.1927\\-277.0242\\0.5278\end{Bmatrix}\quad\{\Gamma_8\}=\begin{Bmatrix}1.0000\\-211.2064\\577.7996\\-806.8768\\843.9178\\-680.1068\\354.4308\\-0.5576\end{Bmatrix}$$

4.4.2.3 Forced vibration $\{T_E\}\neq 0$

To solve the generalized equation 4.10, we continue with the modal coordinates method. After replacing the modal coordinate vector, equation 4.14, and multiplying the whole equation by the traspose $[\Gamma]^T$ of the mode shape matrix

$$[\Gamma]^T.[\tilde{J}_E].[\Gamma]\{\ddot{\gamma}\}+[\Gamma]^T.[\tilde{C}_E].[\Gamma]\{\dot{\gamma}\}+[\Gamma]^T.[\tilde{K}_E].[\Gamma]\{\gamma\}=[\Gamma]^T.\{T_E\} \tag{4.20}$$

The orthogonality properties can be applied in equation 4.18 for the cth modal vector $\{\Gamma_c\}$, its transpose $\{\Gamma_c\}^T$ and natural frequency Ω_{nc}. Note that the excitation vector $\{T_E\}$ is not affected by the sub index c:

$$\{\Gamma_c\}^T.[\tilde{J}_E].\{\Gamma_c\}.\ddot{\gamma}_c+\{\Gamma_c\}^T.[\tilde{C}_E].\{\Gamma_c\}.\dot{\gamma}_c+\{\Gamma_c\}^T.[\tilde{K}_E].\{\Gamma_c\}.\gamma_c=\{\Gamma_c\}^T.\{T_E\} \tag{4.21}$$

The orthogonality property can also be applied to damping matrix $[\tilde{C}_E]$ as it was applied to the stiffness $[\tilde{K}_E]$ and inertia $[\tilde{J}_E]$ matrices; in other words, the damping matrix is proportional to the stiffness and inertia matrices:

$$[\Gamma]^T.[\tilde{C}_E][\Gamma]=\begin{bmatrix} 2\tilde{\tilde{J}}_1\Omega_{n1}\zeta_1 & 0 & 0 & 0 & 0 & 0 & 0 & 0 \\ 0 & 2\tilde{\tilde{J}}_2\Omega_{n2}\zeta_2 & 0 & 0 & 0 & 0 & 0 & 0 \\ 0 & 0 & 2\tilde{\tilde{J}}_3\Omega_{n3}\zeta_3 & 0 & 0 & 0 & 0 & 0 \\ 0 & 0 & 0 & 2\tilde{\tilde{J}}_4\Omega_{n4}\zeta_4 & 0 & 0 & 0 & 0 \\ 0 & 0 & 0 & 0 & 2\tilde{\tilde{J}}_5\Omega_{n5}\zeta_5 & 0 & 0 & 0 \\ 0 & 0 & 0 & 0 & 0 & 2\tilde{\tilde{J}}_6\Omega_{n6}\zeta_6 & 0 & 0 \\ 0 & 0 & 0 & 0 & 0 & 0 & 2\tilde{\tilde{J}}_7\Omega_{n7}\zeta_7 & 0 \\ 0 & 0 & 0 & 0 & 0 & 0 & 0 & 2\tilde{\tilde{J}}_8\Omega_{n8}\zeta_8 \end{bmatrix}$$

we obtain from equation 4.21:

$$\tilde{\tilde{J}}_c.\ddot{\gamma}_c+\tilde{\tilde{C}}_c.\dot{\gamma}_c+\tilde{\tilde{K}}_c.\gamma_c=\sum_{i=1}^{8}\Gamma_{ic}.T_{Ei} \tag{4.22}$$

where:

$$\begin{aligned}\tilde{\tilde{J}}_c&=\{\Gamma_c\}^T.[\tilde{J}_E].\{\Gamma_c\}\\ \tilde{\tilde{C}}_c&=\{\Gamma_c\}^T.[\tilde{C}_E].\{\Gamma_c\}=2.\tilde{\tilde{J}}_c.\Omega_{nc}.\zeta_c\\ \tilde{\tilde{K}}_c&=\{\Gamma_c\}^T.[\tilde{K}_E].\{\Gamma_c\}=\tilde{\tilde{J}}_c.\Omega_{nc}^2\end{aligned} \tag{4.23}$$

ζ_c: damping ratio

placing equation 4.7 in equation 4.22 and rearranging:

$$\tilde{\tilde{J}}_c.\ddot{\gamma}_c+\tilde{\tilde{C}}_c.\dot{\gamma}_c+\tilde{\tilde{K}}_c.\gamma_c=\sum_{i=1}^{8}A_{0i}.\Gamma_{ic}+\sum_{j=1}^{30}\left[\sum_{i=1}^{8}\Gamma_{ic}.a_{ji}.\cos(\frac{j}{2}.\Omega.t)+\sum_{i=1}^{8}\Gamma_{ic}.b_{ji}.\sin(\frac{j}{2}.\Omega.t)\right]$$

$$\tilde{\tilde{J}}_c.\ddot{\gamma}_c+\tilde{\tilde{C}}_c.\dot{\gamma}_c+\tilde{\tilde{K}}_c.\gamma_c=\sum_{i=1}^{8}A_{0i}.\Gamma_{ic}+\sum_{j=1}^{30}\left[c_{jc}.\cos(\frac{j}{2}.\Omega.t-\xi_{jc})\right]$$

$$\tilde{\tilde{J}}_c.\ddot{\gamma}_c+\tilde{\tilde{C}}_c.\dot{\gamma}_c+\tilde{\tilde{K}}_c.\gamma_c=\sum_{i=1}^{8}A_{0i}.\Gamma_{ic}+\mathrm{Re}\sum_{j=1}^{30}\left[c_{jc}.e^{\left(\frac{j}{2}.\Omega.t-\xi_{jc}\right).\hat{k}}\right] \tag{4.24}$$

where $\hat{k}=\sqrt{-1}$

considering the solution of equation 4.24:

$$\gamma_c = \frac{\sum_{i=1}^{8} A_{0i}.\Gamma_{ic}}{\tilde{\tilde{K}}_c} + \mathrm{Re}\sum_{j=1}^{30}\left[\subset_{jc} .e^{\left(\frac{j}{2}.\Omega.t\right).\hat{k}}\right] \tag{4.25}$$

$$\dot{\gamma}_c = \mathrm{Re}\sum_{j=1}^{30}\left[\frac{j}{2}.\Omega.\hat{k}.\subset_{jc} .e^{\left(\frac{j}{2}.\Omega.t\right).\hat{k}}\right]$$

$$\ddot{\gamma}_c = \mathrm{Re}\sum_{j=1}^{30}\left[-\frac{j^2}{4}.\Omega^2.\subset_{jc} .e^{\left(\frac{j}{2}.\Omega.t\right).\hat{k}}\right]$$

replacing the above equations in 4.22 and rearranging to find $\subset_{jc}$:

$$\mathrm{Re}\sum_{j=1}^{30}\left[-\tilde{\tilde{J}}_c.\frac{j^2}{4}.\Omega^2.\subset_{jc} .e^{\left(\frac{j}{2}.\Omega.t\right).\hat{k}} + \tilde{\tilde{C}}_c.\frac{j}{2}.\Omega.\hat{k}.\subset_{jc} .e^{\left(\frac{j}{2}.\Omega.t\right).\hat{k}} + \tilde{\tilde{K}}_c.\subset_{jc} .e^{\left(\frac{j}{2}.\Omega.t\right).\hat{k}}\right] = \mathrm{Re}\sum_{j=1}^{30}\left[c_{jc}.e^{\left(\frac{j}{2}.\Omega.t-\xi_{jc}\right).\hat{k}}\right]$$

$$\subset_{jc} = \frac{c_{jc}.e^{\left(-\xi_{jc}\right).\hat{k}}}{-\tilde{\tilde{J}}_c.\frac{j^2}{4}.\Omega^2 + \tilde{\tilde{C}}_c.\frac{j}{2}.\Omega.\hat{k} + \tilde{\tilde{K}}_c}$$

replacing $\subset_{jc}$ and equation 4.23 in equation 4.25:

$$\gamma_c = \frac{\sum_{i=1}^{8} A_{0i}.\Gamma_{ic}}{\tilde{\tilde{K}}_c} + \mathrm{Re}\sum_{j=1}^{30}\left[\frac{c_{jc}.e^{\left(\frac{j}{2}.\Omega.t-\xi_{jc}\right).\hat{k}}}{-\tilde{\tilde{J}}_c.\frac{j^2}{4}.\Omega^2 + \tilde{\tilde{C}}_c.\frac{j}{2}.\Omega.\hat{k} + \tilde{\tilde{K}}_c}\right] \tag{4.26}$$

In equation 4.26, the only unknown variable is $\tilde{C}_c = 2.\tilde{J}_c.\Omega_{nc}.\zeta_c$, since we do not know the damping ratio for the system. The damping ratio ζ_c could assume different values for the cth mode shape Γ_c and natural frequency Ω_{nc}. This uncertain procedure could lead to many possible different responses for the modes and natural frequencies.

Using the Caughey series [50] in the established 8 by 8 damping matrix $[C_E]$ and with the second term of equation 4.23:

$$\tilde{\tilde{C}}_c = \sum_{d=0}^{7} \alpha_d \tilde{\tilde{J}}_c . \Omega_{nc}^{2.d} = 2. \tilde{\tilde{J}}_c . \Omega_{nc} . \zeta_c$$

Expanding the above equation for ζ_c, c = 1, ...,8, we get

$$2.\zeta_c = \frac{\alpha_0}{\Omega_{nc}} + \alpha_1 . \Omega_{nc} + \alpha_2 . \Omega_{nc}^3 + \alpha_3 . \Omega_{nc}^5 + \alpha_4 . \Omega_{nc}^7 + \alpha_5 . \Omega_{nc}^9 + \alpha_6 . \Omega_{nc}^{11} + \alpha_7 . \Omega_{nc}^{13}$$

There are 8 equations to find each α_d given each damping value ζ_c; however, it should be noted that the Rayleigh damping is given by the first two terms of the above equations [49]. The Rayleigh damping has been checked in different real structures with good results [51], thus:

$$2.\zeta_c = \frac{\alpha_0}{\Omega_{nc}} + \alpha_1 . \Omega_{nc} \qquad (4.27)$$

The coefficients α_0 and α_1 are the coefficients used for the proportional damping matrix $\left[\tilde{C}_E\right] = \alpha_0 . \left[\tilde{J}_E\right] + \alpha_1 . \left[\tilde{K}_E\right]$.

Using the damping ratio from section 4.4.2.1 $\varepsilon_1 = \zeta_2 = \zeta_3$ = 0.01, and with Ω_{n2} = 135.05 rad/s , Ω_{n3} = 286.43 rad/s calculated in section 4.4.2.2, we obtain from equation 4.27 α_0 =1.8355 and $\alpha_1 = 4.7452 \text{x} 10^{-5}$.

Then the other damping ratios using equation 4.27: ζ_4 = 0.0195, ζ_5 = 0.0301, ζ_6 = 0.0395, ζ_7 = 0.0467, ζ_8 = 0.0513.

Replacing equation 4.23 in equation 4.26 and rearranging, we obtain one similar to equation 4.17:

$$\gamma_c = \frac{\sum_{i=1}^{8} A_{0i}.\Gamma_{ic}}{\tilde{K}_c} + \mathrm{Re}\sum_{j=1}^{30} \tilde{M}_{jc}.\tilde{Q}_{jc}.e^{\left(\frac{j}{2}.\Omega.t-\tilde{\xi}_{jc}\right).\hat{k}} \tag{4.28}$$

where:

$$\Omega_{nc} = \sqrt{\frac{\tilde{\tilde{K}}_c}{\tilde{\tilde{J}}_c}}$$

$$\tilde{Q}_{jc} = \frac{\sqrt{\left(\sum_{i=1}^{8}\Gamma_{ic}.a_{ji}\right)^2 + \left(\sum_{i=1}^{8}\Gamma_{ic}.b_{ji}\right)^2}}{\tilde{\tilde{J}}_c.\Omega_{nc}^2}$$

$$\tilde{\xi}_{jc} = tg^{-1}\left(\frac{\sum_{i=1}^{8}\Gamma_{ic}.b_{ji}}{\sum_{i=1}^{8}\Gamma_{ic}.a_{ji}}\right)$$

$$\tilde{M}_{jc} = \frac{1}{\left[1-\left(\frac{j}{2}.\frac{\Omega}{\Omega_{nc}}\right)^2\right] + \left[j.\zeta_c.\frac{\Omega}{\Omega_{nc}}\right].\hat{k}} \tag{4.29}$$

4.4.2.4 Numerical analysis

Numerical evaluation of the components of equation 4.28 when $t = 0$ is carried out. As mentioned in section 4.4.1.3, note that $t = 0$ is not the time when the engine starts running. The engine is already running and $t = 0$ is a selected instant to visualize the behavior of the engine for study. Also note the similarity of equations 4.18 and 4.29. See appendix VI for the corresponding Matlab program.

The total engine twist amplitude γ_c is composed of the engine static and dynamic twist and in the present study the static twist is neglected. We focus our study on the dynamic twist: dynamic magnifier $\widetilde{M}_{jc}$; harmonic intensity, which is the numerator of $\widetilde{Q}_{jc}$; and the critical speeds of the engine Ω_{nc-w}.

Figure 4.21 shows the plot of equation 4.28, showing the engine dynamic twist amplitude γ_2 (real) vs Ω engine speed for its natural speed Ω_{n2}= 135.1 rad/s and mode $\{\Gamma_2\}$. There are 30 peaks in figure 4.21 corresponding to the dynamic magnifier $\widetilde{M}_{jc}$ tending to infinity when the damping ratio ζ_c = 0. This happens when the engine speed Ω passes the critical speed $\Omega_{n2-w} = \frac{2.\Omega_{n2}}{w}$,where w = 1, 2, 3...28, 29, 30. This critical speed Ω_{n2-w} is excited by the natural speed of the engine Ω_{n2}. Some of the critical speeds for Ω_{n2}= 129.6 rad/s are: Ω_{n2-1}= 270.2, Ω_{n2-5}= 54.0 , Ω_{n2-10}= 27.0 , Ω_{n2-15}= 18.0 , Ω_{n2-20}= 13.5 , Ω_{n2-25}= 10.8 and Ω_{n2-30}= 9.0 rad/s.

The engine dynamic twist amplitude γ_2 (real+imaginary) vs engine speed Ω for its natural speed Ω_{n2}= 135.1 rad/s and mode $\{\Gamma_2\}$ is also plotted in the same figure 4.21. Note that the peaks for each critical speed have approximately the same dynamic twist amplitude for γ_2 (real) and γ_2 (real+imaginary).

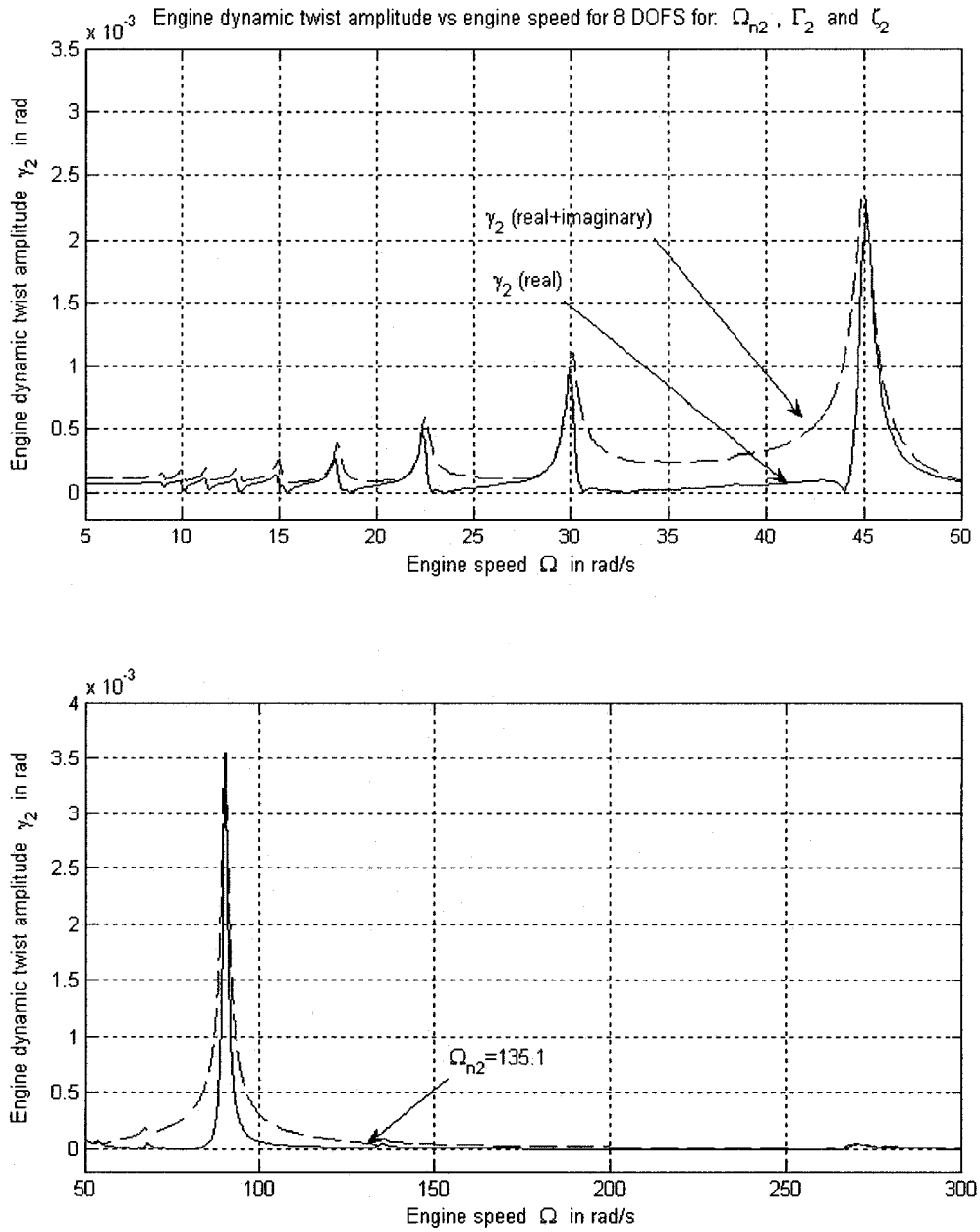

Figure 4.21: Engine dynamic twist amplitude for an 8-DOFS (real and real+imaginary) and a 7-DOFS (real) vs engine speed; for natural frequency Ω_{n2} = 135.1 rad/s and mode $\{\Gamma_2\}$

Figure 4.22 shows the plot of equation 4.28, the engine dynamic twist amplitude γ_3 (real) and γ_3 (real+ imaginary) vs Ω engine speed for its natural speed Ω_{n3} = 286.4 rad/s and mode $\{\Gamma_3\}$. The 30 peaks in figure 4.22 correspond to the dynamic magnifier $\tilde{M}_{jc}$ tending to infinity when the damping ratio ζ_3 = 0. This happens when the engine speed Ω passes the critical speed $\Omega_{n3-w} = \frac{2.\Omega_{n3}}{w}$, where w = 1, 2, 3...28, 29, 30. This critical speed Ω_{n3-w} is excited by the natural speed of the engine Ω_{n3}. Some of the critical speeds for Ω_{n3} = 286.4 rad/s are: Ω_{n3-1} = 572.9, Ω_{n3-5} = 114.6, Ω_{n3-10} = 57.3, Ω_{n3-15} = 38.2, Ω_{n3-20} = 28.6, Ω_{n3-25} = 22.9 and Ω_{n3-30} = 19.1 rad/s. Note that the peaks for each critical speed have approximately the same dynamic twist amplitude for γ_3 (real) and γ_3 (real+ imaginary) and therefore the mathematical equation 4.25 used represents the expected response.

The engine dynamic twist amplitude γ_2 for 7-DOFS vs Ω engine speed for its natural speed Ω_{n2} = 264.2 rad/s and mode $\{\Gamma_2\}$ is also plotted in the same figure 4.22. Although the natural speeds Ω_{n2} = 264.2 rad/s and Ω_{n3} = 286.4 rad/s are not the same, they are close. It is clear that the addition of the new natural speed Ω_{n2} = 135.1 rad/s on the system shifts the critical speeds and changes the modes from $\{\Gamma_2\}$ of 7-DOFS to $\{\Gamma_3\}$ of 8-DOFS. Furthermore, the response has been considerably reduced with the addition of the damper.

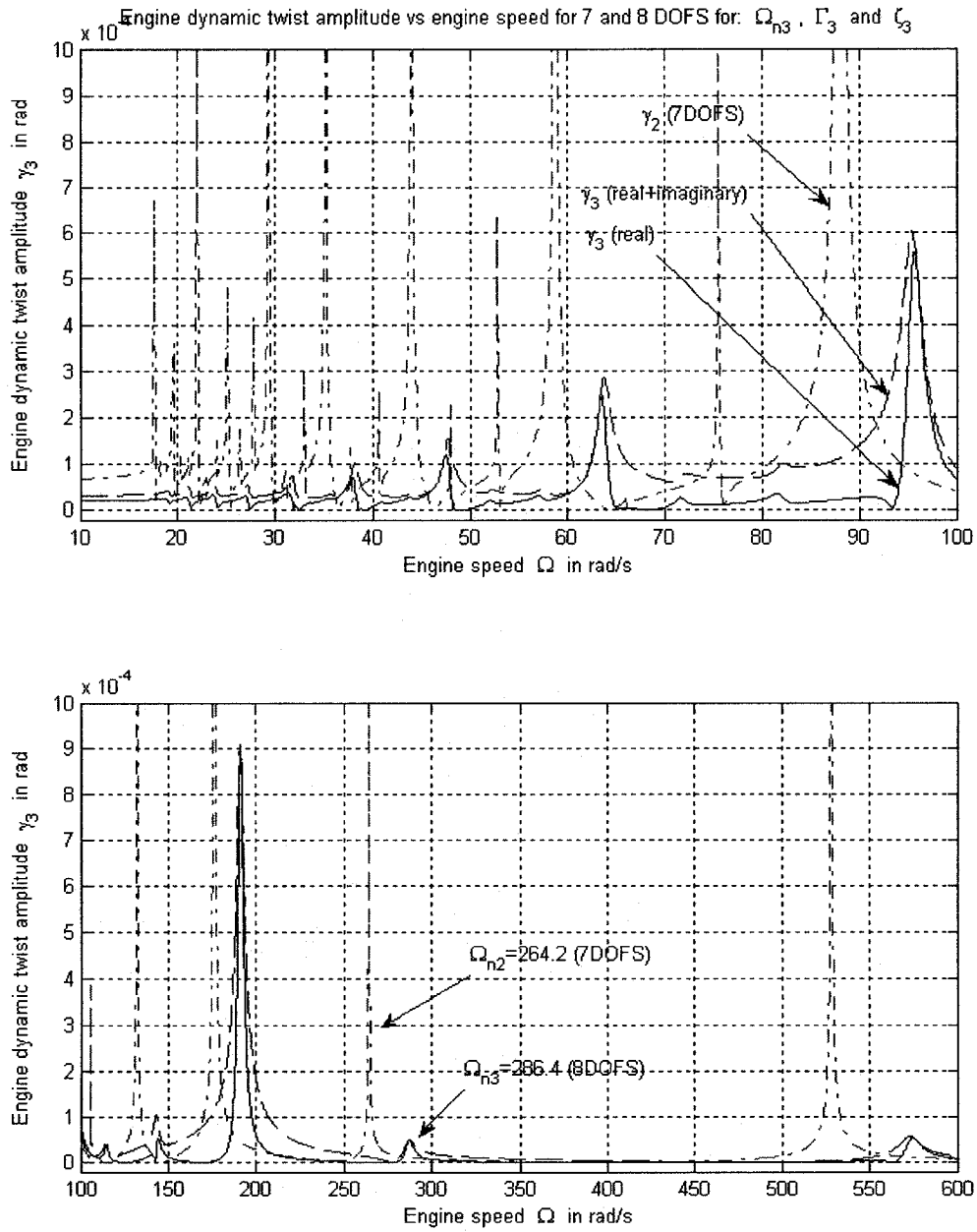

Figure 4.22: Engine dynamic twist amplitude for an 8-DOFS (real and real+imaginary) and a 7-DOFS (real) vs engine speed; for natural frequency Ω_{n3} = 286.4 rad/s and mode $\{\Gamma_3\}$

Figure 4.23 shows the plot of equation 4.28, the engine dynamic twist amplitude γ_4 (real) and γ_4 (real+ imaginary) vs Ω engine speed at its natural speed Ω_{n4} = 773.3 rad/s and mode $\{\Gamma_4\}$. The 30 peaks in figure 4.23 correspond to the dynamic magnifier $\widetilde{M}_{jc}$ tending to infinity when damping ratio ζ_4 = 0. This happens when the engine speed Ω passes the critical speed $\Omega_{n4-w} = \frac{2.\Omega_{n4}}{w}$, where w = 1, 2, 3...28, 29, 30. This critical speed Ω_{n4-w} is excited by the natural speed of the engine Ω_{n4}. Some of the critical speeds for Ω_{n4} = 773.8 rad/s are: Ω_{n4-1} = 1546.6, Ω_{n4-5} = 309.3, Ω_{n4-10} = 154.7, Ω_{n4-15} = 103.1, Ω_{n4-20} = 77.3, Ω_{n4-25} = 61.9 and Ω_{n4-30} = 51.6 rad/s.

The engine dynamic twist amplitude γ_3 for 7-DOFS vs Ω engine speed for its natural speed Ω_{n3} = 767.5 rad/s and mode $\{\Gamma_3\}$ is also plotted in the same figure 4.23. Although the natural speeds Ω_{n3} = 767.5 rad/s and Ω_{n4} = 773.3 rad/s are not the same, they are close. It is clear that the addition of the new natural speed Ω_{n2} = 135.1 rad/s on the system shifts the critical speeds and changes the modes from $\{\Gamma_3\}$ of 7-DOFS to $\{\Gamma_4\}$ of 8-DOFS.

The engine dynamic twist amplitude γ_4 (real) and γ_4 (real+ imaginary) in comparison with γ_3 (real) and γ_3 (real+ imaginary), respectively, for the 8 DOFS is lower. With the results obtained for mode $\{\Gamma_4\}$, the engine dynamic twist amplitude can be neglected.

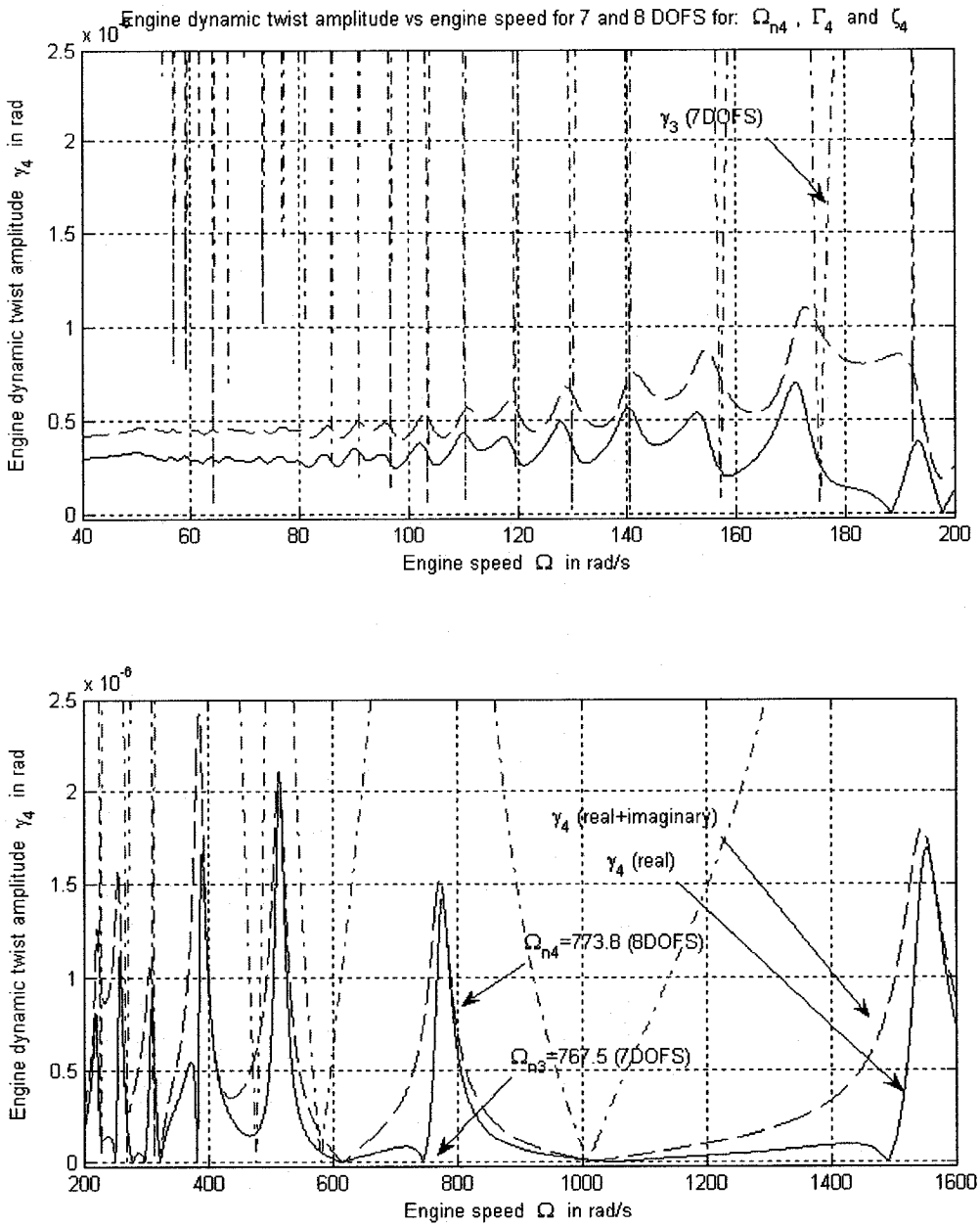

Figure 4.23: Engine dynamic twist amplitude for an 8-DOFS (real and real+imaginary) and a 7-DOFS (real) vs engine speed; for natural frequency $\Omega_{n4} = 773.8\ rad/s$ and mode $\{\Gamma_4\}$

It is clear from figures 4.21, 4.22 and 4.23 that there is no resonance at other speeds Ω, other than in the critical speeds Ω_{nc-k} in each figure.

Figure 4.24 compares the harmonic intensity of modes $\{\Gamma_2\}$, $\{\Gamma_3\}$ and $\{\Gamma_4\}$ for an 8 DOFS. The maximum intensity for 2nd and 3rd modes is at harmonic j = 3, and at harmonic j = 4 for 4th mode.

The intensity for mode $\{\Gamma_2\}$ exhibits very low values in comparison with the other modes and it can be ignored; however, the engine dynamic twist amplitude γ_2 for the same mode $\{\Gamma_2\}$ is higher than the other modes. This is attributed to the denominator of $\widetilde{Q}_{jc}$. The denominator is the product of the two expressions $\widetilde{\widetilde{J}}_c.\Omega_{nc}^2$ where $\widetilde{\widetilde{J}}_c = \{\Gamma_c\}^T.[\widetilde{J}_E].\{\Gamma_c\}$ from equation 4.23 and it depends directly on the modes; i.e., for mode $\{\Gamma_4\}$ with the square of its natural speed Ω_{n4}^2 the product is high and the quotient results are small; whereas for mode $\{\Gamma_2\}$ with the square of its natural speed Ω_{n2}^2 the quotient results are high. Note that mode $\{\Gamma_4\}$ is quite different from the others.

It is clear from figure 4.24 that the harmonic intensity has a direct dependence on the modes more than the firing order, phase angles and harmonic function. Also, for the 8-DOFS, the harmonic intensity behavior gradually diminishes with the increase of the harmonic numbers.

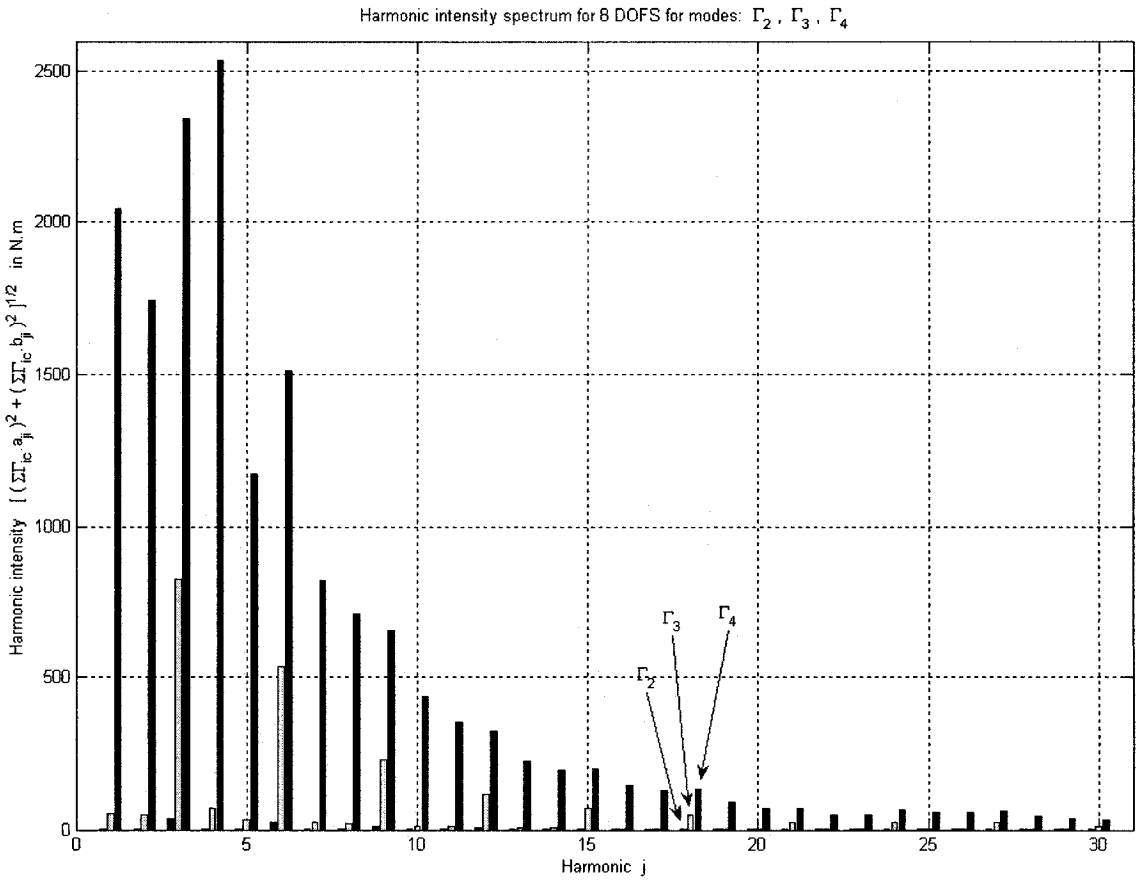

Figure 4.24: Engine harmonic intensity spectrum for an 8-DOFS for modes $\{\Gamma_2\}$, $\{\Gamma_3\}$ and $\{\Gamma_4\}$

Figures 4.25, 4.26 and 4.27 show the 30 critical speeds Ω_{nc-w} on the horizontal axis with their corresponding dynamic twist on the vertical axis. The line with the triangles facing downwards corresponds to the first harmonic (j = 1) of the 30 critical speeds; in other words, it corresponds to the first term of the sumatorial of equation 4.28: $\mathrm{Re}[\tilde{M}_{1c}.\tilde{Q}_{1c}.e^{(-\xi_{1c}).\hat{k}}]$ for every critical speed. The line with the triangles facing upwards corresponds to the sumatorial of the 30 harmonics for each critical speed in equation 4.28.

The other 28 lines in the figure that cannot be seen clearly because some overlap with each other and form an apparent thick line, correspond to the partial summation of the harmonics j for each critical speed Ω_{n2-k}; i.e., the second line: $\mathrm{Re}[\tilde{M}_{1c}.\tilde{Q}_{1c}.e^{(-\xi_{1c}).\hat{k}} + \tilde{M}_{2c}.\tilde{Q}_{2c}.e^{(-\xi_{2c}).\hat{k}}]$ for each critical speed; the third line: $\mathrm{Re}[\tilde{M}_{1c}.\tilde{Q}_{1c}.e^{(-\xi_{1c}).\hat{k}} + \tilde{M}_{2c}.\tilde{Q}_{2c}.e^{(-\xi_{2c}).\hat{k}} + \tilde{M}_{3c}.\tilde{Q}_{3c}.e^{(-\xi_{3c}).\hat{k}}]$ for each critical speed and so on. Note that we are not plotting the total magnitude (real + imaginary) for each dynamic twist γ_c, because as we saw from figures 4.21, 4.22 and 4.23, the peaks for each critical speed have approximately the same dynamic twist amplitude for γ_c (real) and γ_c (real+imaginary).

It is clear from figures 4.25, 4.26 and 4.27 that the dynamic twist γ_c diminishes drastically after the 10th harmonic (j = 10) for all modes.

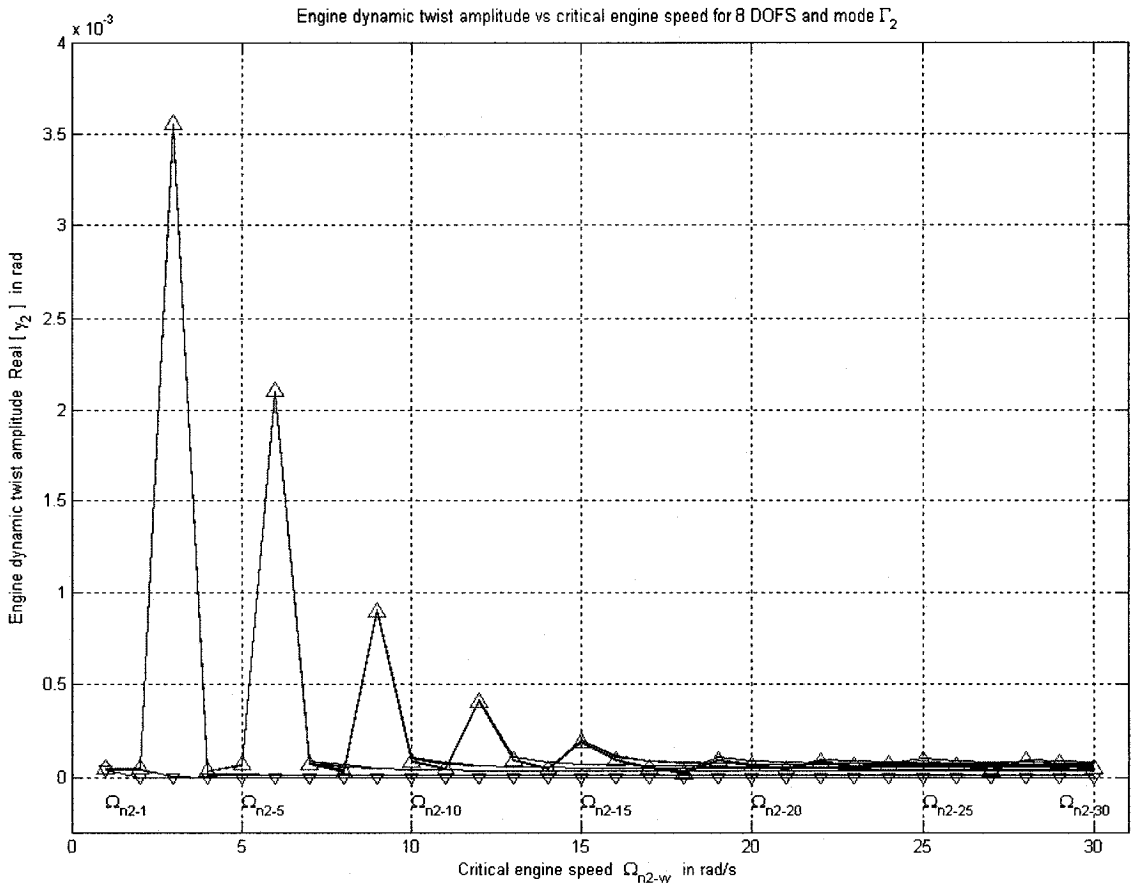

Figure 4.25: Engine dynamic twist amplitude γ_2 vs critical engine speed Ω_{n2-w} for an 8-DOFS and mode $\{\Gamma_2\}$

From figures 4.16 and 4.26, the experimental maximum angular twist of $16.25 x10^{-5}$ from figure 4.16 is lower than the maximum theoretical damped angular twist of $3.6 x10^{-3}$ from figure 4.26, even though the mode shapes $\{\Gamma_2\}$ for 7-DOFS and $\{\Gamma_3\}$ for 8-DOFS and the natural speeds Ω_{n2} = 264.2 rad/s for 7-DOFS and Ω_{n3} = 287.8 rad/s for 8-DOFS, are close in value. The difference is due to the experimental damping (equation 4.20) and the theoretical damping (equation 4.27).

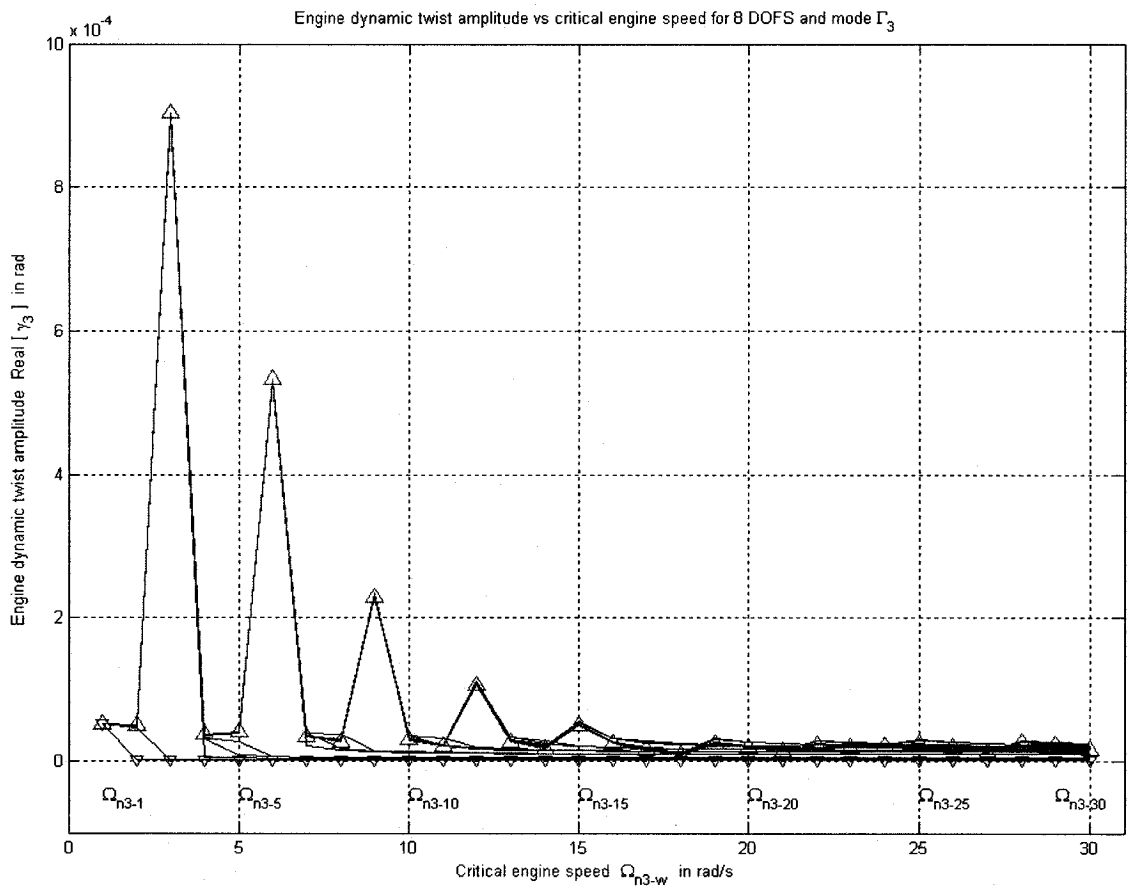

Figure 4.26: Engine dynamic twist amplitude γ_3 vs critical engine speed Ω_{n3-w} for an 8-DOFS and mode $\{\Gamma_3\}$

From figures 4.17 and 4.27, the experimental maximum angular twist of $20x10^{-3}$ from figure 4.17 is higher than the maximum theoretical damped angular twist of $9x10^{-4}$ from figure 4.27. Although the natural speeds Ω_{n3} = 767.5 rad/s for 7-DOFS and Ω_{n4} = 773.8 rad/s for 8-DOFS are close, the mode shapes $\{\Gamma_3\}$ for 7-DOFS and $\{\Gamma_4\}$ for 8-DOFS are considerably different.

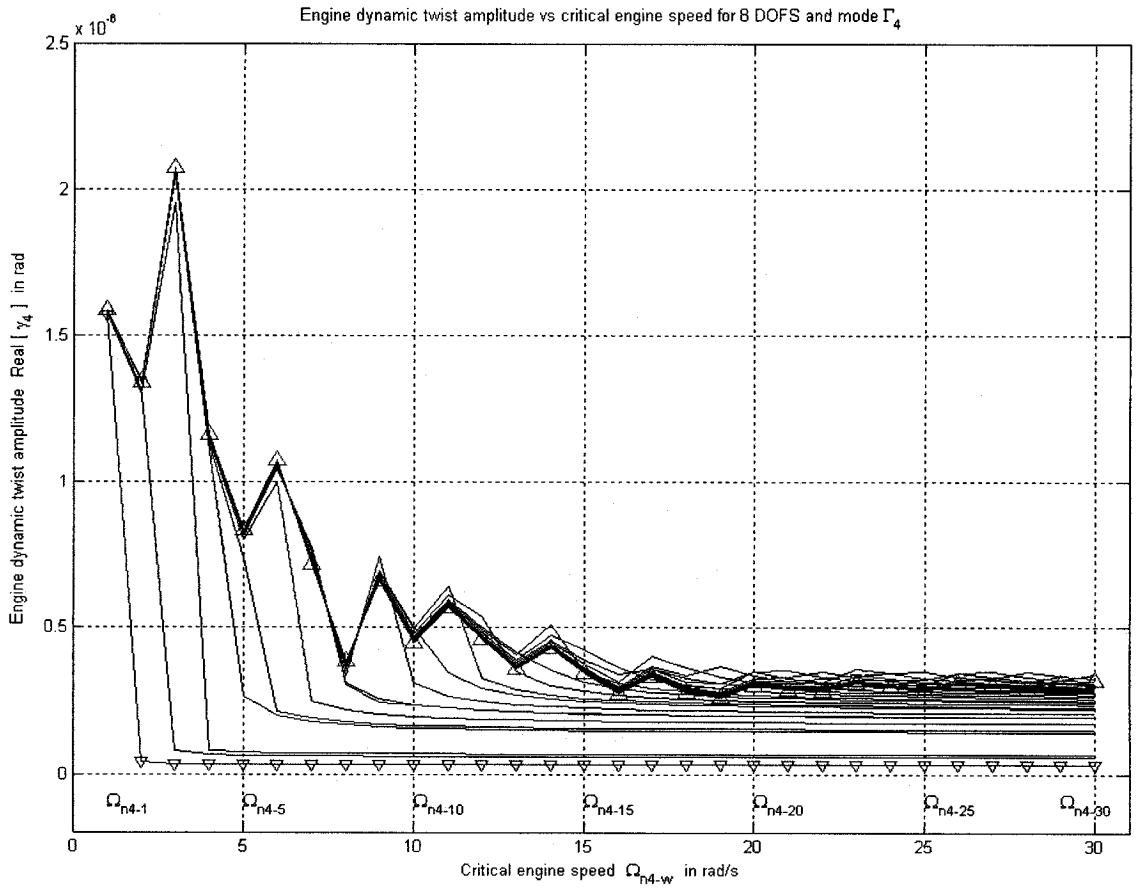

Figure 4.27: Engine dynamic twist amplitude γ_4 vs critical engine speed Ω_{n4-w} for an 8-DOFS and mode $\{\Gamma_4\}$

CHAPTER 5

CONCLUSIONS

5.1 Summary

In Chapters 2 and 3, a two-dimensional mathematical model of a 2-DOFS under torsional excitation on primary system was formulated, ignoring bending and lateral deflections. The second order equations of motion were solved for torsional twist amplitudes for various parameters. The torsional twist amplitudes were plotted to obtain the minimum-maximum torsional twist amplitude, which showed the optimum parameters subject to torsional excitation torque. A series of experimental testing was performed on the actual model under various excitation frequencies and amplitudes for certain theoretical parameters in order to validate the mathematical model. Comparison of the analytical and experimental results were also performed and discussed.

In Chapter 4, a two-dimensional mathematical model for a 4-stroke 6-in-line cylinder internal combustion engine was studied ignoring thermal loads and other types of excitations, except the one from the cylinders. First, the analytical study was performed on a 7-DOFS engine and then for the same engine system with the addition of the damping device, resulting in an 8-DOFS. The optimum

theoretical and experimental parameters from Chapters 2 and 3 were introduced as a reference to size the damping device.

5.2 Conclusions

1. The addition of the spring coupling in the conventional untuned viscous damper (Houdaille) can reduce the response of the system significantly.

2. The mathematical model from this thesis work has been validated against experimental results using non optimum parameters for the damper. Hence, it can be concluded that the use of optimum parameters will significantly reduce the response as predicted by the mathematical model.

3. In the experimental investigation, the spring dashpot damper has a significant effect on the reduction of not only torsional vibrations but also bending vibrations over the untuned viscous damper (Houdaille).

4. The engine dynamic twist is highly dependent on the dynamic magnifier, harmonic intensity, mode shapes and the critical speeds of the engine for the assumed mathematical model. Numerical solution of the mathematical model shows a reduction in the dynamic twist response with the addition of the damping device.

5.3 Recommendations for future work

1. In the present work, the two-dimensional mathematical model was investigated and tested for the spring dashpot absorber. A mathematical model and experimental investigation can be performed on a 3-DOFS as shown in figure 5.1, which may be able to extend the frequency range of application of the damper with a suitable choice of the secondary and tertiary systems.

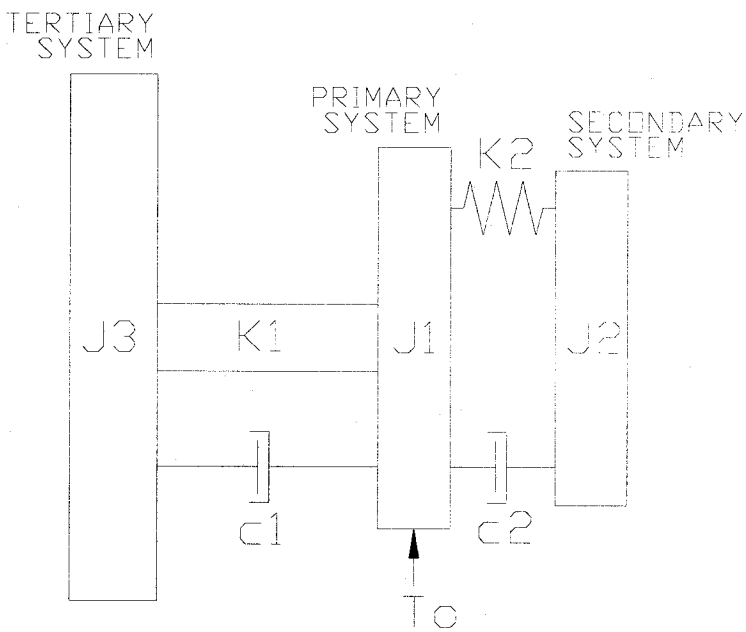

Figure 5.1: Three-degree-of-freedom system with stiffness and damping on primary and secondary systems

2. The two-dimensional mathematical model gives the torsional angular twist in one direction; however, the damper in a real application is subject to excitation torques and forces in three directions. A three-dimensional model considering gyroscopic effect and axial vibrations should be included in order to have a clear understanding of the behavior of the spring dashpot absorber compared with the viscous damper.

3. In the present work, a two-dimensional mathematical model for a 4-stroke 6-in-line internal combustion engine was studied for an instant when $t = 0$ and for a total number of harmonics of 30. The numerical study could be extended for different instants $t \neq 0$ and a greater number of harmonics. The $t \neq 0$ case will include the behavior of the damper in the presence of transient excitations.

4. In the results of the experimental investigation, for each curve it is noticed that there is a smaller peak. Upon quick analytical investigation, it was found that the small peak corresponds to the resonant frequency for bending vibration which could be further studied.

5. Using the same setup, equipment and measuring devices, a pendulum oil-immersed type damper in the untuned viscous seismic mass could be studied analytically and experimentally with the proper arrangement for the existing casing. This new type of damper could be designed and

adapted for different pendulum devices or degrees of freedom (see figure 5.2).

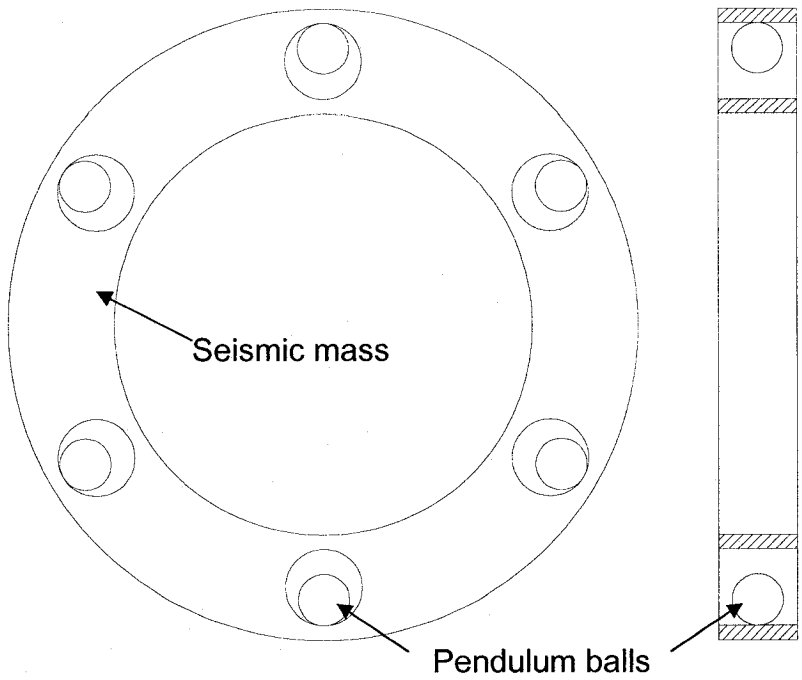

Figure 5.2: Seismic mass showing possible layout of pendulum balls in seismic mass

REFERENCES

1. T. Kodama, K. Wakabayashi, Y. Honda, S. Iwamoto, "Dynamic characteristics of viscous-friction dampers by simultaneous vibration displacement measurement at two points" , SAE World Congress Detroit, March 2001, 2001-01-0281.

2. K. Wakabayashi, Y. Honda, T. Kodama, S. Iwamoto, "The dynamic characteristics of torsional viscous-friction dampers on reciprocating engine shaftings", SAE Trans, New York, Vol. 101, N° 3, 1992, pp. 1734-54.

3. W. K. Wilson, "Practical solution of torsional vibration problems", Devices for controlling vibrations, Vol. 4, 3rd Edition, Wiley, New York, 1956.

4. British International Combustion Engine Research Association (BICERA), "A handbook on torsional vibration", E. J. Nestorides, eds, University Press, Cambridge (Eng.), 1958.

5. International Standard, ISO 2041:1990, 2nd Edition, 1990-08-01.

6. J. P. Den Hartog, J. Ormondroyd, "Torsional-vibration dampers", Trans ASME, Journal of Applied Mechanics, Vol. 52, 1930, pp. 133-152.

7. W. T. Thomson, "Theory of vibration with applications", 5th Edition, Pearson Eduacation Publications, Delhi, 2005.

8. J. P. Den Hartog, "Mechanical vibrations", 4th Edition, McGraw Hill Publications, New York, 1956.

9. S. Krenk, "Frequency analysis of the tuned mass damper." Journal of Applied Mechanics, Vol. 72, 2005, pp. 936-42.

10. G. Nicholson, Lord Corp., "Damper stops wheel wobble", Design News, 09.03.01, pp. 55-56.

11. J. C. Georgian, "Torsional viscous friction damper", Trans ASME, Vol. 71, 1949, pp. 389-399.

12. K. Wakabayashl, Y. Honda, T. Kodama, K. Shimoyamada, S. Iwamoto, "The effect of typical torsional viscous- friction damper on the

reduction of vibrations in the three dimensional space of diesel engine shaftings", SAE Trans, New York, N° 991, 1993, pp. 53-73.

13. B. E. O'Connor, "The viscous torsional vibration damper", SAE Trans, Vol. 1, N° 1, 1947, pp. 87-97.

14. R. D. Rumsey, "The viscous torsional vibration damper", SAE Trans, 1959, 590399.

15. T. Asami, O. Nishihara, A. M. Baz, "Analytical solutions to H_{∞} and H_2 optimization of dynamic vibration absorbers attached to damped linear systems", Journal of Vibration and Acoustics, Vol. 124, Issue 2, 2002, pp. 284-295.

16. T. Asami, O. Nishihara, "H_2 optimization of the three-element type dynamic vibration absorbers", Journal of Vibration and Acoustics, Vol. 124, N° 4, 2002, pp. 583-592.

17. N. Makris, M. C. Constantinou, "Spring-viscous damper systems for combined seismic and vibration isolation", Earthquake Engineering & Structural Dynamics, Vol. 21, N° 8, 1992, pp. 649-664.

18. G. J. Dashefsky, "The elimination of torsional vibration", The Pennsylvania State College Bulletin, School of Engineering, Technical Bulletin, N° 12, November 1 1930, pp.193-267.

19. G. B. Warburton, "Optimum absorber parameters for various combinations of response and excitation parameters", Earthquake Engineering and Structural Dynamics, Vol. 10, 1982, pp. 381-401.

20. S. E. Randall, D. M. Halsted, D. L. Taylor, "Optimum vibration absorbers for linear damped systems", Trans ASME, Journal of Mechanical Design, Vol. 103, 1981, pp. 908-913.

21. T. Ioi, K. Ikeda, "On the dynamic vibration damped absorber of the vibration system", Bulletin of the JSME, Vol. 21, 1978, pp. 64-71.

22. T. Asami, O. Nishihara, "Closed-form exact solution to H^{∞} optimization of dynamic vibration absorbers (application to different transfer functions and damping systems)", Journal of Vibration and Acoustics, Vol. 125, N° 3, 2003, pp. 398-405.

23. A. Soom, M-s Lee, "Optimal design of linear and nonlinear vibration absorbers for damped systems", Trans ASME, Journal of Vibration, Acoustics, Stress and Reliability in Design, Vol. 105, 1983, pp. 112-119.

24. H. Sekiguchi, T. Asami, " Theory of vibration isolation of a system with two degrees of freedom", Bulletin of the JSME, Vol. 27, N° 234, 1984, pp. 2839-46.

25. A. G. Thompson, "Optimum tuning and damping of a dynamic vibration absorber applied to a force excited and damped primary system", Journal of Sound and Vibration, Vol. 77, N° 3, 1981, pp. 403-415.

26. T. R. Screeram, "Graph theory based parametric influences applied to torsional vibration analysis", Advances in Engineering Software, Vol. 36, Issue 4, 2005, pp. 209-224.

27. Y. Wang, T. C. Lim, "An analysis of modal damping sources in a reciprocating engine", Journal of Sound and Vibration, Vol. 242, N° 1, 2001, pp. 179-193.

28. M. Hosek, H. Elmali, N. Olgac, "A tunable torsional vibration absorber: the centrifugal delayed resonator", Journal of Sound and Vibration, Vol. 205, N° 2, 1997, pp. 151-165.

29. J-S. Wu, C-H. Chen, "Torsional vibration analysis of gear-branched systems by finite element method", Journal of Sound and Vibration, Vol. 240, N° 1, 2001, pp. 159-182.

30. V. A. Vapat, H. V. Kumaraswamy, "Effect of primary system damping on the optimum design of an untuned viscous dynamic vibration absorber", Journal of Sound and Vibration, Vol. 63, N° 4, 1979, pp. 469-474.

31. A. G. Krishnan, "Orbital dynamics analysis and scale model testing of galloping transmission lines", Master Thesis, Concordia Univeristy, Montreal, Canada, 2007.

32. EPRI Transmission Line Reference Book, "Wind induced conductor motion, aeolian vibrations", Electrical Power Research Institute, Palo Alto, California, 1979.

33. H. Verma, "The stockbridge damper as a continuous hysteric system in single overhead transmission lines", Master Thesis, Indian Institute of Technology, Chennai, India, 2002.

34. V. G. Fitzsimmons, D. L. Pickett, R. O. Militz, W. A. Zisman, "Dimethyl-silicone-polymer fluids and their performance characteristics in hydraulic systems", Trans ASME, Vol. 68, 1946, pp. 361-369.

35. H. Frahm, "Device for damped vibrations of bodies", US patent N° 989958, October 30, 1909.

36. J. Ormondroyd, J. P. Den Hartog, "Theory of dynamic vibration absorber", Trans ASME, Journal of Applied Mechanics, Vol. 50, N° 7, 1928, pp. 9-22.

37. GERB Vibration Control, "Pipe work dampers", Technical report, 1986.

38. K. J. Schwann, H. H. Reinsch, F. M. Weber, "Description of the features of friction dampers on the basis of equivalent rheological models, presented for pipework dampers", Proc. Vess. Piping Conf., ASME, Vol. 127, 1988, pp. 477-484.

39. W. K. Wilson, "Practical solution of torsional vibration problems", Frequency calculations, Vol. 1, 3rd Edition, Wiley, New York, 1956.

40. F. P. Porter, "Harmonic coefficients of engine torque curves", Trans ASME, Journal of Applied Mechanics, Vol. 65, 1943, pp. A33-A48.

41. M. S. Pasricha, A. Y. Hassan, "Effects of damping on secondary resonances in torsional vibrations of a two-degree-of-freedom system – a variable inertia aspect in reciprocating engines", School of Mechanical Engineering, University Sains Malaysia, Malaysia.

42. R. van Basshuysen, F. Schäfer, "Internal combustion engine handbook", SAE International, 2004.

43. J. S. Rao, "Rotor dynamics", 2nd Edition, Wiley, New York, 1991.

44. W. K. Wilson, "Practical solution of torsional vibration problems", Devices for controlling vibrations, Vol. 3, 3rd Edition, Wiley, New York, 1956.

45. J. H. Gingsberg, "Mechanical and structural vibrations: theory and applications", 1st Edition, Wiley, New York, 2001.

46. P. Zeng, D. N. Assanis, "Cylinder pressure reconstruction and its application to heat transfer analysis", SAE Technical Paper Series, N° 2004-01-0922, March 2004.

47. E. C. Pestel, F. A. Leckie, "Matrix methods in elastomechanics", McGraw Hill, New York, 1963.

48. Lloyd's register of shipping, "Guidance notes on torsional vibrations characteristics of main and auxiliary engine", 1968.

49. E. L. Wilson, J. Penzien, " Evaluation of orthogonal damping matrices", International Journal for Numerical Methods in Engineering, Vol. 4, 1972, pp. 5-10.

50. T. K. Caughey, "Classical normal modes in damped linear systems", Journal of Applied Mechanics, Vol. 82, 1960, pp. 269-271.

51. K. K. Craig, "Structural dynamics", Wiley, New York, 1981.

52. W. K. Wilson, "Practical solution of torsional vibration problems", Amplitude calculations, Vol. 2, 3rd Edition, Wiley, New York, 1956.

53. W. K. Wilson, "Practical solution of torsional vibration problems", Strength calculations, Vol. 3, 3rd Edition, Wiley, New York, 1956.

54. W. K. Wilson, "Practical solution of torsional vibration problems", Vibration measurement, Vol. 5, 3rd Edition, Wiley, New York, 1956.

55. J. B. Vernon, "Linear vibration theory", Wiley, New York, 1967.

56. R. K. Vierck, "Vibration analysis", Int Textbook Company, New York, 1967.

57. G. W. Van Santen, "Introduction to a study of mechanical vibrations", MacMillan, New York, 1958.

58. P.L. Gatty, V. Ferrari, "Applied structural and mechanical vibrations", E&FN Spon, New York, 1999.

59. R. W. Clough, J. Penzien, "Dynamics of structures", McGraw Hill, New York, 1975.

60. W. C. Hurty, M. F. Rubinstein, "Dynamics of structures", Prentice-Hall, New Jersey, 1964.

61. G. C. Hart, K. Wong, "Structural dynamics for structural engineers", Wiley, New York, 2000.

62. V. Wowk, "Machinery vibration: measurement and analysis", McGraw-Hill, New York , 1991.

63. R. H. Wallace, "Understanding and measuring vibrations", Springer-Verlag, New York, 1970.

64. V. Wowk, "Machinery vibration: alignment", McGraw-Hill, New York, 2000.

65. J. S. Rao, "Vibratory condition monitoring of machines", Narosa Publishing House, New Delhi, 2000.

66. J. Kimura, K. Shiono, H. Okamura, K. Sogabe, "Experiments and analysis of crankshaft three-dimensional vibrations and bending stresses in a V-type ten-cylinder engine: influence of crankshaft gyroscopic motion", SAE International, 971995, 1997.

67. Ch-S. Han, K-W. Lee, D-B. Cho, Y-J. Cheon, S-D. Yeo, "Three-dimensional crankshaft vibration analysis including gyroscopic effect", SAE International, 940699, 1994.

68. T. Bengisu, P. Bernier, T. Brunner, "Critical speed vibrations induced by unstable gyroscopic moment", SAE International, 2005-01-2534, 2005.

69. ASTM D-2422-97, "Standard classification of industrial fluid lubricants by viscosity system", 2003.

70. ASTM D-341-93, "Standard viscosity-temperature charts for liquid petroleum products", 2003.

71. ASTM D-445, "Standard test method for kinematics viscosity charts for liquid petroleum products", 2003.

72. Spring Research Association, "Engineering design guidelines helical springs", Oxford University Press, New York , 1974.

APPENDIX I

Program to find optimum parameters ε_{2opt} and k_{opt}, chapter 2

```
interval=0.001;
e1=0.01;
x_initial=0;
x_final=2;

    cu=0;
    for u=.01:.01:1
        cu=cu+1;

        e2_initial=0;
        e2_final=1;

        k_initial=0;
        k_final=1;

        ck=0;
        for k=k_initial:interval:k_final
            ck=ck+1;
            ce2=0;
            for e2=e2_initial:interval:e2_final
                ce2=ce2+1;
                cx=0;
                for x=x_initial:interval:x_final
                    cx=cx+1;
                    m11=-x^2+(2*e1*x)*i+(2*e2*sqrt(u*k)*x)*i+1+k;
                    m12=-k-(2*e2*sqrt(u*k)*x)*i;
                    m21=m12;
                    m22=-u*x^2+(2*e2*sqrt(u*k)*x)*i+k;
                    Denominator=[m11, m12;
                                 m21, m22];
                    Numerator1=[1,m12;
                                0,m22];
                    ampl(cx)=det(Numerator1)/det(Denominator);
                    mod1(cx)=abs(ampl(cx));
                end;
                temp_mod1=-1;
                for ind_x=1:cx%loop calculates the x index
                            %at where the amplitud is maximum
                    if (temp_mod1<mod1(ind_x))
                    temp_mod1=mod1(ind_x);
                    temp_ind_x=ind_x;
                    end;
                end;
                max_ampl(ck,ce2)=max(mod1);
                max_ampl_test(ck,ce2)=temp_mod1;
                max_ind_x(ck,ce2)=temp_ind_x;
            end;
        end;
        temp_max_ampl_test=Inf;%loop finds the optimum k and e2 indexes
        for ind_ck=1:ck        %at where the amplitud is minimum
```

```
            for ind_ce2=1:ce2
                if (temp_max_amp1_test>max_amp1_test(ind_ck,ind_ce2))
                   temp_max_amp1_test=max_amp1_test(ind_ck,ind_ce2);
                   opt_ck=ind_ck;
                   opt_ce2=ind_ce2;
                end;
            end;
        end;
        matrixfinal(cu,1)=e1;
        matrixfinal(cu,2)=u;
        matrixfinal(cu,3)=(opt_ck-1)*interval+k_initial;
        matrixfinal(cu,4)=(opt_ce2-1)*interval+e2_initial;
        matrixfinal(cu,5)=(max_ind_x(opt_ck,opt_ce2)-
1)*interval+x_initial;
        matrixfinal(cu,6)=min(min(max_amp1));
        matrixfinal(cu,7)=max_amp1_test(opt_ck,opt_ce2);
    end;


xlswrite('matrixfinalxx',matrixfinal);
```

APPENDIX II

Gas pressure P_G vs angle ϕ coordinates, figure 4.4

ϕ °	P_G *bar*
0	30.00
10	73.00
20	60.00
30	44.00
40	31.00
50	22.50
60	17.50
70	15.00
80	11.00
90	9.50
100	9.00
110	8.00
120	7.00
130	6.00
140	5.00
150	4.50
160	4.00
170	3.50
180	3.00
190	2.50
200	2.00
210	1.50
220	1.00
230	1.00
240	1.00
250	1.00
260	1.00
270	1.00
280	1.00
290	1.00
300	1.00
310	1.00
320	1.00
330	1.00
340	1.00
350	1.00
360	1.00

ϕ °	P_G *bar*
360	1.00
370	0.90
380	0.80
390	0.70
400	0.60
410	0.50
420	0.40
430	0.30
440	0.20
450	0.10
460	0.20
470	0.30
480	0.40
490	0.50
500	0.60
510	0.70
520	0.80
530	0.90
540	1.00
550	1.17
560	1.33
570	1.50
580	1.66
590	1.83
600	1.99
610	2.16
620	2.33
630	2.50
640	3.00
650	3.50
660	4.00
670	5.00
680	7.50
690	12.00
700	17.50
710	22.50
720	30.00

APPENDIX III

Program for gas pressure P_G vs angle ϕ with Fourier series, figure 4.4

```
total=xlsread('Appendix_II_beta1.xls');
presure=total(:,2); %pressure  in bars
angle=total(:,1); % angle are in degrees
N=length(total);

T=angle(N)-angle(1); % period of curve: pressure vs angle
tN=angle(N);
t1=angle(1);
% Wn=n*2*pi/T, frequency of the fourier function presure
% n: number of harmonic
%iteration to find the slope m and b for each interval
%(inclined line) of the presure vs angle diagram
for h=1:1:N-1
m(h)=(presure(h+1)-presure(h))/(angle(h+1)-angle(h));
b(h)=presure(h)-m(h)*angle(h);
end

%this iteration is to find the A0 coeficient for the fourier series
A0=0;
for h=1:1:N-1
a0 =@(x) (m(h)*x+b(h));
A0 = A0+quadl(a0,angle(h),angle(h+1));
end
A0=A0/T;

%this iteration is to find the An and Bn coeficient
%for the fourier series
NN=72;
for n=1:NN
n
An_sum=0;
Bn_sum=0;
    for h=1:1:N-1
    an=@(x) (m(h)*x+b(h)).*cos(n*2*pi/T*x);
    An_sum=An_sum+(2/T)*quadl(an,angle(h),angle(h+1));
    bn=@(x) (m(h)*x+b(h)).*sin(n*2*pi/T*x);
    Bn_sum=Bn_sum+(2/T)*quadl(bn,angle(h),angle(h+1));
    end
An(n)=An_sum;
Bn(n)=Bn_sum;
end

%this iteration is to obtain the curve with fourier series
counter=0;
for x=t1:1:tN
    counter=counter+1;
    sum=0;
    for n=1:1:NN
        sum=sum+An(n)*cos(n*2*pi/T*x)+Bn(n)*sin(n*2*pi/T*x);
    end
```

```
    fourier_presure(counter)=sum+A0;
    fourier_angle(counter)=x;
end

plot(angle,presure,':k');
hold on
plot(fourier_angle,fourier_presure,'-k');
axis([-20 740 0 75]);
grid on

xlabel('Crankshaft angle \phi in degrees');
ylabel('Gas pressure  P_G  ( \phi )  in bars');
```

APPENDIX IV

Program for total torque T_{FT} with Fourier series, figure 4.8

```
%FIRST MUST RUN APPENDIX III PROGRAM

phase_angle=input('phase angle for cylinder = ');

Ro=35;% in mm, crankshaft radius
L=123;% in mm, conrod length
d=76;%in mm, piston diameter
A=pi*d^2/4;% in mm^2, piston area
W=800; %rotating speed of engine in rad/sec
Mp=.363; % kg, total piston mass
Mc=.096; % kg, total connecting rod mass
a=(Ro/L)^2;

%calculation of torque due to gas presure on crank shaft
for h=1:1:length(fourier_angle)
    fi=fourier_angle(h)-phase_angle;
    coef=sind(fi)+Ro/L*sind(fi)*cosd(fi)/sqrt(1-(Ro/L*sind(fi))^2);
    torque(h)=fourier_presure(h)*coef;%fourier_presure is in bar
end
gas_TORQUE=torque*A*Ro*.1;%N.mm
plot(fourier_angle,gas_TORQUE,'-k');
hold on

%calculation of torque due to inertia forces on crank shaft
for h=1:1:length(fourier_angle)
    fi=fourier_angle(h)-phase_angle;

    constant1=-(1-a*(sind(fi))^2)^(-3/2)*(a*sind(fi)*cosd(fi))^2-(1-
a*(sind(fi))^2)^(-1/2)*a*(cosd(fi))^2+(1-a*(sind(fi))^2)^(-
1/2)*a*(sind(fi))^2;
    constant2=sind(fi)+Ro/L*sind(fi)*cosd(fi)/sqrt(1-
(Ro/L*sind(fi))^2);
    inertia_TORQUE_IO(h)=-
(Mp+2*Mc/3)*W^2*(Ro*cosd(fi)+L*constant1)*constant2*Ro/1000;%N.mm

    piston_speed=W*(Ro*sind(fi)+L*(1-a*(sind(fi))^2)^(-
1/2)*(a*sind(fi)*cosd(fi)));
    inertia_TORQUE_IR(h)=-Mc/3*piston_speed^2/Ro;

    inertia_TORQUE(h)=inertia_TORQUE_IO(h)+inertia_TORQUE_IR(h);
end

plot(fourier_angle,inertia_TORQUE,':k');
hold on

%final_TORQUE=gas_TORQUE+inertia_TORQUE
for h=1:1:length(fourier_angle)
    final_TORQUE(h)=gas_TORQUE(h)+inertia_TORQUE(h);
```

```
end
plot(fourier_angle,final_TORQUE,'-b');
grid on
N1=length(fourier_angle);
T=fourier_angle(N1)-fourier_angle(1); % period of curve: final_TORQUE
vs angle
tN=fourier_angle(N1);
t1=fourier_angle(1);

%iteration to find the slope m and b for each interval
%(inclined line) of the final_TORQUE vs angle
for h=1:1:N1-1
m1(h)=(final_TORQUE(h+1)-final_TORQUE(h))/(fourier_angle(h+1)-
fourier_angle(h));
b1(h)=final_TORQUE(h)-m1(h)*fourier_angle(h);
end

%this iteration is to find the A0 coeficient
%for the fourier series of final_TORQUE
A0T=0;
for h=1:1:N-1
a01 =@(x) (m1(h)*x+b1(h));
A0T = A0+quadl(a01,fourier_angle(h),fourier_angle(h+1));
end
A0T=A0T/T;%N.mm

%this iteration is to find the An and Bn coeficient
%for the fourier series of final_TORQUE
NN1=30;
for n=1:NN1
n
An_sumT=0;
Bn_sumT=0;
    for h=1:1:N1-1
    an1=@(x) (m1(h)*x+b1(h)).*cos(n*2*pi/T*x);

An_sumT=An_sumT+(2/T)*quadl(an1,fourier_angle(h),fourier_angle(h+1));
    bn1=@(x) (m1(h)*x+b1(h)).*sin(n*2*pi/T*x);

Bn_sumT=Bn_sumT+(2/T)*quadl(bn1,fourier_angle(h),fourier_angle(h+1));
    end
AnT(n)=An_sumT;%N.mm
BnT(n)=Bn_sumT;%N.mm
end

%this iteration is to obtain the curve with fourier series
beta=[0,8*pi/3,4*pi/3,10*pi/3,2*pi/3,2*pi];
counter=0;
for x=1:1:N1
    counter=counter+1;
    sum_1=0;
%     sum_2=0;
%     sum_3=0;
%     sum_4=0;
%     sum_5=0;
%     sum_6=0;
    for n=1:1:NN1
```

```
        sum_1=sum_1+AnT(n)*cos(n*2*pi/T*x-
n*beta(1)/2)+BnT(n)*sin(n*2*pi/T*x-n*beta(1)/2);
    end
    fourier_TORQUE1(counter)=sum_1+A0T;
fourier_TORQUE(counter)=fourier_TORQUE1(counter)+fourier_TORQUE2(counte
r)+fourier_TORQUE3(counter)+fourier_TORQUE4(counter)+fourier_TORQUE5(co
unter)+fourier_TORQUE6(counter);
end

plot(fourier_angle,final_TORQUE,'-b');
hold on
plot(fourier_angle,fourier_TORQUE1,'-r');

axis([-20 740 -3e+005 5e+005]);
title(['Cylinder 6, phase angle  ',num2str(phase_angle),'  degrees']);
xlabel('Crankshaft angle \phi in degrees');
ylabel('Torque in  N.mm');
grid on
box on
```

APPENDIX V

Program for 7-DOFS engine dynamic twist γ_c vs engine speed Ω, figures 4.12, 4.13 and 4.14

```
coeficients=xlsread('Harmonic_coeficients.xls');%N.mm
coeficients=coeficients*10; %N.m

Aji2=coeficients(:,1);
Bji2=coeficients(:,2);

Aji3=coeficients(:,3);
Bji3=coeficients(:,4);

Aji4=coeficients(:,5);
Bji4=coeficients(:,6);

Aji5=coeficients(:,7);
Bji5=coeficients(:,8);

Aji6=coeficients(:,9);
Bji6=coeficients(:,10);

Aji7=coeficients(:,11);
Bji7=coeficients(:,12);

delta=[0,0,480,240,600,120,360,0];

Gic=[    1.00000000000000
  -0.24768205424037
  -1.18633565424764
  -0.64481954814462
   0.70122633640183
   1.17236470505899
  -0.00557974031985];

K2=22.82e6; %N.m/rad between J1 and J2
K3=22.82e6; %N.m/rad between J2 and J3
K4=22.82e6; %N.m/rad between J3 and J4
K5=22.82e6; %N.m/rad between J4 and J5
K6=22.82e6; %N.m/rad between J5 and J6
K7=19.21e6; %N.m/rad between J6 and J7

J2=18.64; %kg.m^2 cyl 1
J3=18.64; %kg.m^2 cyl 2
J4=18.64; %kg.m^2 cyl 3
J5=18.64; %kg.m^2 cyl 4
J6=18.64; %kg.m^2 cyl 5
J7=18.64; %kg.m^2 cyl 6
J8=2655; %kg.m^2 flywheel

JE=[J2,0,0,0,0,0,0;
    0,J3,0,0,0,0,0;
    0,0,J4,0,0,0,0;
```

```
    0,0,0,J5,0,0,0;
    0,0,0,0,J6,0,0;
    0,0,0,0,0,J7,0;
    0,0,0,0,0,0,J8];

KE=[K2, -K2,  0, 0,0,0,0;
  -K2,K2+K3,-K3,0,0,0,0;
   0, -K3, K3+K4,-K4,0,0,0;
   0,0,-K4,K4+K5,-K5,0,0;
   0,0,0,-K5,K5+K6,-K6,0;
   0,0,0,0,-K6,K6+K7,-K7;
   0,0,0,0,0,-K7,K7];

Jpc=Gic'*JE*Gic;

Kpc=Gic'*KE*Gic;

wn=sqrt(Kpc/Jpc);

t=0;
c_w=0;

    for w=0:.1:2500
            c_w=c_w+1;

            for j=1:1:30

                    aji2(j)=(Aji2(j)*cosd(j*delta(2)/2)-
Bji2(j)*sind(j*delta(2)/2));

bji2(j)=(Aji2(j)*sind(j*delta(2)/2)+Bji2(j)*cosd(j*delta(2)/2));

                    aji3(j)=(Aji3(j)*cosd(j*delta(3)/2)-
Bji3(j)*sind(j*delta(3)/2));

bji3(j)=(Aji3(j)*sind(j*delta(3)/2)+Bji3(j)*cosd(j*delta(3)/2));

                    aji4(j)=(Aji4(j)*cosd(j*delta(4)/2)-
Bji4(j)*sind(j*delta(4)/2));

bji4(j)=(Aji4(j)*sind(j*delta(4)/2)+Bji4(j)*cosd(j*delta(4)/2));

                    aji5(j)=(Aji5(j)*cosd(j*delta(5)/2)-
Bji5(j)*sind(j*delta(5)/2));

bji5(j)=(Aji5(j)*sind(j*delta(5)/2)+Bji5(j)*cosd(j*delta(5)/2));

                    aji6(j)=(Aji6(j)*cosd(j*delta(6)/2)-
Bji6(j)*sind(j*delta(6)/2));

bji6(j)=(Aji6(j)*sind(j*delta(6)/2)+Bji6(j)*cosd(j*delta(6)/2));

                    aji7(j)=(Aji7(j)*cosd(j*delta(7)/2)-
Bji7(j)*sind(j*delta(7)/2));

bji7(j)=(Aji7(j)*sind(j*delta(7)/2)+Bji7(j)*cosd(j*delta(7)/2));
```

```
sumGic_aji(j)=Gic(1)*aji2(j)+Gic(2)*aji3(j)+Gic(3)*aji4(j)+Gic(4)*aji5(
j)+Gic(5)*aji6(j)+Gic(6)*aji7(j);

sumGic_bji(j)=Gic(1)*bji2(j)+Gic(2)*bji3(j)+Gic(3)*bji4(j)+Gic(4)*bji5(
j)+Gic(5)*bji6(j)+Gic(6)*bji7(j);


Qjc(j)=sqrt(sumGic_aji(j)^2+sumGic_bji(j)^2)/Jpc/wn^2;

                    eta_jc(j)=atan(sumGic_bji(j)/sumGic_aji(j));

                    Mjc(j)=1/(1-(j*w/2/wn)^2);

                    if (Mjc(j)==Inf)|(Mjc(j)==-Inf)
Mjc(j)=3.8/Qjc(j)^.25; end;

                    cos_f(j)=cos(j*w*t/2-eta_jc(j));
            end

            %sum_gamc=Ao;
            sum_gamc=0;
            for h=1:1:30
                sum_gamc=sum_gamc+Mjc(h)*Qjc(h)*cos_f(h);
            end

            gamc(c_w)=sum_gamc;%in radians
            omega(c_w)=w;%in rad/sec
            clear sum_gamc
    end
plot(omega,gamc,'-k');
grid on

gama_c(:,1)=omega';
gama_c(:,2)=gamc';

xlswrite('points_gama_omega_eq_4_17_c_4',gama_c);
```

APPENDIX VI

Program for 8-DOFS engine dynamic twist γ_c vs engine speed Ω, figures 4.21, 4.22 and 4.23

```
coeficients=xlsread('Harmonic_coeficients.xls');%N.mm
coeficients=coeficients*10; %N.m

Aji2=coeficients(:,1);
Bji2=coeficients(:,2);

Aji3=coeficients(:,3);
Bji3=coeficients(:,4);

Aji4=coeficients(:,5);
Bji4=coeficients(:,6);

Aji5=coeficients(:,7);
Bji5=coeficients(:,8);

Aji6=coeficients(:,9);
Bji6=coeficients(:,10);

Aji7=coeficients(:,11);
Bji7=coeficients(:,12);

delta=[0,0,480,240,600,120,360,0];

Gic=[     1.00000000000000,
   0.15966499569224,
   0.13529774698925,
   0.10891490329351,
   0.08090950239633,
   0.05169875409666,
   0.02171782482792,
  -0.01428155083981];

K1=5.9712e5; %N.m/rad between J1 and J2
K2=22.82e6; %N.m/rad between J1 and J2
K3=22.82e6; %N.m/rad between J2 and J3
K4=22.82e6; %N.m/rad between J3 and J4
K5=22.82e6; %N.m/rad between J4 and J5
K6=22.82e6; %N.m/rad between J5 and J6
K7=19.21e6; %N.m/rad between J6 and J7

J1=27.5126;
J2=18.64; %kg.m^2 cyl 1
J3=18.64; %kg.m^2 cyl 2
J4=18.64; %kg.m^2 cyl 3
J5=18.64; %kg.m^2 cyl 4
J6=18.64; %kg.m^2 cyl 5
J7=18.64; %kg.m^2 cyl 6
J8=2655; %kg.m^2 flywheel
```

```
JE=[J1,0,0,0,0,0,0,0;
    0,J2,0,0,0,0,0,0;
    0,0,J3,0,0,0,0,0;
    0,0,0,J4,0,0,0,0;
    0,0,0,0,J5,0,0,0;
    0,0,0,0,0,J6,0,0;
    0,0,0,0,0,0,J7,0;
    0,0,0,0,0,0,0,J8];

KE=[K1,    -K1,      0,     0,  0,        0,      0,  0;
    -K1,   K1+K2, -K2,     0,  0,        0,      0,  0;
    0,      -K2,   K2+K3,-K3,  0,        0,      0,  0;
    0,      0,     -K3, K3+K4,-K4,       0,      0,  0;
    0,      0,      0,   -K4, K4+K5,   -K5,      0,  0;
    0,      0,      0,     0,  -K5,   K5+K6,   -K6,  0;
    0,      0,      0,     0,    0,    -K6,   K6+K7,-K7;
    0,      0,      0,     0,    0,      0,    -K7,  K7];

Jpc=Gic'*JE*Gic;

Kpc=Gic'*KE*Gic;

wnc=sqrt(Kpc/Jpc);

damping_ratio=.01;

Cpc=2*Jpc*wnc*damping_ratio;

t=0;
c_w=0;

    for w=0:.1:2500
            c_w=c_w+1;

            for j=1:1:30

                    aji2(j)=(Aji2(j)*cosd(j*delta(2)/2)-
Bji2(j)*sind(j*delta(2)/2));

bji2(j)=(Aji2(j)*sind(j*delta(2)/2)+Bji2(j)*cosd(j*delta(2)/2));

                    aji3(j)=(Aji3(j)*cosd(j*delta(3)/2)-
Bji3(j)*sind(j*delta(3)/2));

bji3(j)=(Aji3(j)*sind(j*delta(3)/2)+Bji3(j)*cosd(j*delta(3)/2));

                    aji4(j)=(Aji4(j)*cosd(j*delta(4)/2)-
Bji4(j)*sind(j*delta(4)/2));

bji4(j)=(Aji4(j)*sind(j*delta(4)/2)+Bji4(j)*cosd(j*delta(4)/2));

                    aji5(j)=(Aji5(j)*cosd(j*delta(5)/2)-
Bji5(j)*sind(j*delta(5)/2));

bji5(j)=(Aji5(j)*sind(j*delta(5)/2)+Bji5(j)*cosd(j*delta(5)/2));
```

```
                    aji6(j)=(Aji6(j)*cosd(j*delta(6)/2)-
Bji6(j)*sind(j*delta(6)/2));

bji6(j)=(Aji6(j)*sind(j*delta(6)/2)+Bji6(j)*cosd(j*delta(6)/2));

                    aji7(j)=(Aji7(j)*cosd(j*delta(7)/2)-
Bji7(j)*sind(j*delta(7)/2));

bji7(j)=(Aji7(j)*sind(j*delta(7)/2)+Bji7(j)*cosd(j*delta(7)/2));


sumGic_aji(j)=Gic(2)*aji2(j)+Gic(3)*aji3(j)+Gic(4)*aji4(j)+Gic(5)*aji5(
j)+Gic(6)*aji6(j)+Gic(7)*aji7(j);

sumGic_bji(j)=Gic(2)*bji2(j)+Gic(3)*bji3(j)+Gic(4)*bji4(j)+Gic(5)*bji5(
j)+Gic(6)*bji6(j)+Gic(7)*bji7(j);


Qjc(j)=sqrt(sumGic_aji(j)^2+sumGic_bji(j)^2)/Jpc/wnc^2;

                    eta_jc(j)=atan(sumGic_bji(j)/sumGic_aji(j));

                    Mjc(j)=1/((1-
(j*w/2/wnc)^2)+(j*damping_ratio*w/wnc)*i);

                    exponential(j)=exp((j*w*t/2-eta_jc(j))*i);


            end

            %sum_gamc=Ao;
            sum_gamc_real=0;
            sum_gamc_abs=0;
            for h=1:1:30

sum_gamc_real=sum_gamc_real+real(Mjc(h)*Qjc(h)*exponential(h));
sum_gamc_abs=sum_gamc_abs+(Mjc(h)*Qjc(h)*exponential(h));
            end

            gamc_real(c_w)=sum_gamc_real;%in radians
            gamc_abs(c_w)=abs(sum_gamc_abs);%in radians
            omega(c_w)=w;%in rad/sec
            clear sum_gamc_real sum_gamc_abs

    end
plot(omega,gamc_real,'-k');
hold on
plot(omega,gamc_abs,'-r');
grid on
gama_c_real(:,1)=omega';
gama_c_real(:,2)=gamc_real';
xlswrite('points_gama_omega_eq_4_24_real_2.xls',gama_c_real);
gama_c_abs(:,1)=omega';
gama_c_abs(:,2)=gamc_abs';
xlswrite('points_gama_omega_eq_4_24_abs_2.xls',gama_c_abs);
```